



Calhoun: The NPS Institutional Archive
DSpace Repository

Theses and Dissertations

1. Thesis and Dissertation Collection, all items

1998-09

Spray generation for liquid wall jets over smooth and rough surfaces

Merrill, Craig F.

Monterey, California. Naval Postgraduate School

<http://hdl.handle.net/10945/8998>

Downloaded from NPS Archive: Calhoun



<http://www.nps.edu/library>

Calhoun is the Naval Postgraduate School's public access digital repository for research materials and institutional publications created by the NPS community. Calhoun is named for Professor of Mathematics Guy K. Calhoun, NPS's first appointed -- and published -- scholarly author.

Dudley Knox Library / Naval Postgraduate School
411 Dyer Road / 1 University Circle
Monterey, California USA 93943

NPS ARCHIVE
1998.09
MERRILL, C.

DUDLEY KNOX LIBRARY
NAVAL POSTGRADUATE SCHOOL
MONTEREY CA. 93943-5101

NAVAL POSTGRADUATE SCHOOL

Monterey, California



DISSERTATION

SPRAY GENERATION FROM LIQUID WALL JETS OVER SMOOTH AND ROUGH SURFACES

by

Craig F. Merrill

September 1998

Thesis Advisor:

T. Sarpkaya

Approved for public release; distribution is unlimited.

REPORT DOCUMENTATION PAGE

Form Approved
OMB No. 0704-0188

Public reporting burden for this collection of information is estimated to average 1 hour per response, including the time for reviewing instruction, searching existing data sources, gathering and maintaining the data needed, and completing and reviewing the collection of information. Send comments regarding this burden estimate or any other aspect of this collection of information, including suggestions for reducing this burden, to Washington headquarters Services, Directorate for Information Operations and Reports, 1215 Jefferson Davis Highway, Suite 1204, Arlington, VA 22202-4302, and to the Office of Management and Budget, Paperwork Reduction Project (0704-0188) Washington DC 20503.

1. AGENCY USE ONLY (Leave blank)

2. REPORT DATE

September 1998

3. REPORT TYPE AND DATES COVERED

Doctoral Dissertation

4. TITLE AND SUBTITLE

SPRAY GENERATION FROM LIQUID WALL JETS OVER SMOOTH AND ROUGH SURFACES

5. FUNDING NUMBERS

6. AUTHOR(S)

Merrill, Craig F.

7. PERFORMING ORGANIZATION NAME(S) AND ADDRESS(ES)

Naval Postgraduate School
Monterey, CA 93943-5000

8. PERFORMING
ORGANIZATION REPORT
NUMBER

9. SPONSORING / MONITORING AGENCY NAME(S) AND ADDRESS(ES)

10. SPONSORING /
MONITORING
AGENCY REPORT NUMBER

11. SUPPLEMENTARY NOTES

The views expressed in this thesis are those of the author and do not reflect the official policy or position of the Department of Defense or the U.S. Government.

12a. DISTRIBUTION / AVAILABILITY STATEMENT

Approved for public release; distribution is unlimited.

12b. DISTRIBUTION CODE

13. ABSTRACT (maximum 200 words)

This is an experimental investigation of the filaments and drops generated at the free surface of liquid wall jets formed over smooth- and sand-roughened surfaces. The jet characteristics and the geometric properties of the filaments and drops were measured from images captured using high-speed digital cameras. A statistical investigation of the various properties revealed the characteristic behavior of the filaments and drops as a function of the relative wall roughness, wall curvature and jet inertia. For this investigation, the wall jet Reynolds number ranged from 2.6×10^4 to 4.5×10^4 , the Froude number from 19 to 33 and the Weber number from 1600 to 4700.

The emphasis herein was on the physics of the process rather than the development of empirical relationships. As such, the results indicate that spray generation from a wall jet is a boundary-layer-driven phenomenon, requiring that the jet be in a highly supercritical state ($Fr \gg 1$). Wall roughness reduces the minimum necessary level of supercriticality, but it is not a prerequisite condition for the formation of drops. While increasing the jet inertia enhances the drop formation process, concave wall curvature tends to reduce the quantity and the energy of the drop forming events.

14. SUBJECT TERMS

Spray, Drops, Jets, Bow sheets, Turbulent boundary layers, Liquid sheets

15. NUMBER OF
PAGES
200

16. PRICE CODE

17. SECURITY CLASSIFICATION OF
REPORT

Unclassified

18. SECURITY CLASSIFICATION OF
THIS PAGE

Unclassified

19. SECURITY CLASSIFI- CATION
OF ABSTRACT

Unclassified

20. LIMITATION
OF ABSTRACT

UL

Approved for public release; distribution is unlimited

**SPRAY GENERATION FROM LIQUID WALL JETS OVER SMOOTH AND ROUGH
SURFACES**

Craig F. Merrill

Lieutenant Commander, United States Navy

B.S., United States Naval Academy, 1986

M.S.M.E., Naval Postgraduate School, 1993

M.E., Naval Postgraduate School, 1993

Submitted in partial fulfillment of the
Requirements for the degree of

DOCTOR OF PHILOSOPHY IN MECHANICAL ENGINEERING

from the

NAVAL POSTGRADUATE SCHOOL

September 1998

^

ABSTRACT

This is an experimental investigation of the filaments and drops generated at the free surface of liquid wall jets formed over smooth- and sand-roughened surfaces. The jet characteristics and the geometric properties of the filaments and drops were measured from images captured using high-speed digital cameras. A statistical investigation of the various properties revealed the characteristic behavior of the filaments and drops as a function of the relative wall roughness, wall curvature and jet inertia. For this investigation, the wall jet Reynolds number ranged from 2.6×10^4 to 4.5×10^4 , the Froude number from 19 to 33 and the Weber number from 1600 to 4700.

The emphasis herein was on the physics of the process rather than the development of empirical relationships. As such, the results indicate that spray generation from a wall jet is a boundary-layer-driven phenomenon, requiring that the jet be in a highly supercritical state ($Fr \gg 1$). Wall roughness reduces the minimum necessary level of supercriticality, but it is not a prerequisite condition for the formation of drops. While increasing the jet inertia enhances the drop formation process, concave wall curvature tends to reduce the quantity and the energy of the drop forming events.

TABLE OF CONTENTS

I.	INTRODUCTION.....	1
	A. BACKGROUND.....	1
	B. LITERATURE REVIEW.....	2
	1. Free Jets.....	5
	2. Turbulent Boundary Layer and Open Channel Flows	8
	3. Numerical Investigations.....	12
	C. LIQUID WALL JET	13
	D. CONCLUSIONS.....	14
II.	EXPERIMENTAL EQUIPMENT	17
	A. RECTANGULAR LIQUID WALL JET	17
	B. AXISYMMETRIC LIQUID WALL JET	20
	C. RECIRCULATING FREE-SURFACE WATER TUNNEL	22
	D. MEASUREMENT EQUIPMENT	23
	1. Imaging.....	23
	2. Digital Particle Image Velocimetry (DPIV).....	24
III.	EXPERIMENTAL RESULTS	27
	A. PRELIMINARY ANALYSIS.....	27
	B. DATA ACQUISITION PROCESS AND MEASUREMENT DEFINITIONS.....	30
	C. LIQUID WALL JET ATTRIBUTES.....	32
	1. Transition Regions	32
	2. Jet Thickness	35
	D. FILAMENT AND DROP CHARACTERISTICS.....	36
	1. Drop Diameter.....	37
	2. Filament Length and Angle.....	38
	3. Effective Filament Diameter and Slenderness Ratio.....	39

4.	Filament Volume	40
5.	Disturbance Wave Number	41
6.	Drop and Filament Characteristics as a Function of Streamwise Position	42
E.	WATER TUNNEL WALL JET	43
F.	DISCUSSION OF RESULTS	46
1.	Free Surface Characteristics	47
2.	Spray Generation Features	47
3.	Internal Flow Structure of Bow Sheets	52
4.	Wall Curvature and Inclination	54
5.	Numerical Considerations	54
6.	Application to Bow Sheets	55
IV.	CONCLUSIONS	57
V.	RECOMMENDATIONS	59
APPENDIX A.	FIGURES	61
APPENDIX B.	UNCERTAINTY ANALYSIS	129
APPENDIX C.	TABULATION OF DATA	139
LIST OF REFERENCES	171
INITIAL DISTRIBUTION LIST	177

LIST OF FIGURES

1.	Side view of a free liquid jet discharging into air. From Hoyt and Taylor (1977a)	61
2.	Mean velocity distribution across the turbulent boundary layer formed by smooth- and rough-walled surfaces.....	62
3.	Streamwise turbulence intensity across the boundary layer formed by smooth- and rough-walled surfaces.....	63
4.	Vertical turbulence intensity across the boundary layer formed by smooth- and rough-walled surfaces.....	64
5.	Nondimensional sweep and ejection frequency versus boundary layer thickness, η , adjusted for roughness element height. From Raupach (1981)	65
6.	Streamwise and vertical turbulence intensity across a smooth- and rough-walled open channel. $Re = 9800$, $Fr = 0.2$. For the rough wall, $k/h = 0.065$. From Nezu and Nakagawa (1993)	66
7.	Diagram of a liquid wall jet.....	13
8.	CAD drawing of the rectangular liquid wall jet nozzle	67
9.	Photograph of the rectangular liquid wall jet nozzle.....	68
10.	Equipment arrangement for the rectangular liquid wall jet experiments. The fluid flow path is as indicated by the arrows	69
11.	Photograph of the outside of the rectangular nozzle with the cylindrical gate open	70
12.	Photograph of the outside of the rectangular nozzle with the cylindrical gate closed.....	71
13.	Photograph of the rough ($k/h_o = 0.06$) curved-plate used in the rectangular jet experiment.....	72
14.	Photograph of a rough plate installed in the rectangular liquid wall jet apparatus. The plate mount without a plate attached is shown in the upper left-hand corner	73
15.	CAD drawing of the axisymmetric nozzle.....	74

16.	Side view of the axisymmetric nozzle with the test rod assembly installed	75
17.	An image of the free surface profile of the rectangular liquid wall jet. $Re_x = 2.3 \times 10^6$, $Re = 3.6 \times 10^4$, $Fr = 26$, $We = 3000$, $k/h_o = 0.06$	76
18.	An image of a three-dimensional free surface distortion	77
19.	A typical sequence of images captured for the filament and drop analysis. $Re_x = 2.3 \times 10^6$, $Re = 3.6 \times 10^4$, $Fr = 26$, $We = 3000$, $k/h_o = 0.06$	78
20.	Diagram showing how the filament characteristics are simplified for statistical analysis	79
21.	Photographs of the different regions in a liquid wall jet	80
22.	Distances to surface transition (ST), filament formation (FF) and drop generation (DG) as a function of plate roughness, k/h_o . The uncertainty shown for filament formation at $k/h_o = 0.02$ is typical for all positions.....	81
23.	Normalized mean jet thickness at the beginning of the transition to roughness region. Uncertainty regions are bracketed and the average value for the drop-producing runs is 1.4.	82
24.	Normalized mean jet thickness of the liquid wall jet at the beginning of the filament formation region. Uncertainty regions are bracketed and the average value for the drop-producing runs is 1.7.....	83
25.	Normalized mean jet thickness at the beginning of the drop generation region. Uncertainty regions are bracketed and the average value is 2.0	84
26.	A laser light sheet illuminated photograph of the free surface flow over the axisymmetric liquid wall jet. Flow is from right-to-left and the actual width of the image is about four centimeters	85
27.	Normalized mean jet thickness as a function of the nondimensional streamwise coordinate	86
28.	Standard deviation of the mean jet thickness as a function of the nondimensional streamwise coordinate. The symbols are as shown in Fig. 27.....	87
29.	Distribution of the normalized drop diameter as a function of the relative roughness.....	88
30.	Mean normalized drop diameter as a function of the relative roughness.....	89

31.	Distribution of the normalized drop diameter for the coarse-wall ($k/h_o = 0.13$) at high- and low-Weber number.....	90
32.	Distribution of the normalized drop diameter for the flat- and curved-wall ($k/h_o = 0.06$, $We = 3000$)	91
33.	Distribution of the normalized filament length as a function of the relative roughness.....	92
34.	Distribution of the normalized filament length for the flat- and curved-wall ($k/h_o = 0.06$, $We = 3000$)	93
35.	Mean normalized filament length as a function of relative roughness	94
36.	Distribution of the normalized filament length for the coarse-wall ($k/h_o = 0.13$) at high- and low-Weber number.....	95
37.	Photographs of three different runs at the same streamwise location, $x/h_o \approx 90$	96
38.	Distribution of the normalized effective filament diameter as a function of the relative roughness.....	97
39.	Distribution of the normalized effective filament diameter for the coarse-wall ($k/h_o = 0.13$) at high- and low-Weber number.....	98
40.	Mean normalized effective filament diameter as a function of relative roughness.....	99
41.	Distribution of the normalized effective filament diameter for the flat- and curved-wall ($k/h_o = 0.06$, $We = 3000$)	100
42.	Distribution of the normalized filament slenderness ratio as a function of the relative roughness.....	101
43.	Mean normalized filament slenderness ratio as a function of the relative roughness.....	102
44.	Distribution of the normalized filament slenderness ratio for the coarse-wall ($k/h_o = 0.13$) at high- and low-Weber number.....	103
45.	Distribution of the normalized filament slenderness ratio for the flat- and curved-wall ($k/h_o = 0.06$, $We = 3000$).....	104
46.	Mean normalized filament volume as a function of the relative roughness.....	105

47.	Distribution of the normalized filament volume as a function of the relative roughness.....	106
48.	Distribution of the normalized filament volume for the flat- and curved-wall ($k/h_o = 0.06$, $We = 3000$)	107
49.	Distribution of the normalized filament volume for the coarse-wall ($k/h_o = 0.13$) at high- and low-Weber number.....	108
50.	Mean value of the drop to filament volume ratio as a function of the relative roughness.....	109
51.	Mean disturbance wave number at the tip of the filament just prior to drop separation	110
52.	Distribution of the disturbance wave number as a function of the relative roughness.....	111
53.	Distribution of the disturbance wave number for the coarse-wall ($k/h_o = 0.13$) at high- and low-Weber number.....	112
54.	Distribution of the disturbance wave number for the flat- and curved-wall ($k/h_o = 0.06$, $We = 3000$)	113
55.	Normalized mean drop diameter as a function of the nondimensional streamwise coordinate. Here x and X_d denote, respectively, the distance from the leading edge of the plate and the point at which drop generation begins. Only those locations with >30 observations are shown. The uncertainty is approximately 10 percent	114
56.	Normalized mean filament length as a function of the nondimensional streamwise coordinate. Here x and X_d denote, respectively, the distance from the leading edge of the plate and the point at which drop generation begins. Only those locations with >30 observations are shown. The uncertainty is approximately 15 percent	115
57.	Normalized mean effective filament diameter as a function of the nondimensional streamwise coordinate. Here x and X_d denote, respectively, the distance from the leading edge of the plate and the point at which drop generation begins. Only those locations with >30 observations are shown. The uncertainty is approximately 10 percent.....	116
58.	Normalized mean filament slenderness ratio as a function of the nondimensional streamwise coordinate. Here x and X_d denote, respectively, the distance from the leading edge of the plate and the point at which drop generation begins. Only those locations with >30 observations are shown. The uncertainty is approximately 15 percent.....	117

59.	Normalized mean filament volume as a function of the nondimensional streamwise coordinate. Here x and X_d denote, respectively, the distance from the leading edge of the plate and the point at which drop generation begins. Only those locations with >30 observations are shown. The uncertainty is approximately 25 percent	118
60.	Distances to surface transition (ST), filament formation (FF) and drop generation (DG) as a function of plate roughness for the rectangular and the water tunnel wall jet	119
61.	Mean velocity distribution across the liquid wall jet formed in the recirculating free-surface water tunnel at $x/h_o = 53$	120
62.	Photographs of the interior of a rough-wall liquid jet formed in the recirculating water tunnel. $Re_x = 2.3 \times 10^6$, $Re = 2.8 \times 10^4$, $Fr = 9$, $We = 1100$, $k/h_o = 0.08$	121
63.	Two images depicting the free surface distortions and bubbles that are present in the rough-wall jet formed in the recirculating water tunnel. $Re_x = 1.6 \times 10^6$, $Re = 2.8 \times 10^4$, $Fr = 9$, $We = 1100$, $k/h_o = 0.08$	122
64.	A sequence of images illustrating bubble formation below the free surface of the rough-wall jet formed in the recirculating water tunnel. $Re_x = 1.6 \times 10^6$, $Re = 2.8 \times 10^4$, $Fr = 9$, $We = 1100$, $k/h_o = 0.08$	123
65.	A photograph of a filament above and the bubbles present below the free surface of the rough-wall jet formed in the recirculating water tunnel. $Re_x = 2.7 \times 10^6$, $Re = 2.8 \times 10^4$, $Fr = 9$, $We = 1100$, $k/h_o = 0.08$	124
66.	Streamwise and vertical turbulence intensity across the liquid wall jet formed in the recirculating water tunnel at $x/h_o = 53$	125
67.	Contour plots of v -velocity (at three different times) in the rough-wall jet formed in the recirculating water tunnel at $x/h_o = 53$, as acquired with DPIV. The white shade indicates $v \leq -0.5$ m/s, while the black is for $v \geq 0.5$ m/s. The circled regions show "blobs" with large upward velocities.....	126
68.	Summary of the mean value characteristics as a function of the relative roughness.....	48
69.	The jet Weber number versus the jet Froude number for different levels of v'/U_o as estimated by Eq. (10). The circles mark the three combinations of We - Fr examined in this investigation	127

LIST OF TABLES

1.	Plate roughness levels	19
2.	Description of imagers	23
3.	Summary of the rectangular liquid wall jet parameters and analyses	29
4.	Summary of the water tunnel liquid wall jet parameters	44
5.	Uncertainty of observer interpretation, δ_{OBS}	132
6.	Jet thickness uncertainty for each level of plate roughness	136

LIST OF TABLES

1	Plan of the work
2	Characteristics of the work
3	Summary of the work
4	Summary of the work
5	Summary of the work
6	Summary of the work

LIST OF SYMBOLS

A_{dr}	drop cross-sectional area
A_f	filament cross-sectional area
C_d	nozzle discharge coefficient
D_{dr}	drop diameter
D_f	effective filament diameter, A_f/L_f
D_{rod}	diameter of rod used in axisymmetric nozzle
Fr	jet Froude number, $U/(gh)^{1/2}$
g	gravity
h	local jet thickness
\bar{h}	local mean jet thickness
h_o	mean jet thickness at leading edge of plate
h_{trans}	jet thickness at a transition point
k	mean roughness height
k_s	equivalent sand roughness height
k_s^+	$k_s/(v/u^*)$
k_1	[filament] disturbance wave number, $\pi D_f/\lambda$
ℓ	hydrostatic head above centerline of nozzle
L_f	filament length
N	number of observations of a given event or parameter
Re_d	drop Reynolds number, uD_{dr}/ν_{air} or $\nu D_{dr}/\nu_{air}$
Re	jet Reynolds number, Uho/ν
Re_x	Reynolds number based on streamwise location, Ux/ν or U_sx/ν
u	instantaneous streamwise velocity, $U + u'$
u_{rms}	streamwise turbulence intensity, $\sqrt{u'^2}/U_\infty$ or $\sqrt{u'^2}/U_{max}$
u'	fluctuating streamwise velocity
u^*	friction velocity, $(\tau_o/\rho)^{1/2}$
u^+	u/u^*

U	local mean streamwise velocity, $\frac{1}{N} \sum_{k=1}^N u_k$
U_{\max}	maximum mean streamwise velocity
U_0	mean jet velocity, $C_d \sqrt{2g\ell}$
U_s	velocity at the free surface of the jet
U_∞	free stream velocity
\overline{uv}	turbulent shear stress, $-\overline{u'v'}/U^2$
v	instantaneous vertical velocity, $V + v'$
v_{rms}	vertical turbulence intensity, $\sqrt{v'^2}/U_\infty$ or $\sqrt{v'^2}/U_{\max}$
v'	fluctuating vertical velocity
V	local mean vertical velocity, $\frac{1}{N} \sum_{k=1}^N v_k$
V_0	drop vertical velocity at the moment of pinch-off
∇_{dr}	drop volume
∇_f	filament volume
We	jet Weber number, $\rho U^2 h_0 / \sigma$
x	streamwise axis
X_d	streamwise location at the beginning of the drop generation region
X_f	streamwise location at the beginning of the filament formation region
X_{tr}	streamwise location at the beginning of free surface roughening
y	vertical axis
y^+	yu^*/ν
Z	Ohnesorge number, $\mu/(\rho h \sigma)^{1/2}$
δ	boundary layer thickness or uncertainty
λ	disturbance wavelength
ν	kinematic viscosity of water
μ	dynamic viscosity of water
ρ	density of water
σ	surface tension of water

τ_0 shear stress at the wall

Main body of the document containing several paragraphs of text, which is mostly illegible due to fading. The text appears to be organized into sections or paragraphs, with some lines starting with capital letters.

ACKNOWLEDGEMENTS

To express the entire realization of this endeavor within the binding of this writing would be impossible, since it has been an experience that resulted in a great deal of personal growth, and furnished a collection of cherished memories. As is always the case with such milestones in life, there are a number of people who provided a significant amount of support and guidance along the way.

First, I am eternally indebted to Distinguished Professor Sarpkaya. Besides providing intellectual support (and a good deal of patience!) throughout the course of this research, he has helped to instill in me a greater understanding and appreciation of the scientific process. Genuine intellectual curiosity and unlimited creativity are truly the essence of his character. It was an honor to have had the opportunity to work with Professor Sarpkaya.

I thank my wife, Susan, for providing me with unending moral support and unconditional love; and, Zachary and Anne for helping me to never forget the things that are important in life.

It is true that the history of the world is a long and winding road, but it is not a straight line. It is a road that has been traveled by many people, and it is a road that has been traveled in many different ways. The history of the world is a story of many different people, many different cultures, and many different times. It is a story of many different things, and it is a story that is still being written.

There is a great deal of interest in the history of the world, and there is a great deal of interest in the history of the world. The history of the world is a story of many different people, many different cultures, and many different times. It is a story of many different things, and it is a story that is still being written.

I think that the history of the world is a story of many different people, many different cultures, and many different times. It is a story of many different things, and it is a story that is still being written.

I. INTRODUCTION

A. BACKGROUND

How is it that something as ubiquitous as a drop of water could be so intellectually enticing? The seemingly elementary process of a drop releasing from a fixed object and falling in a quiescent medium presents a myriad of formidable fluid dynamic challenges even for the most capable researcher. As a simple example, consider the following three questions:

- What influence does the fluid circulating within the drop have on the events that will transpire and vice versa?
- At what point in the ever-shrinking neck of the drop do the Navier-Stokes equations become singular?
- When does the dynamic variation of surface tension become a concern?

At present, a complete analytical description remains elusive, while computer models that can accurately reproduce this simple laminar hydrodynamic marvel require a good deal of numerical ingenuity.

Now take this same fluid particle, join it with a continuum of others, and direct it into a similar environment. As it flows out to its ultimate destiny (whatever that may be), imbue it with random velocity fluctuations, expose it to shear forces, and perhaps even accelerate it, before once again leaving it to its own demise. Such events transpire an unaccountable number of times per day as individuals drive their cars to work, fight forest fires, or just turn on faucets. Obviously, there are many challenges associated with understanding how a drop forms in such harsh and stimulating environments. In most instances, the physical parameters of the problem have such complex and intertwined relationships that the engineer must rely on correlations that can guide him within a limited range. If the individual ventures outside the range, then new correlations must be established. Nonetheless, many in-roads have been made which enable us to see the

problems more clearly, even if they cannot be completely understood. For example, the description of the breakup of a liquid column by Lord Rayleigh nearly 100 years ago was fundamental to the principles later developed for the design of ink-jet printers.

The investigation of drops (or spray) discussed in this writing is directed towards understanding how drops are produced at the free surface of a sheet of water flowing over a wall; that is, a high-speed liquid wall jet. The motivation for the investigation is the desire to understand the physics behind the spray created by the bow of a ship as it moves through the water. The bow forms bow sheets (or spray roots) along the hull that produce drops at their free surfaces, and also detach from the hull forming thin liquid sheets, which then disintegrate into spray. The consequence of this process is that much of this water spray is deposited on the superstructure of the ship. At a minimum, this frequently results in treacherous topside footing and reduced equipment operability or damage. In more severe cases, when accompanied by subfreezing temperatures, it can lead to a reduction in ship stability as the frozen spray builds up on the superstructure, raising the ship's center of gravity and, reducing its righting moment. In the case of warships, there is the added concern that the wetted surfaces make the vessel more susceptible to electromagnetic detection, which may limit the ship's ability to fulfill its designated mission. Outside of this specific interest, there are many other practical applications for understanding how a continuum becomes a multi-phase flow via a drop formation process: agriculture, spillway hydraulics, chemical warfare and food processing, to name a few. As the first exploration of this type into this process, the investigation is directed towards acquiring a fundamental understanding of the spray formation process, rather than obtaining correlations to describe the gross spray features.

B. LITERATURE REVIEW

Despite the clear application and intellectual challenges of the high-speed liquid wall jet, wall jets do not appear to have been studied before. Only a number of low Reynolds and Froude number investigations can be found in the literature. Hanratty and Engen (1957) examined the effects of a turbulent gas stream blowing over fairly thin (4.1

to 5.3 mm) slow moving ($11.9 \leq Re_x \leq 508$) smooth-walled water channel flows. Their findings show that the free surface of a shallow water channel is more difficult to disturb than a deeper one. They also found that the free surface characteristics of the water are more strongly influenced by the Reynolds number of the water than that of the air, but a later study of flow down an inclined channel suggests otherwise (Roy and Jain 1989). For the deepest channel combined with the highest gas velocity, the maximum surface distortions noted by Hanratty and Engen were approximately 0.75 mm, which are much smaller than those seen here.

Finley et al (1966) also investigated the mean flow properties of water flow in a smooth-walled shallow channel arrangement. Their goal was to determine an empirical equation for the mean streamwise velocity in the “fully developed region of the flow,” which they define as the point where the free surface is disturbed by the turbulent boundary layer. The Reynolds numbers of the flows they investigated were similar to those encountered here ($Re \approx 3 \times 10^4$), but the Froude numbers ($2 < Fr < 9$) were substantially lower. Using Preston Tubes, Finley et al measured the flow to within 0.76 mm of the free surface of a 8.5 mm deep channel, and found that the mean flow in the buffer and inner region could be described by a power law relationship,

$$u^+ = C \left(\frac{yu^+}{\nu} \right)^{1/n} \quad (1)$$

where,

$$8.02 < C < 8.14 \quad 6.5 < n < 6.61.$$

In the outer region they claim that the velocity profiles followed the log-law,

$$u^+ = \frac{1}{0.42} \ln(y^+) + 5.45 + \omega, \quad (2)$$

where ω is a form of Coles' wake function and is described by the following curve-fitted polynomial,

$$\omega = \frac{1}{0.42} \left(\frac{y}{h} \right)^2 \left(1 - \frac{y}{h} \right) + 1.25 \left(\frac{y}{h} \right)^2 \left(3 - 2 \frac{y}{h} \right). \quad (3)$$

They pointed out that this form of the polynomial appears to be independent of the Reynolds number over the range of values they have examined. However, as was the case with Hanratty and Engen (1957), the work of Finley et al is limited to flows over smooth surfaces with minimal free surface distortions.

In an investigation of self-aerated flows, Volkart (1980) was the first to note the drop-producing liquid jet structures at the free surface of an open channel flow. He did not examine the process by which the structures and their subsequent drops were produced, but instead derived an expression describing the drop size and velocity necessary for a drop to entrain air as it impacted the free surface. More recently, Rein (1998) used an energy balance method to discuss the same problem. Rein points out that Volkart's (1980) more empirical approach did not adequately explain the aeration mechanism that led to the formation of large bubbles in the flow, but he also admits that his analytical solution failed to predict the small droplet aeration witnessed in the laboratory and in shallow channels. Brattberg et al (1998) have performed experimental work in supercritical ($Fr \approx 9$) open channel flows. They, too, were primarily concerned with examining the degree of air entrainment within the jet, and make no mention of the free surface characteristics. Apparently all three works assumed that the drop formation is only a result of turbulence existing near the free surface, but they did not discuss the influence of the channel wall and its boundary layer on the production of this turbulence. Rein recognizes that the boundary layer is somehow involved, but concedes that there is a general lack of knowledge of turbulent free-surface flows in the high Froude number regime ($F \gg 1$).

Others have also examined flows of this nature, but their results do not further elucidate the physics important to this study. For example, they were concerned with flows having much lower Reynolds numbers than those cited above (Binnie 1957, Benjamin 1957), extremely thin films (Knuth 1955), or considered instances where the liquid flow is driven with a large shear imposed by a moving gas above the liquid (van Rossum 1959, Miles 1960, Craik 1966).

1. Free Jets

Previous examinations of the factors that contribute to liquids breaking up into drops are mostly found in free jet studies. Although the mechanisms involved are somewhat different than those encountered here, much of the physics noted in these efforts is still relevant to the actions which occur at the free surface of a liquid wall jet. As it is encountered in most studies, the term “free jet” is understood to imply that the jet is issuing into an environment with a substantially lower density than that of itself. In most cases it is also axisymmetric at the point of origin. One of the earliest analytical works examining the breakup of such a liquid jet is the linear analysis of Rayleigh (1945). He found that axisymmetric infinitesimal disturbances with wavelengths greater than the jet circumference are amplified, and that disturbances with wavelengths approximately equal to $4.5 \cdot D_{dr}$ have the maximum rate of amplification. Weber (1931) and Ohnesorge (1936) expanded his results to include the effects of viscosity, which Sterling and Sleicher (1975) then modified to achieve better agreement with the reported experimental data in the nonlinear region of jet breakup. Yuen (1968) and Neyfeh (1970) both developed a complex nonlinear analytical analysis to account for finite-sized disturbances. Each of the above efforts met with a certain degree of success, producing some marginal improvement over the simple analysis of Lord Rayleigh.

Others have used experimental results to describe the breakup process in terms of the Weber, Froude, Ohnesorge and/or Reynolds number of the jet. For example, the following is one of the more popular descriptions by Ranz (1958) and Reitz (1978), and separates the modes of jet breakup into four regimes that are functions of the Weber number:

- Drip mode: Small drops form at the nozzle exit, inertia is negligible, and surface tension and gravity govern the breakup of the jet.
- Rayleigh mode: A low speed coherent jet exists, but its velocity is low enough that the shear interaction with the surrounding gas is negligible.

Inertia and surface tension are the predominate forces, causing the jet to disintegrate into drops with diameters greater than that of the undisturbed jet.

- First wind-induced instability mode: The higher inertia liquid jet develops large instabilities resulting from the relative motion between the jet and the gas. Surface tension acts to stabilize the jet since the disturbance wave numbers produced in this mode are greater than the critical value (Ruff et al 1989).
- Second wind-induced instability mode: As described by Wu et al (1991, 1992), small drops are released from the surface of the liquid, and any small-scale disturbances resulting from pre-existing turbulence serve to enhance the drop formation process. As shown in Fig. 1 (Hoyt and Taylor, 1977a), small-scale surface irregularities appear as a result of the pre-existing turbulence in the jet. These disturbances can produce fluid filaments which extend radially outward, and frequently break up into drops (where $D_{dr} \ll D_{jet}$). Both Hoyt and Taylor and Wu et al (1992) have concluded that aerodynamic shear and drag do not appear to contribute to the formation of these drops. Although the main body of the jet may eventually display large-scale irregularities, the majority of the disintegration process occurs through surface disintegration (Ruff et al 1989). For both wind-induced regimes, the jet length becomes shorter, and the disintegration more chaotic, as the jet velocity increases.
- Atomization mode: The jet breaks up at the nozzle exit, forming a fine spray of drops. The mechanisms leading to atomization are still not fully understood.

The velocity profile at the nozzle exit is also an important jet breakup parameter. As in the case of pipe flows, the length-to-diameter ratio of the nozzle determines the state of the boundary layer and, therefore, the velocity profile at the exit. For laminar jets, the greater the length-to-diameter ratio, the more developed the velocity profile is at the nozzle exit. In studies on the stability of Newtonian jets, Rupe (1962) and Grant and

Middleman (1966) found that the velocity profile does not influence the breakup length of the jet at low Reynolds numbers. However, beyond a certain point within the Rayleigh regime, a flat velocity profile (i.e., slug flow), or a fully developed turbulent profile, produce more stable jets than does a fully developed laminar profile. The results of Sterling and Sleicher (1975), together with those of Tseng et al (1992), support this conclusion for higher velocity jets as well. The physical reason for this is that the greater the variation in the velocity profile, the greater the relaxation the jet undergoes once it exits the nozzle and is no longer constrained by the no-slip condition at the nozzle wall. The redistribution of the momentum tends to promote the growth of disturbances that ultimately break up the jet.

In summary, the surface disintegration of liquid jets (which may be analogous to the surface behavior of liquid wall jets) is primarily a function of the turbulence within the jet. At low enough flow rates, the radial turbulent component is insufficient to produce the drop forming filaments. As the velocity increases into the Wind Induced regimes, the radial turbulent fluctuations become significant enough to lead to drop production along the jet surface. The source of turbulence can be provided by pre-existing turbulence upstream of the nozzle, velocity profile relaxation at the discharge of the nozzle, and/or turbulent boundary development along the inner wall of the nozzle. Further discussion of the present state of knowledge regarding spray formation from a liquid jet may be found in the review of Lin and Reitz (1998).

Although not germane to this research, it must be mentioned for the sake of completeness that there is a large body of knowledge related to the disintegration of thin liquid sheets. Although the mechanics that lead the sheets to deteriorate into filaments of fluid is much different from that presented above, the breakup of the filaments into drops is similar to that of jets in the Rayleigh regime. For a fairly complete discussion of the factors influencing the breakup of thin liquid sheets, see the works of Squire (1953), Dombrowski and Fraser (1954), Brown (1961), Dombrowski and Hooper (1962), Briffa and Dombrowski (1966), Ford and Furnidge (1967), Crapper et al (1973, 1975), Mansour and Chigier (1990, 1991) and Chubb et al (1993).

2. Turbulent Boundary Layer and Open Channel Flows

As mentioned earlier, there has been little investigation into the nature of the subsurface characteristics in high-speed thin liquid wall jets. Experimentally, it is a considerable challenge to measure the flow field in the vicinity of a highly disturbed free surface such as encountered here. Using a two-dimensional laser doppler anemometer in an open channel flow arrangement, Nezu and Rodi (1986) could get no closer than about 5 mm to a free surface possessing only small variations in elevation. Moreover, the work which has been performed in this area is limited to less challenging conditions such as low Reynolds or Froude number flows over smooth surfaces. Hence, it is unclear how the large free surface structures arise from the apparently violent turbulent interactions beneath the surface.

To glean some insight into the subsurface characteristics of the jet, it is beneficial to revisit some of the previous works concerning turbulent boundary layer flows over smooth and rough surfaces. Because we desire to contrast the smooth- and rough-wall behaviors, the nature of these flows will be discussed with their velocity components normalized by either the free stream or mean velocity. The reason for this is that the wall variables are strongly dependent on surface roughness as well as the mean velocity profile in the sublayer. If comparisons are made based on normalizing the velocities (U , u' , v' and w') by u^* , then it is more difficult to draw conclusions about the influence of the roughness on these parameters, since the normalization variable is also affected. Also, the dramatic nature of the flow witnessed at the free surface of the high-speed wall jets examined in this study suggests that the mean behavior in the sublayer does not adequately describe the local behavior, and the instantaneous local shear stress at the wall will not be measured directly. For all of these reasons, it is all the more logical to avoid using the wall variables whenever possible.

Figure 2 combines the experimentally determined mean velocity profile data of Klebanoff (1954), Pimenta et al (1975) and Ligrani et al (1979) for turbulent boundary layer flow over a smooth-wall, fully developed rough-wall, and artificially thickened fully developed rough-wall, respectively. All three curves are plotted for similar values of Re_x .

The "fully developed rough-wall" flow implies that the data are taken at a downstream location where $k_s^+ > 60$. The reduced values near the wall for the rough-surfaces are a consequence of the added drag of the roughness elements. One of the more interesting, and perhaps most relevant, aspects of turbulent boundary layer flow ascertained from the above analyses is the change that occurs in the streamwise turbulence intensity, u_{rms} , in the near-wall region. As shown in Fig. 3, the maximum value of the rough-wall u_{rms} is about 10 percent lower than that of the smooth-wall, and the maximum value occurs at a point further away from the wall. Grass (1971) was one of the first to notice this behavior (further pointing out that as the size of the roughness increases, u_{rms} decreases near the wall). Based on continuity requirements alone, one would then expect that the remaining turbulence intensity values must increase. As shown by Grass, and demonstrated here in Fig. 4, this is indeed the case. Grass' results were for low Reynolds number open channel turbulent flows, but the results of Pimenta et al (1975) and Ligrani et al (1979) show that this behavior is also true for higher Reynolds number boundary layer flows. It has been understood for some time that the turbulence produced by flow over a smooth-wall is largely a result of the bursting phenomenon. That is, the lift-off and breakdown of the streamwise low-speed streaks followed by an in-rush of fluid from the high-speed to the low-speed region. This sequence is often defined in terms of an ejection ($u' < 0, v' > 0$), and sweep ($u' > 0, v' < 0$) process. The existence of these streaks was first noted by Klebanoff and coworkers in the 1950s, and their role in turbulence production later confirmed by others (i.e., Kline et al 1967). Kim et al (1971) claim that all of the turbulence produced within $y^+ = 100$ is via the ejection and sweep process. Although the streaks are also present on rough surfaces, the higher level of turbulent kinetic energy (TKE) (Ligrani et al 1979); the more isotropic nature of the turbulence; and, the structural difference in the turbulence components (Krogstad and Antonia 1994), suggest that the predominant turbulence producing mechanism is altered by the existence of roughness. It is generally thought that, unlike the "gentle" lift-off of the slow moving streaks on a smooth-wall, the ejection and sweep processes on a rough surface are much more violent. Nonetheless, for both surface types Grass (1971) notes—and Raupach (1981)

demonstrates statistically—that the ejected fluid behaves in a quasi-coherent fashion, moving almost vertically through the boundary layer. Raupach further pointed out that:

- Within $y/\delta \approx 0.2$, nearly all of the stress results from the sweep and ejection process, with each making equal contributions. Furthermore, they are the *only* source of high level stress (i.e., from 5 to 10 times \overline{uv}).
- This trend continues until very near the surface of a smooth-wall ($y^+ < 20$) when the sweeps become dominant in the viscous sublayer.
- For rough-walls, sweeps are the predominant contributor to stress from just above the tops of the roughness elements to down in the roughness canopy. The sweeps in this region are capable of producing stresses as high as 20 times \overline{uv} .
- As the number of roughness elements is increased (with sufficient interstitial spacing), the frequency of the ejections and sweeps also increases.

The ejection frequency plot of Raupach, Fig. 5, supports the notion that ejections are coherent motions; and, it shows that the ejection frequency measured at different points in the boundary layer remains essentially constant. This suggests that the ejected fluid proceeds vertically with its motion only minimally influenced by the local boundary layer conditions. In contrast to Raupach's results, Krogstad et al (1992) found that the frequency of the ejection and sweep events increases with roughness; and, that the influence of roughness is not confined to the near wall region as it is often assumed. The reader is referred to the review articles by Robinson (1991) and Smith and Walker (1995) for more detailed discussions on the nature of coherent structures in boundary layer flows.

Another relevant aspect of the boundary layer research which may be applicable to this study are investigations of how the boundary layer responds to changes in surface roughness. Antonia and Luxton (1971) showed that the inner boundary layer adjusts from a fully developed smooth profile to a rough profile within 20δ of the start of the roughened region. In the case of a rough-to-smooth transition, Andreopoulos and Wood

(1982) found that the transition took over 55δ after the flow was exposed to a 150-mm length of roughness. A similar result is also noted by Pimenta et al (1975) who found that a rough-wall boundary layer transitions from laminar to turbulent behavior fairly rapidly near the wall, but much slower in the outer region (and that the turbulent variables continue to evolve long after the mean properties have reached their fully turbulent form). As they suggest, the outer flow appears to have a fairly long “memory” of its upstream conditions. Gibbings and Al-Shukri (1997) conclude that roughness tends to shorten the length of the transition from laminar to turbulent characteristics, in addition to moving the beginning of this transition further upstream.

With the exception of Grass (1971), all of the previous studies were limited to boundary layer flows. Therefore, the question of how the free surface might affect these results needs to be discussed. As was done by Finley et al (1966) for a shallow channel, it is fairly common to use the law of the wall adjusted by a wake parameter to describe the mean smooth-wall open channel flow velocity profile. However, unlike Finley et al, most open channel flow investigations conclude that the law of the wall can be used to describe the entire region. For example, Nezu and Nakagawa (1993) have shown that

$$u^+ = \frac{1}{0.41} \ln(y^+) + A + \frac{2\Pi}{0.41} \sin^2\left(\frac{\pi y}{2h_o}\right) \quad (4)$$

where Π is Coles' wake strength parameter and varies from zero at $Re \approx 3 \times 10^4$ to 0.2 at $Re > 2 \times 10^5$. For rough surfaces they claim the same equation can be used if the middle term is replaced with

$$\frac{1}{0.41} \ln(k_s^+) + A \quad (5)$$

and y/k_s is substituted for y^+ in the first term. As the fully rough region is reached, the actual value of the middle term departs from Eq. (5), and approaches a constant value of 8.5. It is thought that the constant A can be universally defined as 5.0 to 5.3, however the results of Tominaga and Nezu (1992) suggest otherwise, especially at supercritical Froude numbers. Likewise, the value of Coles' wake parameter appears to vary rather unpredictably for changes in k_s , Re and Fr .

As was the case in boundary layer flows, wall roughness influences the u_{rms} and v_{rms} distributions across the channel depth, but not as dramatically. This is clearly seen by comparing data from Nezu and Nakagawa (1993), shown in Fig. 6, with that of Figs. 3 and 4. Figure 6 also shows very little difference between the smooth and rough flows in the outer region of the flow, but this result is apparently limited to low Froude number ($Fr < 1$) flows. As Fr is increased, the turbulent intensities in the outer region grow, and Nezu and Nakagawa attribute this to the formation of waves on the free surface that begin contributing to the turbulence in the region.

Near the free surface, surface tension begins to diminish the vertical velocity fluctuations as described by Davies (1972). Comparing open channel and closed channel flows, Nezu and Rodi (1986) found that the variations in v_{rms} were limited to the region above $y/h_0 = 0.9$, suggesting that the influence of a calm free surface on open channel turbulence is limited to the upper ten percent of the channel. In this region Komori et al (1987) found that u_{rms} increases at the expense of v_{rms} .

3. Numerical Investigations

As well as the analytical efforts mentioned earlier, a number of researchers have used linear and nonlinear techniques to successfully describe the characteristics of laminar jets with finite disturbances (for example, Lee 1974). To effectively predict results in liquid wall jets using a numerical scheme, the code must be capable of modeling the turbulence, free surface deformation and surface tension over a three-dimensional domain. Moreover, if aerodynamic effects are to be considered, it must also be able to do the above while simultaneously solving the Navier-Stokes equations for two fluids of large density ratio (≈ 1000). The ability to incorporate a turbulent model with that of a reliable surface tension model is at the forefront of CFD research. The Theoretical Fluids Group at Los Alamos National Laboratory has successfully demonstrated a two-dimensional laminar free surface code (Kothe and Mjolsness 1992), and work continues on a three-dimensional version incorporating turbulence modeling.

At the present time, however, it has been ascertained that the existing commercial codes are simply not capable of handing this complex problem.

It is important to recognize that the uniqueness and challenges present in the liquid wall jet make it unlikely that a numerical code will successfully consider all of the necessary parameters in a realistic manner a priori. The ability to predict the behavior witnessed in this research will likely depend on the programmer being able to extract the physics of the process based on insight provided by experiments such as this.

C. LIQUID WALL JETS

As suggested by Fig. 7, a liquid wall jet is most simply described as an extremely shallow high-velocity open-channel flow. The liquid jet discharges from a nozzle and is bounded on its lower side by a wall, which can be smooth or rough, and above by a liquid-air interface.

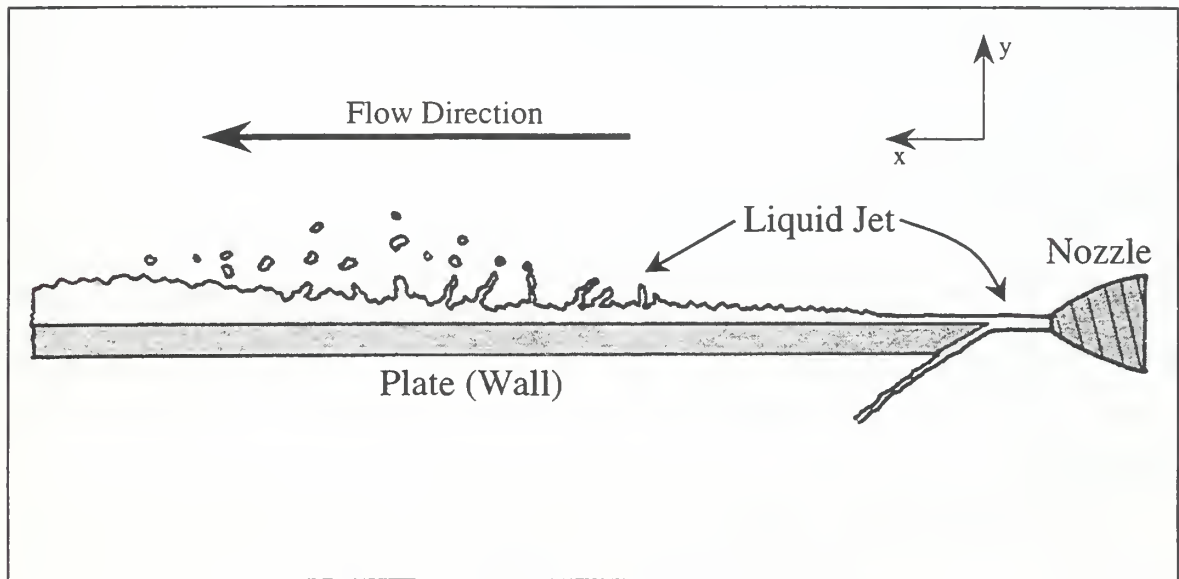


Figure 7. Diagram of a liquid wall jet.

If the Reynolds, Weber and Froude numbers are sufficiently large, the boundary layer formed at the wall quickly reaches the free surface, causing it to form large three-dimensional disturbances. As the agitation increases, some of the disturbances take the

form of long narrow protrusions (also referred to as fluid filaments, ligaments, columns or jets) that can extend far above the level of the local mean free surface. In some instances these filaments break up into one or more drops as surface tension acts on disturbances imbedded within them to reduce the overall energy of the filament. In other cases, they simply retract back into the body of the wall jet if the form of the disturbances or the length of time that the filament exists above the free surface is insufficient to allow surface tension to act.

As the jet flows downstream, the momentum flux to the wall causes the jet to slow and thicken. The falling drops formed by the breakup of the liquid filaments, as well as the downward motion of the larger three-dimensional surface disturbances, draw air into the body of the jet. This self-aeration process adds to the turbulent nature of the flow, and reduces the mass density of the jet as it progresses downstream. All of these factors—which appear to be functions of the relative wall roughness, and the Reynolds, Froude and Weber number of the flow—act to prevent the flow from reaching any type of stable state or dynamic similarity in the regions investigated in this research.

D. CONCLUSIONS

Based on an extensive review of the relevant published literature, it is clear that little work has been performed in the area of interest to this study: spray and drop formation from high-speed liquid wall jets. Nonetheless, some important facts from the related research can be transferred to the present investigation for guidance and interpretation.

Since the immediate concern is a fundamental understanding of the behavior of bow sheets, it is important that the liquid wall jets retain a character similar to that of the ocean surface encountered by a ship as it glides through the water. Therefore, prior to encountering the wall, the liquid jet should have a low turbulence intensity and no boundary layer formation. This makes the nozzle shape a critical element of the experimental design.

Researchers in the field of free jets have concluded that aerodynamics is not a significant factor vis-à-vis drop formation at the surface of the jet. However, the recognized self-aeration process that occurs in many channel flows suggests this may not be entirely true. It will be important to determine whether or not the relative motion between the air and the liquid wall jet, as well as that of the individual fluid filaments, is influential to the process.

The character of the wall surface is important because the wall is the primary source of turbulence in the liquid wall jet. The results of both boundary layer and open channel investigations show that wall roughness alters the mean flow properties and their moments, in addition to the formation process of any quasi-coherent structures existing in the flow. Some studies have concluded that the coherent structures themselves are the main source of turbulent production. While it is obvious that the turbulence generated by the free surface disturbances is important, it is also clear that these disturbances are a product of the boundary layer growth; and, that they alone cannot account for the existence of the liquid filaments and drops. Therefore, the question of how surface roughness and coherent turbulent structures influence the formation of filaments and drops above the jet remains unanswered.

Guided by the purpose of the research, as well of what is currently understood about liquid wall jet phenomena, the goals of this study are to:

- Better elucidate the characteristics of the free surface in high-speed liquid wall jets.
- To explain the physics behind the behavior observed by qualifying and quantifying the influence of the dominant factors such as relative roughness, Reynolds number, Froude number and Weber number.
- To relate the subsurface nature of the jet to that of its free surface.

All of the effort that has gone into investigating the problem points out that there are a number of issues affecting the drop-formation process as well as the techniques used

to investigate it. These issues will be addressed in the body of the thesis, but it is important to point out some of the more significant ones now, enabling the reader to be better prepared and fully aware of some of the limits of the research. For example, it is important to understand that one is dealing with a highly-disturbed free surface that makes the existing tools insufficient for measuring many of the properties of interest. The thickness of the liquid jet is so small that it is impossible to assess many of the properties normally described in boundary layer or channel flows. The large turbulent eddies that are formed change their shape and breakup in a rather random process, as they move rapidly through the jet. The phenomenon of a liquid wall jet is never stationary. From inception, the jet gives up energy to the wall and through the free surface, thereby continuously changing its own character. This energy transfer is so rapid that the jet loses the ability to sustain these same energy transfer mechanisms as it approaches the end of the wall. Reaching this latter stage, the changes in jet character bring about a flow that is of no particular interest to this investigation. All of the above described events transpire in less than two-tenths of a second, over a distance of about one meter.

Again, the aim is to understand the physics of the spray formation process so that action may be taken to reduce the danger this spray presents, primarily resulting from its ability to scatter electromagnetic radiation. Using all means available, we have arrived at the results contained within. They include the size, trends and behavior of the drops and filaments formed at the free surface of liquid wall jets. These jets were developed over smooth and rough surfaces that were either flat or curved.

II. EXPERIMENTAL EQUIPMENT

A. RECTANGULAR LIQUID WALL JET

The nozzle which forms the rectangular jet was fabricated out of two solid blocks of aluminum using the wire electron discharge machining (EDM) process, and its surfaces were covered with a smooth polymer coating to prevent corrosion. Because it is recognized that the nozzle characteristics have a significant impact on the resulting jet—and that these characteristics are not easily quantified—every effort was made to incorporate the experience of previous researchers in this design (Dombrowski and Fraser 1954, Hoyt and Taylor 1977a and 1977b, McCarthy and Malloy 1974, Rouse and Abol-Fetouh 1950 and Rouse et al 1951, Wu and Faeth 1995). The design goal was a nozzle which produced a rectangular jet containing a minimum amount of turbulence and an extremely thin boundary layer, so that the flow at the exit would have a nearly flat velocity profile (i.e., "slug flow"). By doing so we ensure that the jet characteristics were a result of the fluid dynamic influences occurring outside the nozzle body.

The nozzle contracts on its upper and lower surfaces, as shown in Figs. 8 and 9, but the sidewalls remain parallel. Its area-contraction ratio is 13.9 and the shape of the contraction is taken from that which Rouse et al (1951) determined to be an optimum shape for producing an axisymmetric jet with a maximum breakup length. As previously explained, a maximum breakup length is indicative of a jet possessing a minimum amount of free-stream turbulence and a flat velocity profile at the nozzle exit. The entrance to the rectangular nozzle was streamlined to ensure that the flow entering it was smooth and undisturbed, and the discharge coefficient for this nozzle system was 0.91 over the range of flow rates considered. As shown in Fig. 10, the nozzle is mounted to one side of a 23,000 liter U-tunnel that was previously used in the oscillating flow research of Sarpkaya (1977, 1986). The water discharged from the nozzle and formed an 8-mm thick by 300-mm wide rectangular free jet. After a "free flight" distance of 7.6 cm, the main body of the jet flowed over a sharp-edged plate, thereby forming the liquid wall jet. The water eventually runs off the end of the plate (except for a small amount which flows over the sides), and falls down into a catch tank which is tilted away from the U-

tunnel at a 5° angle, allowing the lower end to act as a weir. A five horsepower pump takes suction on the bottom of the tank and pumps the water back into the *opposite* leg of the U-tunnel.

The hydrostatic head in the tunnel determines the mean velocity of the water at the exit of the nozzle. During test runs, this head is maintained constant by throttling the ball valve at the discharge side of the pump. The net positive suction head (NPSH) to the pump is maintained constant by keeping the pump flow rate slightly less than that of the nozzle. This caused the catch tank to overflow a small amount at its lower end, allowing the weir to keep the tank level—and hence, the pump NPSH—constant at the height of the lower end. Providing a small steady addition of city water during operation compensated for the spillage.

With this arrangement, it was possible for the system to be operated continuously for an indefinite period of time. Moreover, the large water volume of the tunnel kept the water velocity through the horizontal section of the tunnel below 1.5 cm/sec even at the highest jet velocity of nearly 8 m/s. This low internal flow rate resulted in long fluid recirculation times which, along with a six-inch thick foam divider plate placed across the horizontal mid-section, ensured that the water entering the nozzle was quiescent. This fact was verified by performing flow visualization with food dye inside the U-tunnel.

The flow through the nozzle is controlled via a pneumatically operated cylindrical gate. When the gate is lifted as shown in Fig. 11, the water discharges from the nozzle, and after the short free flight, flows over a plate with a sharp leading edge. In Fig. 12 the gate is closed over the nozzle opening. The plate mount is designed to accommodate plates of various geometries (i.e., flat, curved or varied geometry) and is capable of inclining a given plate up to 15° from the horizontal. Figure 7 provides a side view of the jet discharging over a simple flat plate and demonstrates how the sharp leading edge is positioned to cut off a thin portion (about 2 mm) of the bottom side of the liquid jet. This further ensures that the flow engaging the upper surface of the plate is free from any free shear layer effects that may have developed upon exiting the nozzle.

It was discovered by trial-and-error that using a plate that is slightly wider than the nozzle minimizes the side spray produced when the surface-edges of the jet (distorted

by surface tension) encounter the corners of the plate. To permit flow visualization near the wall, five 0.8 mm diameter dye ports were drilled about 5 cm from the leading edges of the smooth and roughest flat plates used in this experiment. All of the flat plates were fabricated from 2.0 or 2.5 cm thick acrylic sheets. The concave curved plate, Fig. 13, was fabricated from a 3 mm thick acrylic sheet bent to a 3 m radius of curvature. The first 13 cm of the curved plate is flat and bonded to the top of a 2.5 cm thick acrylic piece to prevent vibration. A 0.8 mm wide dye injection slot (angled back at 45°) was machined into this thicker region about 5 cm from the leading edge. The curve of the plate begins 13 cm back from the leading edge, and is held rigid by vertical supports that fasten to the plate mount on their lower edges. All of the plates were cut and the edges machined, resulting in a final width of 33 cm and a length of either 120 or 180 cm. The leading edge of each plate was milled to produce a 30° leading edge with the sharp-edge having a radius of curvature of not more than 0.4 mm. This ensured that the edge was sharp enough to prevent the flow from separating, yet thick enough to prevent it from being easily damaged.

As shown in Table 1, three different levels of plate (or wall) roughness were used in this investigation. The roughness elements consist of sand which was sifted numerous times to achieve the desired size range. The roughness is applied to the plate by coating the top with an extremely thin layer of epoxy (applied with a brush), and then gently shaking a sand-filled sifter over the surface. This resulted in walls with evenly coated rough surfaces.

Roughness Description	Minimum element size (mm)	Maximum element size (mm)	Mean element size (mm)
Fine	0.104	0.147	0.13
Medium	0.300	0.355	0.33
Coarse	0.590	0.840	0.72

Table 1. Plate roughness levels.

The walls were mounted in the experimental facility by bolting them from underneath to a mount fabricated out of 6.4 mm aluminum. As shown in Fig. 14, the front and rear of the mount rests on two horizontal rods, and the ends of these rods are

individually pinned to fine-control traversing mechanisms. This allows the attached wall to be placed at angles of attack from -5° to $15^\circ \pm 0.25^\circ$, and provides a small amount of lateral angle adjustment. The slots in the top of the mount permit the wall to be placed at various axial positions, however, for all of the experiments presented here the plate was positioned to give the jet a free-flight distance of 7.6 cm.

The thickness of the jet was measured along the centerline of the plate at various streamwise positions using a scale inserted from above. The scale was fabricated from a 0.23-mm thick, 4-mm long, stainless steel razor blade. The device was placed in the jet with its length parallel to the direction of flow, and adjusted so that it produced no noticeable wake. The jet thickness was then determined by reading the division markings at the front of the scale (from video recordings). An attempt was made to use a capacitance probe, but it proved to be highly non-linear and the results were not repeatable. The reasons for this will be explained later.

B. AXISYMMETRIC LIQUID WALL JET

An axisymmetric jet facility was constructed to overcome some of the experimental and visualization limitations experienced with the rectangular jet and to allow for different geometry wall jets. The nozzle, Fig. 15, is mounted in the horizontal section of the U-tunnel, downstream of the foam divider plate. The entrance region is streamlined using a half-toroidal (or "donut") shape that mounts against the wall of the tank and possesses an inner diameter identical to that of the nozzle exit. The overall contraction ratio is 17.6 and the discharge coefficient of the system was experimentally determined to be 0.77. The flow rate through this nozzle is substantially smaller than the rectangular nozzle, so it is not necessary to provide it with a recirculation system. Instead, the nozzle discharges into a catch basin that empties to the laboratory drainage system. The head in the U-tunnel is maintained constant by throttling on the city supply line.

It is envisioned that a variety of shapes such as cones, rods or wedges could be placed at the outlet of the nozzle, but for this work, only a rod is used. Figure 16 provides a side view of the apparatus. A thick-walled tube is mounted on the end of the

acrylic test rod, and a plate with a foam face is mounted near the point where the tube and the rod are joined. When the assembly is fully out, the foam-covered plate acts as a stopper—with the assistance of hydrostatic pressure—to block flow through the nozzle. When the assembly is fully inserted against the back wall of the U-tunnel, flow passes out of the nozzle and along the test rod. The pole over which the assembly moves, and the linear bearing that supports the far end of the test rod, are carefully positioned to ensure the device is centered in the nozzle. This guarantees that the jet thickness is uniform about the rod when it exits the nozzle. The significance of this arrangement is that there is no stagnation point where the flow encounters the rod. Thus, no undesirable spray or other disturbances are produced; and, it provides a clearer visual presentation of the events that occur since one is not viewing the region of interest through many centimeters of other flow disturbances. The limitation of the system is that there is only a short region over which the flow may be examined before gravity begins to noticeably alter the jet thickness about the rod.

A single test rod was roughened (using the medium roughness sand) as described for the flat plates except that the rod was slowly rotated on a lathe during the application process. Additionally, two 1 mm wide by 10 cm long diametrically opposed strips were clear of roughness to permit a laser light sheet to pass through the rod for flow visualization. As shown in Fig 15, the nozzle exit diameter is 3.18 cm, while the rod in Fig. 16 has a diameter of 2.54 mm, giving a jet thickness of 3.18 mm (about half that of the rectangular nozzle).

Unlike the rectangular nozzle that produces a jet with a fixed initial thickness, h_0 , the axisymmetric arrangement allows h_0 to be varied by simply installing a different diameter rod (a quick and easy process). This provides a greater variety of jet Reynolds, Weber and Froude number combinations which can be examined. However, before substituting the axisymmetric results for those of the rectangular device, it must first be verified that h_0/D_{rod} , where D_{rod} is the diameter of the test rod, is small enough to prevent the region of interest from being affected by the curvature of the rod.

C. RECRICULATING FREE-SURFACE WATER TUNNEL

Both of the above nozzle systems provide the capability to visualize and quantify the surface features of liquid wall jets. However, the narrow jet thickness coupled with the large free surface distortions made it impossible to measure the subsurface characteristics with any degree of certainty. Clearly, one could do so with a somewhat thicker jet, provided that the sides of the jet are optically transparent walls that will permit the use of a digital particle image velocimeter laser (DPIV). A low-turbulence water tunnel used in previous works (Sarpkaya and Neubert 1994) provided the most direct means of achieving this objective. The tunnel has a test section with thick Plexiglas bottom and sidewalls. A 35 horsepower pump provides flow through a 38 x 70 x 125 cm test section via a flow straightening honeycomb mesh and a settling chamber. For this experiment, a 2.5 cm thick clear acrylic plate is mounted to the bottom. The plate extended 30 cm into the settling chamber and had a semi-circular leading edge. The sides of the plate are machined to exactly match the width of the test section, and the desired jet thickness is obtained by clamping a vertical aluminum gate to the wall at the entrance of the test section. The gate is fabricated from a 6.4 mm thick aluminum sheet, with the upstream bottom edge machined to a 3.2 mm radius of curvature, and the trailing edge into a sharp 90° corner. The gate can be raised or lowered to achieve the desired jet thickness.

The entrance region to the water tunnel jet was significantly different from that of the rectangular jet since it was not formed using an optimum nozzle shape, nor did it have an interval of free flight before encountering the wall. The wall itself acted as the lower half of the nozzle and the contraction of the settling chamber provided a small amount of fluid acceleration. The majority of the area-contraction was achieved by the vertical plate at the entrance to the test section. Overall, the fluid in the water tunnel experienced an effective contraction ratio of about 55 before reaching the test section. The recirculating pump of the water tunnel had a variable speed controller capable of providing flows with mean velocities from 0.5 m/s to 10 m/s for the wall jet examined in this investigation.

The surface of the flat plate is roughened by applying sand to the surface of a 3 mm thick acrylic sheet, and then attaching this sheet to the flat plate installed in the test

section. A 1.0 mm wide strip along the center region of the roughened plate was clear of sand to allow a laser light sheet to penetrate into the flow region. A rough plate made from the coarse sand, and a smooth plate were examined in this research.

All the analyses performed in the water tunnel were constrained to the center of the test section to eliminate the influence of the sidewalls on the observed flow.

D. MEASUREMENT EQUIPMENT

Two primary means were used to gather the data in this research. The first is that of high-speed imagers and cameras. The second is digital particle image velocimetry (DPIV) which was used to obtain the subsurface data in the water tunnel. The constantly varying optical path and narrowness of the region made the use of DPIV and laser doppler velocimetry (LDV) impractical for the rectangular and axisymmetric jets.

1. Imaging

As listed in Table 2, various coupled capacitive discharge (CCD) imagers (also referred to as cameras) were used to collect data for flow visualization as well as images that could later be quantitatively analyzed.

Imager	Speed (frames/sec)	Recording Time	Shutter Speed (sec)	Recording Media
NAC HSV-500	250 or 500	14 min	1/250 - 1/10,000	SVHS Tape
Redlake HR 2000	50 - 8,000	4 - 8 sec	1/50 - 1/40,000	Camera RAM
NEC TI-22P	30	120 min	1/30	SVHS Tape

Table 2. Description of imagers.

The data used for quantitative analysis of the surface of the rectangular liquid wall jet was gathered using the NAC camera. It was mounted on a tripod along side of the wall jet at the desired location downstream of the leading edge of the plate ($x/h_o = 0$). During the image capturing process, a scale was placed in the focal plane and recorded for later dimensional scaling. A typical example of the jet free surface image is shown in Fig. 17 (in this and all subsequent figures, flow is from right-to-left). After an image or a

sequence of images was captured on videotape, it was downloaded to a PC using a frame grabber (Imagraph Imascan Prism/Spectrum Board Set), and subsequently analyzed using the Optimas 6.1 and Optimas MA 3.1 software. This software permits the user to define points, lines and areas in an image, and to track these objects through a sequence of images to determine their positions, velocities, accelerations, etc. Once all of the values of interest have been identified, the Optimas software then provides the output in a text format or directly loads it into a Microsoft Excel spreadsheet. Virtually all of the images obtained in this manner were captured using a medium intensity diffused backlighting, and a high quality camera lens. The lighting was consistently set so as to maintain a minimum depth of field, ensuring that only features appearing in the central region of the plate were in clear focus. In all instances the total depth-of-field was less than 8 cm with a horizontal field-of-view of about 12 cm.

A time history of a given set of surface structures was acquired by moving the camera as near as possible to the velocity of the flow. This was also used to capture the transition of the surface, as well as the development of filaments and the formation and demise of drops in the streamwise direction.

Additional flow visualization was performed by injecting food coloring through small dye ports, or by positioning a laser light sheet at various angles relative to the streamwise direction. As discussed later, these techniques aided in verifying that the flow in the center of the liquid wall jet formed over flat and curved walls is unaffected by the side conditions. Therefore, based on observations, the subsequent data analysis of the rectangular jet was limited to the center of the plate, so the results can confidently be said to be those exhibited by a "two-dimensional" jet.

2. Digital Particle Image Velocimetry (DPIV)

As previously discussed, the DPIV system was used exclusively in the low-turbulence water tunnel to determine the jet's subsurface characteristics (U , v' , u' , u_{rms} and v_{rms}) in a plane defined by the laser light sheet. The TSI DPIV system is comprised of a PC containing a high-speed digital frame grabber and the TSI Insight 1.3 software for system control. A separate synchronizer coordinated the pulses of the dual YAG

lasers with that of a Kodak MegaPlus digital imager possessing a 1008x1016 pixel resolution. The software was capable of capturing up to 1,000 sequential images. The laser pulse separation was held at 0.01 ms while operating the system at its highest image capture rate of 30 Hz.

The system was always used in the two-frame crosscorrelation frame-straddling mode. The advantage is that the frame-straddling mode provides the greatest system bandwidth (Keane and Adrian, 1992). The disadvantage of this method is that two separate images are needed for each flow field calculation. However, even if the system were operated in a different mode which made use of its highest capture rate, the maximum frequency that could be determined based on the Nyquist criterion was 15 Hz. For the anticipated time scales present in this flow, this data rate is still too low to obtain meaningful time history information or perform useful spectral analysis. Therefore, the sequentially obtained PIV data must be analyzed as an ensemble of samples regardless of the operating mode, so using the system in frame-straddling presented no actual system limitation.

The flow was seeded with 8 μm glass beads having a specific gravity of about 1.08, and the back wall of the test section below the mean free surface was blackened to enhance particle identification. The area above the surface was well lit to prevent the camera from also capturing dust particles moving in the air (which made it more difficult to distinguish between motions above and below the free surface). Regardless, the free surface disturbances and occasional free surface reflections of the laser light made it impossible to acquire data close to the free surface.

During post-processing of the images, the Whittaker peak search algorithm was used to analyze the images since it is accurate and requires a minimum amount of computational effort (Lourenco and Krothapalli 1995). The seeding was sufficient to allow the minimum spot size of 16 pixels to be used with fewer than about 5% of the velocity vectors categorized as invalid. The small spot size (which has a diameter of about 0.5 μm), combined with a 50% spot overlap, resulted in fairly smooth vorticity and instantaneous velocity contour plots, and provided the possibility that fluid behaving in a

quasi-coherent fashion might be identifiable. The total area examined during a PIV run was about 500 mm^2 (15 x 33 mm).

III. EXPERIMENTAL RESULTS

A. PRELIMINARY ANALYSIS

The overall characteristics of filaments and drops were examined prior to the data gathering process. The examination was carried out by making high-speed recordings of the liquid wall jet from the side and directly above. A stroboscope directed down toward the surface of the jet confirmed that the early stages of the surface were laminar, but it was also noted that the surface contained many small streamwise capillary streaks. Hoyt and Taylor (1979) noticed a similar occurrence in their round nozzle experiments, which they attributed to minute machining grooves that existed on the inner wall of the nozzle. Nonetheless, because this apparatus is significantly different from that of Hoyt and Taylor, it was important that steps be taken to remove the streaks, or at least to identify their cause. To start with, the water in the U-tunnel was allowed to set for many days before use so that it could self de-aerate. A foam-covered splash plate was also installed just below the pump discharge to reduce the amount of air entrained as the recirculated water dropped back into the tunnel (Fig. 10). A small viewing window and a movable dye-injection rig were installed on the tunnel wall directly behind the nozzle. These were used to perform flow visualization around the nozzle entrance region inside the U-tunnel, and to verify that the inner surface of the nozzle was clean and free of air bubbles. Based on the results of these actions, it was concluded that the small (< 0.25 mm) streamwise streaky structures must be the consequence of minute irregularities on the inner nozzle surface. Moreover, their existence was also seen to be a function of U_o , the jet velocity at the nozzle exit. As U_o was reduced, the streaks eventually disappeared, leaving a glass-like free surface. The flow visualization, also confirmed that large air bubbles or debris on the wall of the nozzle were capable of producing large ($\frac{1}{2}$ to 2 mm) capillary waves that danced back and forth across the free surface. Thus, for each run, the nozzle surface was cleaned and polished before filling the tunnel.

Laser-induced fluorescence (LIF) was used to investigate the free surface of the jet by directing a laser light sheet downward onto the surface, and then positioning it at various angles to the flow. This examination made it clear that the free surface

characteristics were uninfluenced by the edges of the jet and wall over a central transverse span in excess of 20 centimeters. It further indicated that most of the well-defined filaments were axisymmetric in nature and possessed no significant lateral motion: they grew and receded in the (x,y) plane as they traversed with the flow in the x -direction. This is not to say that three-dimensional surface disturbances do not exist (Fig. 18), but only that most drop-forming filaments were similar to that of Fig. 19.

During the early stages of the investigation, dye lines were connected to the dye ports that spanned the center section of the smooth and the roughest wall. The flow through the lines was sufficiently restricted so that the suction provided by the jet gently drew the dye (food coloring) near the plate surface. Hence, the movement of dye into the body of the jet had little impact on the flow field. This examination revealed that the flow at the wall became turbulent very near the dye ports regardless of the level of wall surface roughness; and, that the near-wall flow in the center region was unaffected by the wall edges. The same results were witnessed in the curved wall flow also.

For all of the runs except one, the plate was positioned parallel to the direction of flow, with the height set so that the sharp leading edge trimmed off a small amount of the bottom side of the liquid jet (Fig. 7). This ensured that the flow encountering the wall was absent of nozzle shear layer effects, and of the previously described capillary waves. This resulted in an experimental apparatus that was a simplified version of a bow sheet produced by a ship hull. The trimming-off of the lower side of the jet, combined with a small amount of contraction at the nozzle exit, resulted in a jet with a mean initial thickness, h_0 , of about 5.7 mm. In the following discussion, the results of the same jet over different surfaces are compared and contrasted.

It was not known a priori which of the parameters (Re , We , Fr or Z) governed and which influenced the creation of filaments and drops at and above the free surface. Perhaps not entirely unexpected, the smooth plate proved to be very resilient to drop formation: although the roughest plate displayed drops for velocities as low as 3 m/s, the smooth plate did not do so until the velocity approached 7 m/s. At this high of a jet velocity, the free surface for the rough-wall case was too violent to allow the evaluation of individual filaments and drops. It is primarily because of this reason that the filament

and drop analysis were performed at $U_o = 6.2$ m/s for all rough-walls, and at $U_o = 7.7$ m/s for the smooth-plate. This higher smooth-wall velocity was the minimum necessary to obtain a statistically significant sample of filaments and drops. The roughest wall was also analyzed at a jet velocity of $U_o = 4.5$ m/s to examine the effect of lower speed jets over rough surfaces. The effect of the surface curvature—an integral element of the ship bow-sheet phenomena—was investigated through the use of a rough-plate ($k/h_o = 0.06$) having a 3 meter concave radius-of-curvature (Fig. 13). This amount of curvature, at this level of roughness, is similar to that found on the bows of large ships (Schlichting, 1978). The Ohnesorge number, Z , remained constant at 0.0015 because all experiments were performed using fresh water and a fixed jet thickness.

In addition to the filament and drop quantification analysis, the free surface transition regions were visually identified. This analysis was performed for all of the above scenarios, as well as the smooth-wall at $U_o = 6.2$ m/s and a medium-roughness wall inclined at a 15° angle. Table 3 provides a summary of all the rectangular jet experiments and their relevant parameters.

Plate	k (mm)	U_o (m/s)	$\frac{k}{h_o}$	$(Re_x/x) \times 10^{-6}$ (m^{-1})	$Re \times 10^{-4}$	Fr	We	Filament and drop analysis	Transition region analysis
Smooth	0.00	6.2	0.00	6.3	3.6	26	3000		●
Smooth	0.00	7.7	0.00	7.9	4.5	33	4700	●	●
Fine	0.13	6.2	0.02	6.3	3.6	26	3000	●	●
Medium	0.33	6.2	0.06	6.3	3.6	26	3000	●	●
Coarse	0.72	6.2	0.13	6.3	3.6	26	3000	●	●
Coarse	0.72	4.5	0.13	4.6	2.6	19	1600	●	●
Medium 15° angle	0.33	6.2	0.06	6.3	3.6	26	3000		●
Medium 3 m radius	0.33	6.2	0.06	6.3	3.6	26	3000	●	●

Table 3. Summary of the rectangular liquid wall jet parameters and analyses.

The Reynolds, Weber and Froude numbers could not be varied independently, so knowing any one of them implied knowledge of the other two. Therefore, specific test runs are frequently described by their relative roughness and Weber number. For example, "0.06/3000" stands for the wall jet run over the plate with a relative roughness

of $k/\rho = 0.06$ and a Weber number of 3000. It is further understood that the terms jet "speed", "velocity" and "inertia" will be used interchangeably.

B. DATA ACQUISITION PROCESS AND MEASUREMENT DEFINITIONS

In the course of the presentation and discussion of the results, the most important outward manifestation of the free surface (i.e., filament or ligament) will be referred to quite frequently. It is for this reason that we will define a "filament" as precisely as possible within the statistical bounds of its finite life. To be sure, the definition is a subjective matter. Qualitatively, a filament should be long and thin, and its two-dimensional image must readily lend itself to a mental translation of a three-dimensional axisymmetric object. Quantitatively, it was required that the slenderness ratio (L_f/D_f) reach a value of about 1.5 to 2 prior to forming a drop. The only exception being nascent filaments which were considered acceptable if they behaved axisymmetrically and reached a value of $L_f/D_f \approx 2$ before drop formation. In most cases, the selected filaments were already "mature," with slenderness ratios greater than three, by the time they were under consideration for analysis. Based on a summary of general observations, one could be quite certain that if a filament possessed a three-dimensional character (other than small axisymmetric or longitudinal irregularities), it would make itself known within two or three sequential images. Filaments meeting the above criteria also had to be measurable over a period of time. Hence, their bases and profiles had to be clear of other disturbances that might be present. In the case of runs 0.00/4700, 0.02/3000 and 0.13/1600 (i.e., low k/ρ or low We), most of the filaments appeared as "trees in the desert." That is, the surrounding disturbances were typically much smaller than the filament. In run 0.13/3000, however, the free surface profile was more like a forest, and suitable filaments often had to be bypassed as their images were blocked by other filaments and large disturbances. Run 0.06/3000 was a transition between these two extremes. In rare instances, small filaments actually formed from large three-dimensional disturbances as shown in Fig. 18. Filaments such as this were avoided since it was felt that there was a greater risk of their genesis not being directly linked to the subsurface events.

The video images used in the quantitative analysis of the rectangular liquid wall jet were captured using the NAC HSV-500 imaging system operated at 500 frames/sec and a shutter speed of 5000 sec^{-1} . The camera was placed on the same horizontal plane as the wall over which the jet formed, and perpendicular to the streamwise direction. Before recording, the jet flow was started and given sufficient time to stabilize (5 to 10 min). As mentioned previously, the focal plane of the camera was at the center of the wall and had a 12-cm wide field-of-view. Starting at $x = 0 \text{ cm}$, the imaging system recorded the jet profile long enough to provide sufficient data for analysis, before being repositioned 12 cm further downstream and the recording process repeated. This sequence of events was continued along the length of the jet. This particular camera position was chosen because:

- It guaranteed that only filaments and drops along the centerline of the jet were in focus; hence, the results were not influenced by the edges of the jet.
- It was close enough to ensure that the filament and drop features could be accurately defined.
- It was far enough away to capture from 8 to 15 images of identifiable filaments and drop(s) as they passed across the field-of-view of the camera. This was sufficient to ensure that the desired silhouette of the filament exhibited an axisymmetric character, and that the drops remained nearly circular.

Figure 19 provides an example of a sequence of images used to analyze a filament and drop (the filament of interest is indicated with an arrow). For this investigation, over 800 filament-drop pairs such as this were analyzed, which amounts to approximately 8,000 individual image analyses.

All of the recorded images were obtained using the same camera, lens and lighting arrangement. After carefully reviewing the tape, the images of filaments and drops whose motions were identifiable with little or no ambiguity were digitized and downloaded to a PC, and the sequence of images then analyzed. The cross-sectional area

of the filament and/or drops were outlined with the help of a "mouse," and the base and tip of the filament were marked. The Optimas software calculated the cross-sectional area, length, position, angle, velocity and acceleration of every feature identified in the digitized image sequence, based on the specified length-scale and the time between the images (2 ms). The uniqueness of each filament required, a simplified means of identifying and comparing their characteristics. As explained earlier, the analysis was limited to those filaments possessing an apparent axisymmetry. It was therefore, reasonable to identify their geometry with that of a cylinder as shown in Fig. 20. The major uncertainties associated with this filament model were that the base could not be precisely defined, and that the shape, as per definition, was axisymmetric. However, independent analysis by two separate observers indicated that the overall filament uncertainty is less than 10 percent. The mean diameter of a drop is determined from the average of its cross-sectional area measurements. A complete discussion of the uncertainty involved with the filament and drop analysis is presented in Appendix B.

C. LIQUID WALL JET ATTRIBUTES

For each of the eight runs listed in Table 3, the regions of surface transition and jet thickness were determined to help elucidate any general trends or features that might be present in the flow. The plate positions were carefully set, and the flow was allowed to stabilize (as indicated by a constant water level in the U-tunnel) prior to beginning any of the measurements.

1. Transition Regions

In examining the gross features of liquid wall jets, it was found that the surface characteristics could be divided into four identifiable regions, with examples of three of the four depicted in Fig 21. The gradual nature of surface transitioning defies precise position identification, as in all "transitions" in fluid motion, nonetheless, these locations was measured as accurately as possible (± 3 cm) using a number of different camera angles, frame speeds, shutter speeds and lighting arrangements.

The first transition, *transition to roughness* (Fig. 21.a), is the region in which the turbulent boundary layer reaches the free surface, noticeably roughening it. In this region, three-dimensional disturbances appear, but filaments are not yet evident. Although these disturbances are small, they do manage to completely obliterate the streamwise capillary waves in very short order (2 to 3 cm). Flow visualization showed that the turbulent boundary layer began almost immediately regardless of the wall roughness, but the distance necessary for it to reach the free surface (about 30 h_o to 55 h_o), did depend on k/h_o and U_o . Figure 22 shows that the distance to the surface transition is only slightly affected by roughness for $k/h_o < 0.06$, and is virtually unchanged for roughness levels above this. It is also essentially unaltered by the reduced jet velocity for 0.13/1600 ($k/h_o = 0.13/We = 1600$), but increases noticeably for the high velocity jet on the smooth-wall. In the case of boundary layer flow over a smooth flat surface, the thickness of the turbulent boundary layer as predicted by Schlichting (1978) is,

$$\frac{7}{72} \frac{d\delta}{dx} = 0.0225 \left(\frac{v}{U_{\infty} \delta} \right)^{1/4}. \quad (6)$$

Substituting U_o for U_{∞} , and local mean jet thickness, \bar{h} , for the boundary layer thickness, δ , Eq. (6) is seen to over-estimate the distance to this transition for runs 0.00/3000 and 0.00/4700 by about 60 percent and 45 percent, respectively. Davies (1972) credits van der Hegge-Zijnen (1928) with deriving the following equation for predicting the turbulent boundary layer thickness over a rough-wall:

$$\delta = 0.26 \cdot k \left(\frac{x}{k} \right)^{2/3}. \quad (7)$$

As pointed out by Davies, Eq. (7) suggests that δ is no longer a function of U_{∞} . Again, \bar{h} is substituted for δ in an attempt to predict the transition point for the free surface of the rough-wall jets. Just as was the case for the smooth-wall, Eq. (7) over-estimates these transition locations by 25 to 100 percent.

From the leading edge of the plate to the beginning of the surface transition region, the temporal mean jet thickness increases by 15 to 50 percent, with an average increase of about 40 percent (Fig. 23). By the end of this very short region, the thickness is about 50 to 100 percent greater than h_o .

In the second region, *filament formation*, those disturbances that are going to produce filament-like structures become apparent. As suggested in Fig. 21.b, the length of the filaments, as well as their frequency, tend to increase as the flow progresses downstream. Figure 22 shows that this region appears to be more strongly influenced by roughness than was the point of transition to roughness. It is also apparent that the potential energy loss incurred by a jet flowing over an angled or curved wall is not significant enough at this point to affect the location of the beginning of filament growth. However, changes in the inertia of the jet do seem to have a notable impact on the location of this event. For the coarse-wall (i.e., $k/h_o = 0.13$), increasing the flow rate reduces the distance to filament formation from $47h_o$ to $31h_o$, while for the smooth-wall a similar increase reduces this distance from $105h_o$ to $83h_o$. It is apparent in Fig. 24 that there is more variation in the mean jet thickness at the beginning of the filament formation region than in the transition to roughness region. This is a result of the continued growth in size and quantity of the free surface disturbances.

The *drop generation* region is the most dynamic and is the one of primary interest in this research. As shown in Fig. 19, the key elements of this region are the necking of the filament, and the drop separation (pinch-off) that ensues from it. As indicated in Fig. 20, the distance from the tip of the filament to the necked region is called the disturbance length, λ , and more often than not, a single drop forms from a single disturbance. Fig. 17 shows this most common drop separation event, but there are others. For example, the filament may separate near its base forming a large elongated drop that either contracts into a spherical drop, or breaks up into two or more satellite drops. The filament may also disintegrate into multiple drops of various sizes—typically two or three, and sometimes as many as six. Occasionally, a long-necked region will produce a smaller satellite drop as seen in free jets (Goedde and Yuen 1970). The subsequent drop analysis presented here will concentrate on the characteristic behavior of these tip-formed drops, because the vast majority of filaments (≈ 80 percent) form a single drop at the tip.

The production of drops in the drop generation region depends on k/h_o and jet velocity, as was the case in the filament formation region. Figure 22 indicates that at higher values of k/h_o , the dependence of X_d/h_o (location of the beginning of drop

generation) on We is weak, but below $k/h_0 \approx 0.06$ it is unmistakable. For run 0.00/3000, drops are nonexistent, however at $U_0 = 7.7$ m/s (run 0.00/4700) drops begin to appear at $x/h_0 \approx 130$. Although the apparent influence of the jet inertia on the beginning of drop generation in the coarse-wall is not as pronounced as it was in the filament formation region, it is still statistically significant. As was the case in other regions, the wall angle and curvature have no noteworthy influence on the location of this transition.

Figure 25 provides a comparison of the temporal mean jet thickness for each of the runs at the point of drop generation. The variation associated with \bar{h}/h_0 at the beginning of this region is slightly less than that seen in the previous two regions, and the values are all very similar ($\bar{h}/h_0 \approx 2.0$) despite the large difference in k/h_0 and X_d/h_0 . Nevertheless, it still suggests that run 0.13/1600 gives rise to a jet that is slightly thicker when it begins to produce drops. A difference in \bar{h} between the angled- and flat-wall jet—both of which are at $k/h_0 = 0.06$ and $We = 3000$ —also becomes apparent, with the angled-plate mean jet thickness being slightly less when drops begin to form. It is noteworthy that the value of \bar{h}/h_0 where the mean jet thickness for the smooth non-drop-producing jet levels off, the other flows are just beginning to produce drops ($\bar{h}/h_0 \approx 1.9$).

The last region of *decreasing activity* (not shown in Fig. 21) is marked by a gradual reduction in the size and number of three-dimensional surface disturbances and filaments. The onset of this region blends smoothly with that of drop generation, and as such, its exact beginning cannot be readily identified. It appears as a gradual relaxation of the jet free surface. The jet has apparently lost the prerequisites (kinetic energy, surface energy, critical depth, etc.) to produce filaments. An example of the character of this region is provided in Fig. 26 that was taken from the axisymmetric jet apparatus.

2. Jet Thickness

The temporal mean jet thickness increases as it moves through each of these transition regions. Figure 27 shows how this thickness varies as a function of x/h_0 for each of the runs considered. For runs other than 0.00/3000, 0.02/3000 and 0.13/1600, the instantaneous surface fluctuations are very large beyond $x/h_0 \approx 60$ (or $x/h_0 \approx 135$ for the

high-We smooth-wall run). As the standard deviation values for the jet thickness suggest, Fig. 28, these large and rapid variations in the free surface elevation make the present measurement technique inaccurate beyond the points presented in Fig. 27. Furthermore, it is not clear as to why \bar{h} at a given location should be more meaningful than the spectrum of the fluctuations at the same point. It is believed that the violent nature of the jet free surface was, in large part, responsible for the ineffectiveness of the capacitance probe in measuring \bar{h} .

At first glance it appears that, with the exception of run 0.00/4700, all of the jet thickness profiles shown in Fig. 27 behave in a very similar manner: a gradual increase in \bar{h} followed by a steep change, and then a return to a gradual increase (and eventually one would expect the flow to revert to a subcritical state, i.e., form a hydraulic jump). However, run 0.00/4700 is not truly different, it is simply an expanded version of the other curves. The region from $0 < x/h_0 < 100$ is the gradually increasing profile, with the steep change beginning around $x/h_0 = 110$. Recall from Fig. 22 that the transition regions for run 0.00/4700 are substantially further out than that of the others, so it is not unexpected that these \bar{h} variations would occur over a longer distance.

If one compares the shape of \bar{h}/h_0 between the runs, it is apparent that below some level of relative roughness between 0.02 and 0.06, the aforementioned thickness gradients, $d\bar{h}/dx$, become smaller. Conversely, for $k/h_0 \geq 0.06$, the initial rate of jet thickening is rather insensitive to the variation in wall roughness.

D. FILAMENT AND DROP CHARACTERISTICS

In the drop generation region, a minimum of 30 filament/drop events were measured in most of the x/h_0 regions recorded. Near the end of the wall, the flow for most runs was well into the decreased activity region, therefore measurements were not typically carried out beyond $x = 130$ cm. Those runs that did continue generating drops beyond $x = 130$ cm did so at a very low rate (the only exception was run 0.00/4700, which did not begin generating drops until $x \approx 75$ cm). As the end of the wall was

reached, the influence of secondary effects, such as splashing from the end of the experimental enclosure, became significant.

Although all of the drops recorded were measured, the present discussion will focus on those formed at the filament tips. As noted here and in other studies (Volkert 1980), the majority of the filaments give birth to only one drop at the filament tip. Even for those that form more than one, the "tip drop" is almost always the first and the largest. The few drops not produced by this process were very small ($D_{dr} \sim 0.25$ mm), and their formation appeared to be similar in nature to that of free surface jetting (Rein, 1996).

There are a number of additional measurements that could have been taken from the digitized images. However, here the analysis is directed toward those measurements that appeared to be the best indicators of the drop generation mechanism to be discussed in detail later. Those indicators are the drop size, velocity and relative position; and, the filament length, diameter, angle and tip velocity just before drop pinch-off (in most cases this length is synonymous with the maximum filament length). It is felt that these measurements give the clearest possible indication of the events causing the drop formation, as well as the energy associated with their vertical motion. Only the measurements of velocities and turbulence within the jet body could have made the mechanisms of filament and drop formation clearer.

In the ensuing discussion, histograms will be used frequently to compare and contrast the results of the six runs listed in Table 3. Although the smooth-wall run (0.00/4700) was at a higher flow rate, it will be grouped with the three flat rough-wall runs. A separate comparison between the high-flow (0.13/3000) and low-flow (0.13/1600) coarse-wall case will be used to help elucidate the influence of jet velocity. The effects of wall curvature are also discussed separately.

1. Drop Diameter

Figure 29 is a histogram showing the drop-diameter distribution of the four flat-wall runs. It indicates that as the roughness of the plate is increased, the mean value of D_{dr}/h_o becomes slightly larger and the distribution broadens out. The variation of the mean value is clearer in Fig. 30. The uncertainty in D_{dr}/h_o , as well as that of the other

normalized mean-value characteristics of the filaments and drops presented, is less than or equal to the height of the corresponding symbols shown in the figures (unless otherwise stated). The difference in D_{dr}/h_0 is almost insignificant among the rough-plates, but D_{dr}/h_0 is smaller for the smooth-wall case. Reducing the coarse-wall Weber number from 3000 to 1600 has no apparent influence on the mean drop diameter size, but it does increase the production of smaller drops (Fig. 31). Figure 32 presents a comparison of the flat and curved plate distributions for $k/h_0 = 0.06$. The shape of the distributions are essentially the same, but the curved-plate values are shifted to the left. This is consistent with its lower mean value in Fig. 30. In short, the drop diameter relative to the initial jet thickness increases slightly with roughness and it does not appear to depend on We (at least for coarse roughness). D_{dr}/h_0 is smaller, as expected, for the smooth-plate; and, for the same medium roughness ($k/h_0 = 0.06$) is also somewhat smaller for a concave curved-plate. The latter may be due to the inhibiting effects of centrifugal acceleration on the growth of the filaments from which the drops are born.

2. Filament Length and Angle

The distribution of the filament length just before drop pinch-off, Fig. 33, exhibits a more apparent skew relative to that of the drop diameter. As the relative roughness increases, the distribution broadens and shifts to the right, while the influence of concave curvature moves the distribution to the left (Fig. 34). It is evident from Fig. 35 that both curvature (i.e., centrifugal acceleration) and jet inertia have, as expected, a substantial effect on the maximum length of the filament (the former decreases it while the latter increases it). Figure 36, clearly demonstrates that a reduction in Weber number reduces the likelihood of long filament formation. Based on this observation, Fig. 35 implies that if the rough-wall had been sampled at the same Weber number as the smooth ($We = 4700$), one might have seen filaments 30 to 50 percent longer. Also, the medium roughness on a flat-plate would have yielded smaller filaments lengths at $We = 1600$ relative to $L_f/h_0 \cong 2$ at $We = 3000$. However, it is strongly anticipated that there are upper limits to the filament size as We and k/h_0 individually or simultaneously increase. Although not measured in this investigation, it is clear from numerous observations (i.e.,

see Fig. 37) that increasing roughness or flow rate causes dramatic increases in the drop and filament density (drops/cm³).

Changes in the flow inertia or plate-surface condition over the ranges considered did not appear to influence the angle of the filaments. For all of the runs, the mean filament angle was approximately 81° (measured CCW from the negative x-direction as shown in Fig. 20). In other words, most of the filaments leaned slightly backwards as they moved downstream, as in Figs. 2 (Hoyt and Taylor, 1977a) and 19. Additionally, for a random sampling of 196 filaments, the change in angle from the moment a filament entered the viewing area of the camera until just before drop release was measured at +4°. This implies that there is no apparent change in the mean filament angle, because the angle estimation is only accurate to within about ±5°.

3. Effective Filament Diameter and Slenderness Ratio

Figure 38, shows the distribution of the effective filament diameter, D_f/h_o . The distribution widens and moves toward larger values of D_f/h_o as roughness increases, but only marginally so for k/h_o from 0.02 to 0.06. Although the change is larger between $k/h_o = 0.06$ and 0.13, it is still not as significant as the difference between the smooth and fine-roughness walls. Comparing these changes with that between the high- and low-Weber number coarse-wall flows, Fig. 39, it is apparent that the lower flow rate shifts the filament diameter distribution slightly towards smaller values of D_f/h_o . Looking at Fig. 40, it is seen that the form of the variation of D_f/h_o is similar to that of the Drop diameter (Fig. 30). Recall that D_f/h_o is estimated by dividing the filament cross-sectional area (as determined using the Optimas MA software) by the filament length. Although the uncertainty analysis shows a great deal of uncertainty for the individual filament diameters, the mean values remain fairly good predictors of the overall population. The influence of curvature on the distribution is shown in Fig. 41. It indicates that the shape is largely the same, but the distribution is shifted to lower values of D_f/h_o . Again, this is very similar to the drop diameter behavior noted in Fig. 32, and the same summary statement applies.

Having examined both the filament length and diameter, it is now worthwhile to consider the filament slenderness ratio, L_f/D_f , just prior to drop formation. Figure 42 shows the L_f/D_f distribution for the four nominal runs. The variance is extremely small for the smooth-wall, but gradually increases with roughness. The mean value of L_f/D_f in Fig. 43 also increases as roughness increases. The 25 percent reduction in the slenderness ratio for the low-Weber number coarse-wall case suggests that the smooth-wall value of 4.1 is somewhat enhanced by the higher Weber number of that flow. As shown in Fig. 44, increasing the velocity of the jet broadens the distribution in addition to increasing the mean value. The influence of curvature, Fig. 45, is similar to what was noted before: the variance of the distribution and the mean value are reduced a small amount. As noted earlier, the said increases with k/h_0 and/or We are expected to have reasonable upper bounds, perhaps accompanied by new transformations such the total disintegration (atomization) of the wall jet.

4. Filament Volume

As previously explained, the filaments are idealized as cylindrical columns (Fig. 20). This idealization can be used to consider a number of filament geometric properties; e.g., a comparison of the effective diameter, angle, disturbance wave number and volume of the filaments. Such calculations should provide reasonable results because most of the drop-forming filaments were axisymmetric in nature, and only those which clearly exhibited this behavior were considered in the study. For the case of the filament volume, one has

$$V_f \approx \frac{\pi}{4} D_f^2 L_f.$$

The uncertainty associated with an individual filament volume estimate is large, but the mean value is still good because it is based on about 100 to 150 samples (see Appendix B). The small uncertainty regions of Fig. 46, which displays the mean nondimensional filament volumes, V_f/h_0^3 , makes this point clear. Although the large measurement uncertainty (about 40 percent) may significantly add to the variance of the distributions shown in Figs. 47 through 49, they are still of some value. For example, even with the

uncertainty tending to contribute a large amount of scatter, the plots still suggest that the distribution is rather narrow compared to the other measured parameters. From Fig. 46, the volume appears to decrease linearly with roughness for $k/h_o \geq 0.02$, but falls off more sharply for a value of k/h_o less than this. Comparing the mean drop volume based on the D_{dr}/h_o values provided earlier (Fig. 30) with the filament volumes shown here, it is seen in Fig. 50 that, on average, a drop consumes about 50 to 60 percent of the filament volume at pinch-off. The figure suggests that there may be a slight decrease in the volumetric ratio, ∇_{dr}/∇_f , with increasing k/h_o and We . Nonetheless, it seems apparent that the small change in drop diameter with k/h_o allows the drop to maintain a fairly constant volumetric ratio with the filament, despite significant changes in filament volume.

5. Disturbance Wave Number

Consideration is now given to the disturbance wave number, just prior to drop pinch-off,

$$k_1 = \frac{\pi D_f}{\lambda}.$$

The individual wave numbers carry an uncertainty of about 20 percent because the determination of the wavelength, λ , requires more subjective interpretation than some of the other parameters. It is expected that this uncertainty is random in nature, so that the mean value calculations still provide reasonable estimates. Figure 51 shows that the mean values of k_1 do not display a clear trend, and that the average value for flat-plate flows is about 1.8. There was also no consistent behavior seen in the *individual* filament wavelengths. During the life of a filament, some disturbances grew, some shrank and some were unidentifiable until just before drop pinch-off. However, k_1 does display a fairly constant mean value and a Gaussian-like distribution (Fig. 52 through 54) for all wall jets considered.

6. Drop and Filament Characteristics as a Function of Streamwise Position

All of the physical attributes of filaments and drops were measured in different areas of the drop generation region. The above discussion considered the region as a whole, but it may now be useful to consider how these values vary from area to area within the region. Figures 55 through 59 show only those locations where 30 or more observations were made. In addition, all abscissa values are plotted in terms of $(x - X_d)/h_o$ to make comparisons between runs clearer.

The local mean drop diameter, Fig. 55, shows a slight increase in drop size in the downstream direction. With the exception of the fine-roughness (0.02/3000) and low velocity (0.13/1600) runs where the drop size is decreasing, or beginning to decrease, as $\Delta x/h_o$ increases. Regardless, the change is very slight and the drop size remains on the order of $h(x)$ throughout the region.

The behavior of the mean filament length with position, Fig. 56, is fairly constant given the level of uncertainty. However unclear, there is perhaps a mild downward trend for the fine-roughness and the low-Weber number flows. The large value of L_f/h_o seen at the end of the coarse-wall flow is a result of the existence of a few rather large filaments, and the uncertainty of this value is actually closer to 20 percent. For the mean filament diameter, Fig. 57 indicates that these values are also reasonably constant over the length of x/h_o considered, exhibiting a character similar to D_{df}/h_o (Fig. 55). The trend of the curved-wall, for which D_f/h_o is consistently smaller, agrees with the mean value results of Fig. 40.

In Fig. 58, which depicts the mean local slenderness ratio of the filaments for each run, the uncertainty is up to about 15 percent, so one should be cautious about reading too much into the mild trends which exist. However, the consistency of the reduction in L_f/D_f in the streamwise direction for all runs suggests that the trend is probably real. Finally, for completeness, Fig. 59 presents the mean local filament volume. The uncertainty is now in the 25 percent range (and as high as 30 for some of the larger values). The curves generally agree with the mean filament volume of Fig. 46: an

increase in inertia or roughness tends to increase the volume of the filament just before drop pinch-off.

In summary of the foregoing, one may reasonably argue that the basic characteristics of the drops and filaments and their volumes remain relatively constant over the area of measurement, with small and often statistically insignificant variations, along the streamwise direction. Having said this, there is undoubtedly some transitional variations in the said characteristics at the beginning and the end of the measurement regions. Additionally, any variations are obscured or masked by their Gaussian distribution at any given section of the area.

E. WATER TUNNEL WALL JET

The previous sections examined the different regions, and the filament and drop characteristics, of a rectangular liquid wall jet. It was not possible to make measurements within the jet because of its extremely violent nature and shallow depth. The goal of the water tunnel investigation was to help gain some insight into the nature of the flow below the free surface. The tools of choice for this investigation were a digital particle velocimetry system (DPIV) and a Redlake High-Speed Digital Imager (Table 2).

It was possible to produce a high-speed jet with velocities equal to that of the rectangular wall jet by arranging the test section of the water tunnel as described in section II.D. Although the tunnel had the ability to support a wide variety of wall jet parameters, there were explicit limits on the choices for h_0 and U_0 . If h_0 was selected too large, then the experiment would leave the realm of wall jets, becoming a subcritical or mildly supercritical open channel flow (i.e., with a relatively undisturbed free surface). If h_0 were too small, then it would be impractical to visualize the interior of the jet on a scale providing any sort of useful insight. For low values of U_0 , the flow again becomes more of an open channel flow. However, for large values of U_0 for a given h_0 (i.e., high Froude number), the free surface is excessively disturbed and essentially destroys the optical path between the side of the test section and the center of the wall jet. High flow rates at large depths were also of no use because the surface transitions that are distinctive of wall jets would not occur within the short length of the test section. Thus, it

was necessary to achieve the best possible flow circumstances in order to get a glimpse of what might be transpiring below the free surface. Therefore, a single Uo-ho setting that would meet all the necessary conditions was found after considerable trial runs. It was determined that a vertical plate height of 11-mm with the pump providing a flow rate of approximately 3 m/s, produced a wall jet with $h_o = 9.5$ mm at the vena-contracta. The resulting jet was similar to run 0.00/3000 when the wall was smooth (i.e., no drops formed), but was capable of producing a few filaments and drops near the end of the test section when the wall was roughened with 0.72 mm sand particles. Table 4 lists the parameters of the two water tunnel wall jets.

Plate	k (mm)	U_{\max} (m/s)	$\frac{k}{h_o}$	$(Re_x/x) \times 10^{-6}$ (m^{-1})	$Re \times 10^{-4}$	Fr	We	$Z \times 10^3$
Smooth	0.00	3.5	0.00	3.6	3.4	11	1600	1.2
Rough	0.72	2.9	0.08	3.0	2.8	9	1100	1.2

Table 4. Summary of the water tunnel liquid wall jet parameters.

Figure 60 provides an idea of how the water tunnel rough-wall jet behaved in comparison to the other jets. It reinforces the fact that the free surface transition point is relatively inert to changes in k/h_o and velocity. Considering the large difference in Weber number between this and the previous rectangular wall jet (1100 versus 3000), it is somewhat surprising that the transition to filament formation is not further out. The beginning of the drop generation region changes substantially, and is similar to that of run 0.02/3000. The smooth-wall jet did undergo transition to roughness on the free surface, but the process was too gradual for the location of the event to be determined.

The mean velocity profile of the jet was measured over both smooth and rough walls using a DPIV system. Figure 61 shows the results of these measurements along with those of Klebanoff (1954) in a fully-developed smooth-wall boundary layer, and Grass (1971) in a fully-rough channel flow. The jet velocities were recorded at $x/h_o \approx 50$, which is roughly the beginning of the filament formation region.

The visualization of the tunnel wall jet was conducted using the Redlake high-speed camera positioned along side the wall jet. The interior of the jet was illuminated

with a diffused backlight, or from directly beneath the center of the test section using the DPIV laser light sheet as an ultra-high-speed two-dimensional flash. The visualization results for the smooth-wall flow were of no interest and will not be presented. Conversely, the subsurface flow over the rough-wall was quite fascinating, as seen in Fig. 62. Here one sees the light sheet highlighting a number of bubbles that have been drawn into the flow. The bottom of the images show the roughness and the dark areas at the top are a result of the time-dependent free surface variations existing along the optical path. The flow in the images is from left-to-right. Figure 62.a presents an elongated bubble that has not separated from the top, yet it is nearly in contact with the rough-wall. In Fig. 62.b there is a similar type of event, except that the photograph is taken shortly after the bubble has pinched off from the free surface. A number of bubbles of different size and shape are shown in Fig. 62.c. The size of the bubbles generally vary from $< 0.25\text{mm}$ to one-half of the jet thickness, but in most cases they appear to be about one-fourth to one-sixth of $h(x)$. A few of the smaller bubbles resulted from air-entrainment at the end of the test section (and subsequently recirculated in the system), but most were seen to be introduced by free surface disturbances as shown. Some of the larger bubbles in Fig. 62 suggest that there may be a preferential angular orientation (about 125° to 135°). Figure 63 is similar to Fig. 62, except it is taken with the jet back-lit and the camera angled upward to get a clearer view of the free surface. These images were captured just downstream of the position where the velocity profile was acquired. It is the appearance of the bubbles in this region (dark blobs in Fig 63.b) that prevented the recording of DPIV data at points further downstream than $x/h_o \approx 50$, as it was not clear what influence the bubbles would have on the DPIV velocity-vector calculations. Figure 64 is a sequence of back-lit images showing how bubbles are introduced into the flow. The free surface fluctuations in this region were fairly moderate (same region as Fig. 63), however this sequence leaves little doubt that these disturbances have a profound impact on the character of the jet. As the bubbles move downstream, most never make it back to the free surface prior to reaching the end of the test section ($x/h_o \approx 110$). The bubbles rotate, stretch and dart about randomly and rapidly, and some of those that reach the bottom will bounce along the wall as they move downstream. Although the stretching (Figs. 62.a and

64) is a clear indication that the bubbles are undergoing shear, there was absolutely no evidence that they felt any type of drag from the liquid flow: the bubbles neither collapsed nor distorted in any sort of preferential way along their trajectories. Figure 65 is a unique photograph that simultaneously captures a filament above the free surface and bubbles below.

The mean velocity profiles presented earlier are the result of over 450 horizontally averaged DPIV image-pair vector plots. The root-mean-squared velocity values were also calculated from this data set, Fig. 66, but over 20,000 vector plots would be necessary to make them statistically significant. Notwithstanding the large uncertainties that are recognized to exist (and which may explain the anomalies present in the v_{rms} figure), these results are presented for what they are worth.

Instantaneous v -velocity contour plots of the DPIV data taken at $x/h_o \approx 50$ are shown in Fig. 67. This is also part of the same data set that was used to calculate the mean velocity profiles in Fig. 61. The whited-out regions near the top left corner are areas where insufficient valid vectors were calculated (usually due to surface reflections). The circled region on each plot annotates a fluid "clump" with a vertical velocity greater than 0.5 m/s ($v'/U \approx 0.18$). It is interesting that such large, seemingly coherent, fluid structures with significant upward velocities exist this far upstream. Considering their present vertical position and velocity, as well as the velocity of the jet, all three of these structures should reach the free surface zone prior to $x/h_o = 70$.

F. DISCUSSION OF RESULTS

The most important contribution of this investigation is the quantification of the physical manifestations of the liquid wall jets. The aforementioned effort has resulted in numerous individual measurements of filament length, diameter, angle, disturbance wavelength and velocity; drop diameter(s) and velocity; and, the mean temporal jet thickness. The reliability of the information is related to the number of individual realizations, hence, the data gathering was an enormously time-consuming affair (which perhaps explains why it has not been done before).

In addition to providing a basis for identifying the governing and influential parameters in the present study, these values will be essential for gaining even deeper insight from future studies of this nature. There is no doubt that the structures of the free surface affect the flow beneath, and the underlying characteristics of the flow affect the structures of the free surface. In fact, one may conclude that the spray problem is the determination of this interaction for smooth, rough and concave or convex walls in supercritical wall jets.

1. Free Surface Characteristics

This work has identified four separate surface transition regions that were witnessed in all of the drop-forming flows. The first, where the free surface disturbances begin to appear, leads to the second region where some of the disturbances continue to grow into vertical columns of fluid (or filaments). In the third region, some of the filaments give rise to drops (usually just one). The number and size of the drops are strongly influenced by the jet velocity and relative wall roughness, among other things. The last region is one of decaying free surface activity, where the flow is still highly supercritical (i.e., $Fr = U/\sqrt{gh} \gg 1$), but is below some minimum threshold necessary for filaments and drops to be produced. As this region progresses, the free surface continues to calm, becoming reminiscent of shallow channel flows with their boils and kolks. The influence of roughness on the location of the transitions was most obvious at lower roughness levels. Beyond a certain value of k/h_0 , the influence of roughness was more apparent in the quantity of the free surface structures, rather than the location of their introduction.

2. Spray Generation Features

It is critically important to recognize that the entire drop production phenomena is of a statistical nature, and therefore necessitates a statistical analysis for its interpretation. By using such an approach, it was possible to ascertain many of the fundamental attributes associated with the formation of the filaments and drops. Figure 68 provides a

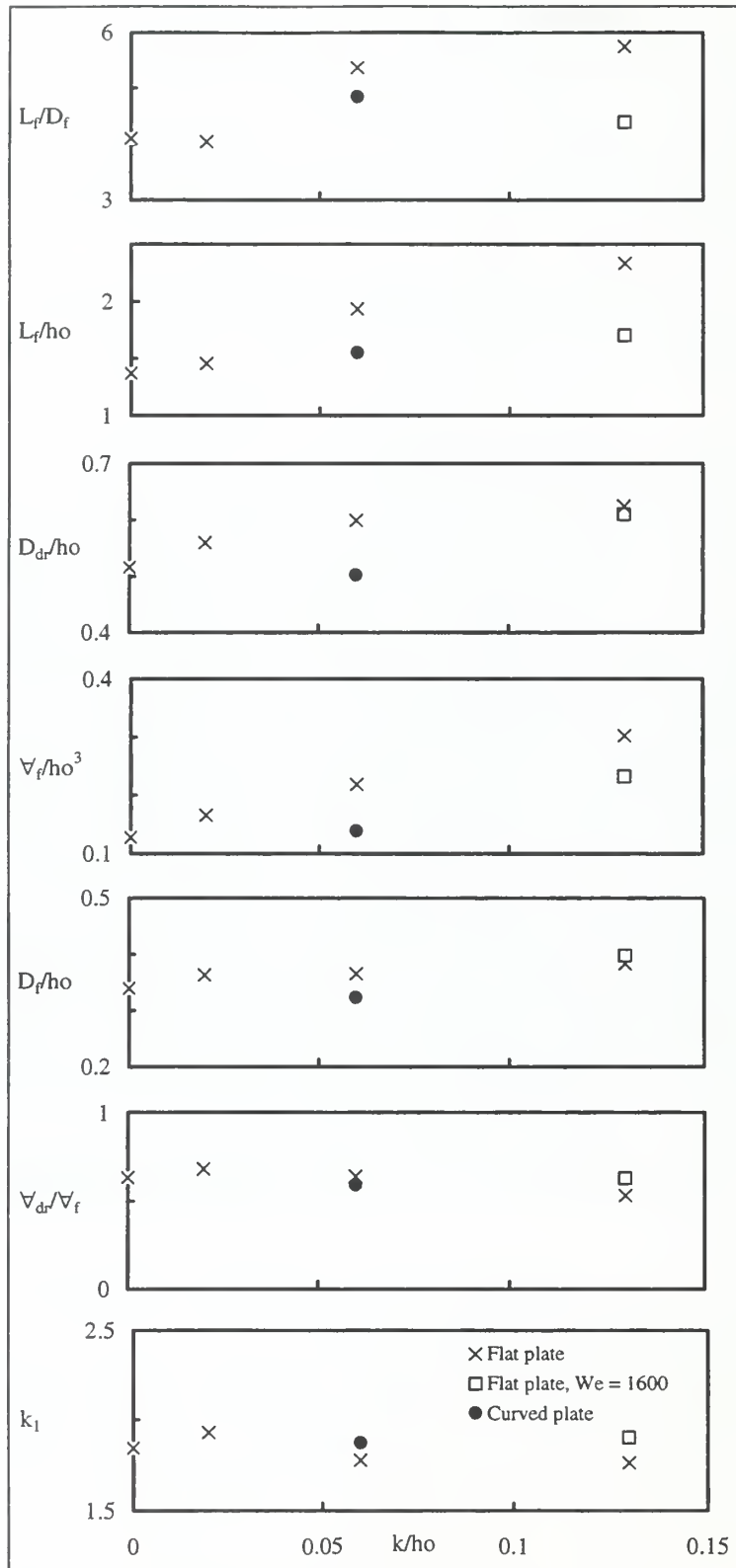


Figure 68. Summary of the mean value characteristics as a function of the relative roughness.

summary of the mean value of those characteristics as a reference for the following discussion.

In all of the liquid wall jets examined, the thickness of the jet increases substantially as the jet relinquishes part of its momentum to the wall. Roughness enhances this process, and as such leads to more rapid jet thickening. Perhaps more importantly, higher levels of roughness result in greater temporal mean variations in the local values of h , even to the point where the measurement technique employed here is no longer viable.

In the case of the drop diameters, it was apparent that the mean value remained essentially constant over all flat rough-walls regardless of roughness level ($D_{dr} \approx 0.58h_o$), but that the smooth-plate values were smaller ($D_{dr} \approx 0.51$). The distribution of the drop size about the mean is well-described by a normal distribution curve, where the standard deviation of the curve increases with k/h_o . This behavior conforms with that previously noted in typical boundary layer flows by Blake (1970) and Krogstad, et al (1992). Blake found that the larger interstitial region present around larger roughness elements produced a greater range of eddy sizes and, similarly, Krogstad et al showed that the spectral distribution of energy containing eddies is wider in rough-wall flows as compared to smooth. Others have identified the Gaussian nature present in the features which describe the motion of the large turbulent eddies developed in boundary layer flows (e.g., Raupach, 1981).

The filament length distributions presented a clear trend toward the lower filament lengths, which is different than that described for the aforementioned drop diameter. From a physical viewpoint, this makes sense because a filament must have a finite length to form a drop ($L_f > D_{dr}$), and very large filaments would necessitate a turbulent fluctuation with an exceedingly high vertical velocity. These physical boundary conditions act to limit how small (or large) the filaments can be, but the lower energy requirement of short filaments make their existence more probable. The lengths of the filaments strongly increase with roughness, suggesting that roughness enhances the vertical velocity fluctuations in the flow, enabling the eddies to "stretch" the fluid continuum to a greater extent. Again, the influence of roughness on this parameter is not

unlike that seen in typical turbulent boundary layer flows: increasing k/ho results in more frequent and higher energy quasi-coherent ejections of fluid from the wall region (Grass, 1971; Raupach, 1981).

The constancy of the filament disturbance wavelength, k_1 , and its Gaussian distribution suggest that it is what it appears to be: an indication of the diameter of the drop which is about to form. Nonetheless, its mean value of about 1.8 does provide some additional evidence into the nature of the filament formation process. Using a two-dimensional linear analysis, Rayleigh (1945) demonstrated that k_1 must be greater than unity for the disturbance along a liquid column to grow. The disturbance of maximum growth rate was shown to be $k_1 \approx 0.7$, while values greater than one were stable. Even the more contemporary solutions, which include the effects of viscosity and finite amplitude disturbances, do not deviate from these values greatly. One of the reasons for this is that the non-linear effects of disturbance growth do not become important until the last 10 to 20 percent of the length of the jet (McCarthy and Molloy, 1974). However, unlike jets in the Rayleigh regime, the filaments examined here display bumps, wrinkles and kinks, and k_1 consumes about 40 percent of the entire filament length. Thus, it is not likely that their character can be described by a two-dimensional analysis, regardless of whether it is linear or non-linear. These filaments also do not conform to any of the other characteristic descriptions provided by the jet breakup modes mentioned in the introduction.

Based on what is known about drop behavior in shear fields (e.g., Clift, et al, 1978), it is evident that there is little or no aerodynamic influence affecting the motion of the drops. For the filaments, the best quantitative measure of aerodynamics in the change in ligament angle which was shown to be negligible. The two DPIV experiments demonstrated that the flow of the air above the free surface could not be differentiated from that of the liquid near the free surface zone. Hence, the observational data combined with the statistical results suggest that there is little or no aerodynamic influence on the above-free-surface character of the wall jet.

Trends in the geometric data (i.e., L_f , D_f , L_f/D_f , D_{dr} , k_1 and \forall_f) as a function of the streamwise direction were also considered, but the degree of random scatter coupled with

the restricted number of observations at each location limited the amount of information they provided. For all runs except two, the drop and filament diameters showed a slight increase with x . The two exceptions were for the lowest roughness plate and the lowest velocity (coarse) plate, so it is possible that their results portray a transitioning below some critical nature.

It was not feasible to measure the properties inside of the rectangular wall jet for the reasons mentioned previously. However, by using the known filament parameters, it is possible to work backwards to get some idea of the jet characteristics that gave rise to their existence. For example, using a simple energy balance that accounts for kinetic, potential and surface energy, one may derive the vertical velocity needed below the free surface to produce a given filament:

$$v' \approx \sqrt{2gL_f + \frac{8\sigma}{\rho D_f}}. \quad (8)$$

Dividing both sides of Eq. (8) by U_o and performing a small amount of additional manipulation leads to

$$\frac{v'}{U_o} \approx \sqrt{\frac{2}{Fr^2} \left(\frac{\bar{h}}{h_o} \right) + \frac{8}{We} \left(\frac{h_o}{D_f} \right)}, \quad (9)$$

where Fr and We are the Froude and Weber numbers of the jet, respectively. Equation (9) may be used to calculate the eddy fluctuation necessary to give birth to each of the individual filaments. This results in mean turbulent fluctuations that vary from about 9 percent for the smooth-plate to nearly 17 percent for the 0.13/3000 case, with an average value of $v'/U_o \approx 0.12$.

Perhaps even more useful, Eq. (9) can be used to derive a rough approximation of the turbulent fluctuations necessary for the inception of drop formation. By applying average values for local mean jet thickness, filament length, and effective filament diameter, one arrives at an expression for the estimated turbulence intensity in terms of Fr and We alone

$$\frac{v'}{U_o} \geq \sqrt{\frac{4}{Fr^2} + \frac{22}{We}}, \quad (10)$$

which is similar to the technique used by Merrill and Sarpkaya (1998). As plotted in Fig. 69, Eq. (10) more clearly demonstrates the relationship between the sub-surface velocity fluctuations and the Froude and Weber numbers. The importance of the level of supercriticality of the jet becomes very apparent in Fig. 69, which suggests that a wall jet with a "low" level of supercriticality, requires very large values of v'/U_o (especially in the outer regions of the flow) to generate drop-forming filaments. It was previously pointed out that the relative roughness is a key factor in drop formation, yet it does not appear explicitly in Eq. (10). The reason for this is that D_f/h_o and \bar{h}/h_o are the only terms affecting the numerators in Eq. (10) (see Eq. (9)). D_f/h_o can be treated as essentially constant (Fig. 68) and \bar{h}/h_o does not depend on k/h_o for drop inception (see Fig. 25). Hence, a jet that is sufficiently supercritical and reaches a value of $\bar{h}/h_o \approx 2$, at the levels of Fr and We shown in Fig. 69, embodies all of the features necessary to produce nascent drop-forming filaments. Roughness, therefore, does not specify what level of v'/U_o is necessary for drop inception; rather, it increases the likelihood that a given flow is capable of producing that level of v'/U_o . Regardless of roughness, however, Fig. 69 strongly suggests that for drops to be realizable events, the flow must have reached a minimum supercritical state.

Although the above expression was based on the events observed at the free surface, the results make it clear that the nature of the filaments and drops is inextricably linked to the subsurface nature of the jet.

3. Internal Flow Structure of Bow Sheets

A complete understanding of the drop formation phenomena requires not only a knowledge of what exists above and near the free surface, but also (unfortunately) what is beneath it, all the way to the wall and the internal structures that form on it. Such a total awareness would necessitate a comprehensive edification of the creation, convection and diffusion of turbulence within the jet. Recognizing that the free surface disturbances serve to couple what is above with what is below, and that they provide a path for each "world" to communicate with the other, knowledge of their behavior is a necessary—but not a sufficient—condition for describing the subsurface behavior.

From what has been seen and measured, it is evident that the internal flow structure of the wall jet (or bow sheet) is not the same as either a typical boundary layer or a submerged wall jet. The velocity profile in the latter is largely influenced by the strong shear at the periphery of the jet (in addition to the distance from the nozzle, velocity profile and turbulence contained within the jet at birth), a factor not present in bow sheets. The difference between this jet and a typical turbulent boundary layer becomes more evident when one attempts to predict when the boundary layer in the wall jet will reach the free surface using analytically determined equations such as Eqs. (6) and (7). The free surface fluctuations that develop in the drop generation region—which temporally change the local jet thickness by as much as 50 percent—must alter the boundary layer character in the outer region, since the latter extends to the free surface long before this point. The free surface disturbances in the mildly supercritical flow of the water tunnel readily introduced a noticeable amount of air into the body of the jet. It is, therefore, not unreasonable to suspect that this effect would be even more dramatic in the case of the rectangular wall jet which was thinner, flowed at a higher velocity and produced larger disturbances. Open channel flows are acceptably well-described by classic boundary layer analyses near the wall, and the relatively docile free surface variations caused by slowly rising boils and kolks do not compare to the violent interactions witnessed here.

Besides the noted free surface eruptions, the DPIV measurements in the tunnel jet point out some additional differences between wall jets and other boundary layer flows. Figure 60 shows that the evolving boundary layer of the finite thickness jet (for both the smooth and rough surface) has a great deal of influence on the behavior of the flow in the free surface zone. In ordinary wall jets or boundary layers, the presence of the wall and the influence of the large near-wall velocity gradient diminishes quickly with distance from the wall, contradictory to those of the finite liquid wall jets over plane and curved surfaces (as in the present study). The turbulent profiles of Fig. 66 suggest that higher levels of turbulence are also manifest further from the wall in agreement with the value of v'/U_o calculated using Eq. (9) (compare with Figs. 4, 5 and 7). It is important to point out that the open channel data of Grass (1971) in Fig. 61 is at nearly the same level of

relative roughness as the wall jet, but it is also a subcritical flow, and this is the likely crux of the difference. As the flow becomes less *supercritical* (vis-à-vis U and h), the velocity and turbulence of the inner flow begins to look like a typical boundary layer or submerged wall jet.

What distinguishes the bow sheet from other boundary layer flows is that it is highly supercritical, and develops eddies with sizes on the order of h . Additionally, the inherent fluidity of the free surface allows it to continuously interact with the body of the jet, changing the entire dynamics of the internal flow.

4. Wall Curvature and Inclination

Curvature and inclination of the bow of a ship are inescapable realities that add another dimension to the bow sheet problem. The results of the single concave curved-wall jet examined here show that curvature reduces the density of the spray, as well as the energy of the drop-forming eddies. Part of the cause may be attributable to the potential energy sacrifice required for the flow to progress up the wall, but it also seems certain that changes in internal flow characteristics are occurring due to centrifugal acceleration, as suggested by the smaller mean drop size. A reduction in turbulence intensity (which in the wall jet appears as fewer and shorter filaments) has been seen in other low radius-of-curvature wall jet flows (Kobayashi and Fujisawa, 1983); however, based on the previous discussion, it is not clear if the same results can be applied here. Neither inclination nor curvature had a noticeable impact on the location of the free surface transitions, so it is not possible to ascertain the complete nature of any subsurface differences based on what was observed. However, based on the filament and drop characteristics alone, it is certain that curvature has attenuated the drop-forming events occurring in and above the free surface zone.

5. Numerical Considerations

The nonisotropy of the turbulence and the near impossibility of finding a suitable turbulent model that incorporates the near surface hydro/aerodynamics is an insurmountable task—particularly when the free surface possesses such random motion.

These characteristics also make it unlikely that any realistic results will be obtained using anything less than a full three-dimensional model. As mentioned in the introduction, there are specific efforts being directed in this area. To date, some CFD models have demonstrated the ability to model flows pouring over a weir and the "simple" axisymmetric drop pinch-off problems. It is still undetermined if the ability to model all of the fluid dynamic components exhibited in a wall jet presently exists. Regardless, it is hoped that the quantitative data obtained here will provide a source for numerical verification, and perhaps provide some direction for future numerical model-design consideration.

6. Application to Bow Sheets

This project never lost sight of its ultimate purpose. By examining the characteristics of high Froude, Weber and Reynolds number jets, we wanted to simulate the bow sheet formed by ships, thereby providing a means of predicting the factors that contribute to spray formation. In so doing we have identified two of the primary elements which govern their nature. Specifically, increasing the supercriticality of the flow and the roughness of the wall leads to a greater manifestation of drops and spray. Hence, the very first suggestion is to make ships smoother, giving the greatest attention to the leading edge of the bow.

Some consideration should also be given to the shape of the bow (recognizing that there are other factors which also influence its selection) since fixed curvature proved to be a spray inhibitor. It is possible that more complex shape considerations such as varying the rate of curvature, or using subsurface appendages to change the pressure distribution near the bow, could result in thicker bow sheets (or no bow sheets, as in the case of many supertankers) which are less susceptible to spray formation. This does not preclude the possibility that smoothing coupled with bow shaping might result in even greater reductions in spray generation and all of its attendant consequences.

IV. CONCLUSIONS

The following conclusions can be made based on the characteristics that have been observed and measured within the scope of this investigation:

- Spray generation from liquid wall jets (bow sheets) requires a highly supercritical (in terms of U and h) flow. There exists some minimum value of supercriticality, below which drops will not form. If the local plate conditions are below this level (either because U_0 is too low or x/h_0 is sufficiently large), drop-forming filaments will not develop.
- Wall roughness is not required for spray generation, but it significantly reduces the minimum jet velocity necessary for this event to transpire. The greater the level of relative roughness, the sooner and more abundant is the resulting spray. Moreover, one need only reduce the roughness below some reasonable finite level (perfect smoothness is not required), to substantially reduce the sensitivity of a wall jet to drop production, or to reduce the frequency of the drop forming events.
- The filament and drop production process is of a statistical nature.
- The free surface provides a path for interaction between the above surface events and the internal flow dynamics. This interaction guarantees that the wall jet boundary layer is fundamentally different from that of typical turbulent flows.
- Wall curvature appears to inhibit the formation of filaments and drops.
- Aerodynamics do not influence the characteristic behavior of the filaments and drops; however, free surface disturbances may act to introduce air bubbles into the body of the jet.

The following conditions are to be observed in the use of the above mentioned material:

1. The material is to be used only for the purpose for which it was intended and is not to be used for any other purpose.

2. The material is to be used only in the manner in which it was intended and is not to be used for any other purpose.

3. The material is to be used only in the manner in which it was intended and is not to be used for any other purpose.

4. The material is to be used only in the manner in which it was intended and is not to be used for any other purpose.

V. RECOMMENDATIONS

The following research is recommended as food for thought:

- Make quantitative measurements of the subsurface flow region of the jet.
- Explore the mean of the direct measurement of the local wall shear stress.
- The wall jet should be examined in other facilities that will allow the Reynolds, Weber and Froude numbers of the flow to be uncoupled so that the influence of inertia, surface tension and gravity can be analyzed independently.
- An effort should be made to expand the "margins" of the current information database. That is, determine if higher levels of supercriticality lead to additional phenomenological transitions; and, ascertain what the minimum levels of supercriticality are for various degrees of relative roughness.
- Thoroughly examine the effects of curvature by investigating how its influence on spray formation is shaped by jet velocity and wall roughness.

The following table is a summary of the data collected.

- The first part of the table shows the results of the first experiment.
- The second part of the table shows the results of the second experiment.
- The third part of the table shows the results of the third experiment.
- The fourth part of the table shows the results of the fourth experiment.
- The fifth part of the table shows the results of the fifth experiment.
- The sixth part of the table shows the results of the sixth experiment.
- The seventh part of the table shows the results of the seventh experiment.
- The eighth part of the table shows the results of the eighth experiment.
- The ninth part of the table shows the results of the ninth experiment.
- The tenth part of the table shows the results of the tenth experiment.

APPENDIX A. FIGURES

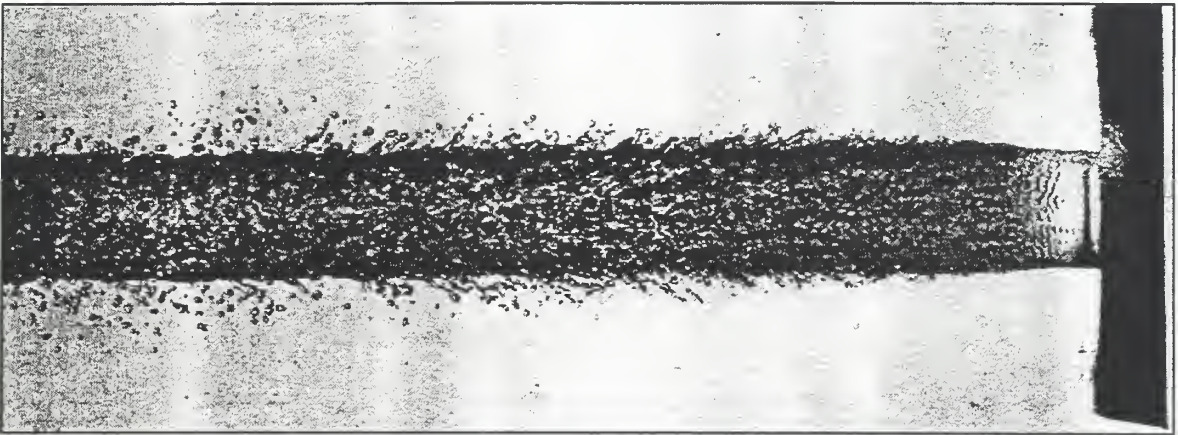


Figure 1. Side view of a free liquid jet discharging into air. From Hoyt and Taylor (1977a).

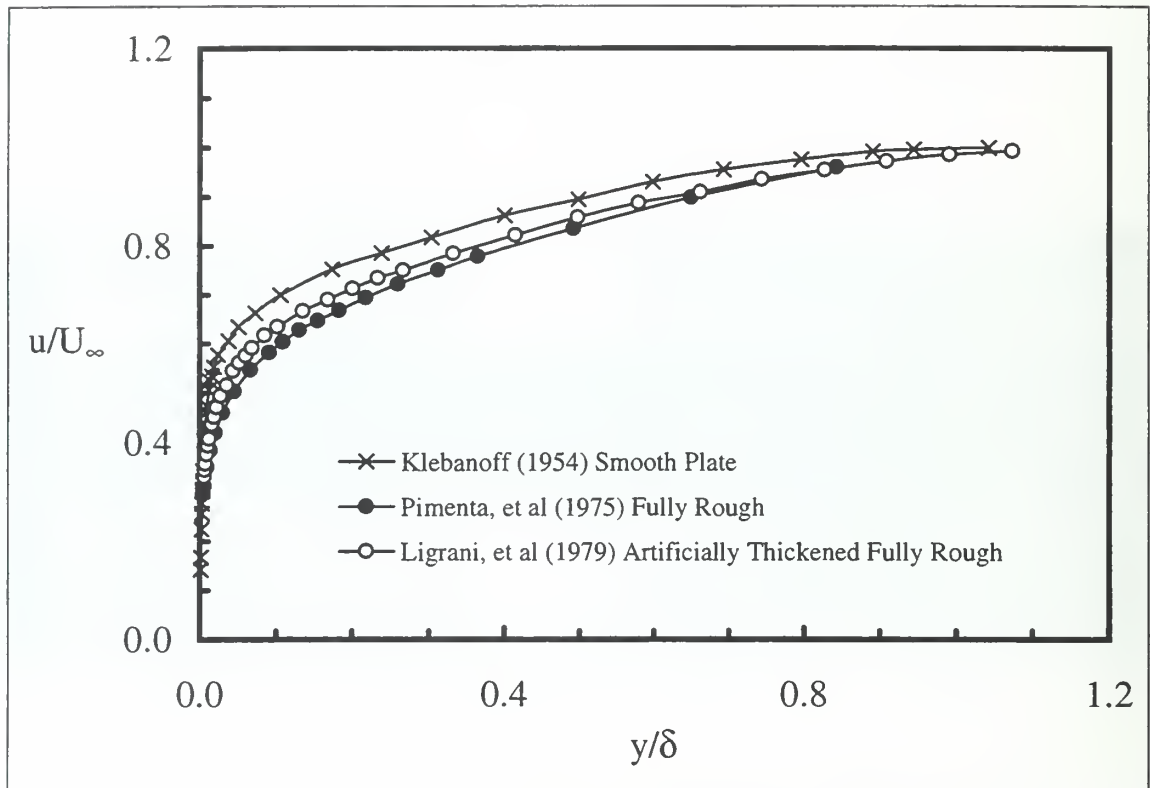


Figure 2. Mean velocity distribution across the turbulent boundary layer formed by smooth- and rough-walled surfaces.

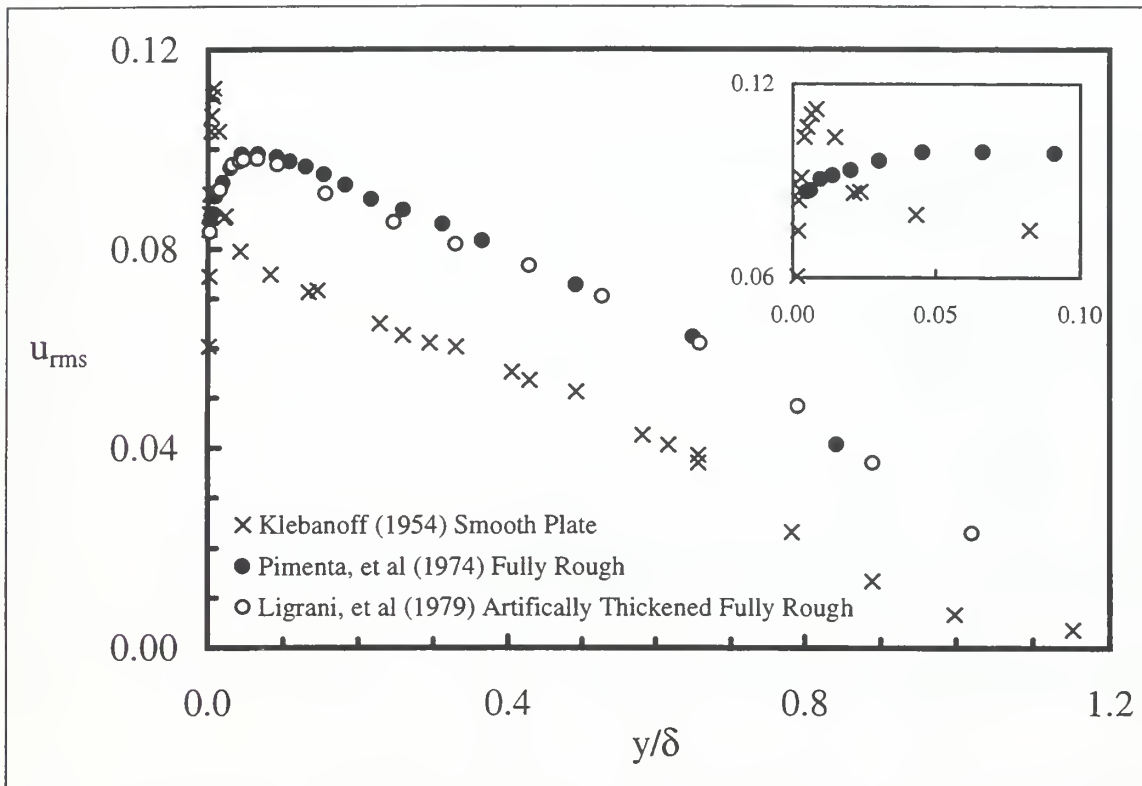


Figure 3. Streamwise turbulence intensity across the boundary layer formed by smooth and rough-walled surfaces.

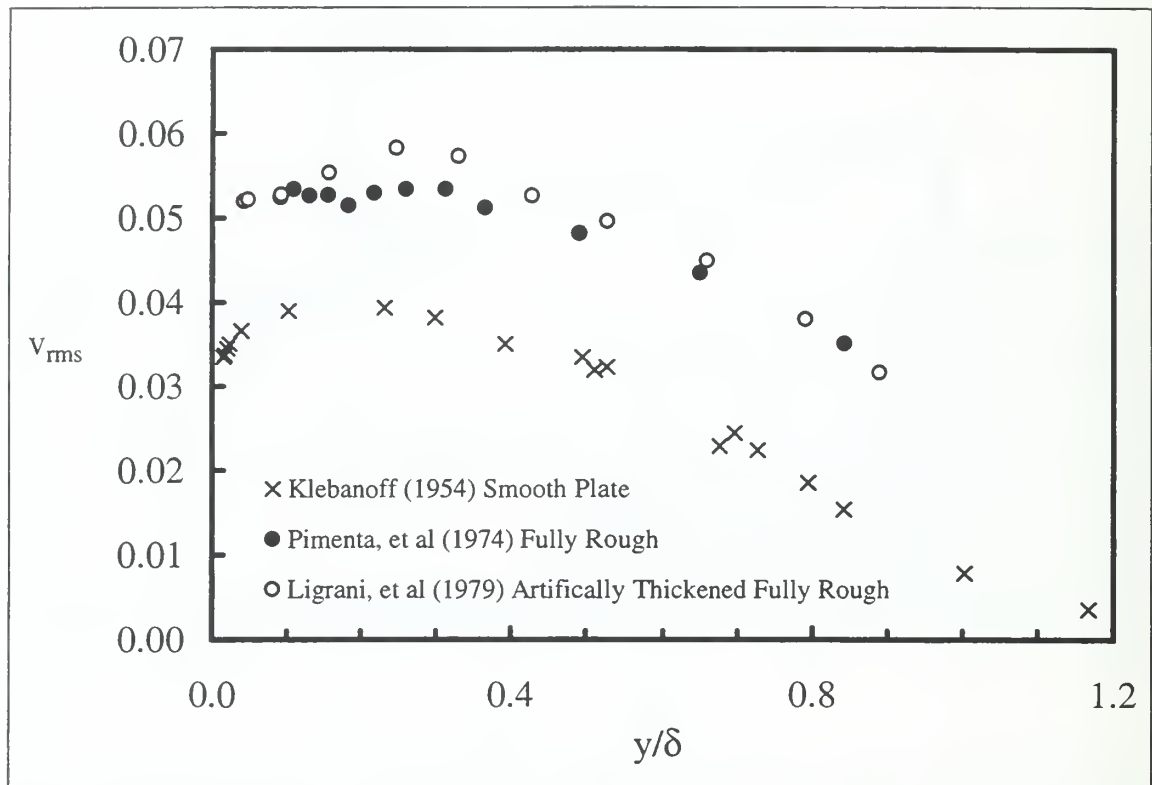


Figure 4. Vertical turbulence intensity across the boundary layer formed by smooth- and rough-walled surfaces.

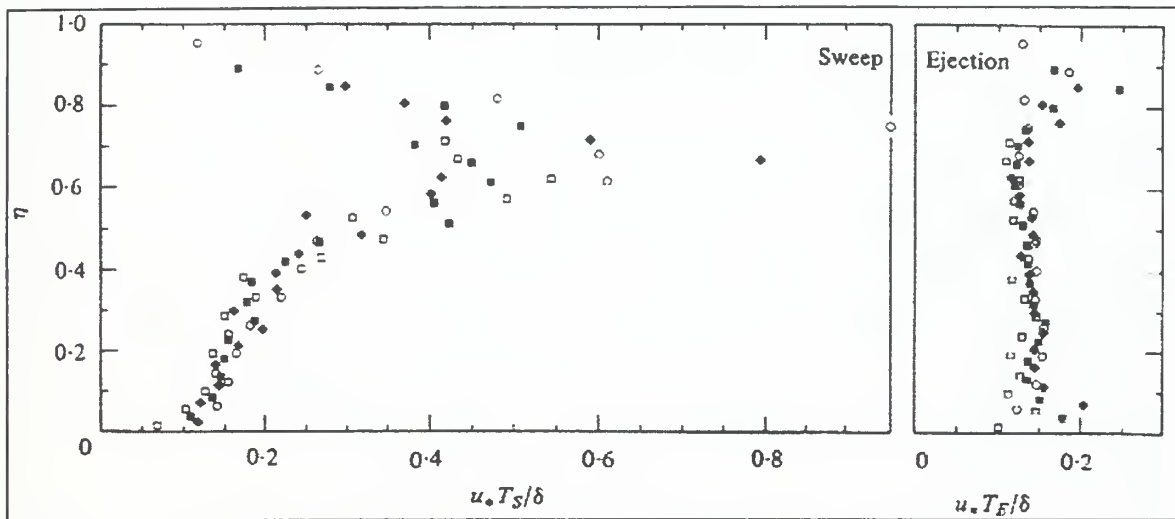


Figure 5. Nondimensional sweep and ejection frequency versus boundary layer thickness, η , adjusted for roughness element height. From Raupach (1981).

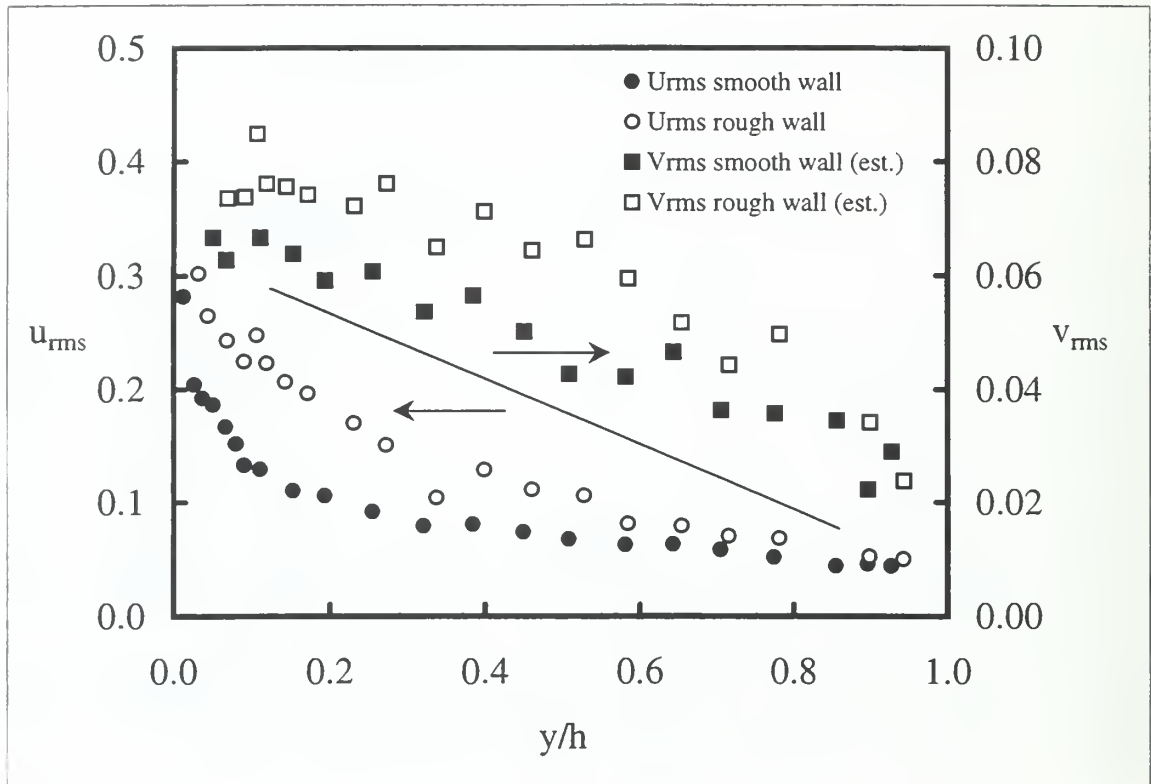


Figure 6. Streamwise and vertical turbulence intensity across a smooth- and rough-walled open channel. $Re = 9800$, $Fr = 0.2$. For the rough wall, $k/h = 0.065$. From Nezu and Nakagawa (1993).

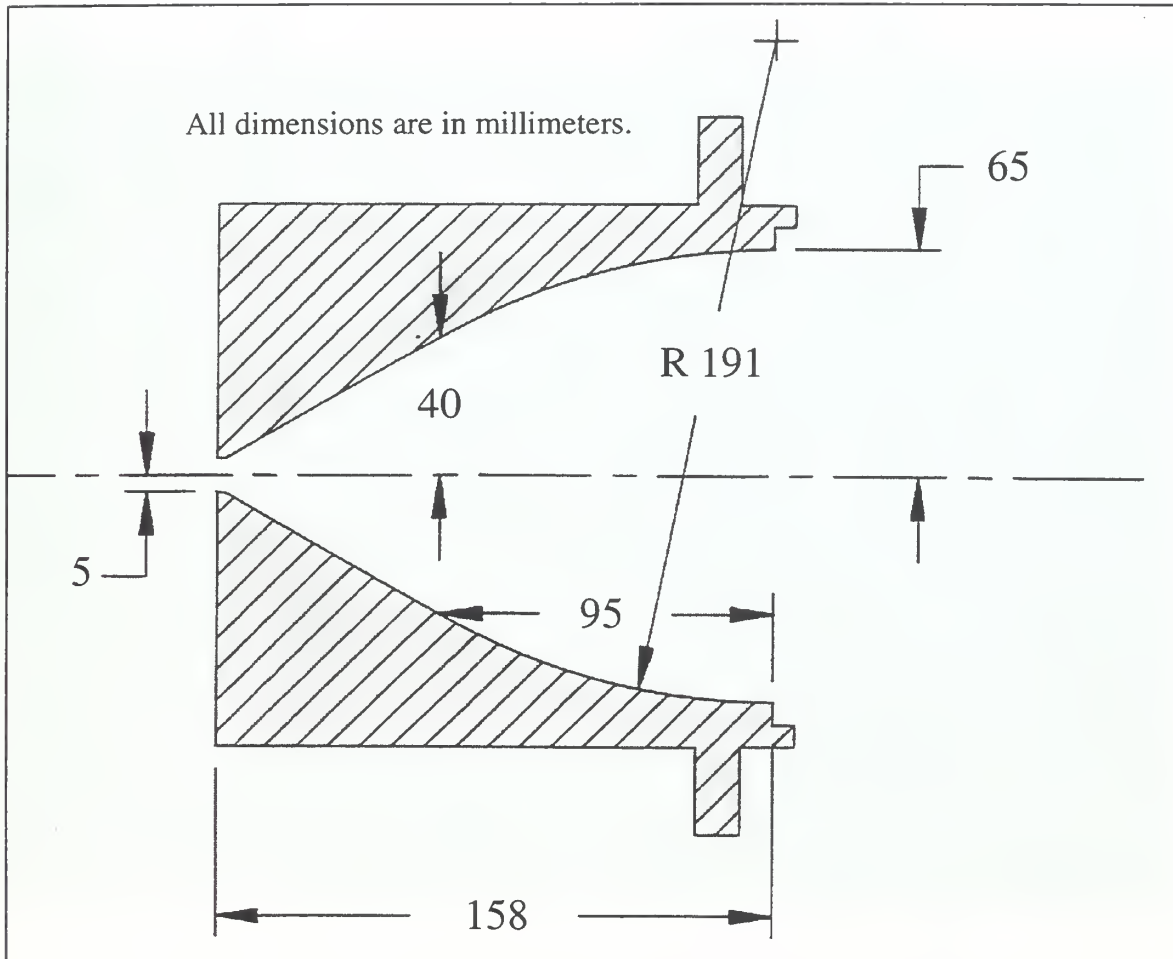


Figure 8. CAD drawing of the rectangular liquid wall jet nozzle.

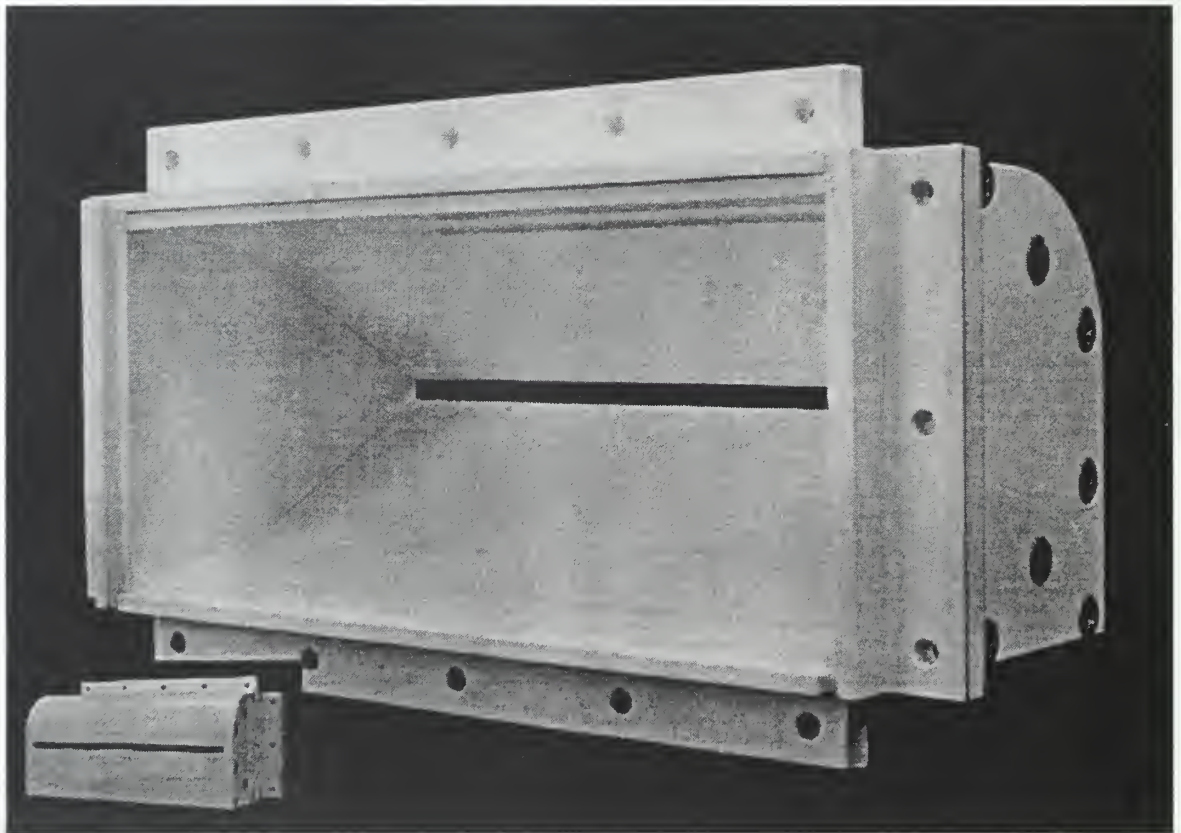


Figure 9. Photograph of the rectangular liquid wall jet nozzle.

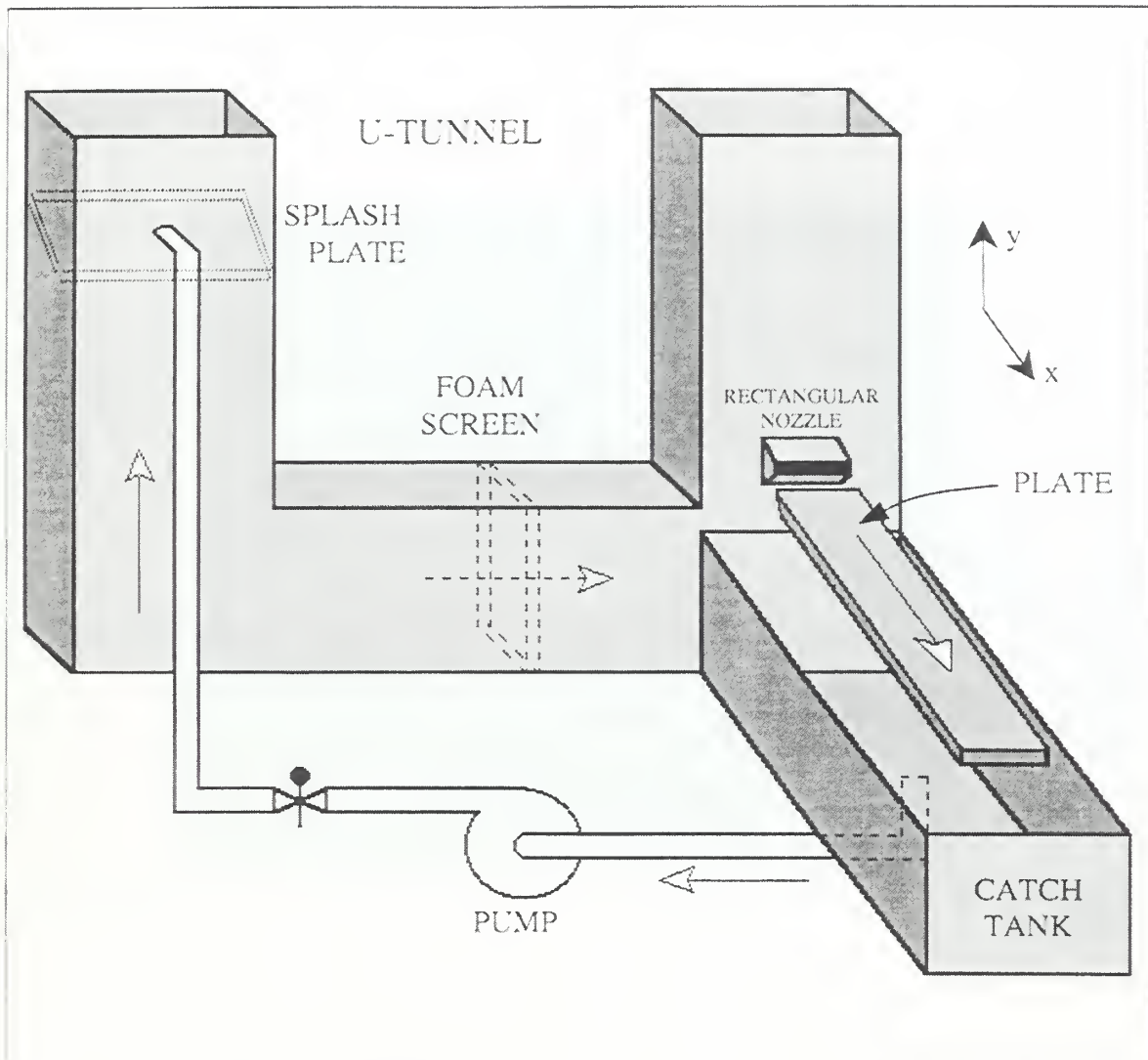


Figure 10. Equipment arrangement for the rectangular liquid wall jet experiments. The fluid flow path is as indicated by the arrows.

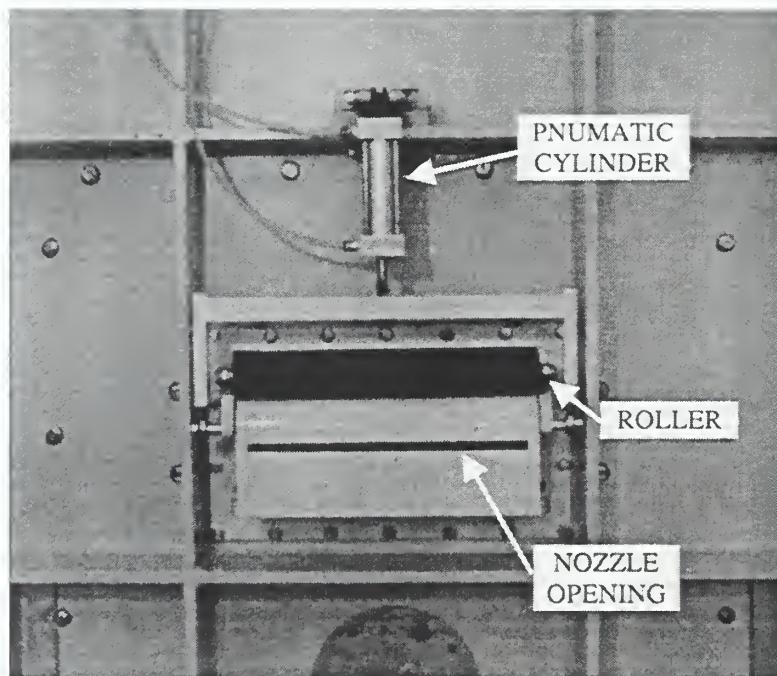


Figure 11. Photograph of the outside of the rectangular nozzle with the cylindrical gate open.

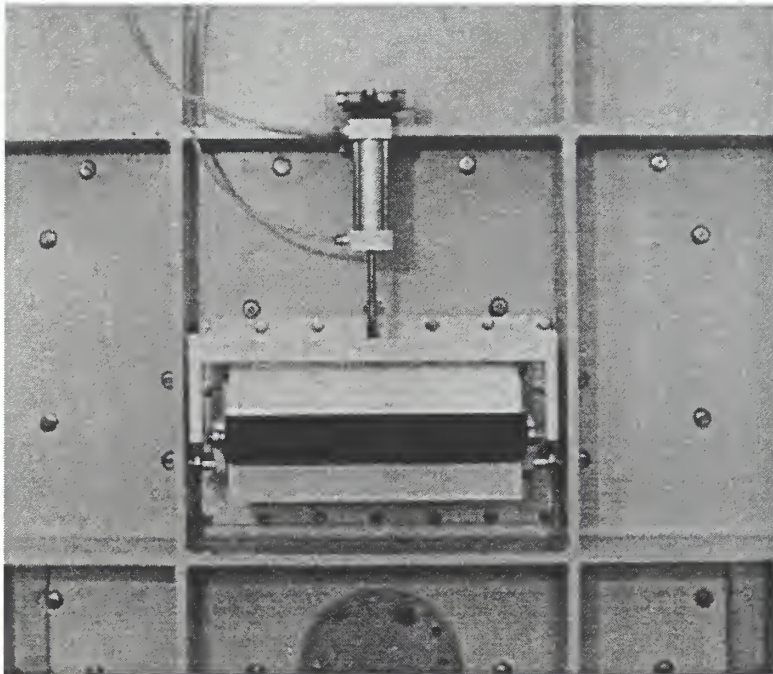


Figure 12. Photograph of the outside of the rectangular nozzle with the cylindrical gate closed.

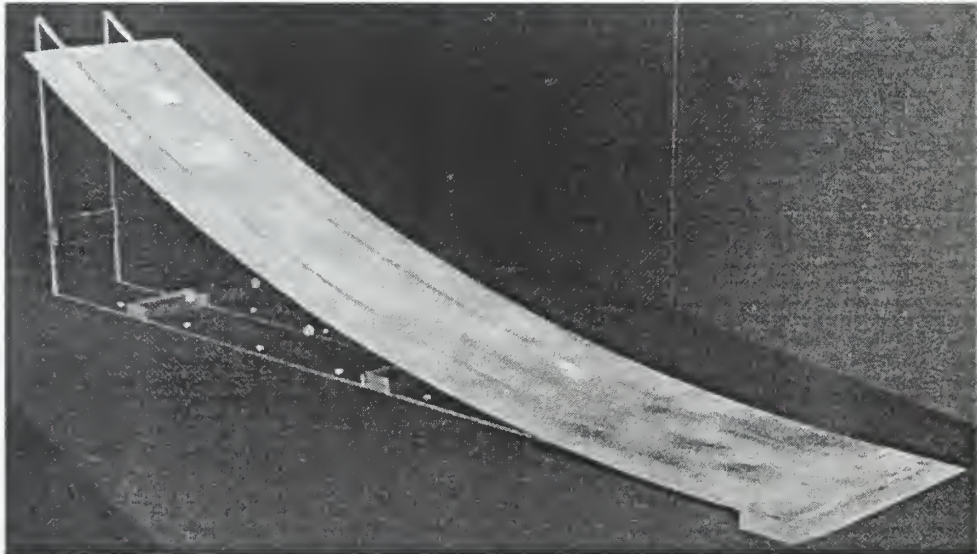


Figure 13. Photograph of the rough ($k/h_o = 0.06$) curved plate used in the rectangular jet experiment.

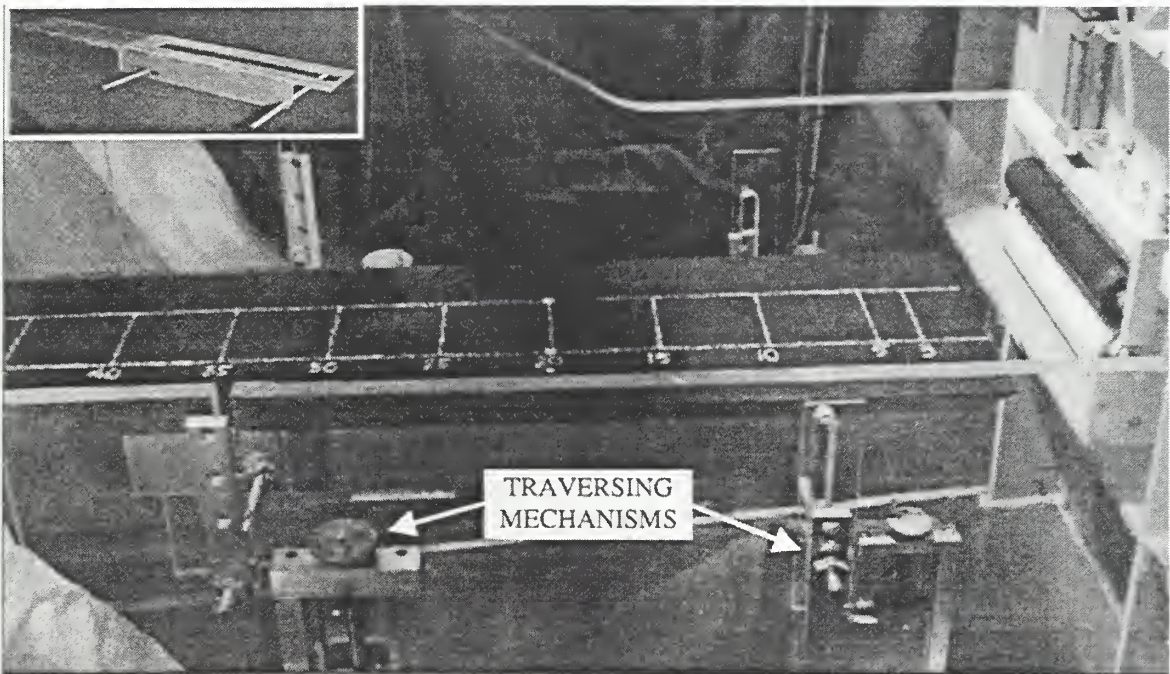


Figure 14. Photograph of a rough plate installed in the rectangular liquid wall jet apparatus. The plate-mount without a plate attached is shown in the upper left-hand corner.

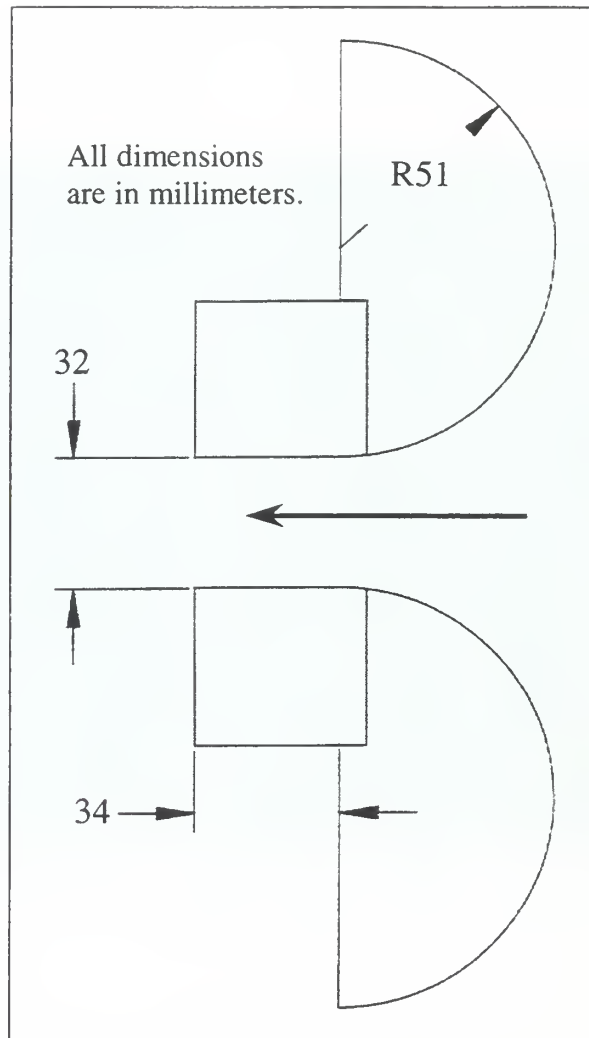


Figure 15. CAD drawing of the axisymmetric nozzle.

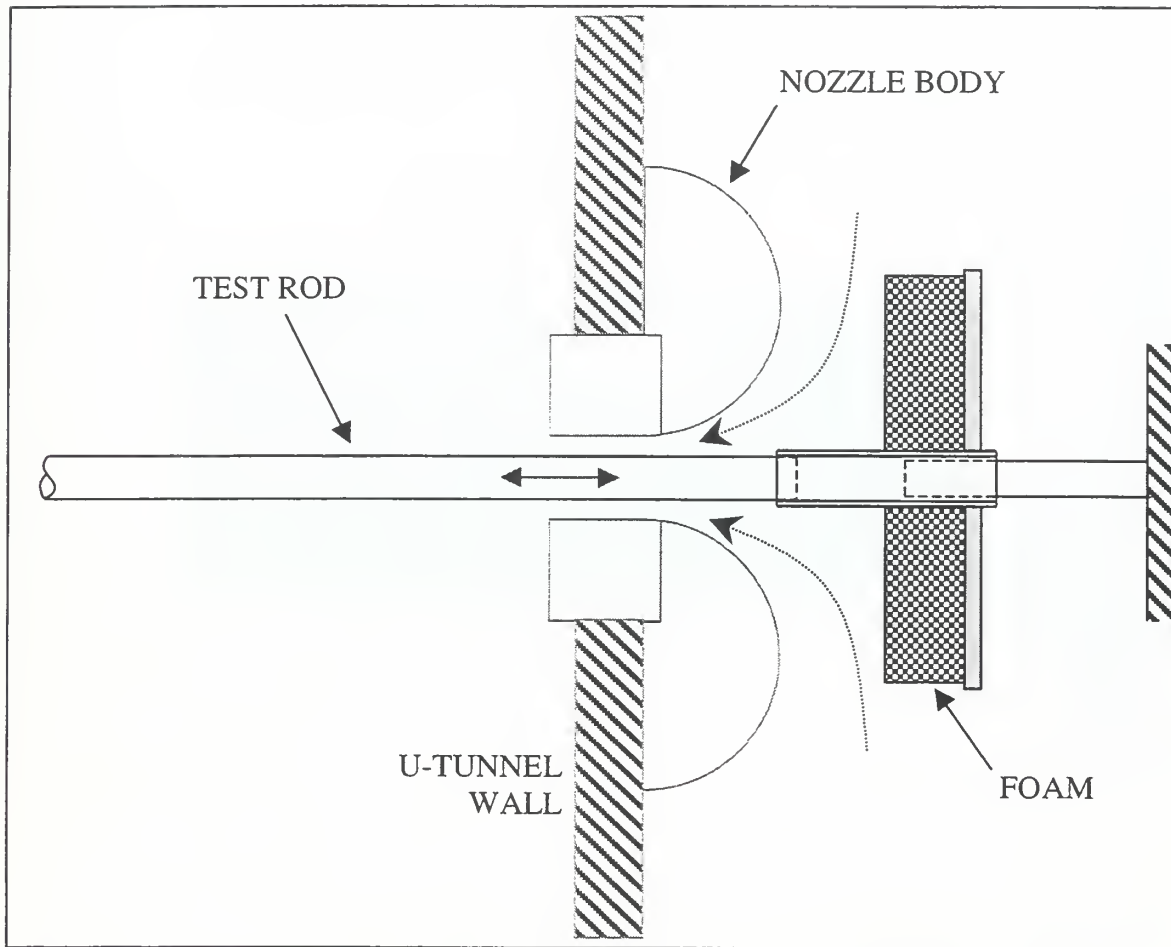


Figure 16. Side view of the axisymmetric nozzle with the test rod assembly installed.



Figure 17. An image of the free surface profile of the rectangular liquid wall jet.
 $Re_x = 2.3 \times 10^6$, $Re = 3.6 \times 10^4$, $Fr = 26$, $We = 3000$, $k/ho = 0.06$.



Figure 18. An image of a three-dimensional free surface distortion.

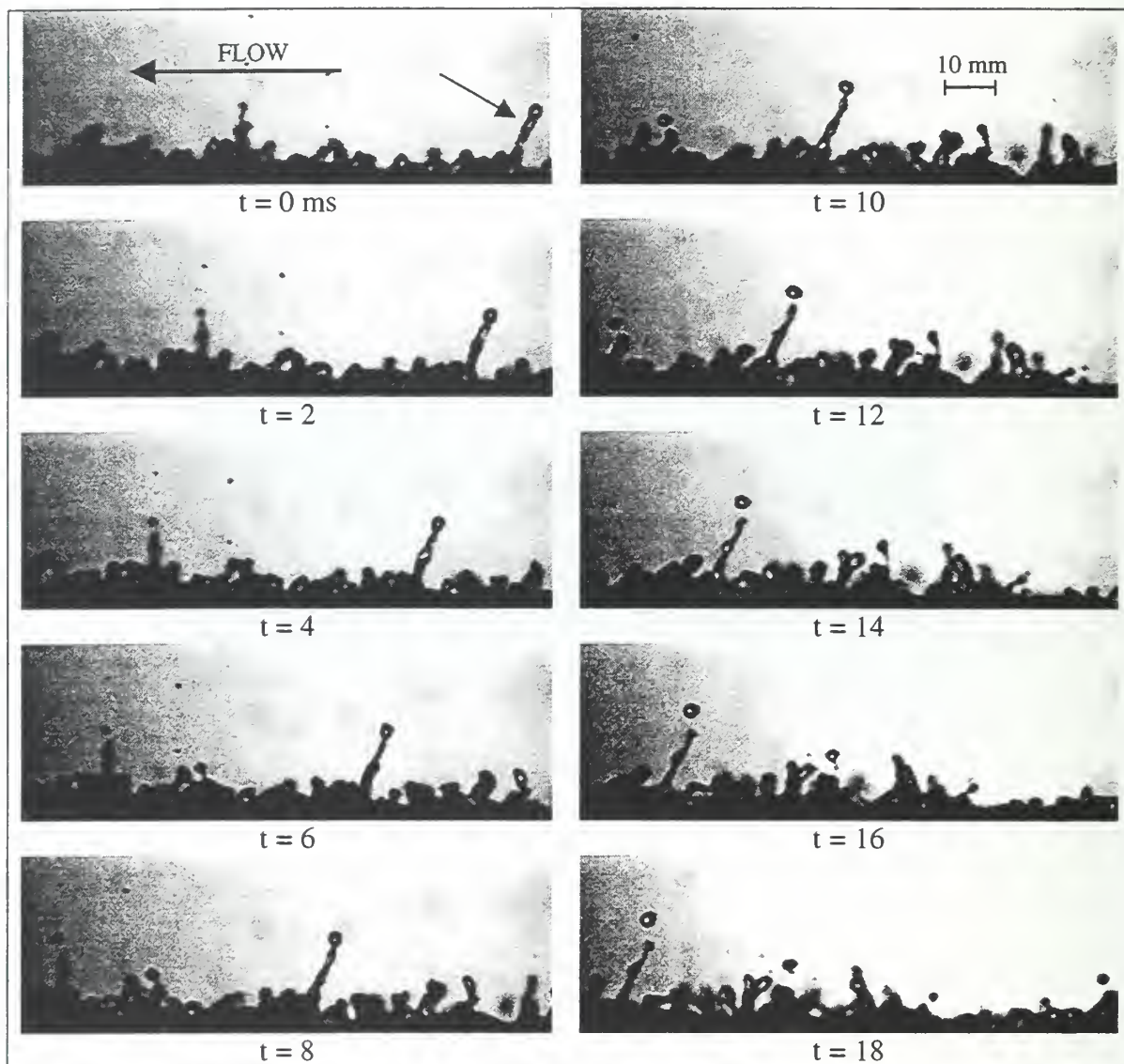


Figure 19. A typical sequence of images captured for the filament and drop analysis.
 $Rex = 2.3 \times 10^6$, $Re = 3.6 \times 10^4$, $Fr = 26$, $We = 3000$, $k/ho = 0.06$.

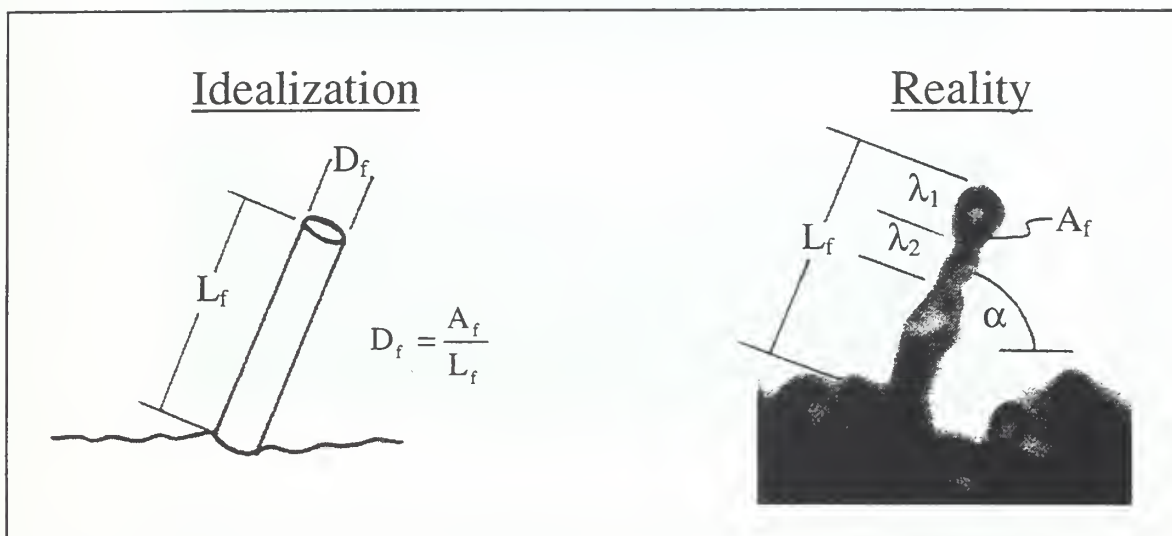
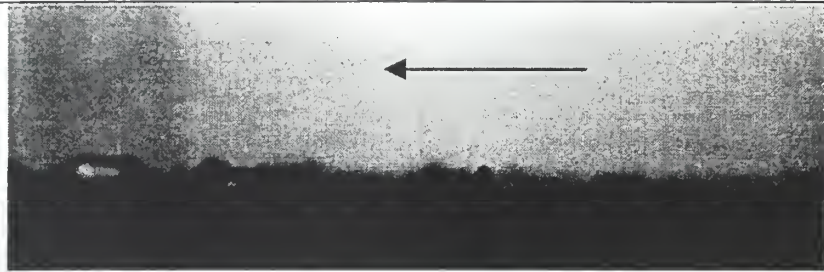


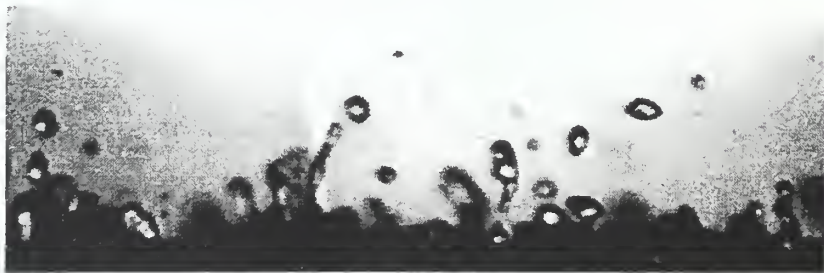
Figure 20. Diagram showing how the filament characteristics are simplified for statistical analysis.



a. Transition to roughness.



b. Filament formation.



c. Drop generation.

Figure 21. Photographs of the different regions in a liquid wall jet.

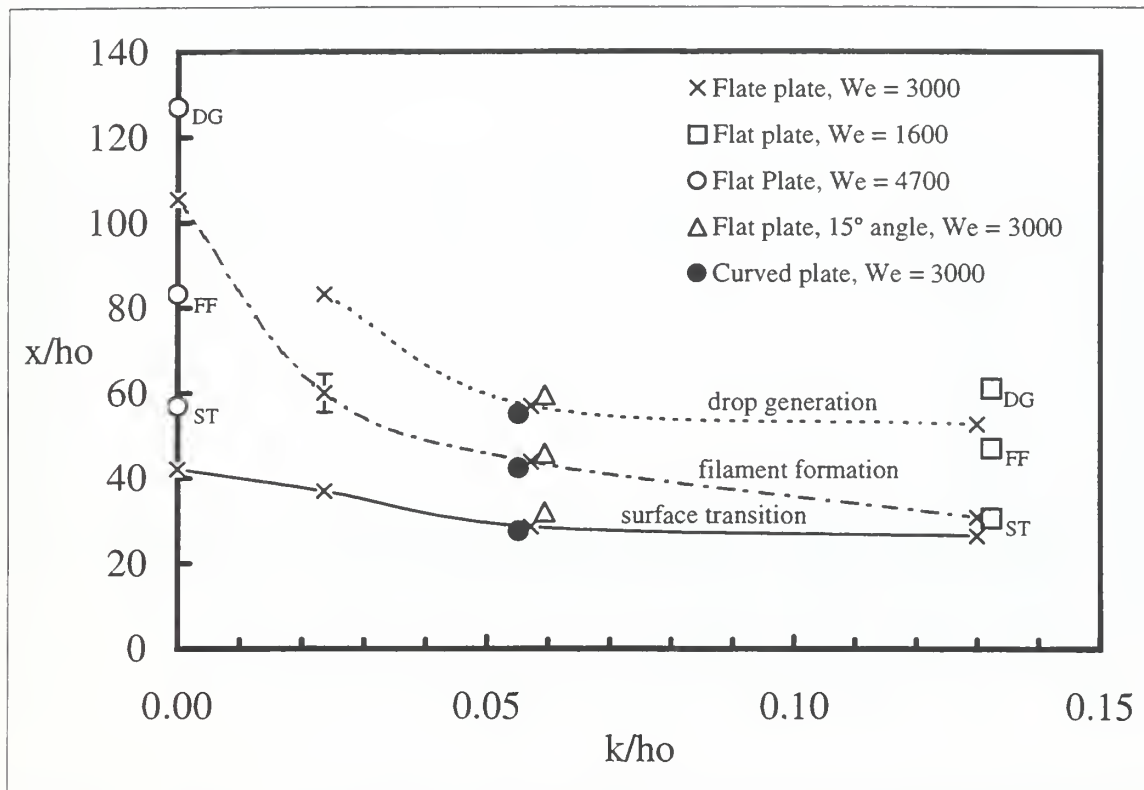


Figure 22. Distances to surface transition (ST), filament formation (FF) and drop generation (DG) as a function of plate roughness, k/h_o . The uncertainty shown for filament formation at $k/h_o = 0.02$ is typical for all positions.

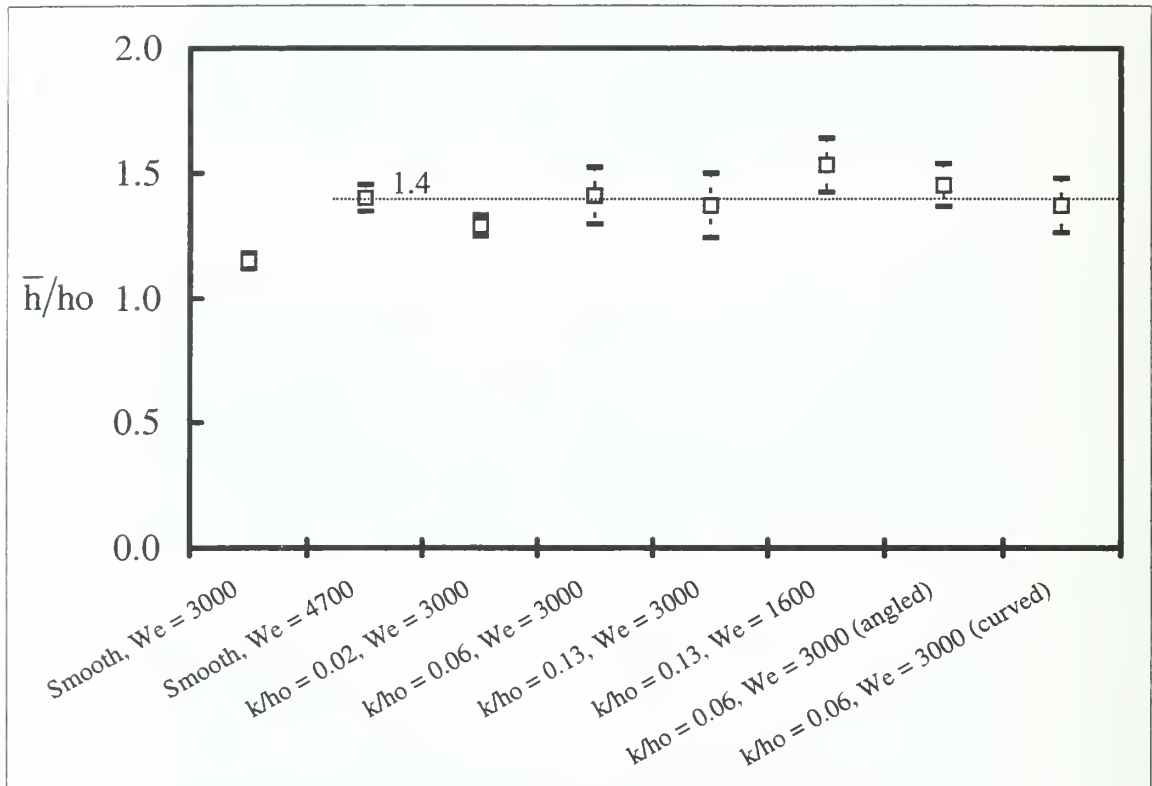


Figure 23. Normalized mean jet thickness at the beginning of the transition to roughness region. Uncertainty regions are bracketed and the average value for the drop producing runs is 1.4.

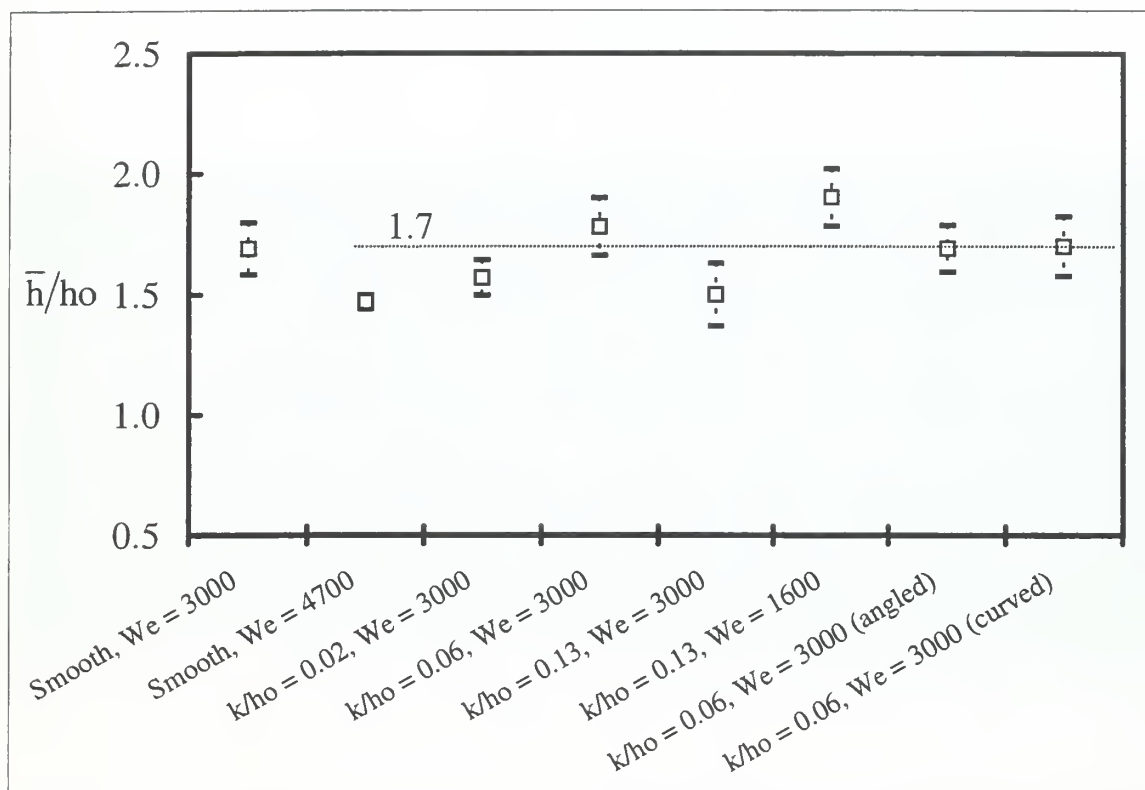


Figure 24. Normalized mean jet thickness of the liquid wall jet at the beginning of the filament formation region. Uncertainty regions are bracketed and the average value for the drop-producing runs is 1.7.

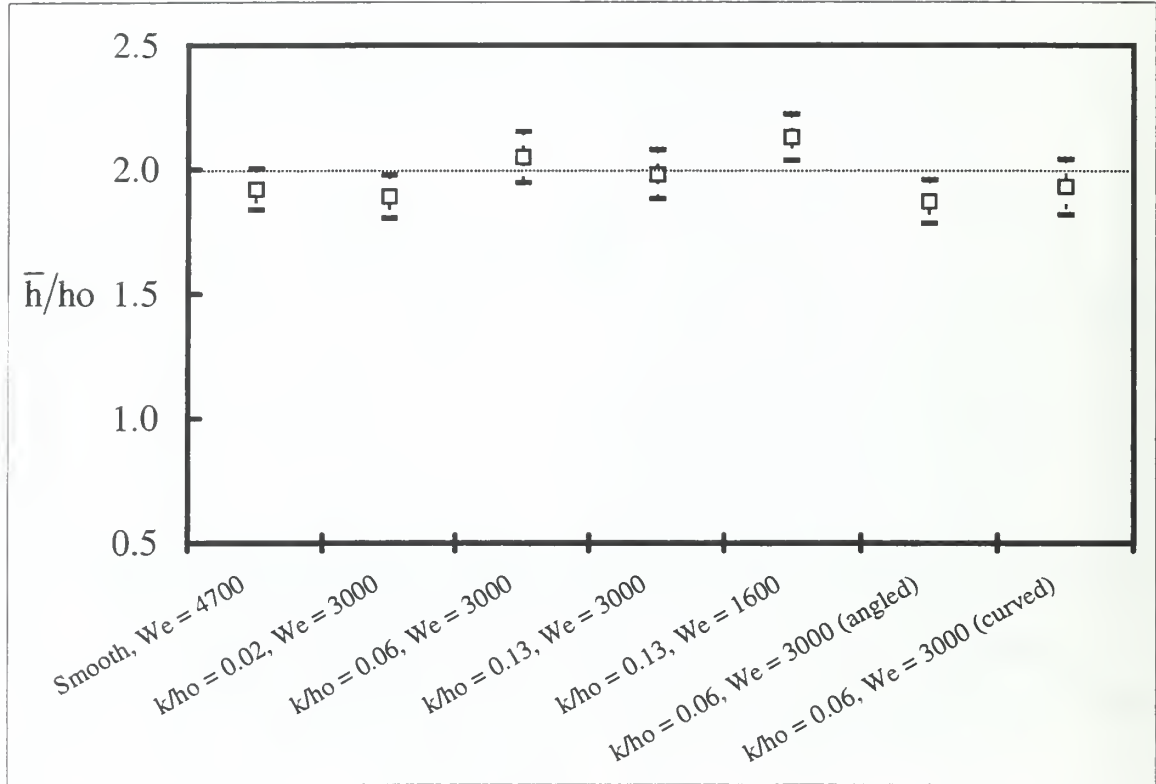


Figure 25. Normalized mean jet thickness at the beginning of the drop generation region. Uncertainty regions are bracketed and the average value is 2.0.

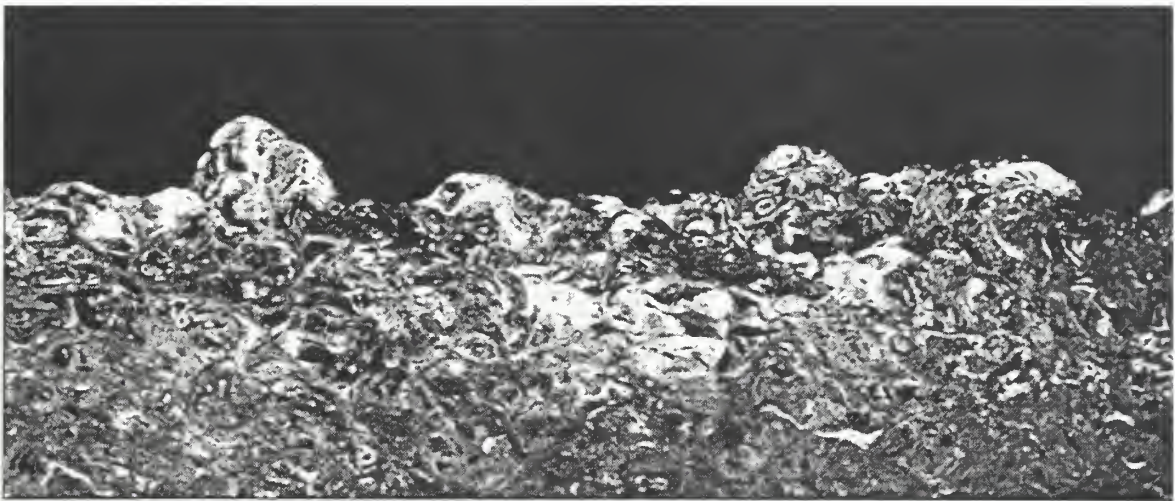


Figure 26. A laser light sheet illuminated photograph of the free surface flow over the axisymmetric liquid wall jet. Flow is from right-to-left and the actual width of the image is about four centimeters.

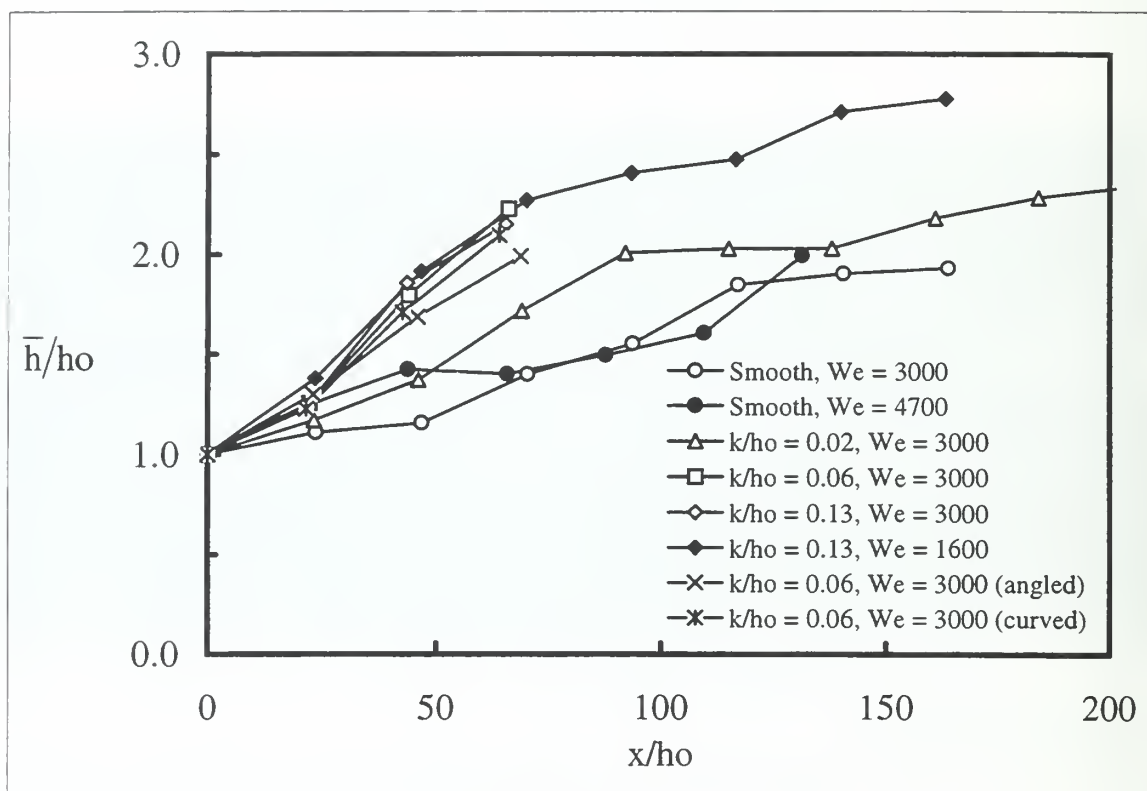


Figure 27. Normalized mean jet thickness as a function of the nondimensional streamwise coordinate.

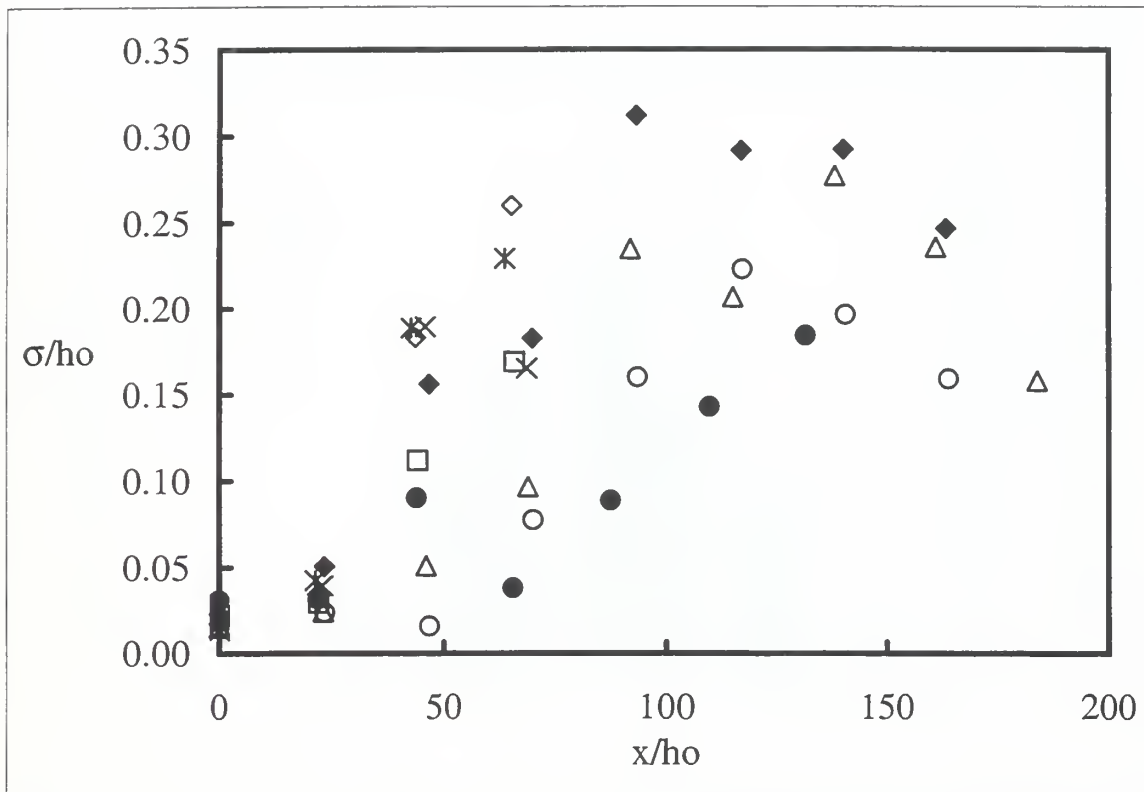


Figure 28. Standard deviation of the mean jet thickness as a function of the nondimensional streamwise coordinate. The symbols are as shown in Figure 27.

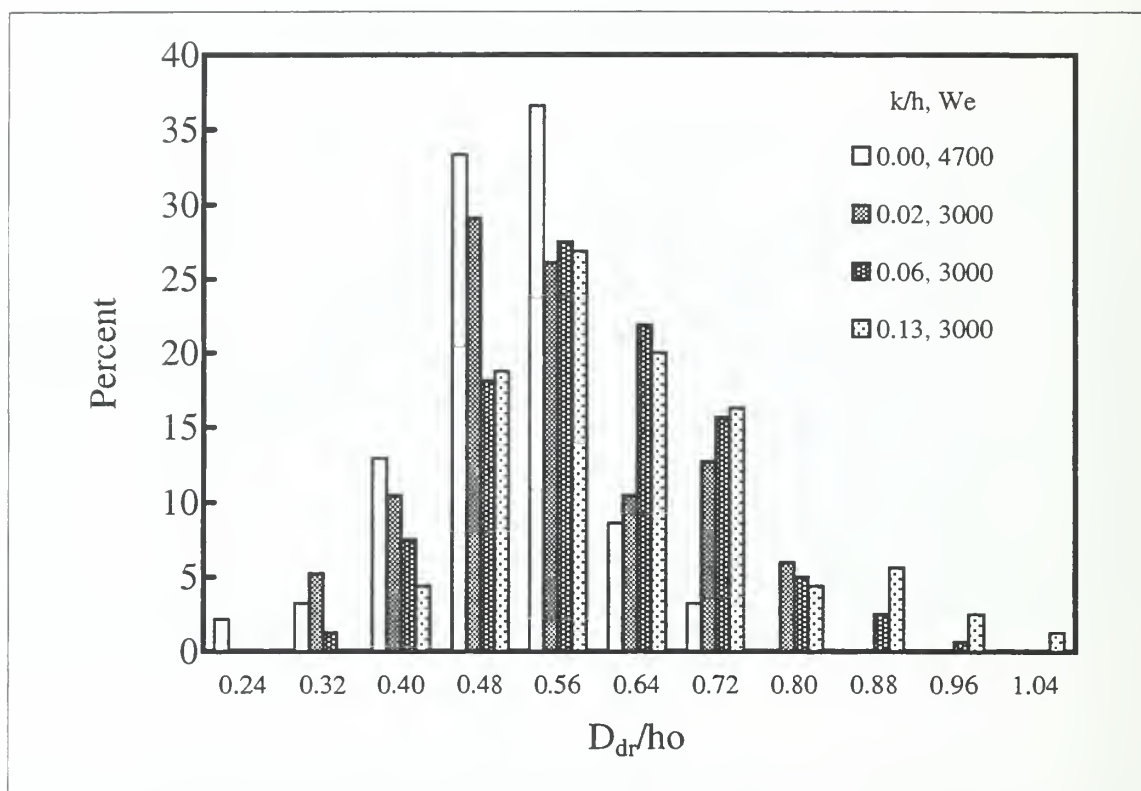


Figure 29. Distribution of the normalized drop diameter as a function of relative roughness.

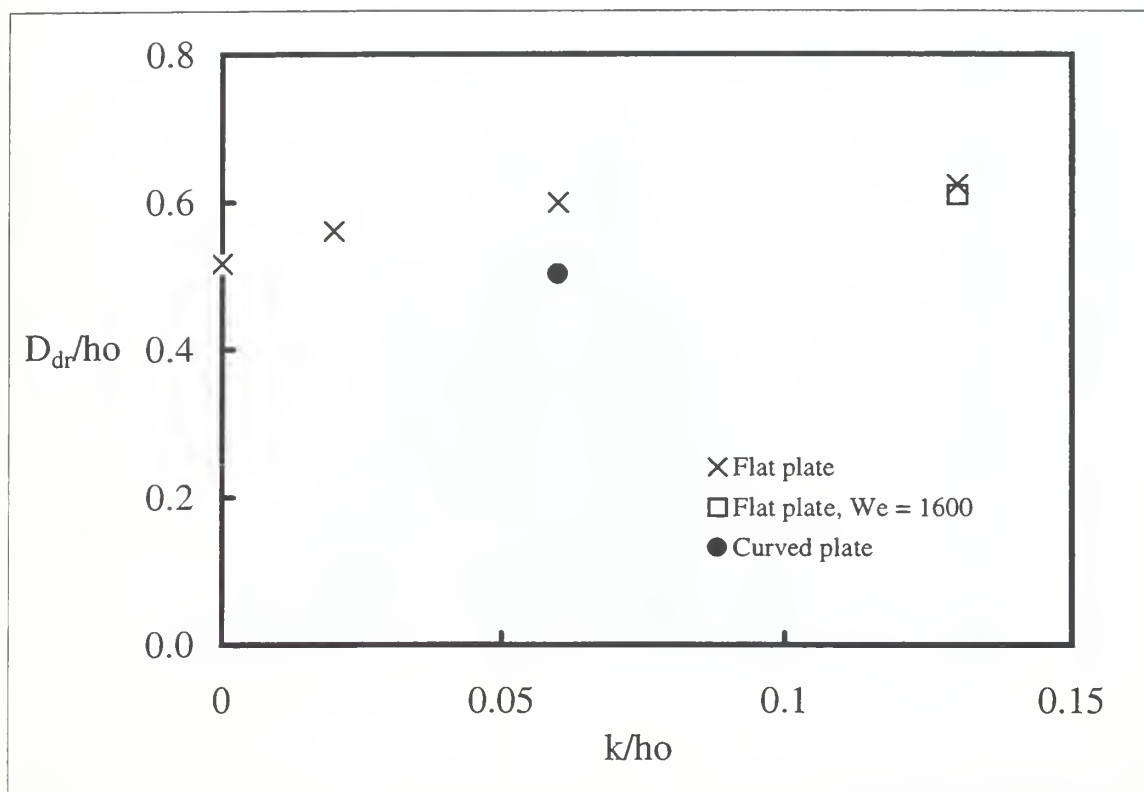


Figure 30. Mean normalized drop diameter as a function of the relative roughness.

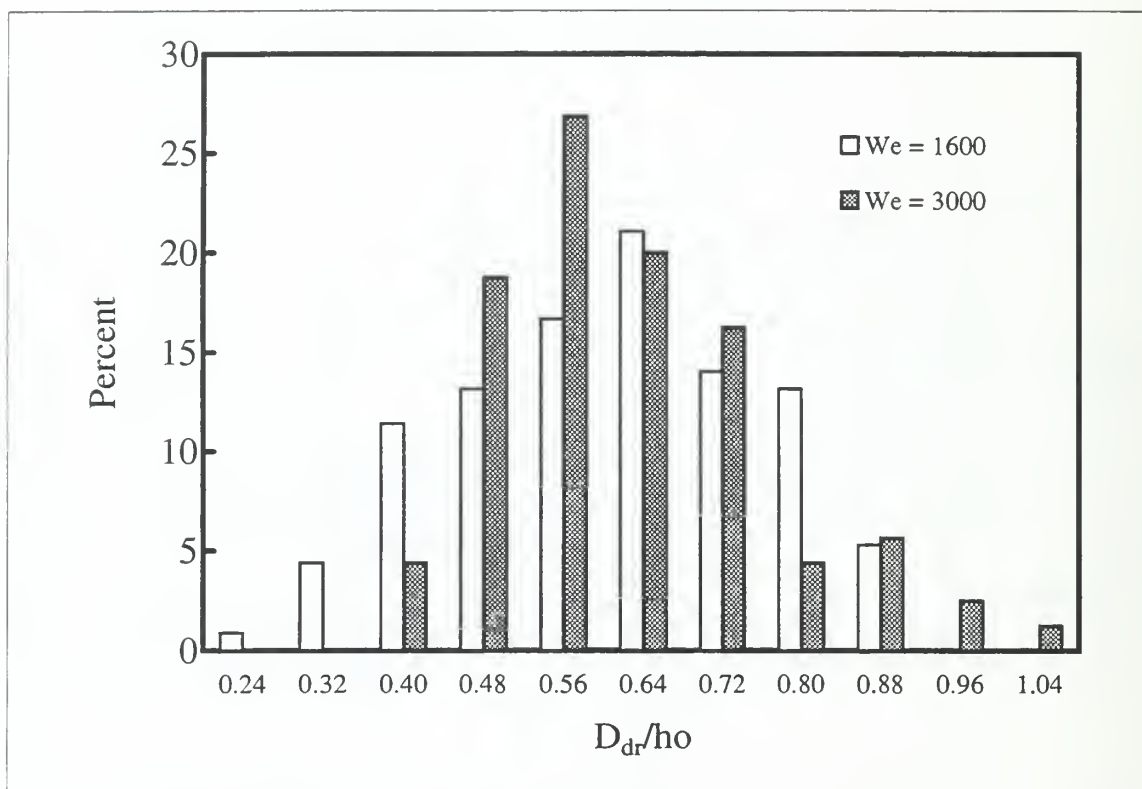


Figure 31. Distribution of the normalized drop diameter for the coarse-wall ($k/h_o = 0.13$) at high- and low-Weber number.

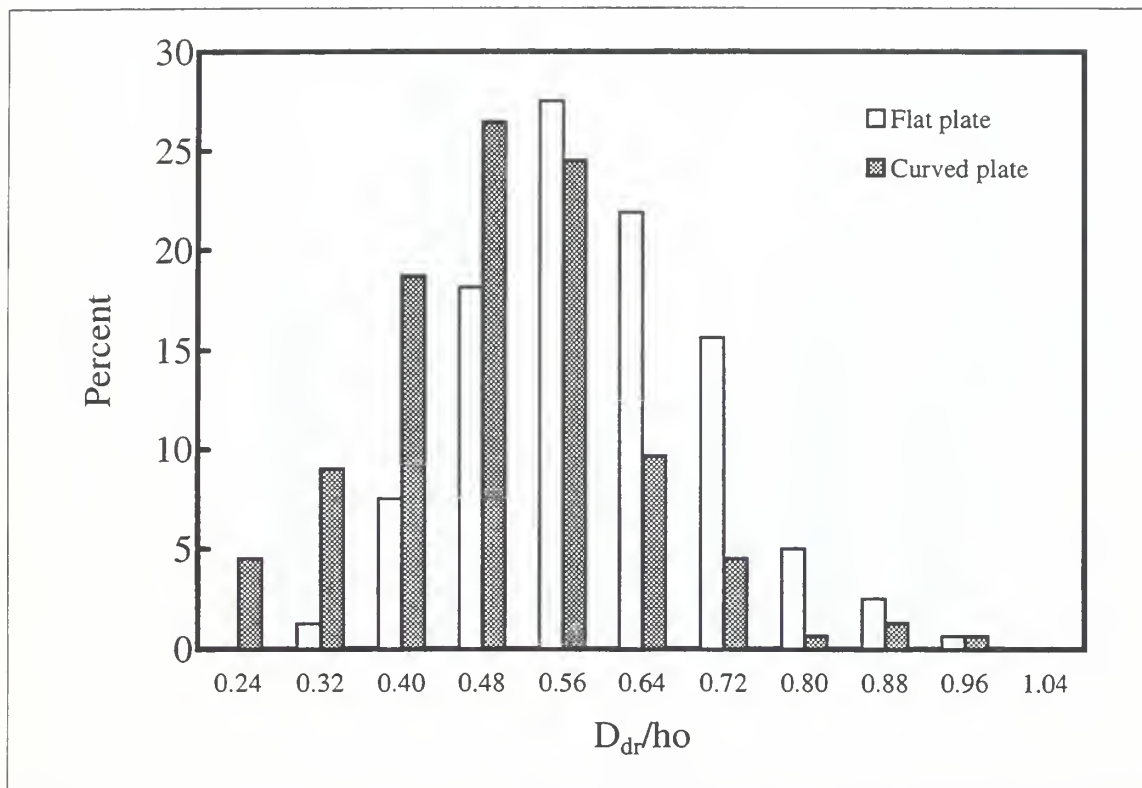


Figure 32. Distribution of the normalized drop diameter for the flat- and curved-wall ($k/h_o = 0.06$, $We = 3000$).

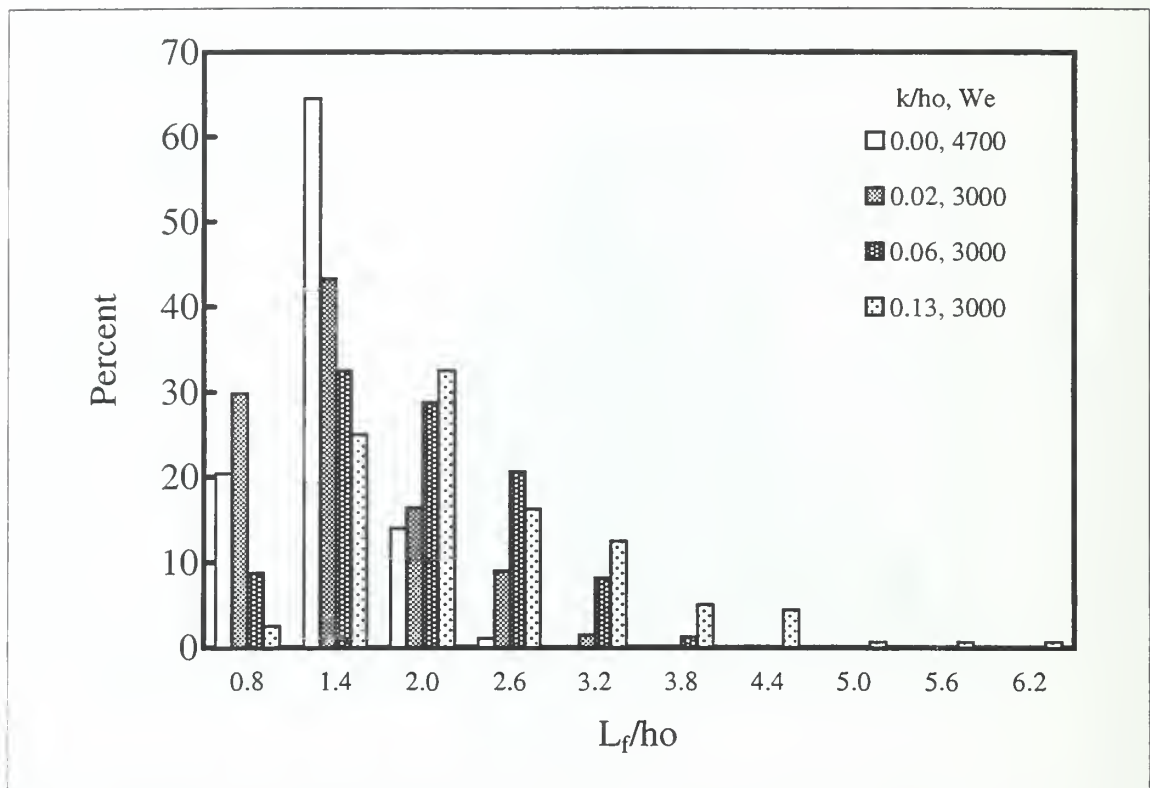


Figure 33. Distribution of the normalized filament length as a function of the relative roughness.

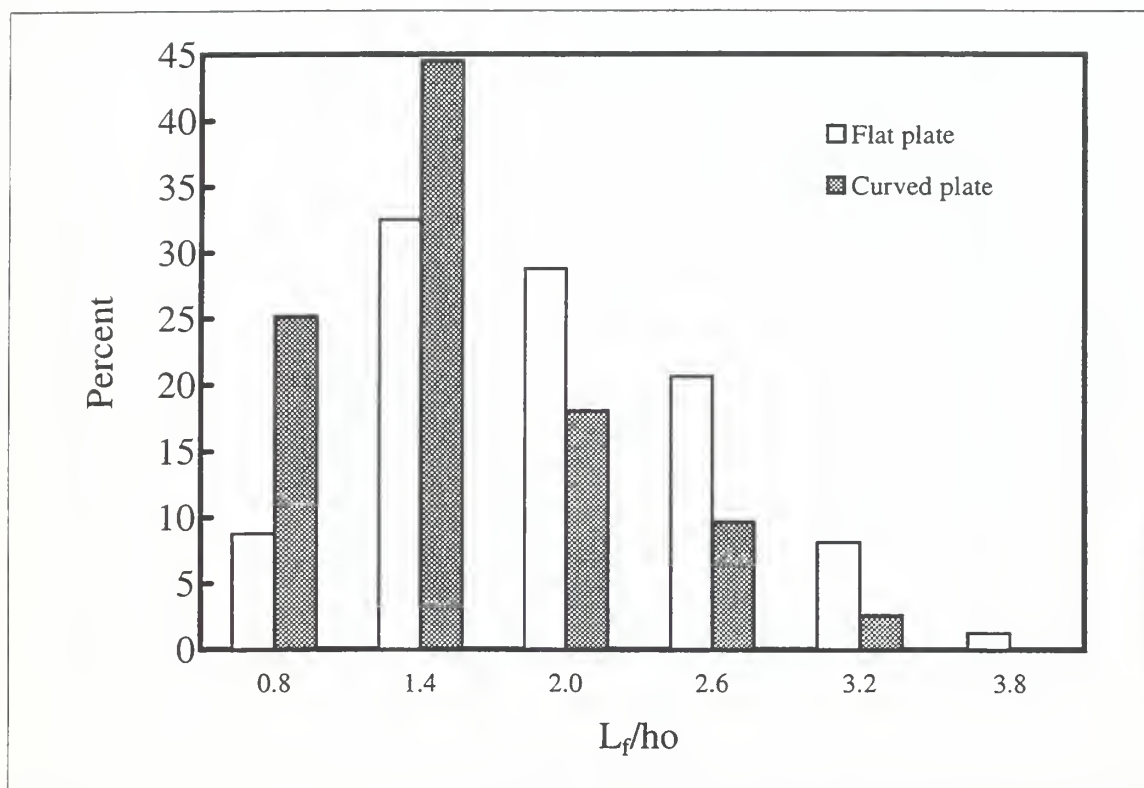


Figure 34. Distribution of the normalized filament length for the flat- and curved-wall ($k/h_o = 0.06$, $We = 3000$).

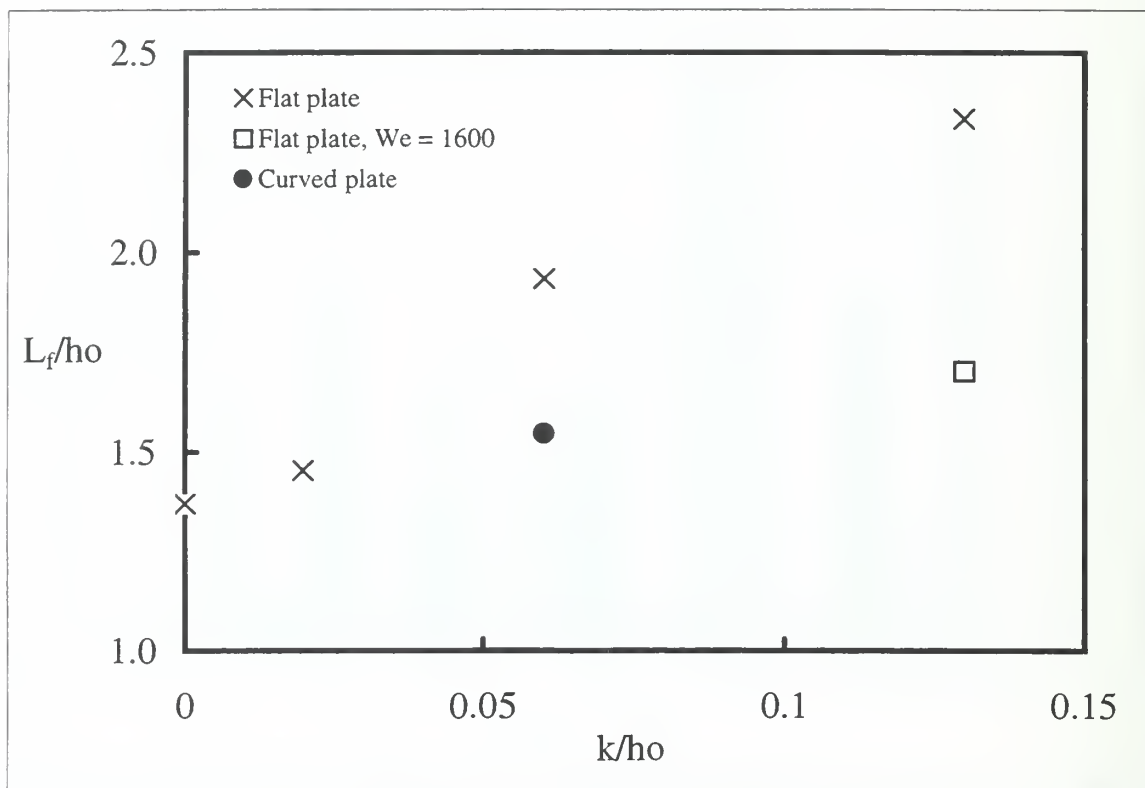


Figure 35. Mean normalized filament length as a function of relative roughness.

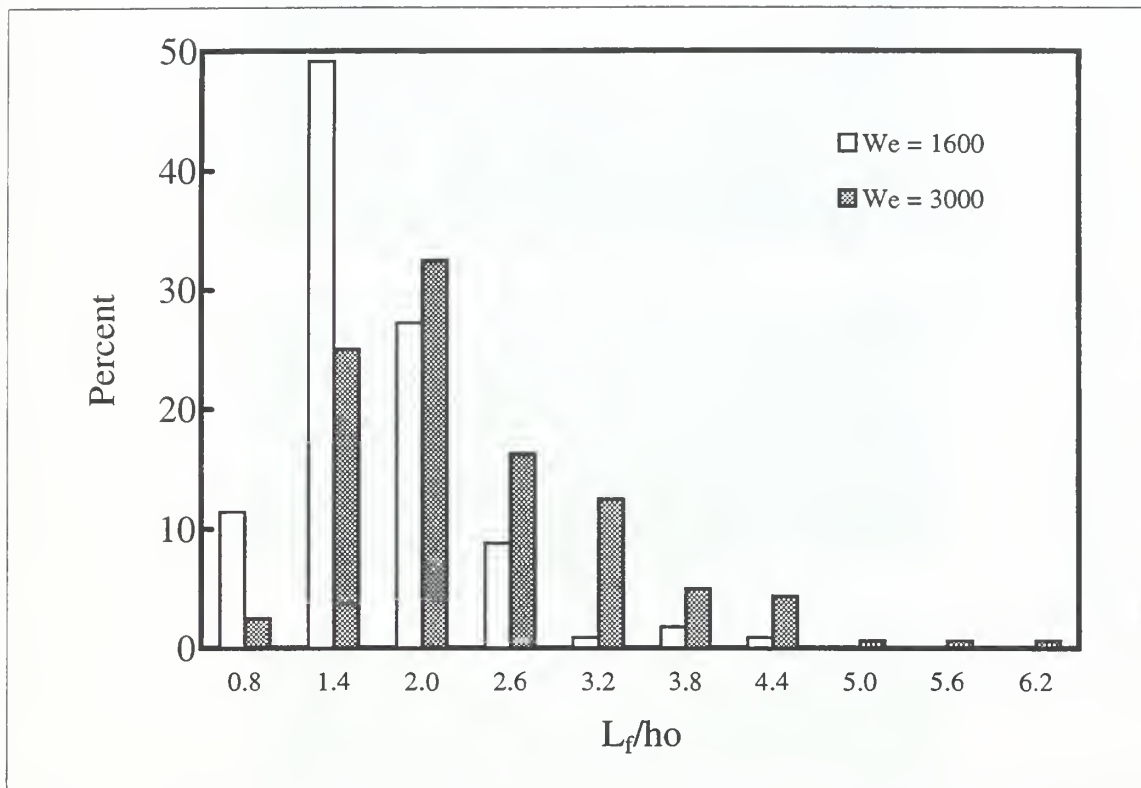


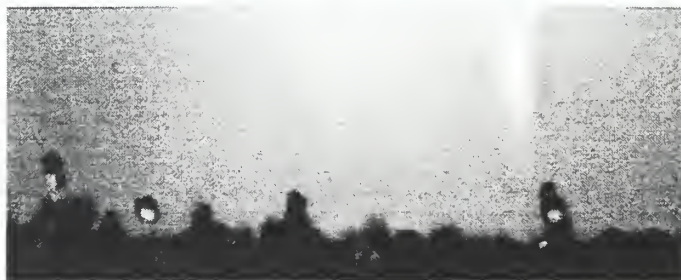
Figure 36. Distribution of the normalized filament length for the coarse-wall ($k/ho = 0.13$) at high- and low-Weber number.



$k/h_o = 0.13, We = 3000$



$k/h_o = 0.13, We = 1600$



$k/h_o = 0.02, We = 3000$

Figure 37. Photographs of three different runs at the same streamwise location, $x/h_o \approx 90$.

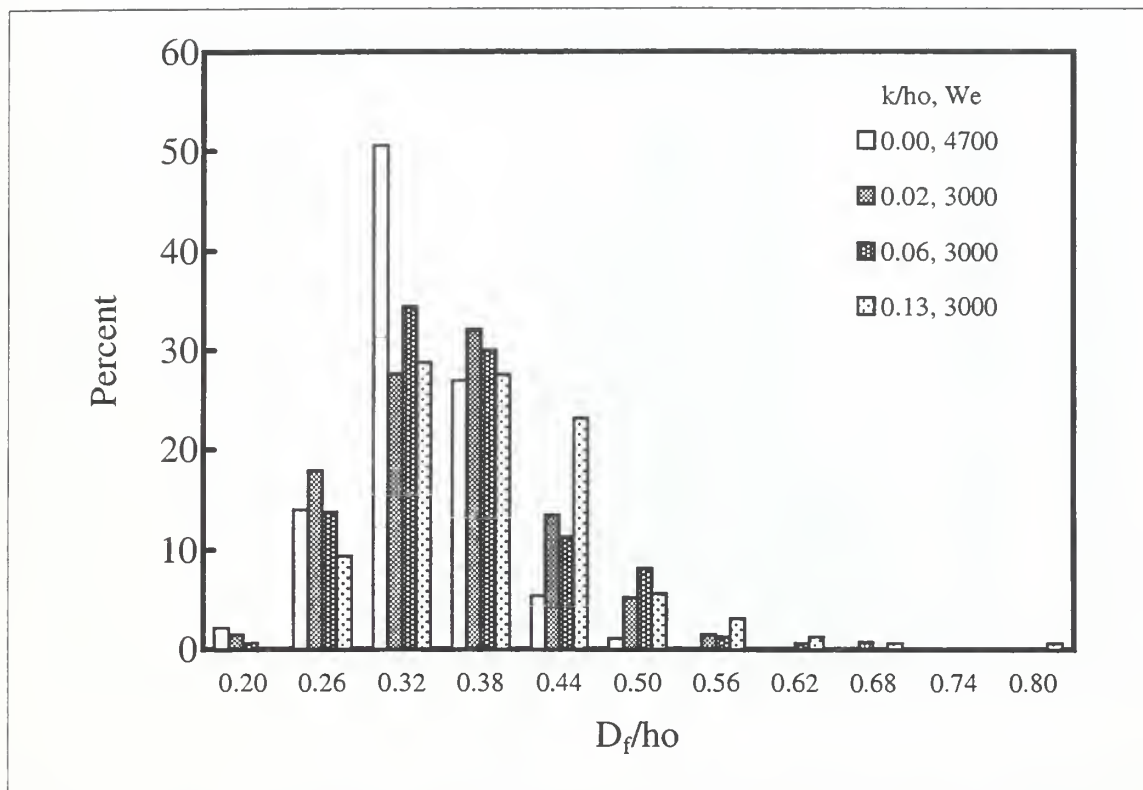


Figure 38. Distribution of the normalized effective filament diameter as a function of the relative roughness.

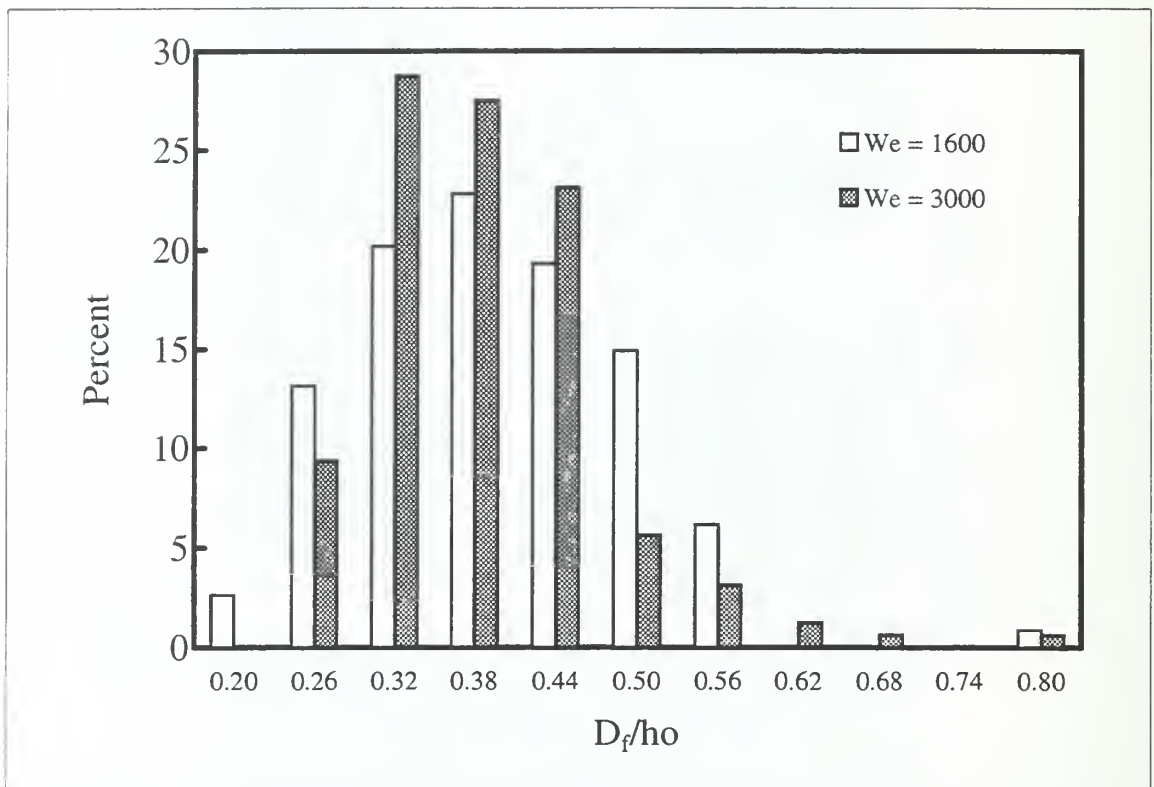


Figure 39. Distribution of the normalized effective filament diameter for the coarse-wall ($k/h_o = 0.13$) at high- and low-Weber number.

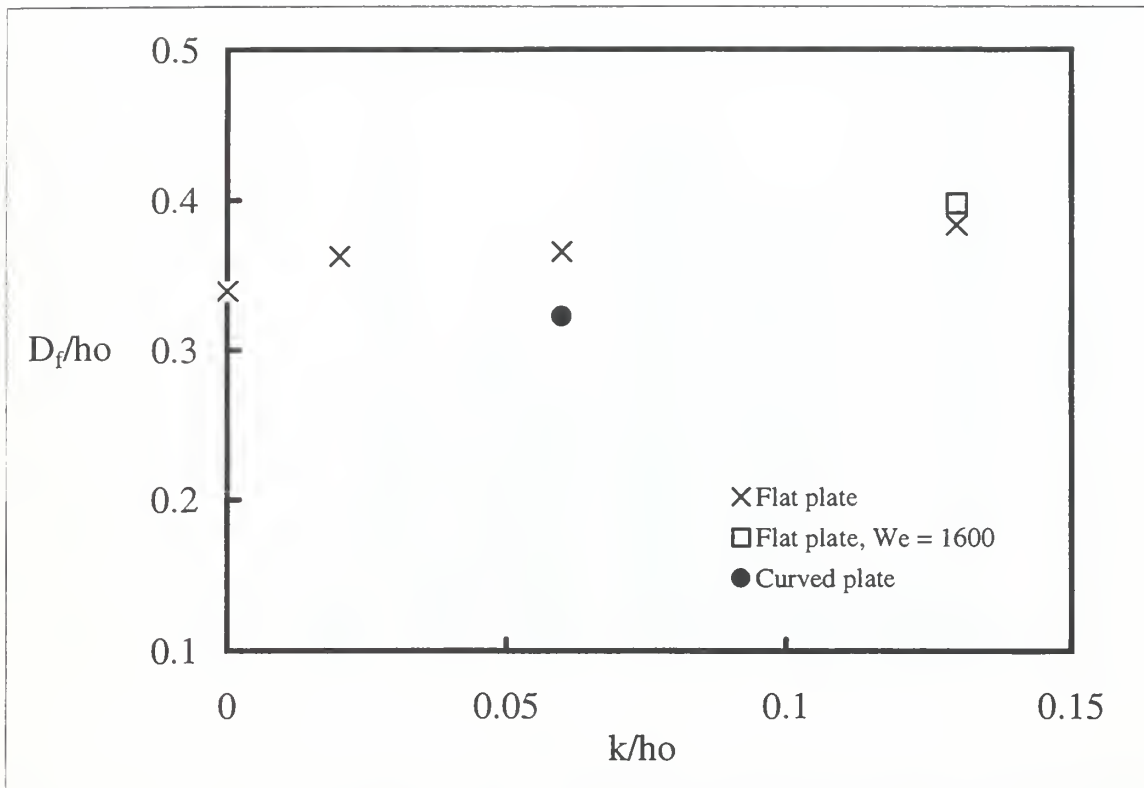


Figure 40. Mean normalized effective filament diameter as a function of relative roughness.

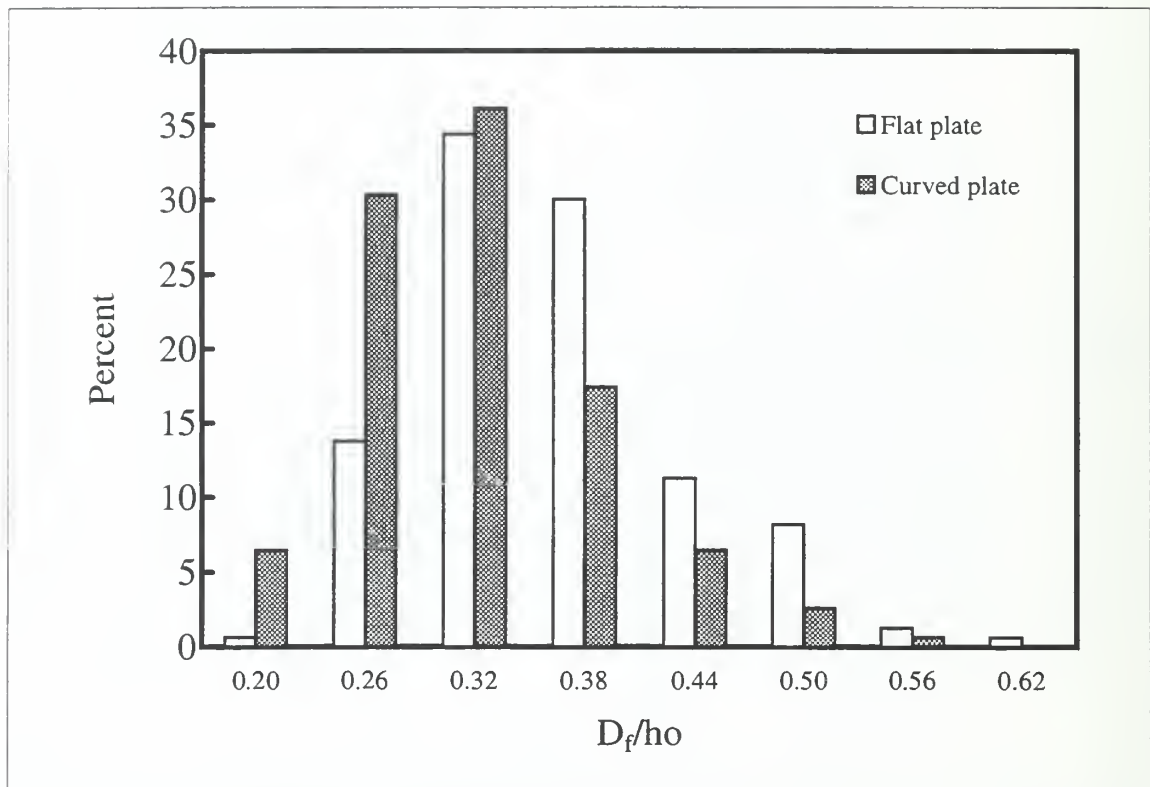


Figure 41. Distribution of the normalized effective filament diameter for the flat- and curved-wall ($k/h_o = 0.06$, $We = 3000$).

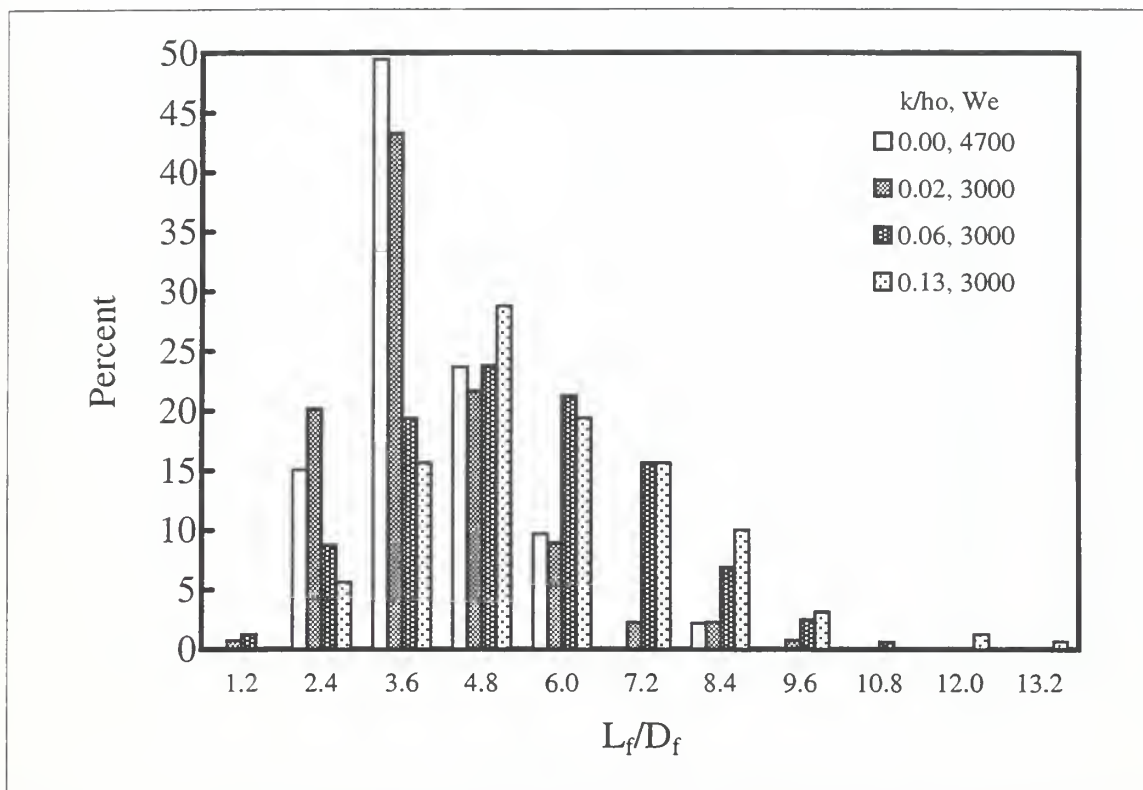


Figure 42. Distribution of the normalized filament slenderness ratio as a function of the relative roughness.

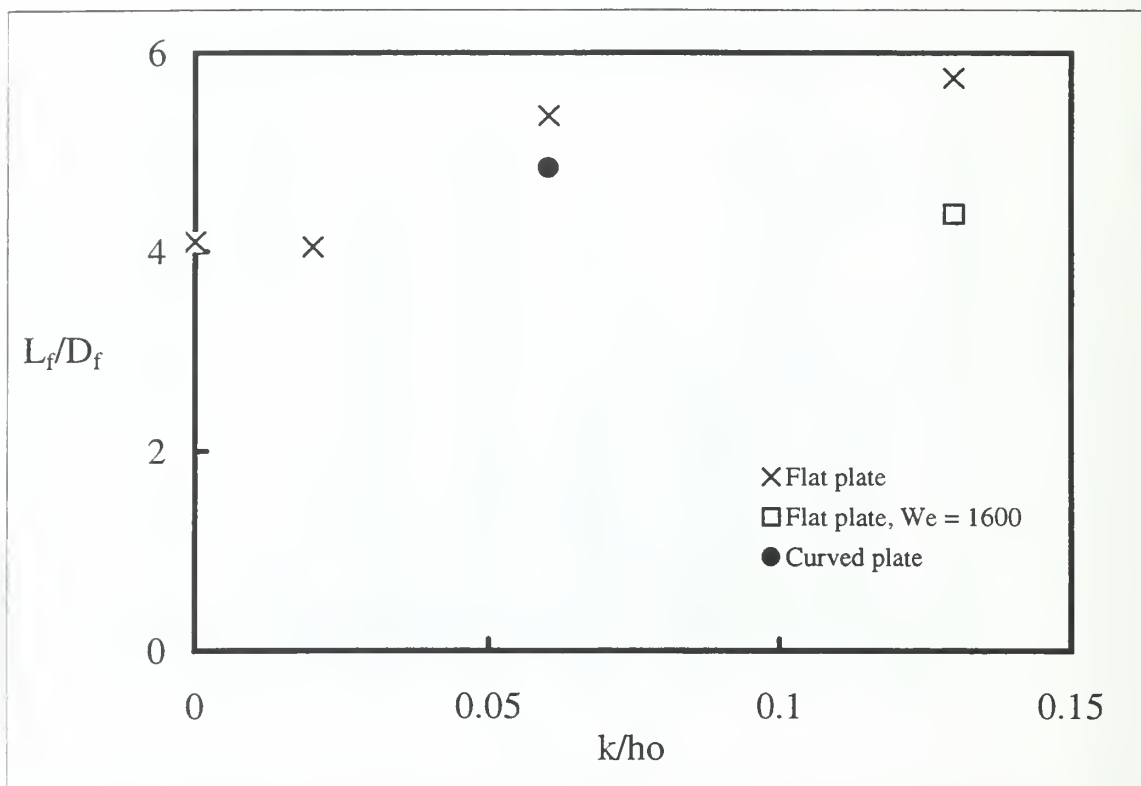


Figure 43. Mean normalized filament slenderness ratio as a function of the relative roughness.

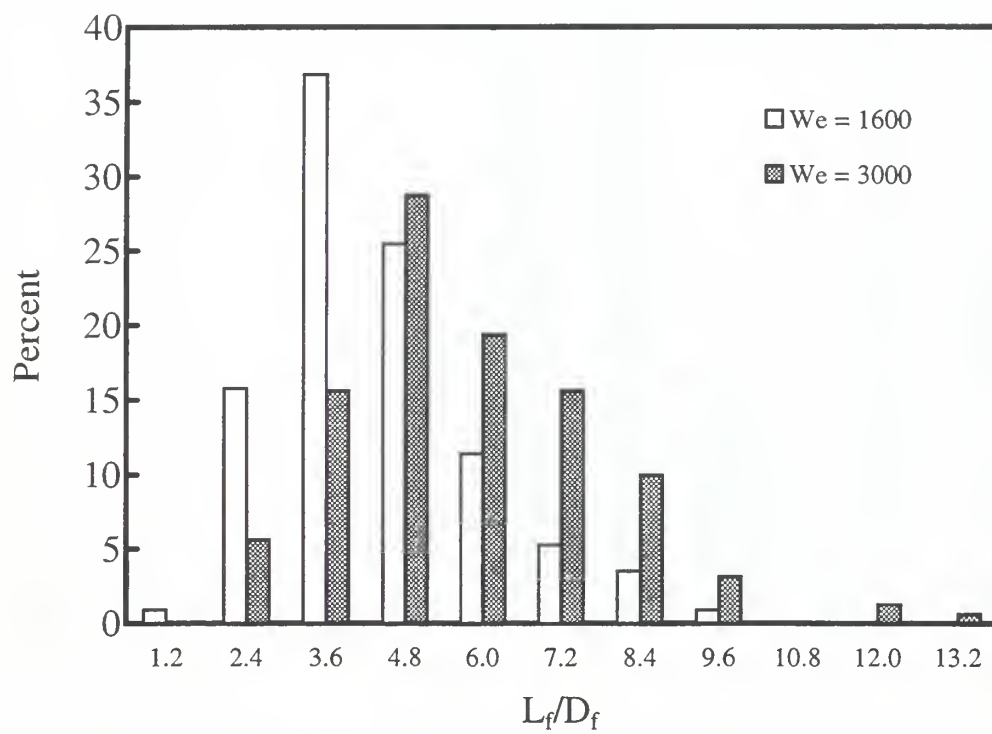


Figure 44. Distribution of the normalized filament slenderness ratio for the coarse-wall ($k/h_o = 0.13$) at high- and low-Weber number.

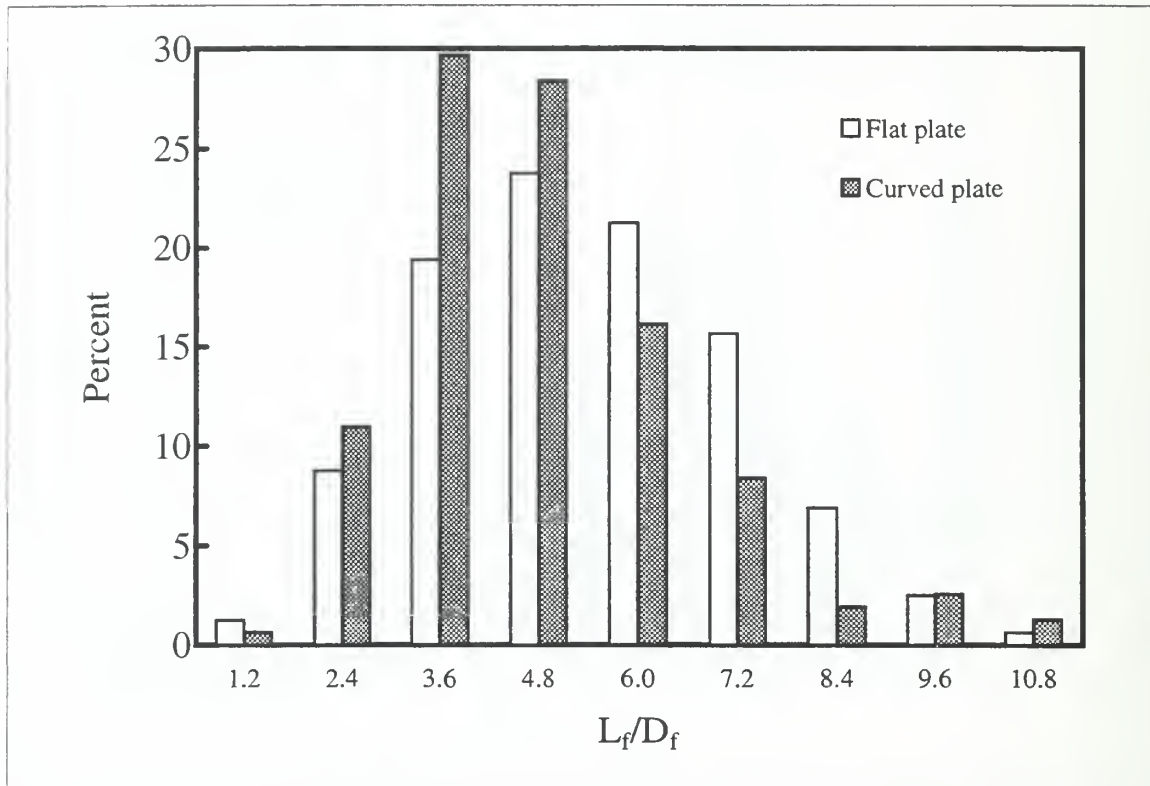


Figure 45. Distribution of the normalized filament slenderness ratio for the flat- and curved-wall ($k/h_o = 0.06$, $We = 3000$).

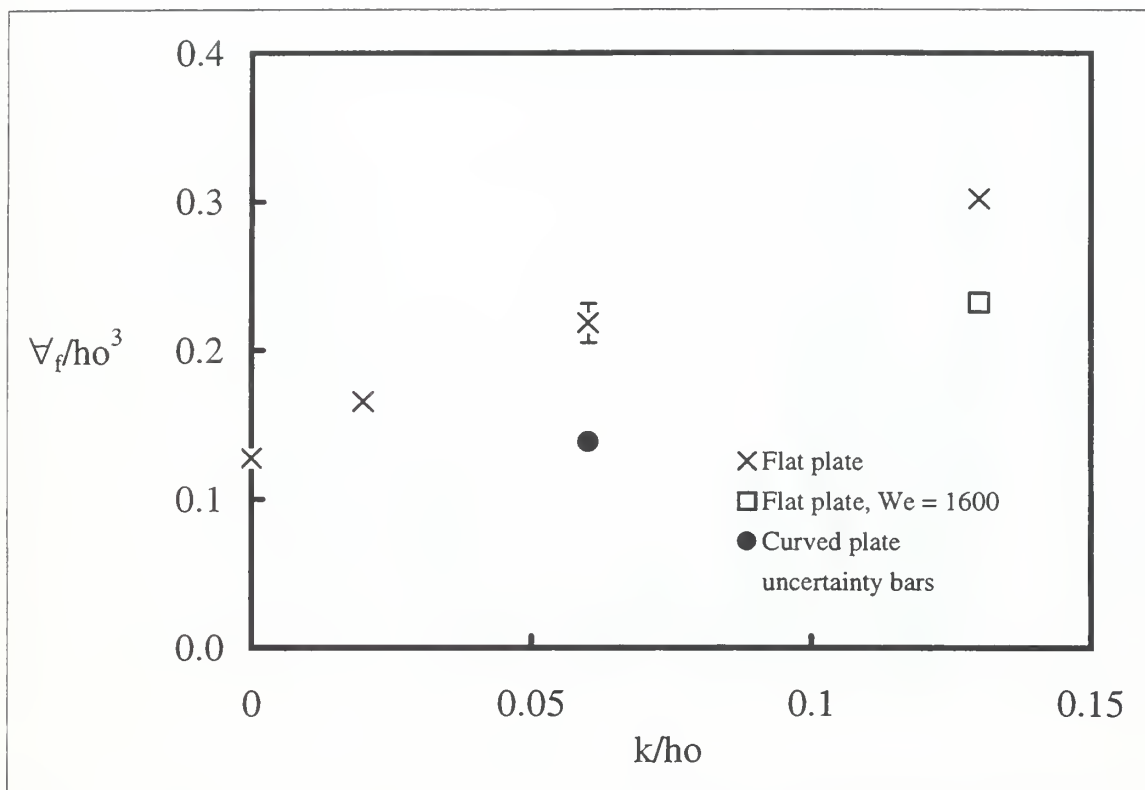


Figure 46. Mean normalized filament volume as a function of the relative roughness.

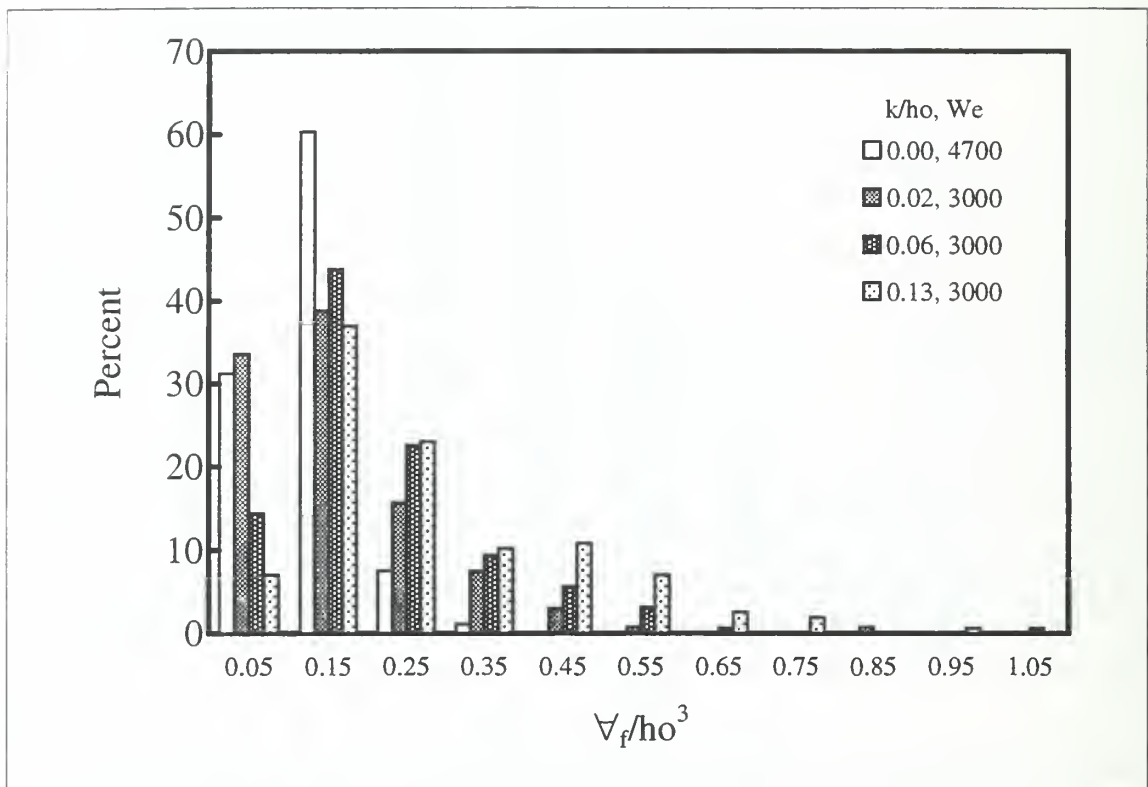


Figure 47. Distribution of the normalized filament volume as a function of the relative roughness.

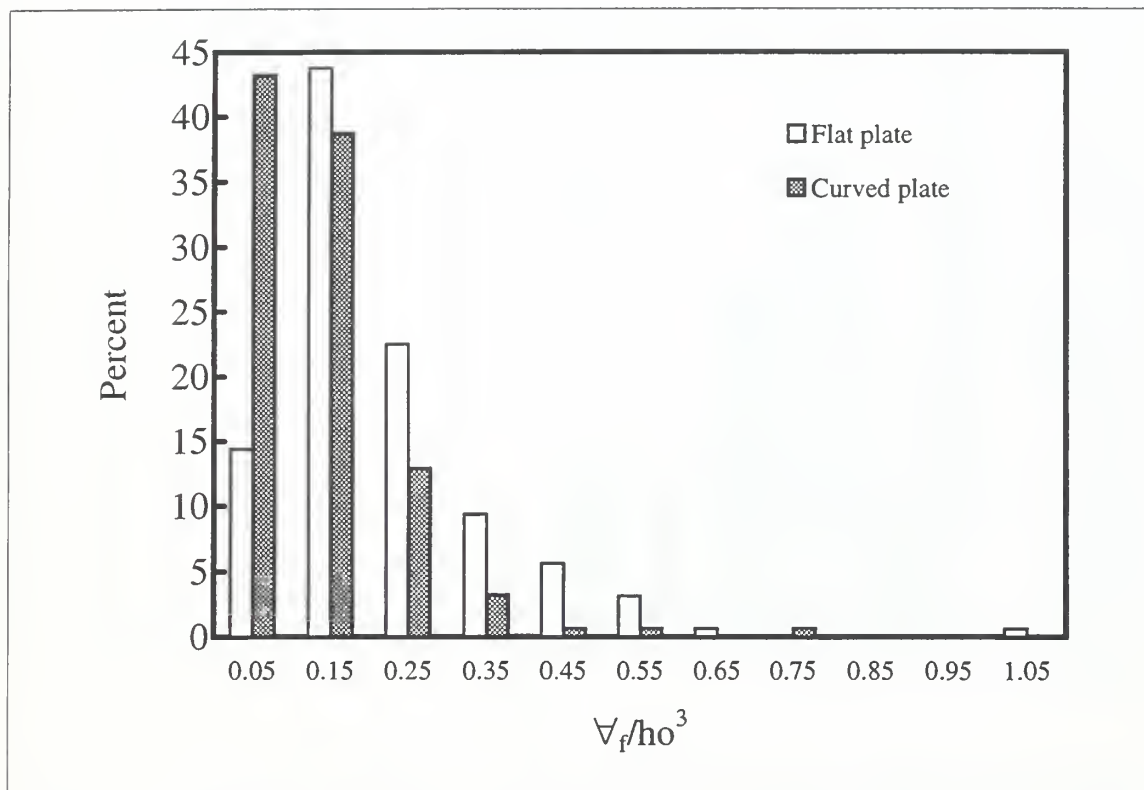


Figure 48. Distribution of the normalized filament volume for the flat- and curved-wall ($k/ho = 0.06$, $We = 3000$).

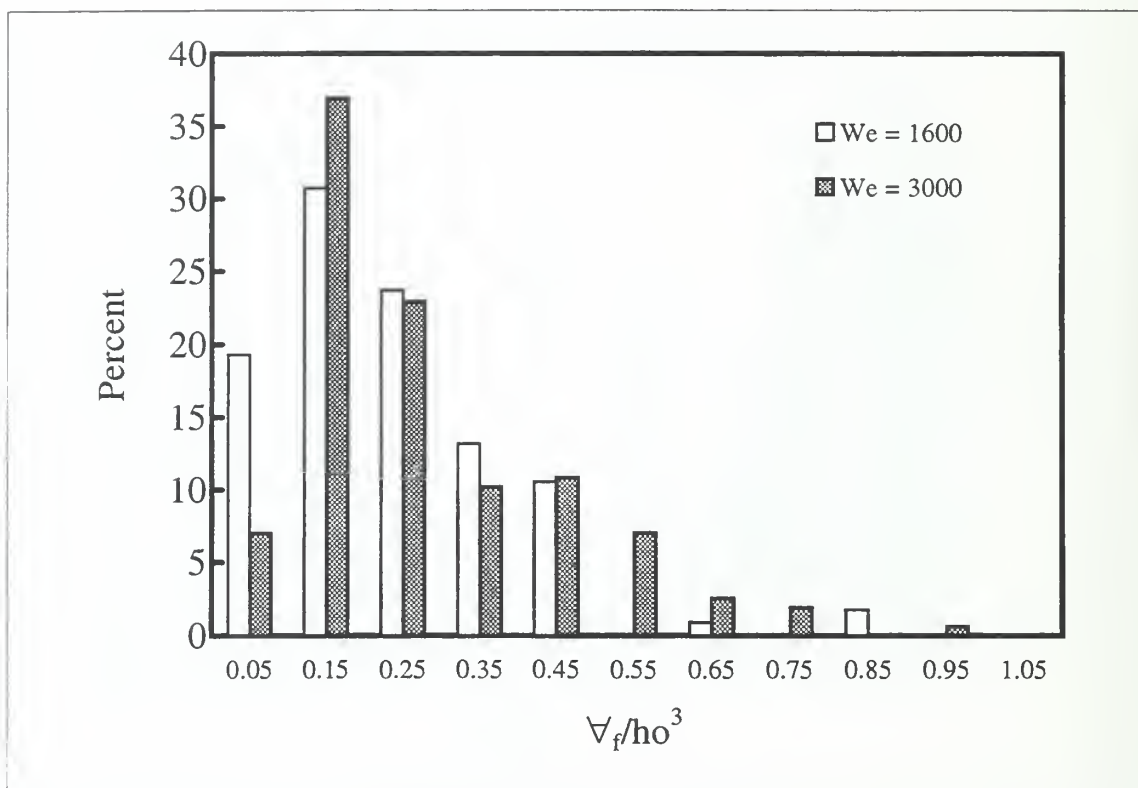


Figure 49. Distribution of the normalized filament volume for the coarse-wall ($k/ho = 0.13$) at high- and low-Weber number.

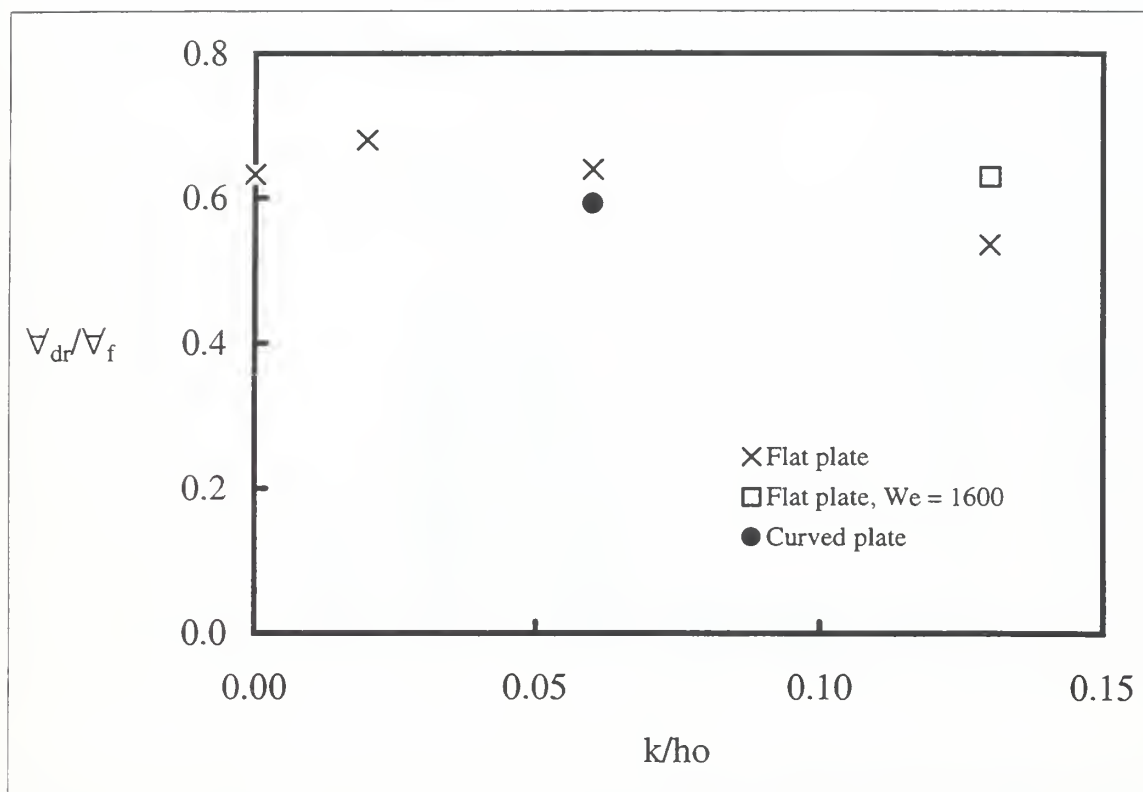


Figure 50. Mean value of the drop to filament volume ratio as a function of the relative roughness.

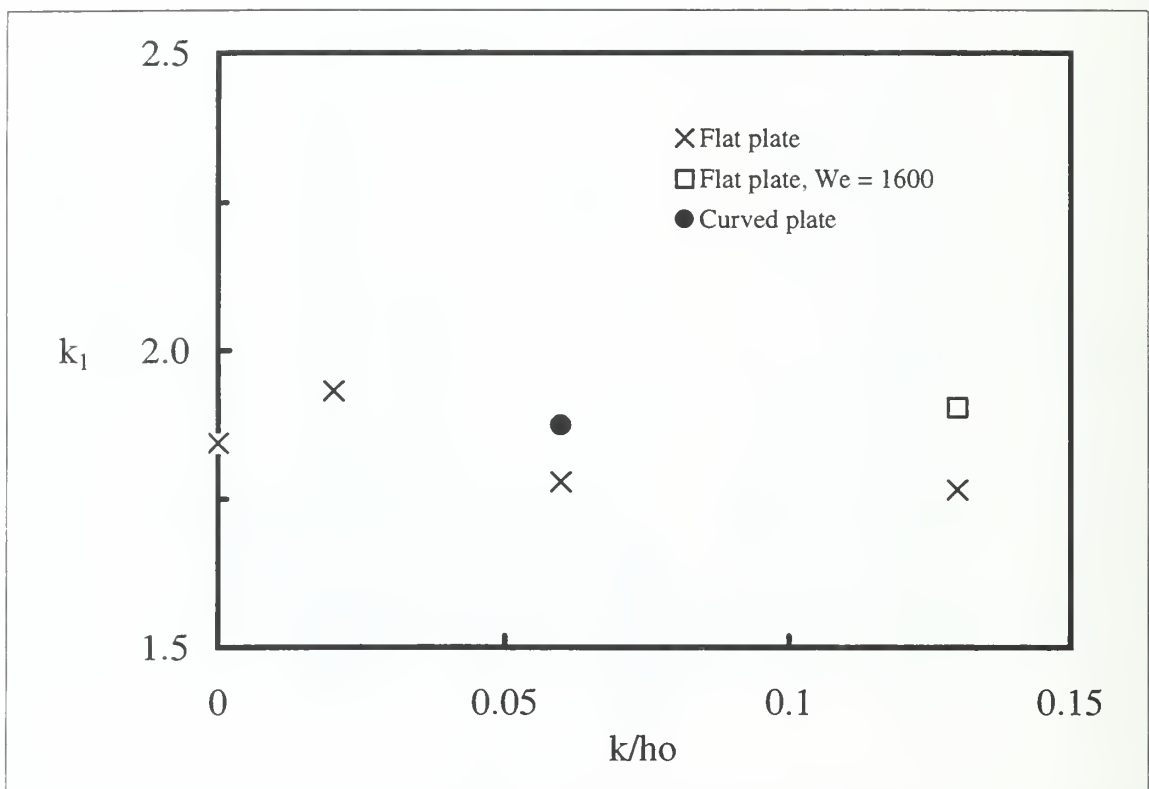


Figure 51. Mean disturbance wave number at the tip of the filament just prior to drop separation.

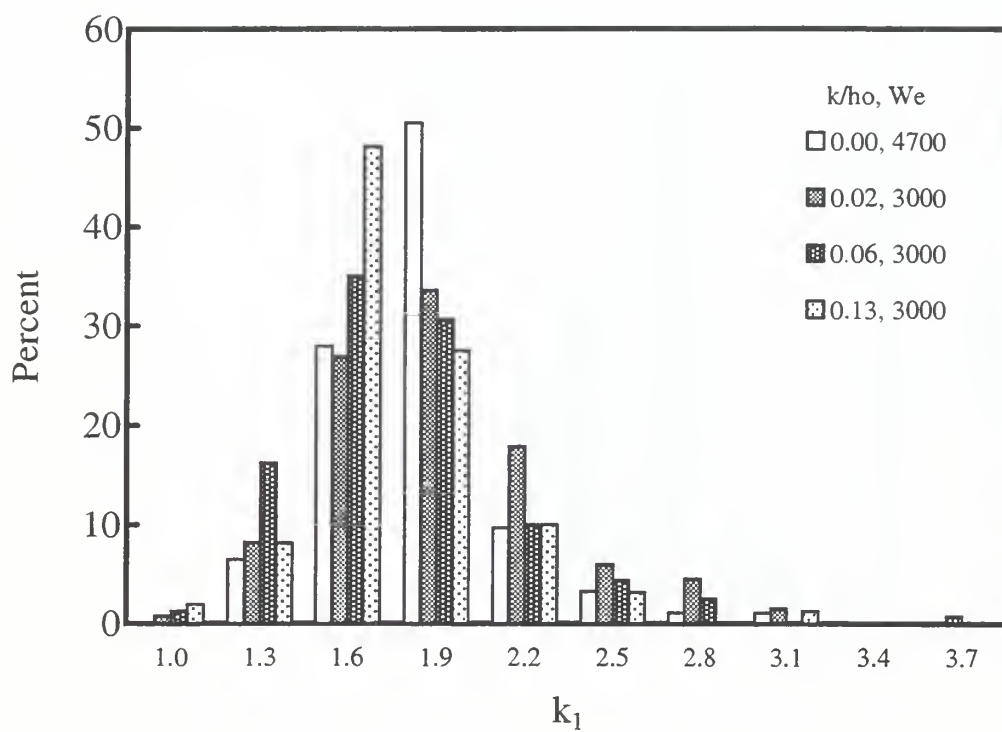


Figure 52. Distribution of the disturbance wave number as a function of relative roughness.

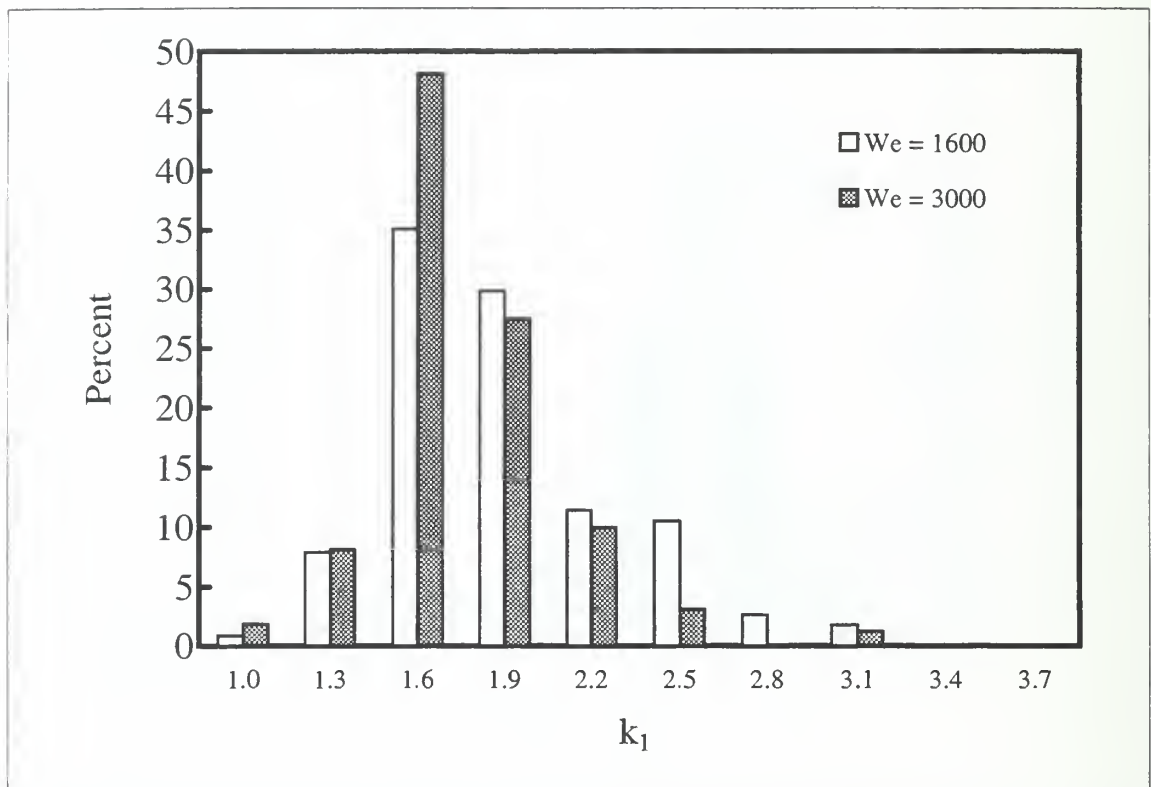


Figure 53. Distribution of the disturbance wave number for the coarse-wall ($k/h_o = 0.13$) at high- and low-Weber number.

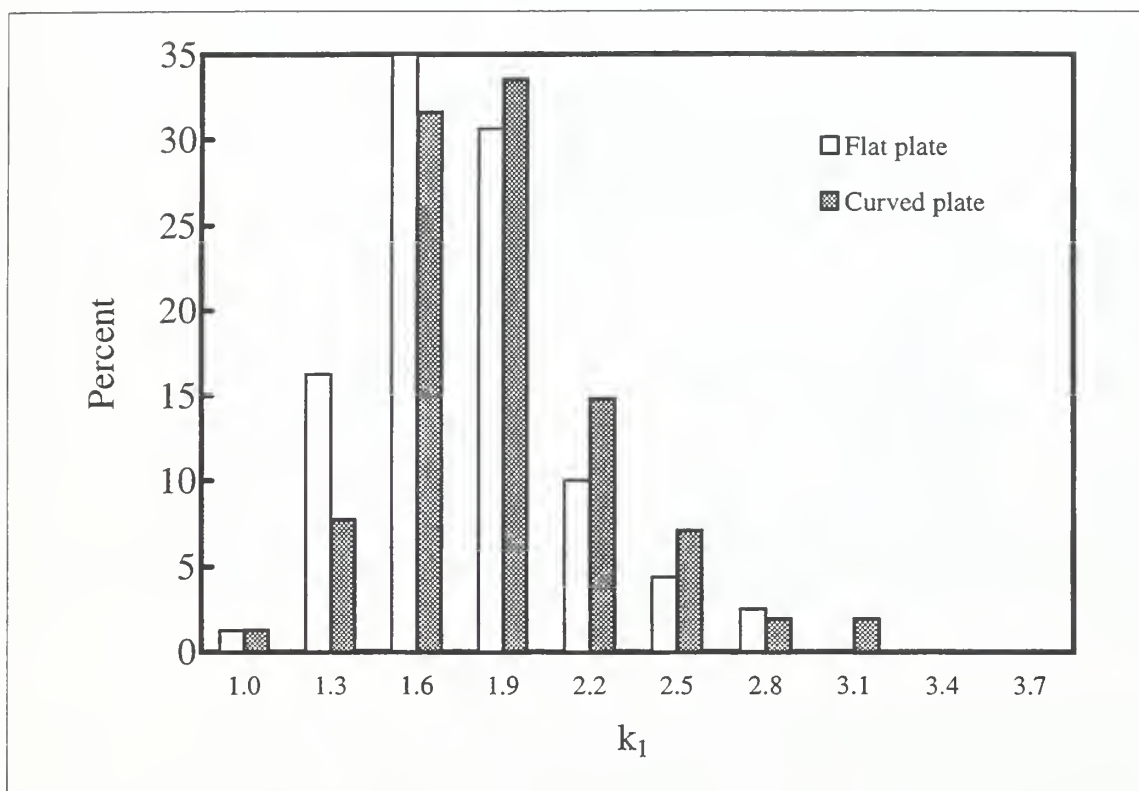


Figure 54. Distribution of the disturbance wave number for the flat- and curved-wall ($k/h_0 = 0.06$, $We = 3000$).

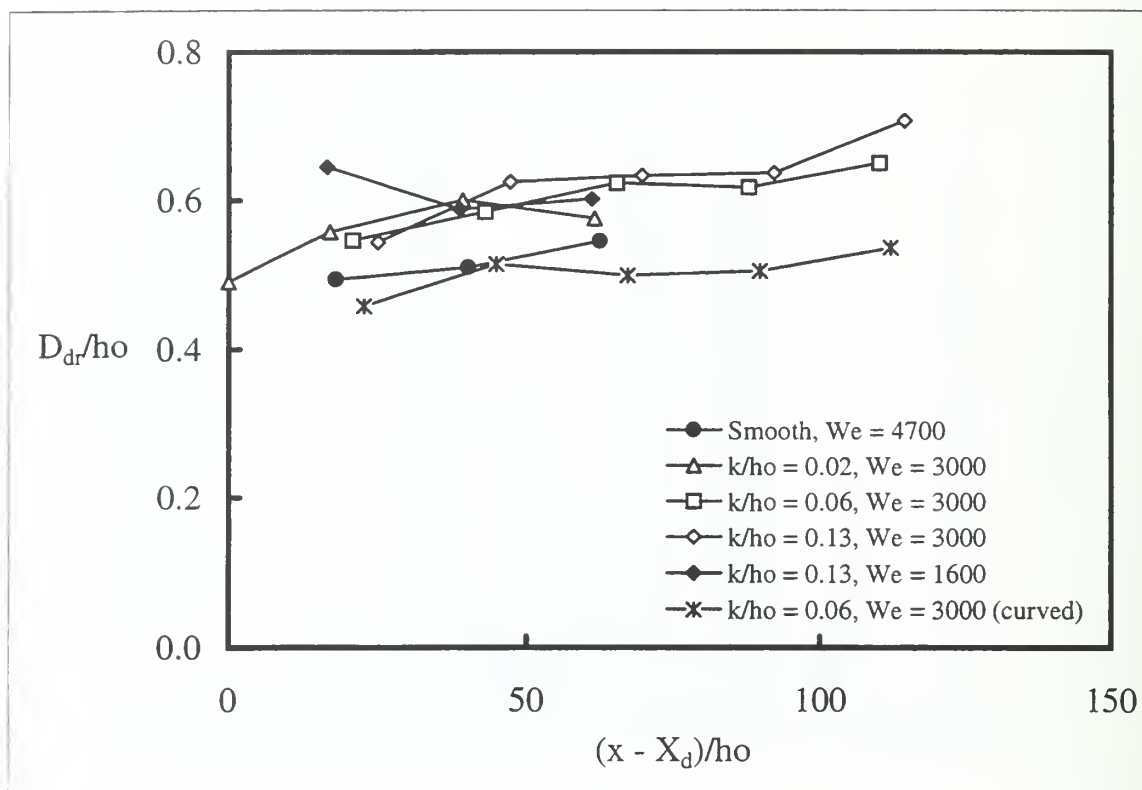


Figure 55. Normalized mean drop diameter as a function of the nondimensional streamwise coordinate. Here x and X_d denote, respectively, the distance from the leading edge of the plate and the point at which drop generation begins. Only those locations with >30 observations are shown. The uncertainty is approximately 10 percent.

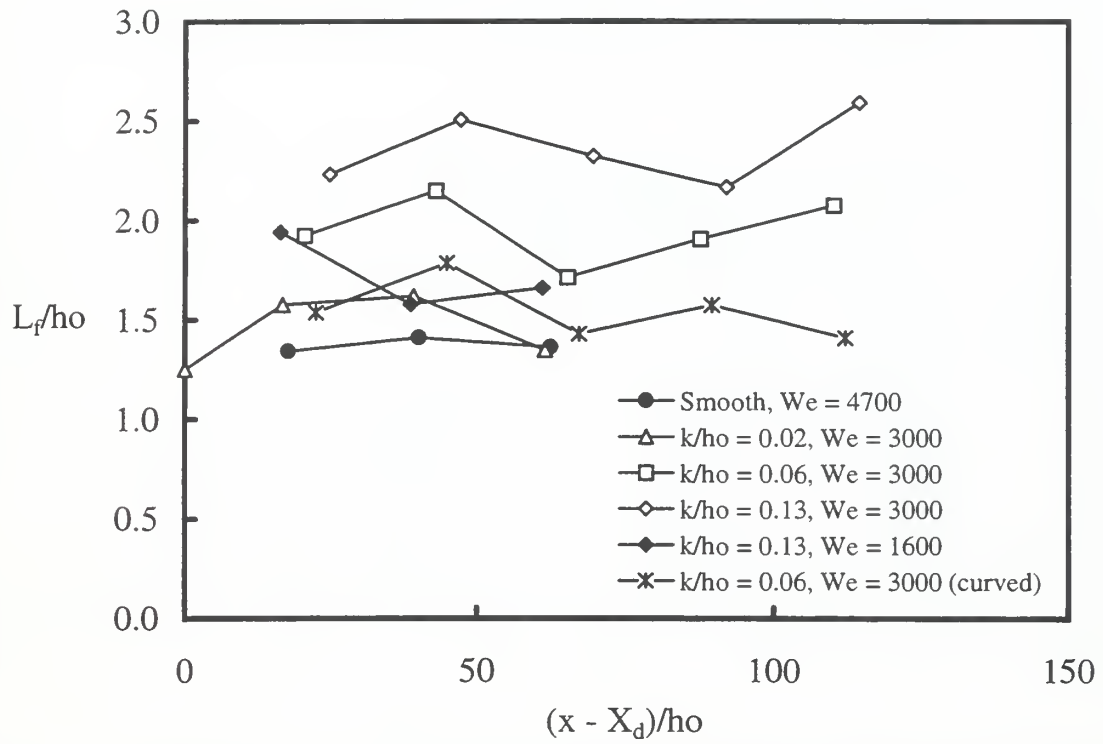


Figure 56. Normalized mean filament length as a function of the nondimensional streamwise coordinate. Here x and X_d denote, respectively, the distance from the leading edge of the plate and the point at which drop generation begins. Only those locations with >30 observations are shown. The uncertainty is approximately 15 percent.

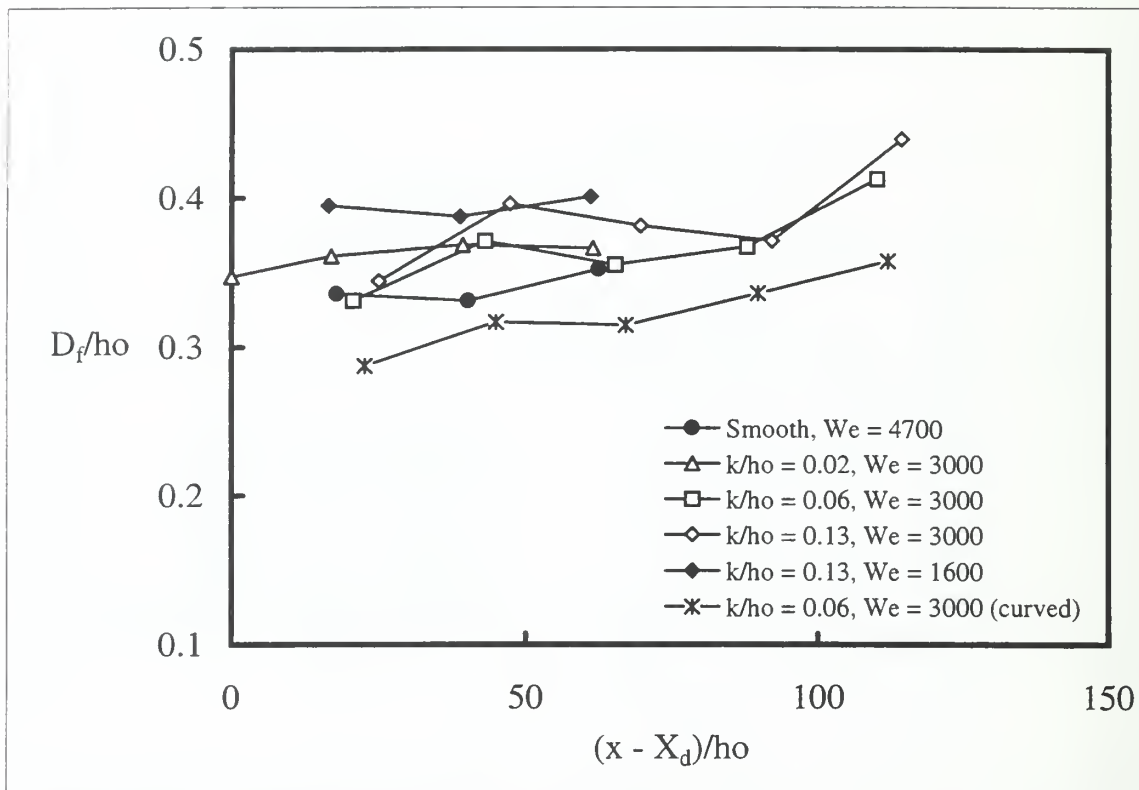


Figure 57. Normalized mean effective filament diameter as a function of the nondimensional streamwise coordinate. Here x and X_d denote, respectively, the distance from the leading edge of the plate and the point at which drop generation begins. Only those locations with >30 observations are shown. The uncertainty is approximately 10 percent.

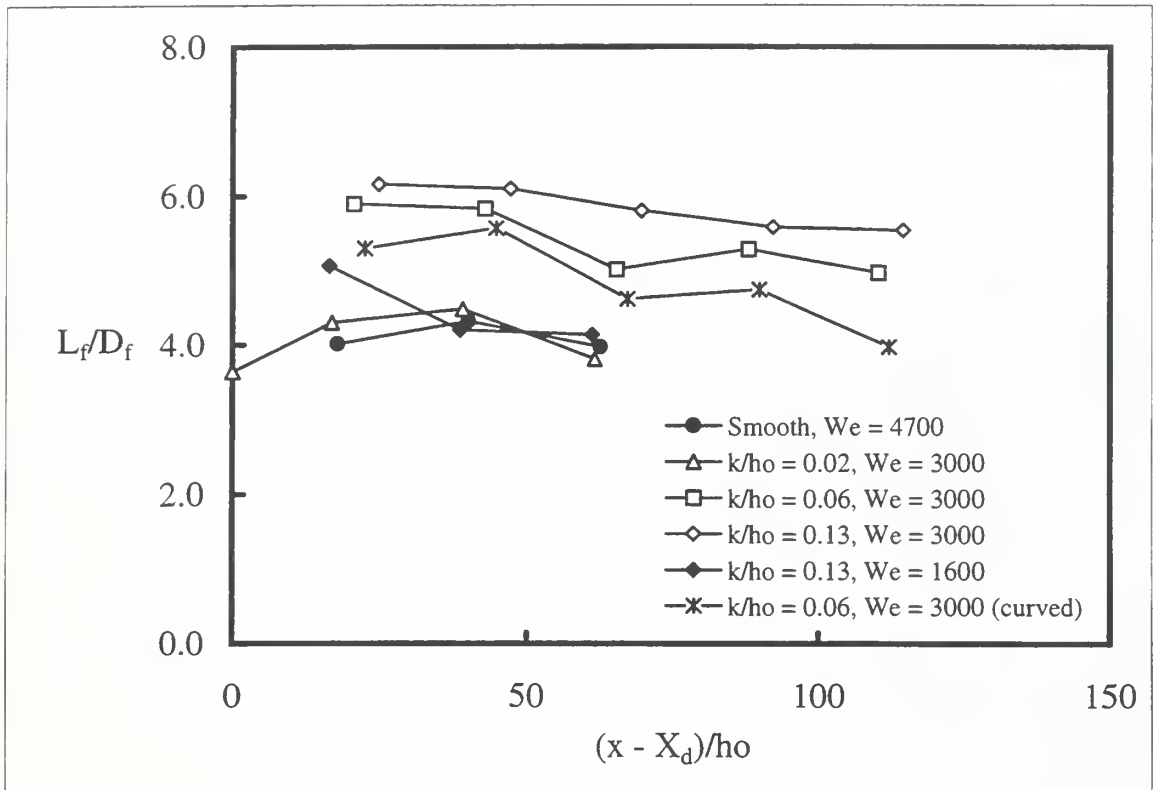


Figure 58. Normalized mean filament slenderness ratio as a function of the nondimensional streamwise coordinate. Here x and X_d denote, respectively, the distance from the leading edge of the plate and the point at which drop generation begins. Only those locations with >30 observations are shown. The uncertainty is approximately 15 percent.

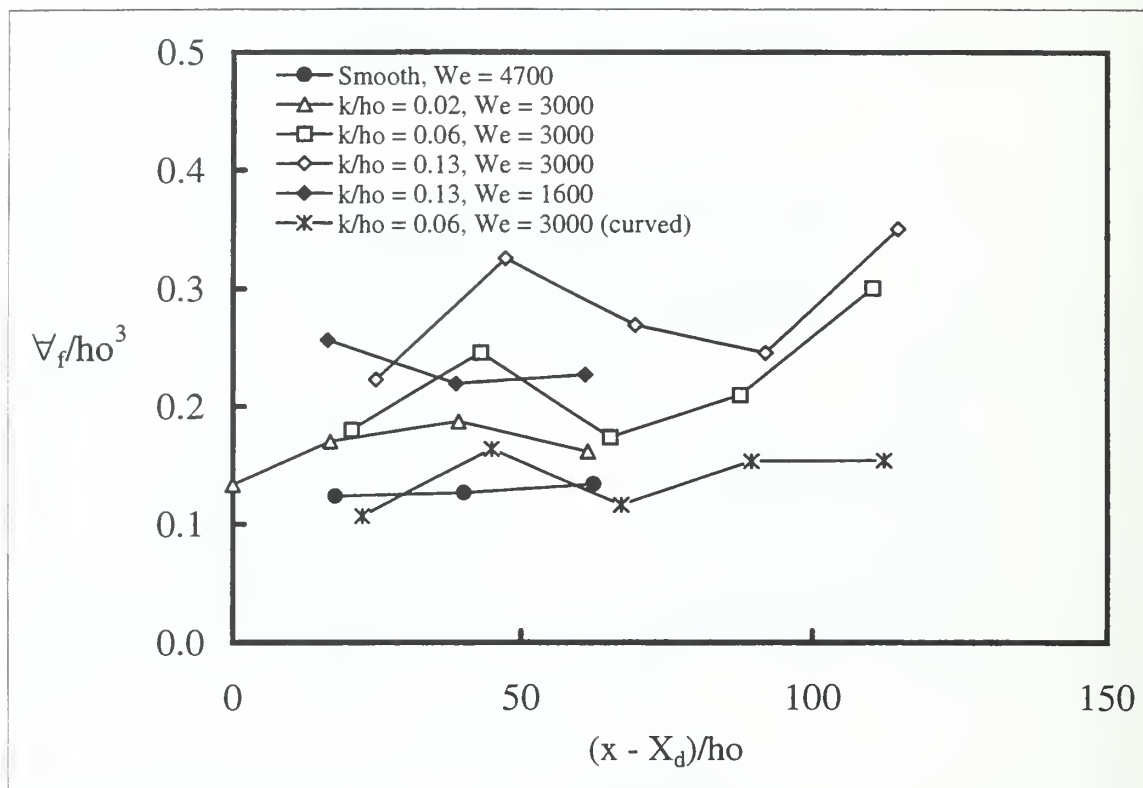


Figure 59. Normalized mean filament volume as a function of the nondimensional streamwise coordinate. Here x and X_d denote, respectively, the distance from the leading edge of the plate and the point at which drop generation begins. Only those locations with >30 observations are shown. The uncertainty is approximately 25 percent.

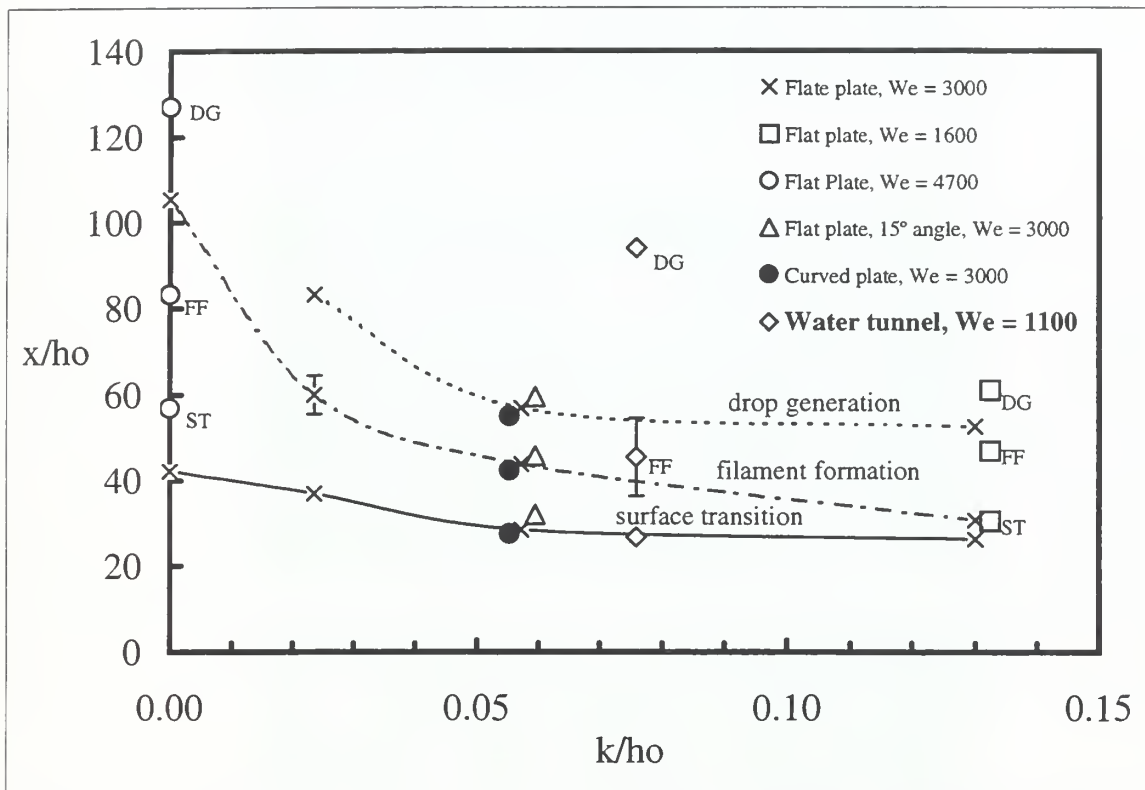


Figure 60. Distances to surface transition (ST), filament formation (FF) and drop generation (DG) as a function of plate roughness for the rectangular and the water tunnel wall jet.

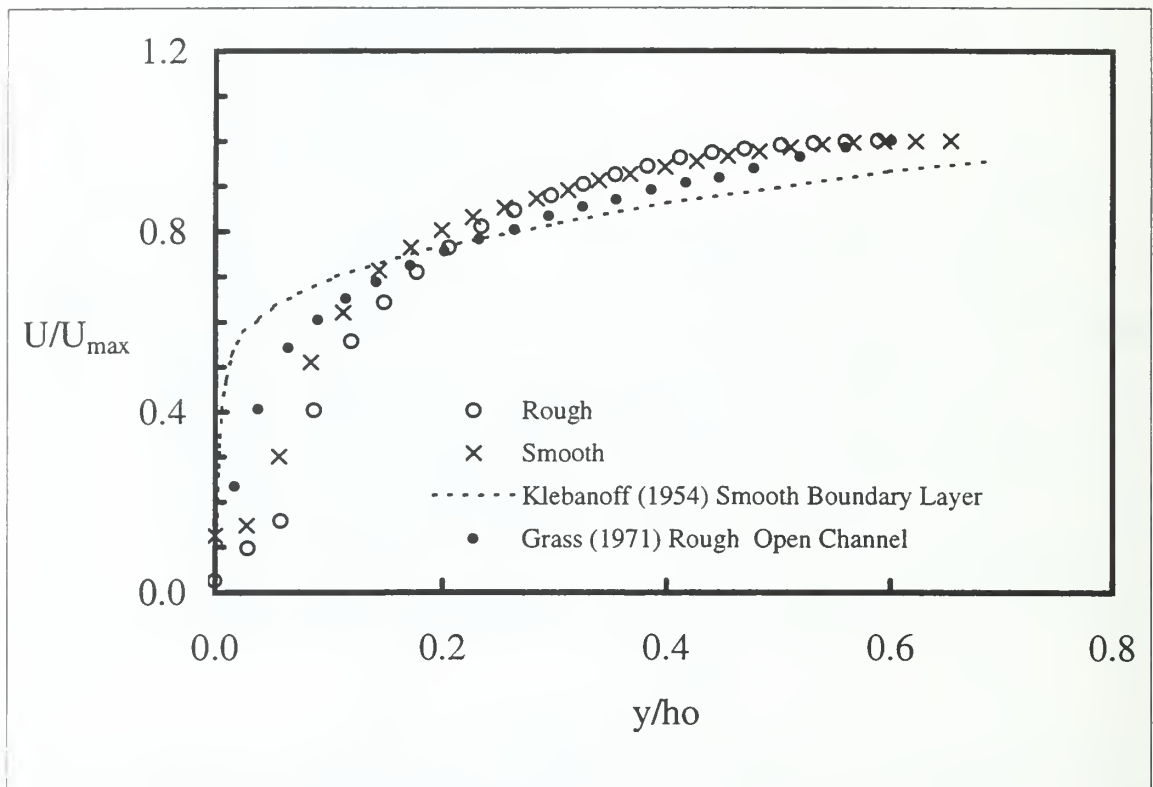


Figure 61. Mean velocity distribution across the liquid wall jet formed in the recirculating free-surface water tunnel at $x/h_o = 53$.



Figure 62. Photographs of the interior of a rough-wall liquid jet formed in the recirculating water tunnel. $Re_x = 2.3 \times 10^6$, $Re = 2.8 \times 10^4$, $Fr = 9$, $We = 1100$, $k/h_0 = 0.08$.

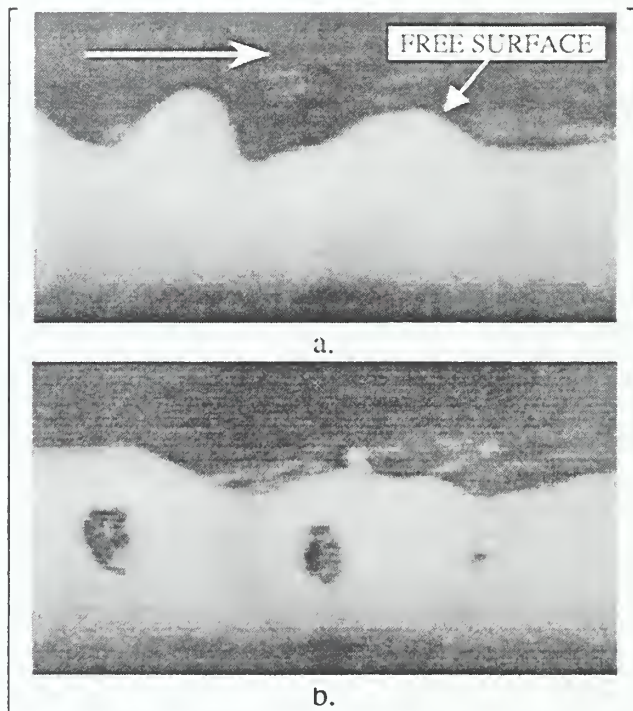


Figure 63. Two images depicting the free surface distortions and bubbles that are present in the rough-wall jet formed in the recirculating water tunnel.
 $Re_x = 1.6 \times 10^6$, $Re = 2.8 \times 10^4$, $Fr = 9$, $We = 1100$, $k/ho = 0.08$.

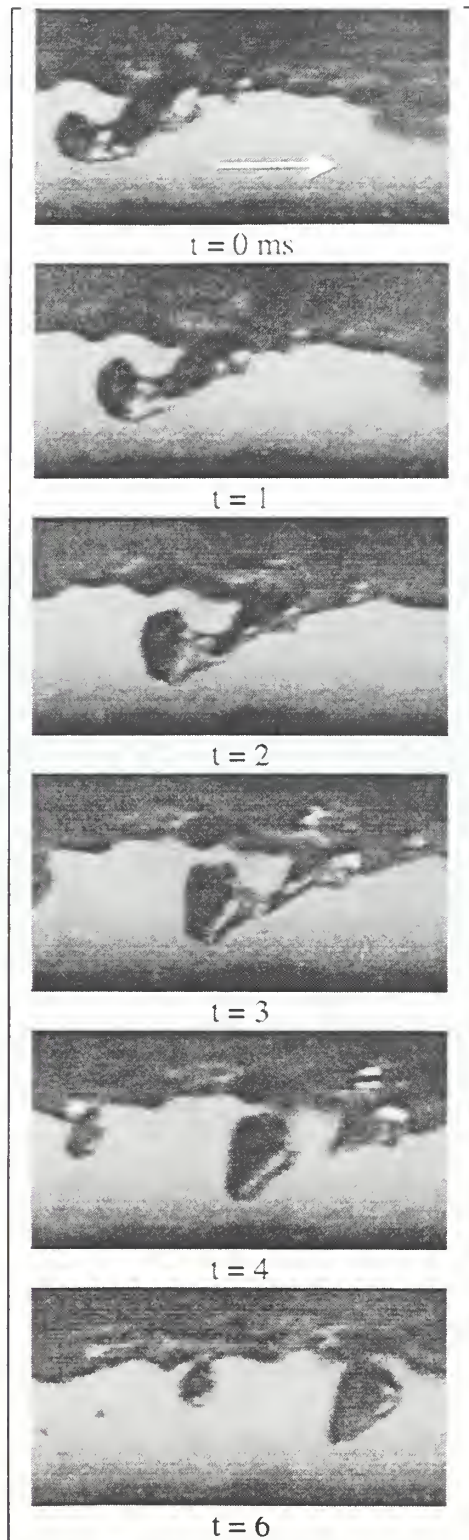


Figure 64. A sequence of images illustrating bubble formation below the free surface of the rough-wall jet formed in the recirculating water tunnel.

$Re_x = 1.6 \times 10^6$, $Re = 2.8 \times 10^4$, $Fr = 9$, $We = 1100$, $k/ho = 0.08$.

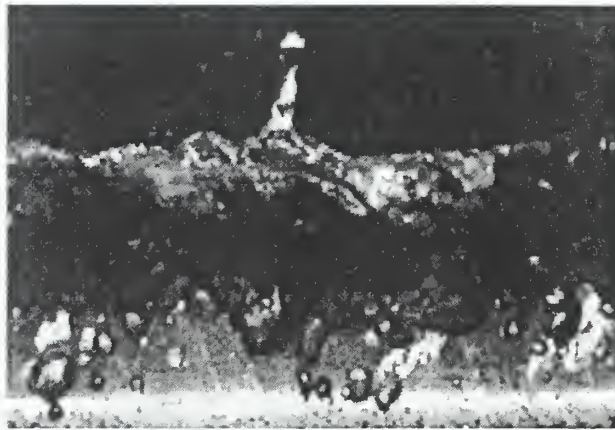


Figure 65. A photograph of a moment above and the bubbles present below the free surface of the rough-wall jet formed in the recirculating water tunnel.
 $Re_x = 2.7 \times 10^6$, $Re = 2.8 \times 10^4$, $Fr = 9$, $We = 1100$, $k/ho = 0.08$.

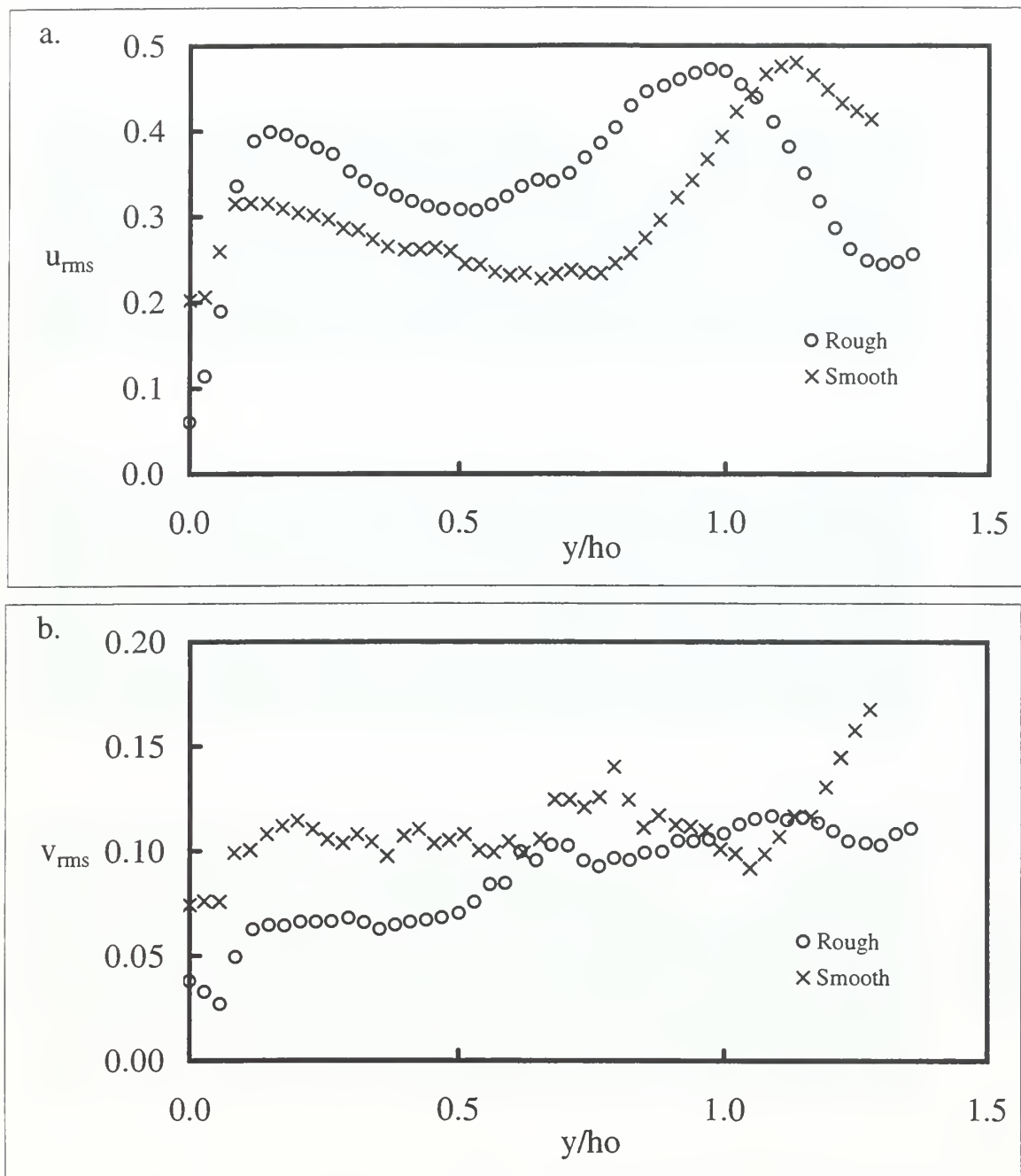


Figure 66. Streamwise and vertical turbulence intensity across the liquid wall jet formed in the recirculating water tunnel at $x/h_o = 53$.

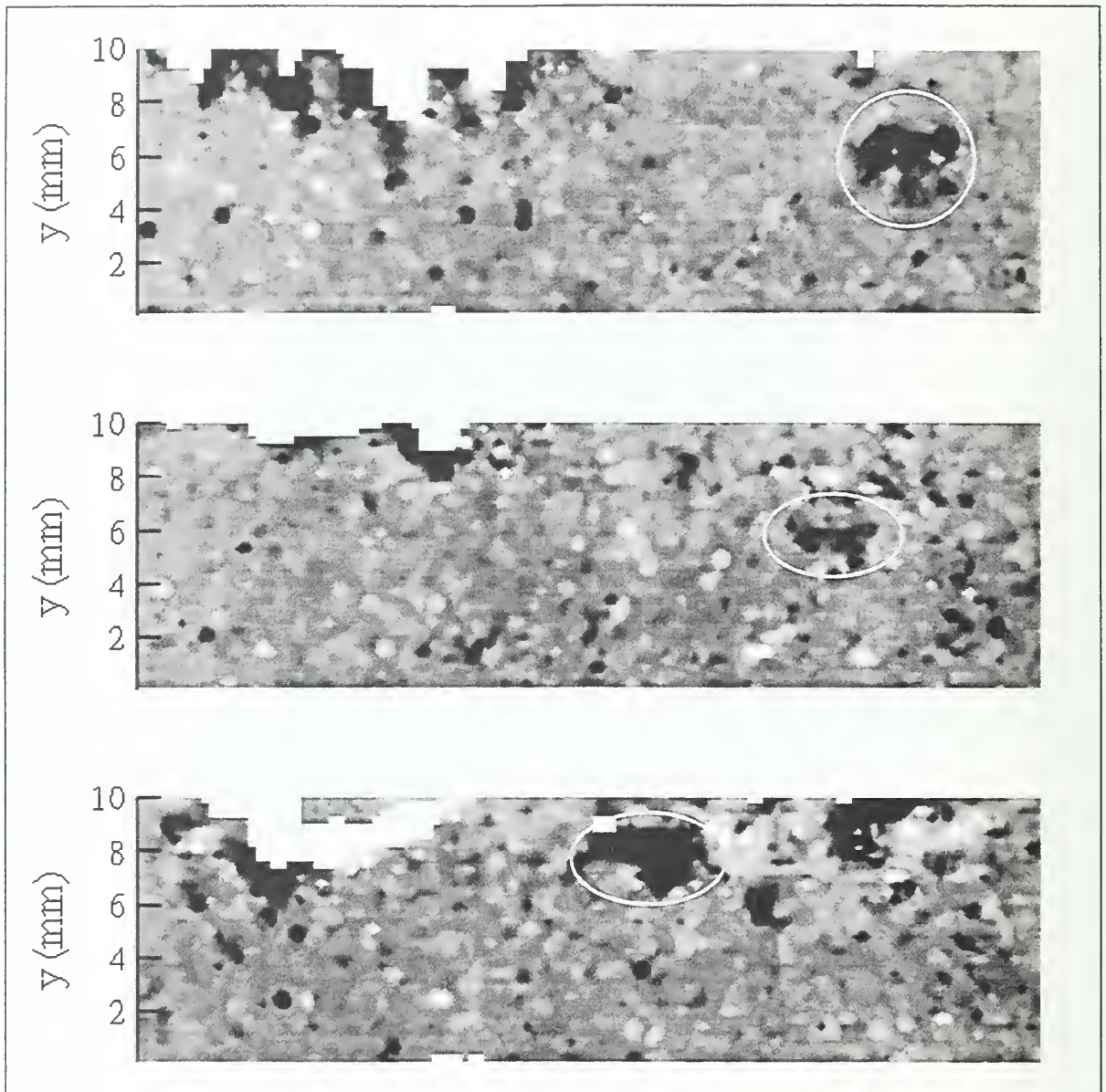


Figure 67. Contour plots of v -velocity (at three different times) in the rough-wall jet formed in the recirculating water tunnel at $x/h_o = 53$, as acquired with DPIV. The white shade indicates $v \leq -0.5$ m/s, while the black is for $v \geq 0.5$ m/s. The circled regions show "blobs" with large upward velocities.

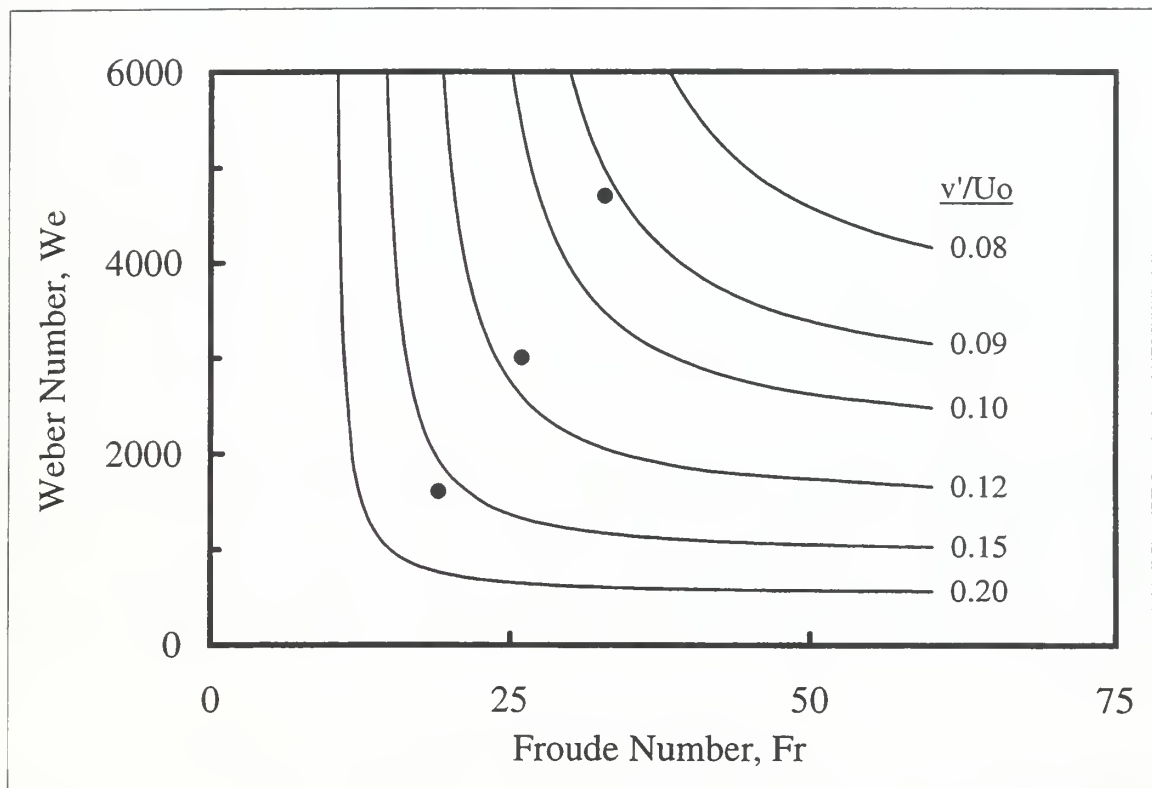


Figure 69. The jet Weber number versus the jet Froude number for different levels of v'/U_o as estimated by Eq. (10). The circles mark the three combinations of We - Fr examined in this investigation.



APPENDIX B. UNCERTAINTY ANALYSIS

The uncertainty of the data presented herein was determined at a 95 percent confidence interval. The biases associated with the measurements appeared inconsequential relative to the random variance of the data and the precision level of the individual measurements. Therefore, the data variance and the number of observations dictate the mean-value uncertainty, while the individual measurement uncertainties are precision controlled. To minimize the uncertainty, it is important to record as many observations as reasonably possible, and to arrange the measuring equipment to maximize its accuracy. Since this is the first investigation into the physics of this type of drop formation process, there is no a priori knowledge of the various parameter distributions. Hence, the number of observations of a given feature is ≥ 30 whenever practical, so that the implicit analytical assumption of a Gaussian distribution does not introduce significant error into the mean-value confidence intervals (Kline & McClintock 1953).

The surface characteristics (i.e., liquid filaments and drops) of the rectangular liquid wall jet are recorded on videotape using a high-speed camera (imager). The videotape is then reviewed to find filaments and drops that can be analyzed with a reasonable degree of accuracy. The criteria used to make this determination are:

- The base of the filament is clearly discernable.
- The filament behaves in an axisymmetric manner (as witnessed by its behavior in numerous images) and has a slenderness ratio of about 1.5 to 2.
- The entire filament, and the drops it produces, are unobstructed by other surface structures.
- The filament and drops are in focus.
- The drops are nearly circular in images used to measure their areas.
- The drops and filaments can be measured in at least three sequential images.

The images of filaments and drops meeting these criteria are digitized, and then analyzed on a PC using the Optimas MA software. Optimas allows the user to mark points and lines, and to trace out the areas of the objects seen in the digitized image. It is able to track these features throughout a sequence of images, and it allows the user to redefine the objects in each image. Based on the length scale prescribed and the time between the images, Optimas calculates the two-dimensional areas, angles, lengths, centroids, and relative positions, as well as velocities and accelerations of the various items. After the image analysis is complete, Optimas writes the selected values to a text file or a Microsoft Excel spreadsheet.

Using a high-quality Fuji 105mm/f1.8 lens, and placing the camera at an appropriate position, the center of the wall jet can be brought near the minimum focal distance with the lens f-stop at f1.8. This maintains a consistently small depth of field for the given lighting, thereby ensuring that only those filaments and drops formed in the center of the liquid jet are subsequently analyzed. This focal distance is short enough to make these filaments and drops appear sufficiently large for accurate evaluation, while ensuring that the camera far enough back to capture a sequence of images of a given feature (typically 8 to 15) without having to move it.

The uncertainty analysis performed for this study uses the constant odds (root-mean-square) formula, and 95 percent confidence level uncertainty intervals as recommended by Moffat (1982). Adding a bit of complexity to the calculations is the fact that some of the parameters requiring uncertainty analysis are not measured directly. For example, the calculation of the drop diameter is based on its measured cross-sectional area. Nonetheless, the primary uncertainties associated with this analysis are a function of the overall imaging system characteristics, and the user's ability to accurately identify the free surface features using the Optimas software. For the items measured directly with Optimas, the identifiable uncertainties and their estimated values are listed below:

- Object definition (OBJ). This describes the uncertainty associated with the user's ability to outline the exact shape of an object. For all objects measured, there is some blurring around the edges because of object motion and limited

digital resolution. Hence, this uncertainty is not a function of the size of the object, but is instead a fixed value applied to all area objects. An analysis of a clear glass sphere and a small acrylic rod moving through the range of velocities considered in this study show $0.08 \text{ mm} \leq \delta_{\text{OBJ}} \leq 0.20 \text{ mm}$. For the following uncertainty analysis $\delta_{\text{OBJ}} = 0.14 \text{ mm}$ will be used.

- Object not at the focal plane (FOCUS). This describes the uncertainty introduced when objects measured are not at the precise focal plane of the lens (not at the center of the wall jet), but still appear in focus (within the optical depth of field). By considering objects placed both closer and further from the lens, this uncertainty is estimated as $\delta_{\text{FOCUS}} = 4 \%$.
- Lens distortion (LENS). Because imperfections will exist in the optics of any lens, there will be some amount of distortion—most likely near the edges of the image. However, for the lens used in this experiment, the distortion is negligible: $\delta_{\text{LENS}} \approx 0 \%$.
- Length scale calibration error (LENGTH). Optimas bases its dimensional calculations on the user's length-scale definition. By using Optimas to draw a line over a known distance on the scale, say 10 mm, and comparing the Optimas-calculated length with the actual length, this uncertainty is estimated as $\delta_{\text{LENGTH}} = 0.9 \%$.
- Optimas area calculation approximation (AREA). Optimas determines the area of an outlined shape by adding up the pixels contained within the defined region. If an outline passes through a pixel, then the entire pixel may contribute to the estimated object area if a large enough fraction of it is within the outline. Therefore, the same shape at a different location in the image may have a slightly different area. By outlining three different size shapes, placing them in various locations on different images, and having Optimas calculate the area at each location, this uncertainty is estimated to be $\delta_{\text{AREA}} = 0.3 \%$.
- Observer interpretation (OBS). Different individuals will define an object somewhat differently. The uncertainty of this factor is determined for each measurement by having two individuals independently analyze a number of

identical image sequences. As shown in the table below, the result is a function of what is measured, and is generally the largest contributor to the precision uncertainty.

Filament Area	Drop Area	Filament Length	Filament Angle	Filament Disturbance	Point (mm)
0.15	0.07	0.06	0.05	0.18	0.44

Table 5. Uncertainty of observer interpretation, δ_{OBS} .

- Scale error (SCALE). This is the uncertainty associated with the inaccuracy of the rule used to define the length scale in Optimas. By comparing the one used with that of a six-inch machinist rule of known accuracy (+ 0.102 mm, - 0.051 mm), the scale error is estimated at $\delta_{\text{SCALE}} < 0.2$ mm. However, this is only applied when determining point position uncertainty. In the case of areas and filament lengths, this error is part of δ_{OBJ} .

As mentioned previously, the drop diameter is calculated based on the cross-sectional area of the drop in the image. For each drop, its "final" diameter is obtained by averaging the values obtained for the drop in each image for which it appears. Because the size of the drop is fairly constant from frame-to-frame, it is assumed that the uncertainty of the drop diameter in each frame is the same giving

$$\frac{\delta D_{\text{dr}}}{D_{\text{dr}}} = \frac{1}{\sqrt{N}} \cdot \frac{2}{\pi} \left(\frac{\delta A_{\text{dr}}}{D_{\text{dr}}^2} \right), \quad (\text{A.1})$$

where N is the number of images in which the drop area is measured. This can be as few as three or as many as ten, but a typical number of images is five. Using this value for N , the relative uncertainty for the range of drop sizes considered in this study is

$$0.03 \leq \frac{\delta D_{\text{dr}}}{D_{\text{dr}}} \leq 0.10.$$

It is found that $\delta D_{\text{dr}}/D_{\text{dr}} \approx 0.04$ for the majority of the drops.

Similarly, the relative uncertainty of the effective filament diameter is estimated from its cross-sectional area assuming, for the purpose of the uncertainty calculation, that $A_f = D_f L_f$. This results in the following relationship:

$$\frac{\delta D_f}{D_f} = \left\{ \left(\frac{\delta A_f}{A_f} \right)^2 + \left(\frac{\delta L_f}{L_f} \right)^2 \right\}^{1/2}. \quad (\text{A.2})$$

This equation requires the relative uncertainty of the filament length in addition to that of the filament area. Using four of the measurement values cited earlier (δ_{OBJ} , δ_{FOCUS} , δ_{LENGTH} and δ_{OBS}) the length uncertainty is

$$\frac{\delta L_f}{L_f} \approx 0.075 \quad \text{for all filaments.}$$

This then leads to a filament diameter uncertainty of

$$0.17 \leq \frac{\delta D_f}{D_f} \leq 0.21.$$

As expected, this particular diameter has a higher level of uncertainty than that of the drop. This outcome is attributed to the larger number of uncertainties involved; the approximation of defining the filament area as the sum of its length and mean diameter; and, the fact that the filament diameter is not the average of multiple measurements, as is the drop.

The relative uncertainty of the filament slenderness ratio

$$0.19 \leq \frac{\delta(L_f/D_f)}{(L_f/D_f)} \leq 0.22,$$

and volume

$$0.35 \leq \frac{\delta V_f}{V_f} \leq 0.43$$

are functions of the filament length and diameter uncertainties given above. Additionally, the estimate of the filament volume uncertainty assumes that $V_f = \pi D_f^2 L_f / 4$.

Neither the determination of filament angle nor filament disturbance length lends itself to a full uncertainty analysis. Since both are simple user interpretations—and are

not used in any analytical analysis—it is appropriate to only consider the observer interpretation uncertainties of these values. As such, $\delta\alpha/\alpha \approx 0.06$ and $\delta k_1/k_1 \approx 0.18$.

The wall jet analysis also measures the U- and V-velocity of the drop centroid, and the points marking the filament base and tip. Optimas calculates velocity by comparing the change in spatial position of an object in a pair of sequential images ($U = \Delta X/\Delta T$, $V = \Delta Y/\Delta T$), resulting in a basic uncertainty equation of

$$\frac{\delta U}{U} = \left\{ \left(\frac{\delta(\Delta X)}{\Delta X} \right)^2 + \left(\frac{\delta(\Delta T)}{\Delta T} \right)^2 \right\}^{1/2}. \quad (\text{A.3})$$

Therefore, the uncertainty of this calculation is a function of the spatial precision associated with an object, and the timing precision of the NAC HSV-500 imaging system. According to the manufacturer, the imaging system precision is better than 10^{-4} ms. In the case of the drop velocity estimation, ΔX and ΔY measure the change in position of the drop centroid from one image to the next. Therefore, the spatial resolution is a function of how well the area of the drop is defined in each image: $(\Delta X, \Delta Y) = f[A_{\text{dr}}(t=1), A_{\text{dr}}(t=2)]$. Using the measurement uncertainties associated with the drop area calculations, and the given timing accuracy for a fixed ΔT of 0.002 s, the drop U-velocity uncertainty is

$$0.06 \leq \frac{\delta U_{\text{dr}}}{U_{\text{dr}}} \leq 0.25.$$

By virtue of their cross-sectional area, over 90 percent of the drops identified have relative U-velocity uncertainties of ≤ 0.10 . The drop V-velocity component has an uncertainty range of

$$0.13 \leq \frac{\delta V_{\text{dr}}}{V_{\text{dr}}} \leq 0.55.$$

For the velocity of the filament base and tip points we must now consider scale error, δ_{SCALE} , and the observer interpretation uncertainty, δ_{OBS} , associated with a point in both images. For the range of U-velocities witnessed in this study (4 to 8 m/s), the point uncertainty is

$$0.026 \leq \frac{\delta U_{\text{point}}}{U_{\text{point}}} \leq 0.04.$$

On the other hand, the uncertainty in the V-velocity component has a much wider range since the velocity magnitude varies from zero to four meters per second. Although many near-zero vertical point velocities are recorded, the uncertainty is not reduced to a reasonable level (say $\delta V_{\text{point}}/V_{\text{point}} \approx 0.35$) unless the velocity exceeds one meter per second. Additionally, the U-velocity uncertainties are lower for both drops and points because they are averaged over several images. Doing so reduces the uncertainty by $1/\sqrt{N}$, where N is the number of image pairs.

Now let us consider the uncertainty of the jet velocity at the exit of the rectangular nozzle, U_o . Defining this velocity by the discharge coefficient of the nozzle and the hydrostatic head in the U-tunnel, results in a relative uncertainty equation of

$$\frac{\delta U_o}{U_o} = \left\{ \left(\frac{\delta C_d}{C_d} \right)^2 + \left(\frac{\delta \ell}{2\ell} \right)^2 \right\}^{1/2}. \quad (\text{A.4})$$

Substituting in the maximum variation of the discharge coefficient ($\delta C_d = 0.03$), the mean value of the discharge coefficient ($C_d = 0.91$), the U-tunnel levels during experimentation ($\ell \geq 1.2$ m), and the maximum error of the manometer ($\delta \ell = 25$ mm) into Eqn. (A.4) gives:

$$\frac{\delta U_o}{U_o} \approx 0.035.$$

Combining this with the result of Eqn. (A.3) allows one to determine the uncertainty of any velocity nondimensionalized by U_o .

The next uncertainty to consider is that associated with the jet thickness measurement. The uncertainties of this result include Optimas length scale calibration, δ_{LENGTH} , scale error, δ_{SCALE} , scale interpolation, δ_{INTP} , and the jet thickness variation resulting from measuring the thickness over a rough surface, δ_{ROUGH} . The estimate of the first three uncertainties is 0.9 percent, ≤ 0.25 mm and ≤ 0.05 mm, respectively. The surface roughness uncertainty is estimated at two-thirds of the roughness element size variation shown in Table 1 (Chapter 2). Assuming a normally distributed element-size

distribution, this roughly equates to two standard deviations. Table A2 shows the values of roughness uncertainty for the four surfaces examined.

	Smooth	Fine Roughness	Medium Roughness	Coarse Roughness
δ_{ROUGH} (mm)	0.00	0.014	0.018	0.083
$\delta h/h$	0.046	0.046	0.046	0.048

Table 6. Jet thickness uncertainty for each level of plate roughness.

The uncertainty equation for jet thickness is

$$\frac{\delta h}{h} = \left\{ \frac{0.07 + \delta_{\text{ROUGH}}^2}{h^2} + 7.92 \times 10^{-5} \right\}^{1/2}, \quad (\text{A.5})$$

with the solutions to Eqn. (A.5) are also provided in Table A2 (second row).

Finally, one must examine the uncertainty of the mean jet thickness, \bar{h} , at values of x/h_0 for which the thickness was not measured. For example, the jet thickness at the points marking the beginning of the three surface transitions, X_{tr}/h_0 , X_f/h_0 and X_d/h_0 . The uncertainty of \bar{h} at these locations is a function of the mean jet thickness at the locations where h is measured, and the estimated streamwise location of the surface transition point. From videotape analysis, the x/h_0 values have been identified to within ± 30 mm. \bar{h}_{trans} , the mean jet thickness at the transition locations, is found by linearly interpolating between the known values of \bar{h} . Differentiating this line with respect to x gives the slope of the line, m , which is then used in the uncertainty estimate:

$$\frac{\delta \bar{h}_{\text{trans}}}{h_0} = \left\{ \left(\frac{\delta \bar{h}}{h_0} \right)^2 + \left(m \frac{\delta X}{h_0} \right)^2 \right\}^{1/2}. \quad (\text{A.6})$$

Based on a mean jet thickness of 5.7 mm, $\delta X/h_0$ is estimated at 4.5 for all three transition locations. The first term in Eqn. (A.6) is found by linearly interpolating between the confidence intervals for the known values of \bar{h} .

The confidence intervals for all of the mean-value parameters presented in this study are evaluated by employing commonly used single-sample analysis techniques

(Coleman & Steele 1989). That is, an estimate of the population standard deviation is determined using the unbiased estimator,

$$S_x = \left[\frac{1}{N-1} \sum_{i=1}^N (X_i - \bar{X})^2 \right]^{1/2}.$$

The sample mean standard deviation is then approximated by

$$S_{\bar{X}} = S_x / \sqrt{N}.$$

Finally, this value is multiplied by 2.0 to establish the 95 percent confidence level of the sample mean value. Unless otherwise stated, the number of observations in the sample is ≥ 30 .

APPENDIX C. TABULATION OF DATA

This appendix contains a listing of the data discussed in the thesis. The first three pages are a summary of the statistical parameters associated with the measurements. They provide the group parameters describing the statistics of the data when arranged in a histogram format. The sample statistics shown are based on the individual observations for each run. The remaining pages list the individual filament and drop measurements (arranged by run) as described in the writing.

k/ho We	L _f /ho					
	0.00	0.02	0.06	0.13	0.13	0.06
	4700	3000	3000	3000	1600	3000
	Flat	Flat	Flat	Flat	Flat	Curved
Group Mean	1.37	1.45	1.94	2.33	1.69	1.52
Group Variance	0.14	0.34	0.47	0.92	0.39	0.36
Group Std Dev	0.37	0.58	0.69	0.96	0.63	0.60
Group Skewness	0.30	0.79	0.36	1.17	1.45	0.77
Group Kurtosis	3.53	3.12	2.55	4.60	6.56	3.13
Sample Mean	1.37	1.45	1.93	2.33	1.70	1.55
Sample Variance	0.12	0.30	0.44	0.90	0.36	0.34
Sample Std Dev	0.34	0.54	0.66	0.95	0.60	0.58
Sample Skewness	0.85	0.85	0.52	1.26	1.58	0.94
Sample Kurtosis	1.08	0.10	-0.26	2.08	3.48	0.38
Sample Mode	1.26	0.91	1.31	1.89	1.52	1.28
Sample Median	1.31	1.32	1.83	2.11	1.58	1.40

k/ho We	D _{dr} /ho					
	0.00	0.02	0.06	0.13	0.13	0.06
	4700	3000	3000	3000	1600	3000
	Flat	Flat	Flat	Flat	Flat	Curved
Group Mean	0.510	0.550	0.596	0.625	0.606	0.496
Group Variance	0.008	0.015	0.014	0.019	0.023	0.017
Group Std Dev	0.092	0.122	0.120	0.137	0.152	0.129
Group Skewness	-0.384	0.291	0.298	0.788	-0.128	0.463
Group Kurtosis	3.773	2.513	2.970	3.357	2.259	3.904
Sample Mean	0.516	0.560	0.600	0.624	0.610	0.502
Sample Variance	0.009	0.014	0.014	0.019	0.024	0.015
Sample Std Dev	0.093	0.120	0.117	0.139	0.154	0.123
Sample Skewness	-0.345	0.345	0.296	0.782	-0.167	0.526
Sample Kurtosis	1.123	-0.421	0.091	0.354	-0.814	0.759
Sample Mode	0.540	0.490	0.560	0.493	0.650	0.540
Sample Median	0.520	0.560	0.590	0.602	0.625	0.500

k/ho We	D _f /ho					
	0.00	0.02	0.06	0.13	0.13	0.06
	4700	3000	3000	3000	1600	3000
	Flat	Flat	Flat	Flat	Flat	Curved
Group Mean	0.334	0.359	0.362	0.385	0.392	0.318
Group Variance	0.003	0.006	0.005	0.007	0.010	0.005
Group Std Dev	0.052	0.077	0.074	0.086	0.099	0.069
Group Skewness	0.235	0.750	0.686	1.247	0.568	0.708
Group Kurtosis	3.699	4.414	3.412	6.201	4.186	3.622
Sample Mean	0.339	0.363	0.366	0.384	0.398	0.322
Sample Variance	0.002	0.006	0.005	0.007	0.009	0.004
Sample Std Dev	0.049	0.076	0.072	0.086	0.097	0.066
Sample Skewness	0.300	0.872	0.626	1.440	0.553	0.758
Sample Kurtosis	0.548	1.639	0.499	4.034	1.222	1.086
Sample Mode	0.330	0.380	0.330	0.341	0.330	0.280
Sample Median	0.330	0.360	0.360	0.370	0.390	0.310

k/ho We	k _j					
	0.00	0.02	0.06	0.13	0.13	0.06
	4700	3000	3000	3000	1600	3000
	Flat	Flat	Flat	Flat	Flat	Curved
Group Mean	1.848	1.925	1.765	1.754	1.882	1.875
Group Variance	0.090	0.179	0.127	0.105	0.162	0.149
Group Std Dev	0.300	0.423	0.356	0.323	0.402	0.385
Group Skewness	1.056	1.006	0.676	1.060	0.791	0.759
Group Kurtosis	6.067	4.929	3.557	5.904	3.469	3.990
Sample Mean	1.844	1.930	1.778	1.764	1.903	1.873
Sample Variance	0.085	0.185	0.119	0.096	0.156	0.137
Sample Std Dev	0.290	0.429	0.344	0.309	0.394	0.369
Sample Skewness	1.097	1.075	0.652	1.003	0.857	0.797
Sample Kurtosis	3.195	2.603	0.482	3.771	0.762	1.209
Sample Mode	1.770	1.830	1.750	1.570	2.020	1.650
Sample Median	1.800	1.870	1.750	1.720	1.840	1.800

k/ho We	L_f/D_f					
	0.00	0.02	0.06	0.13	0.13	0.06
	4700	3000	3000	3000	1600	3000
	Flat	Flat	Flat	Flat	Flat	Curved
Group Mean	4.04	4.05	5.35	5.74	4.38	4.82
Group Variance	1.42	2.03	3.54	3.95	2.50	3.17
Group Std Dev	1.19	1.43	1.88	1.99	1.58	1.78
Group Skewness	1.13	1.20	0.26	0.76	0.89	0.96
Group Kurtosis	5.17	5.00	2.68	3.95	3.72	4.15
Sample Mean	4.10	4.04	5.36	5.74	4.37	4.84
Sample Variance	1.27	2.17	3.55	3.96	2.41	3.17
Sample Std Dev	1.12	1.47	1.88	1.99	1.55	1.78
Sample Skewness	1.12	1.27	0.34	0.87	0.95	1.12
Sample Kurtosis	2.13	2.25	-0.06	1.13	0.61	1.57
Sample Mode	3.98	3.07	5.76	4.47	3.73	3.59
Sample Median	3.98	3.78	5.27	5.39	4.03	4.59

k/ho We	V_f/ho^3					
	0.00	0.02	0.06	0.13	0.13	0.06
	4700	3000	3000	3000	1600	3000
	Flat	Flat	Flat	Flat	Flat	Curved
Group Mean	0.128	0.164	0.215	0.276	0.229	0.135
Group Variance	0.004	0.015	0.020	0.029	0.024	0.011
Group Std Dev	0.062	0.123	0.141	0.172	0.154	0.103
Group Skewness	0.450	1.917	1.971	1.150	1.372	2.228
Group Kurtosis	3.682	9.335	10.033	4.092	6.064	11.542
Sample Mean	0.128	0.166	0.218	0.302	0.232	0.139
Sample Variance	0.003	0.014	0.019	0.107	0.023	0.010
Sample Std Dev	0.051	0.117	0.137	0.173	0.154	0.100
Sample Skewness	0.774	2.028	2.025	5.840	1.648	2.643
Sample Kurtosis	0.832	6.628	7.201	47.442	4.355	11.531
Sample Mode	0.093	0.128	0.077	0.149	#N/A	0.123
Sample Median	0.114	0.127	0.177	0.217	0.195	0.115

Wall type: Smooth, Flat

$U_0 = 7.7$ m/s

$h_0 = 5.8$ mm

$k = 0.00$ mm

L_r/h_0	D_r/h_0	angle(deg)	k_1	D_{dr}/h_0	V_{tip}/U_0	Vo/U_0	U_{base}/U_0	U_{tip}/U_0	U_{drop}/U_0
1.38	0.39	120.6	2.01	0.52	0.034	0.049	0.96	0.91	0.97
1.65	0.38	86.3	1.83	0.54	0.028	0.025	0.95	0.94	0.95
1.32	0.30	117.5	1.99	0.40	0.034	0.017	0.95	0.92	0.95
1.33	0.32	95.7	1.72	0.48	0.056	0.036	0.92	0.97	0.95
1.48	0.31	62.2	1.62	0.56	0.019	0.023	0.99	0.97	0.97
1.17	0.35	130.4	1.62	0.55	-0.016	0.019	0.99	0.93	0.98
1.01	0.32	86.7	2.41	0.46	0.022	0.016	0.90	0.95	0.95
1.48	0.35	79.4	1.68	0.59	0.043	-0.002	0.93	0.99	0.99
1.30	0.43	124.4	1.78	0.55	0.003	0.014	1.02	1.03	1.03
1.24	0.33	95.7	1.60	0.47	0.028	0.014	0.96	0.95	0.95
1.26	0.34	87.0	1.93	0.30	0.062	0.077	0.98	0.95	0.95
1.17	0.35	105.1	2.00	0.44	0.016	0.026	0.99	1.05	0.77
1.22	0.32	63.4	1.81	0.48	0.037	0.028	0.96	0.96	0.96
2.30	0.39	77.8	1.61	0.54	0.071	0.047	0.94	0.94	0.93
1.57	0.32	116.2	1.92	0.54	0.025	0.012	0.93	0.93	0.94
0.84	0.27	98.5	2.07	0.41	0.050	0.045	0.94	0.93	0.95
0.89	0.34	84.1	1.77	0.52	0.003	0.028	0.92	0.94	0.94
0.77	0.29	61.2	2.04	0.45	0.053	0.056	0.89	0.97	0.97
1.30	0.27	54.6	1.44	0.49	0.037	0.036	0.98	1.01	0.96
1.29	0.21	41.4	1.26	0.47	0.037	0.043	0.96	0.97	0.92
1.06	0.33	82.6	1.67	0.50	0.009	0.021	0.96	0.99	0.99
1.49	0.37	78.5	2.92	0.32	0.143	0.123	1.00	0.97	0.96
1.70	0.36	74.5	2.03	0.57	0.043	0.034	1.05	1.03	1.03
1.45	0.37	55.0	1.96	0.57	0.050	0.017	0.97	1.03	0.96
2.09	0.35	64.9	2.16	0.46	0.053	0.059	0.96	0.95	0.92
1.10	0.40	107.5	2.00	0.55	0.003	0.007	0.94	0.97	0.96
1.12	0.36	63.3	1.79	0.57	0.031	0.000	0.94	0.96	0.95
1.07	0.31	113.6	2.01	0.45	0.019	0.020	0.96	0.84	0.94
2.03	0.36	80.2	1.68	0.61	-0.003	0.019	0.94	0.97	0.96

L_i/ho	D_i/ho	angle(deg)	k_i	D_{gr}/ho	V_{tip}/U_o	Vo/U_o	U_{base}/U_o	U_{tip}/U_o	U_{drop}/U_o
1.60	0.32	92.1	1.87	0.54	0.050	0.057	0.98	0.98	0.97
0.85	0.29	83.3	2.00	0.41	0.034	0.047	0.99	1.00	1.00
1.18	0.33	110.7	2.35	0.39	0.037	0.042	0.93	0.91	0.93
1.96	0.34	75.0	1.56	0.52	0.028	0.008	0.95	0.95	0.94
1.26	0.36	76.9	1.55	0.58	-0.025	-0.013	0.88	0.91	0.91
1.49	0.39	102.7	1.74	0.75	-0.012	-0.020	0.94	0.91	0.96
1.59	0.37	67.5	2.06	0.47	0.052	0.028	0.95	0.97	0.96
1.13	0.35	67.9	1.77	0.51	0.000	-0.003	0.96	0.97	0.94
1.34	0.33	51.9	1.52	0.54	0.009	-0.022	0.94	1.10	0.96
1.41	0.34	103.2	1.80	0.52	0.025	0.027	0.93	0.92	0.95
1.73	0.29	91.9	1.77	0.22	0.028	0.018	0.95	0.92	0.93
1.39	0.34	111.9	1.78	0.58	0.003	-0.004	0.94	0.94	0.94
1.21	0.23	120.0	1.71	0.41	0.019	0.026	0.96	0.92	0.96
1.29	0.27	58.9	1.74	0.41	0.056	0.047	0.93	0.97	0.93
1.53	0.38	99.0	1.81	0.54	0.015	0.004	0.96	0.94	0.96
1.92	0.33	88.8	1.69	0.58	0.009	0.014	0.94	0.93	0.96
1.98	0.39	94.3	1.76	0.56	0.009	-0.008	0.94	0.95	0.97
1.26	0.32	55.4	1.61	0.59	-0.022	-0.021	0.97	1.04	0.97
1.31	0.32	81.7	1.78	0.49	0.043	0.012	0.93	0.93	0.93
1.17	0.31	70.8	1.60	0.47	0.003	0.001	0.95	0.97	0.94
0.97	0.27	51.9	1.77	0.45	-0.031	0.018	0.97	0.96	0.96
0.84	0.29	72.5	2.20	0.35	0.040	0.054	0.94	0.94	0.93
1.63	0.27	51.8	1.25	0.50	0.015	0.027	0.94	0.97	0.92
1.30	0.36	95.4	1.81	0.55	0.000	-0.009	0.98	0.97	0.98
1.18	0.35	98.4	1.80	0.59	0.022	-0.005	0.93	0.93	0.94
0.85	0.29	107.4	2.96	0.27	0.108	0.105	0.95	0.97	0.99
1.06	0.32	157.9	1.77	0.55	-0.019	-0.010	0.96	0.86	0.92
1.22	0.41	105.2	1.80	0.68	-0.009	-0.003	0.96	0.93	0.94
1.26	0.30	87.4	1.95	0.42	-0.003	0.015	0.93	0.92	0.94
2.13	0.27	108.2	1.33	0.57	0.031	0.024	0.96	0.97	0.99
1.73	0.38	90.5	2.25	0.50	0.012	0.013	0.90	0.87	0.89
1.81	0.46	77.7	1.83	0.66	-0.025	-0.016	0.97	0.97	0.97
1.51	0.30	39.1	1.30	0.58	-0.012	-0.004	0.92	0.96	0.89
1.31	0.42	75.6	1.75	0.72	0.013	-0.013	0.97	0.94	0.95

L_r/h_o	Δ_r/h_o	Δ_r/h_o angle(deg)	k_1	Δ_r/h_o	V_{tip}/U_o	Vo/U_o	U_{base}/U_o	U_{tip}/U_o	U_{drop}/U_o
0.84	0.26	42.6	1.75	0.48	0.019	0.028	0.95	0.95	0.94
0.90	0.34	96.9	2.02	0.50	0.000	-0.002	0.93	0.92	0.94
1.31	0.41	80.5	2.00	0.60	-0.016	-0.022	0.93	0.92	0.92
1.00	0.33	39.9	1.72	0.52	0.028	0.020	0.93	0.99	0.92
2.57	0.30	60.2	1.93	0.47	0.050	0.058	0.96	0.97	0.95
1.40	0.37	63.7	2.05	0.53	0.035	0.013	0.93	0.97	0.94
1.30	0.32	49.2	1.76	0.54	-0.013	-0.007	0.95	1.00	0.93
1.26	0.31	74.7	1.63	0.54	0.000	-0.017	0.94	0.94	0.93
1.76	0.37	83.2	1.47	0.64	-0.022	0.002	0.97	0.94	0.94
1.69	0.30	80.6	1.81	0.49	0.028	0.035	0.99	0.98	0.98
0.88	0.39	101.0	2.07	0.65	-0.035	-0.020	0.93	0.91	0.91
1.18	0.33	60.0	1.91	0.50	0.003	0.002	0.94	1.00	0.94
1.70	0.33	77.3	1.72	0.53	0.019	0.028	0.91	0.94	0.91
1.82	0.34	66.7	1.52	0.65	-0.041	-0.039	0.94	0.97	0.93
1.09	0.38	93.1	2.04	0.54	0.009	0.017	0.93	0.92	0.93
1.29	0.33	83.7	2.01	0.55	-0.009	-0.005	0.93	0.96	0.95
1.67	0.40	62.3	1.77	0.67	-0.003	0.015	0.93	1.00	0.96
1.08	0.40	77.9	2.05	0.59	0.025	-0.006	0.92	0.96	0.95
1.50	0.34	109.8	1.56	0.52	0.000	-0.008	0.91	0.88	0.92
1.34	0.30	68.9	1.76	0.48	0.013	-0.003	0.94	0.95	0.92
1.01	0.49	77.6	2.17	0.69	-0.006	-0.005	0.97	0.98	0.97
1.46	0.29	36.2	1.45	0.51	0.006	0.002	0.95	0.96	0.91
1.34	0.34	83.6	1.76	0.54	0.006	0.018	0.98	0.97	0.97
1.42	0.43	95.4	2.13	0.56	0.000	-0.011	0.97	0.98	0.98
1.48	0.42	104.0	1.81	0.42	-0.028	0.005	0.87	1.04	0.95
1.76	0.33	70.3	1.80	0.44	0.013	-0.005	0.91	0.95	0.92
1.32	0.30	103.5	2.45	0.42	0.075	0.072	0.93	0.91	0.92
1.16	0.33	81.8	2.38	0.40	0.025	0.007	0.98	0.98	0.98
1.15	0.41	99.2	1.48	0.68	0.000	-0.010	0.94	0.91	0.95
1.22	0.30	82.2	1.92	0.52	-0.006	0.012	0.90	0.91	0.90

Wall type: Rough, Flat

$U_0 = 6.2 \text{ m/s}$

$h_0 = 5.5 \text{ mm}$

$K = 0.13 \text{ mm}$

L_f/h_0	D_f/h_0	angle(deg)	K_1	D_{gr}/h_0	V_{tip}/U_0	V_0/U_0	U_{base}/U_0	U_{tip}/U_0	U_{drop}/U_0
1.54	0.40	83.6	1.84	0.49	0.021	0.030	0.98	1.00	0.96
1.68	0.42	79.1	1.85	0.52	0.116	0.111	0.93	0.96	0.93
1.28	0.27	86.1	1.83	0.35	0.073	0.080	0.94	0.96	0.76
1.49	0.32	74.7	2.51	0.49	0.034	0.050	0.92	0.93	0.90
1.47	0.43	89.3	2.24	0.50	0.060	0.050	0.93	0.93	0.92
1.20	0.38	87.7	1.88	0.57	0.000	-0.009	0.90	0.90	0.91
0.89	0.28	98.7	1.93	0.46	0.017	0.037	0.92	0.97	0.96
1.25	0.48	123.4	3.21	0.56	0.170	0.012	0.96	0.89	0.92
0.70	0.36	64.1	2.07	0.52	-0.021	-0.011	0.96	0.92	0.94
1.94	0.40	59.4	2.54	0.52	0.060	0.079	0.99	0.98	0.91
1.37	0.51	87.6	3.06	0.52	0.021	0.005	1.00	0.95	0.92
1.01	0.32	75.2	1.74	0.52	-0.009	-0.011	0.97	0.96	0.96
1.14	0.36	91.4	2.12	0.51	0.017	0.004	1.01	1.00	0.99
1.70	0.27	40.4	1.33	0.53	0.030	0.040	0.92	0.93	0.89
1.71	0.33	103.0	1.94	0.56	0.017	0.023	0.90	0.92	0.93
0.88	0.28	105.1	1.77	0.47	0.009	0.033	0.93	0.99	0.95
0.89	0.30	126.3	1.86	0.45	0.030	0.044	0.86	0.92	0.90
1.19	0.29	82.1	1.64	0.60	0.017	0.062	0.93	1.02	0.96
0.97	0.28	80.4	1.73	0.48	0.039	0.029	0.96	0.95	0.97
0.93	0.30	109.9	2.02	0.49	0.043	0.020	0.96	0.95	0.98
0.91	0.29	85.2	1.68	0.41	0.039	0.021	0.99	1.01	0.99
1.94	0.47	90.9	2.30	0.50	0.043	0.030	0.94	0.96	0.95
1.14	0.22	117.0	1.48	0.45	0.034	0.034	0.92	0.92	0.95
0.73	0.39	94.3	3.82	0.31	0.116	0.073	0.96	0.95	0.96
1.35	0.35	72.6	1.89	0.56	0.009	0.002	0.94	0.98	0.92
1.36	0.29	80.3	2.06	0.46	0.069	0.091	0.91	0.91	0.89
0.55	0.31	92.0	2.81	0.40	0.034	0.017	1.00	1.02	1.00
0.62	0.26	88.2	1.85	0.41	0.017	0.051	0.96	0.97	0.93
2.57	0.48	39.9	2.86	0.52	0.051	0.049	0.93	0.88	0.87

L_f/h_o	D_r/h_o	angle(deg)	k_1	D_{dr}/h_o	V_{tip}/U_o	Vo/U_o	U_{base}/U_o	U_{tip}/U_o	U_{drop}/U_o
1.44	0.36	88.9	2.04	0.49	0.060	0.041	0.95	0.92	0.93
0.91	0.36	40.7	1.61	0.59	0.004	0.009	0.92	0.90	0.90
1.67	0.36	55.0	1.99	0.44	0.094	0.092	0.94	0.93	0.88
1.62	0.38	77.4	1.77	0.58	0.039	0.050	0.91	0.91	0.90
2.55	0.46	77.9	1.63	0.68	0.009	0.011	0.93	0.94	0.92
2.99	0.34	43.6	0.98	0.65	0.026	0.022	0.94	1.04	0.91
2.42	0.32	60.1	1.22	0.65	0.064	0.055	0.90	0.91	0.87
0.97	0.44	80.9	2.42	0.57	0.017	0.028	0.91	0.89	0.92
0.91	0.28	100.4	2.23	0.42	0.043	0.031	0.87	0.87	0.86
1.36	0.38	70.3	2.41	0.42	0.043	0.042	0.88	0.91	0.87
1.38	0.34	106.2	2.02	0.49	0.021	0.022	0.91	0.90	0.93
2.66	0.41	32.0	1.47	0.73	0.000	0.004	0.88	0.90	0.87
1.32	0.40	86.7	1.62	0.71	-0.051	-0.035	0.91	0.92	0.90
1.40	0.37	111.3	1.71	0.63	-0.013	-0.017	0.93	0.89	0.92
1.84	0.45	96.0	2.16	0.60	-0.017	-0.005	0.92	0.92	0.93
1.10	0.36	109.4	1.57	0.64	-0.021	-0.037	0.90	0.90	0.92
0.91	0.41	102.1	1.79	0.62	-0.017	-0.026	0.88	0.90	0.88
2.06	0.38	35.2	1.78	0.58	0.017	0.049	0.93	1.00	0.91
2.43	0.45	73.7	1.71	0.71	-0.009	0.010	0.91	0.95	0.91
2.77	0.34	45.4	1.67	0.64	0.047	0.039	0.94	1.04	0.91
1.05	0.29	89.0	1.36	0.57	0.034	0.029	0.96	1.00	0.98
1.23	0.36	100.8	2.01	0.60	0.017	0.025	0.94	0.92	0.95
1.24	0.34	96.6	2.78	0.49	0.017	0.025	0.92	0.91	0.92
0.92	0.41	97.8	1.83	0.58	-0.030	0.004	0.90	0.97	0.93
0.98	0.32	78.1	2.00	0.51	0.034	0.015	0.93	0.91	0.90
1.70	0.26	89.0	1.21	0.50	0.043	0.056	0.89	0.92	0.93
1.19	0.31	101.6	2.08	0.35	0.051	0.033	0.91	0.93	0.92
1.75	0.42	96.6	2.42	0.49	0.034	0.032	0.88	0.88	0.88
1.11	0.29	69.9	2.33	0.39	0.098	0.107	0.90	0.87	0.85
1.19	0.37	91.4	2.28	0.59	0.009	0.029	0.87	0.88	0.86
1.23	0.28	39.6	1.55	0.51	0.009	0.023	0.94	0.89	0.88
1.78	0.39	78.5	1.88	0.60	0.026	0.003	0.93	0.97	0.95
1.04	0.28	93.2	2.74	0.33	0.081	0.107	0.95	0.96	0.93
1.68	0.31	54.0	2.33	0.60	0.009	-0.001	0.85	0.92	0.85

L_r/ho	D_r/ho	angle(deg)	k_1	D_{dr}/ho	V_{tip}/U_o	Vo/U_o	U_{base}/U_o	U_{tip}/U_o	U_{drop}/U_o
0.94	0.24	67.9	1.96	0.36	0.038	0.057	0.87	0.88	0.85
1.13	0.31	112.0	1.52	0.51	-0.004	0.008	0.87	0.86	0.86
2.31	0.48	57.0	1.89	0.75	0.043	0.012	0.83	0.89	0.84
1.64	0.37	83.0	1.36	0.70	0.009	-0.004	0.92	0.93	0.92
1.04	0.31	99.0	1.63	0.53	-0.030	-0.007	0.89	0.92	0.90
0.95	0.26	96.9	2.32	0.35	0.107	0.079	0.91	0.91	0.92
2.97	0.30	69.1	1.55	0.56	0.064	0.038	0.83	0.87	0.81
1.96	0.32	64.2	2.03	0.47	0.013	0.046	0.81	0.85	0.84
1.19	0.37	69.8	1.70	0.58	-0.009	-0.007	0.92	0.92	0.90
1.22	0.57	51.1	2.16	0.82	-0.038	-0.016	0.86	0.87	0.87
0.90	0.27	97.4	1.98	0.40	0.013	0.030	0.82	0.85	0.85
1.50	0.38	60.2	1.65	0.72	0.000	0.010	0.90	0.91	0.88
1.77	0.36	42.2	1.24	0.76	-0.026	-0.029	0.89	0.93	0.88
2.29	0.46	106.0	1.52	0.81	0.009	-0.025	0.99	0.92	0.97
2.04	0.39	44.0	1.46	0.69	0.017	0.004	0.86	0.89	0.83
2.05	0.44	68.9	1.50	0.82	0.013	0.006	0.92	0.95	0.93
1.31	0.43	99.3	1.93	0.64	0.013	-0.013	0.93	0.91	0.95
1.47	0.47	73.0	1.82	0.74	-0.017	-0.027	0.85	0.88	0.87
2.34	0.44	68.2	2.15	0.58	0.056	0.065	0.86	0.86	0.83
1.38	0.28	62.4	1.96	0.36	0.094	0.102	0.82	0.80	0.76
1.47	0.41	65.4	1.93	0.62	0.026	0.006	0.86	0.87	0.86
1.02	0.38	76.5	2.26	0.49	0.017	-0.002	0.93	0.95	0.92
1.51	0.46	98.4	2.40	0.74	0.034	-0.004	0.88	0.90	0.89
2.58	0.41	92.3	1.66	0.76	0.030	0.034	0.93	0.92	0.92
1.36	0.32	47.0	1.44	0.60	0.034	0.020	0.88	0.93	0.86
1.16	0.38	93.8	2.95	0.41	0.034	0.010	0.90	0.89	0.89
1.47	0.29	87.4	1.80	0.48	0.051	0.031	0.91	0.89	0.88
1.91	0.40	83.1	2.31	0.56	0.073	0.088	0.97	0.97	0.96
2.49	0.36	35.8	1.35	0.69	0.013	0.008	0.87	0.84	0.83
1.12	0.25	45.4	1.70	0.50	0.081	0.039	0.84	0.88	0.81
1.08	0.38	87.0	1.81	0.57	-0.038	-0.019	0.90	0.92	0.91
1.82	0.33	104.3	2.01	0.47	0.076	0.079	0.82	0.83	0.86
1.22	0.45	102.2	2.04	0.75	-0.017	-0.019	0.80	0.82	0.82
1.57	0.38	78.8	2.28	0.48	0.021	0.001	0.83	0.83	0.82

L_r/h_o	D_r/h_o	angle(deg)	k_1	D_{gr}/h_o	V_{tip}/U_o	V_o/U_o	U_{base}/U_o	U_{tip}/U_o	U_{drop}/U_o
1.23	0.30	142.9	1.73	0.60	-0.017	-0.026	0.84	0.80	0.86
1.43	0.33	81.2	2.04	0.47	0.034	0.034	0.91	0.91	0.90
1.05	0.31	89.5	1.83	0.44	0.059	0.033	0.84	0.85	0.84
2.45	0.48	47.7	1.51	0.77	0.025	0.028	0.81	0.84	0.79
2.08	0.39	90.5	1.74	0.69	0.030	0.020	0.85	0.86	0.86
2.09	0.25	48.0	1.22	0.54	0.017	0.041	0.81	0.85	0.79
1.03	0.53	85.8	2.14	0.75	-0.055	-0.037	0.91	0.89	0.89
0.84	0.31	78.2	1.75	0.50	-0.034	-0.026	0.84	0.86	0.85
1.30	0.25	64.0	1.62	0.46	0.051	0.069	0.82	0.84	0.81
0.88	0.30	118.5	2.23	0.43	0.043	0.030	0.82	0.83	0.83
1.03	0.37	64.2	1.58	0.63	0.004	0.012	0.86	0.88	0.86
0.52	0.23	78.9	1.87	0.55	0.021	0.009	0.87	0.89	0.86
1.08	0.35	112.3	2.37	0.47	0.047	0.044	0.79	0.79	0.83
1.49	0.37	55.7	1.57	0.67	0.013	-0.004	0.82	0.87	0.80
0.66	0.35	121.4	2.27	0.49	-0.004	0.013	0.80	0.81	0.78
1.91	0.42	35.0	1.66	0.71	-0.004	-0.010	0.81	0.87	0.78
1.61	0.50	122.2	1.98	0.79	-0.017	0.013	0.87	0.81	0.90
1.12	0.33	105.8	2.24	0.43	0.034	0.011	0.81	0.80	0.83
1.01	0.36	86.8	1.88	0.56	0.021	-0.007	0.86	0.86	0.87
2.00	0.26	32.8	1.30	0.56	0.021	0.024	0.82	0.88	0.80
1.18	0.37	114.3	2.73	0.38	0.064	0.062	0.84	0.84	0.87
0.98	0.40	67.2	1.87	0.56	-0.008	0.012	0.86	0.88	0.86
2.24	0.68	77.3	2.38	0.82	0.004	-0.022	0.90	0.95	0.89
1.29	0.32	119.6	1.81	0.49	0.021	0.000	0.83	0.79	0.84
1.29	0.33	38.7	1.34	0.63	0.008	0.000	0.85	0.84	0.84
1.27	0.32	85.3	1.57	0.56	0.017	0.013	0.85	0.84	0.84
1.01	0.40	59.3	1.89	0.60	-0.008	-0.011	0.88	0.86	0.87
2.62	0.44	26.8	1.74	0.80	-0.030	-0.019	0.82	0.86	0.78
0.96	0.34	87.2	1.86	0.58	-0.013	0.008	0.83	0.82	0.83
1.11	0.32	73.1	1.83	0.53	0.038	0.034	0.78	0.79	0.79
0.81	0.30	121.1	1.90	0.49	-0.025	-0.021	0.77	0.79	0.78
1.74	0.40	103.0	1.84	0.62	-0.013	0.004	0.80	0.77	0.81
1.61	0.38	85.6	2.08	0.57	-0.008	-0.017	0.78	0.82	0.82
1.32	0.43	88.8	1.58	0.75	-0.004	-0.021	0.79	0.85	0.84

L_f/h_o	D_f/h_o	angle(deg)	k_1	D_{gr}/h_o	V_{tip}/U_o	V_o/U_o	U_{base}/U_o	U_{tip}/U_o	U_{drop}/U_o
2.13	0.56	66.6	2.13	0.82	-0.038	-0.029	0.77	0.86	0.80
2.07	0.35	89.5	1.55	0.61	0.006	0.036	0.74	0.77	0.76
0.91	0.34	96.6	2.32	0.43	0.030	0.026	0.78	0.77	0.78

Wall type: Rough, Flat

$U_0 = 6.2 \text{ m/s}$

$h_0 = 5.8 \text{ mm}$

$k = 0.33 \text{ mm}$

L_r/h_0	D_r/h_0	angle(deg)	k_1	D_{dr}/h_0	V_{tip}/U_0	V_0/U_0	U_{base}/U_0	U_{tip}/U_0	U_{drop}/U_0
1.31	0.33	53.4	2.46	0.41	0.036	0.047	0.98	1.01	0.96
1.52	0.31	52.5	1.94	0.50	0.004	0.039	0.98	1.00	0.94
0.61	0.27	85.8	1.82	0.41	0.043	0.045	0.90	0.92	0.92
1.35	0.27	59.1	1.67	0.44	-0.004	0.000	0.97	0.98	0.99
1.81	0.35	68.9	1.69	0.54	0.040	0.053	0.89	0.90	0.88
2.46	0.49	56.3	2.02	0.78	0.080	0.074	0.94	0.90	0.86
2.39	0.49	84.7	2.70	0.51	0.072	0.064	0.90	0.85	0.86
2.70	0.37	68.3	1.97	0.59	0.064	0.067	0.93	0.93	0.91
2.49	0.31	62.7	1.94	0.48	0.084	0.088	0.88	0.91	0.84
1.76	0.31	65.9	1.75	0.55	0.040	0.071	0.88	0.89	0.87
1.25	0.34	47.8	1.61	0.61	0.052	0.042	0.88	0.88	0.84
3.06	0.33	31.9	1.52	0.63	0.072	0.057	0.91	0.96	0.82
2.05	0.30	112.9	1.54	0.59	0.060	0.043	0.92	0.91	0.93
1.73	0.32	88.0	2.01	0.47	0.084	0.082	0.92	0.92	0.92
2.03	0.34	82.3	1.60	0.55	0.052	0.048	0.94	0.92	0.90
1.88	0.33	83.8	1.41	0.60	0.008	0.029	0.92	0.93	0.93
2.41	0.42	65.8	1.52	0.53	0.187	0.191	0.91	0.84	0.80
1.48	0.31	83.7	1.86	0.60	0.056	0.056	0.95	0.97	0.97
1.43	0.34	89.7	1.68	0.61	0.060	0.074	0.96	0.96	0.97
1.95	0.34	83.3	1.59	0.51	0.072	0.071	0.93	0.94	0.93
1.98	0.26	87.1	1.12	0.56	0.048	0.110	0.91	0.90	0.92
1.06	0.25	117.6	1.48	0.40	0.044	0.035	0.89	0.89	0.92
1.48	0.26	73.4	2.21	0.36	0.108	0.106	0.90	0.95	0.89
1.88	0.34	76.2	1.75	0.56	0.056	0.047	0.91	0.93	0.92
2.13	0.40	94.1	2.05	0.58	0.040	0.047	0.95	0.94	0.93
1.71	0.27	62.6	1.78	0.48	0.048	0.050	0.88	0.93	0.89
1.63	0.29	94.3	1.46	0.57	0.094	0.078	0.88	0.88	0.90
1.23	0.34	107.7	2.02	0.50	0.028	0.031	0.86	0.83	0.85
1.89	0.19	75.0	1.18	0.43	0.072	0.070	0.93	0.89	0.89

L_f/h_o	D_f/h_o	angle(deg)	k_1	D_{dr}/h_o	V_{tip}/U_o	V_o/U_o	U_{base}/U_o	U_{tip}/U_o	U_{drop}/U_o
2.75	0.39	50.4	1.97	0.56	0.044	0.056	0.96	0.96	0.90
2.43	0.32	61.3	1.43	0.53	0.080	0.044	0.88	0.85	0.83
2.08	0.40	66.5	1.50	0.71	0.016	0.040	0.83	0.91	0.85
1.38	0.28	97.4	1.77	0.47	0.052	0.040	0.88	0.89	0.89
1.78	0.30	77.6	2.09	0.48	0.068	0.041	0.90	0.91	0.90
1.29	0.31	61.8	1.75	0.59	0.080	0.046	0.84	0.86	0.81
1.81	0.33	106.0	1.83	0.54	0.068	0.052	0.91	0.87	0.88
1.85	0.40	51.0	2.01	0.53	0.073	0.062	0.90	0.86	0.85
2.47	0.37	60.3	1.48	0.67	0.044	0.041	0.84	0.87	0.82
2.37	0.31	69.0	1.10	0.32	0.040	0.048	0.88	0.97	0.86
2.71	0.37	89.5	1.72	0.56	0.020	0.026	0.84	0.85	0.83
3.24	0.47	91.8	1.48	0.76	0.044	0.051	0.85	0.83	0.85
2.32	0.37	78.3	1.58	0.68	-0.004	-0.015	0.88	0.90	0.86
1.67	0.34	79.7	1.63	0.65	0.000	-0.006	0.86	0.87	0.85
2.63	0.31	50.8	1.27	0.67	0.052	0.027	0.86	0.92	0.82
3.25	0.42	62.7	2.18	0.66	0.000	0.013	0.85	0.86	0.84
2.03	0.52	101.2	2.01	0.74	0.012	-0.006	0.87	0.85	0.86
2.01	0.40	53.3	1.42	0.61	-0.024	-0.026	0.85	0.94	0.84
1.43	0.36	103.9	1.98	0.52	0.000	-0.003	0.89	0.86	0.88
2.83	0.37	92.3	1.61	0.57	0.036	0.052	0.91	0.90	0.91
3.13	0.46	82.6	2.15	0.55	-0.016	-0.016	0.90	0.93	0.86
2.27	0.34	61.1	1.66	0.66	0.077	0.046	0.85	0.87	0.81
3.38	0.33	77.6	1.25	0.61	0.097	0.066	0.84	0.82	0.80
2.41	0.48	115.1	2.07	0.67	0.004	0.013	0.87	0.85	0.86
1.79	0.33	77.8	1.60	0.61	-0.016	-0.008	0.86	0.90	0.88
1.84	0.32	53.6	1.56	0.60	0.008	0.009	0.84	0.86	0.82
1.23	0.34	112.4	1.72	0.51	-0.012	-0.020	0.81	0.77	0.82
1.94	0.34	42.0	1.57	0.63	0.000	-0.004	0.86	0.91	0.83
1.01	0.44	76.1	2.16	0.63	0.004	-0.011	0.93	0.90	0.89
2.78	0.37	66.7	1.70	0.57	0.043	0.037	0.87	0.90	0.87
1.39	0.38	100.8	1.80	0.57	-0.032	-0.024	0.84	0.85	0.87
0.93	0.34	101.5	2.36	0.39	0.083	0.077	0.78	0.79	0.81
2.63	0.33	96.6	1.73	0.52	0.012	0.010	0.88	0.86	0.88
1.19	0.30	68.0	1.92	0.52	0.016	0.003	0.90	0.90	0.88

L_f/h_o	D_f/h_o	angle(deg)	k_1	D_{dr}/h_o	V_{tip}/U_o	Vo/U_o	U_{base}/U_o	U_{tip}/U_o	U_{drop}/U_o
2.60	0.46	84.3	2.18	0.60	0.028	0.034	0.80	0.82	0.81
2.76	0.32	48.5	1.75	0.56	0.063	0.052	0.79	0.78	0.74
1.05	0.25	91.4	1.35	0.43	0.012	0.008	0.94	0.93	0.93
1.50	0.36	92.9	2.15	0.54	0.016	0.021	0.84	0.77	0.80
2.04	0.33	87.4	1.34	0.61	0.036	0.018	0.80	0.83	0.83
1.71	0.38	103.8	1.63	0.65	0.000	0.011	0.86	0.83	0.85
3.21	0.36	58.4	1.36	0.64	0.000	0.036	0.79	0.87	0.78
2.06	0.36	140.7	1.18	0.84	-0.012	0.001	0.77	0.82	0.83
1.74	0.26	65.4	1.54	0.51	0.032	0.039	0.81	0.79	0.80
1.33	0.46	65.9	1.81	0.70	-0.076	-0.052	0.88	0.89	0.90
1.02	0.47	84.2	1.89	0.72	-0.004	-0.025	0.77	0.80	0.79
2.73	0.33	68.2	1.68	0.46	0.128	0.135	0.83	0.82	0.79
1.68	0.43	60.6	1.75	0.73	-0.008	-0.032	0.79	0.89	0.83
1.31	0.35	105.5	1.48	0.66	-0.032	-0.005	0.81	0.81	0.83
2.58	0.35	86.2	1.39	0.70	0.056	0.045	0.83	0.81	0.82
1.48	0.38	74.4	2.04	0.45	0.072	0.067	0.70	0.73	0.73
2.29	0.29	77.1	1.27	0.64	0.060	0.058	0.83	0.85	0.83
1.22	0.41	57.9	1.97	0.69	-0.032	0.000	0.84	0.85	0.82
2.43	0.36	113.8	1.48	0.73	-0.008	-0.003	0.90	0.85	0.90
2.05	0.32	83.8	2.18	0.40	0.188	0.172	0.83	0.82	0.81
0.94	0.48	78.0	2.09	0.71	-0.032	-0.016	0.78	0.79	0.79
1.42	0.36	56.7	1.38	0.69	-0.020	-0.009	0.84	0.85	0.83
1.47	0.36	107.9	1.70	0.74	-0.012	-0.016	0.73	0.72	0.75
1.35	0.27	65.5	1.42	0.54	0.008	0.019	0.81	0.83	0.82
0.98	0.42	92.0	2.48	0.47	-0.052	-0.051	0.83	0.90	0.87
2.21	0.37	59.0	1.55	0.69	0.044	0.046	0.77	0.78	0.76
2.96	0.49	49.3	1.85	0.87	-0.008	-0.010	0.76	0.94	0.82
1.58	0.27	106.3	1.60	0.48	0.012	0.011	0.86	0.88	0.90
1.98	0.25	40.5	1.35	0.59	0.080	0.059	0.70	0.74	0.72
0.96	0.36	96.6	1.84	0.61	-0.032	-0.016	0.83	0.87	0.87
1.31	0.38	94.5	1.85	0.68	-0.008	-0.030	0.91	0.88	0.88
1.48	0.25	76.0	2.00	0.47	0.000	-0.016	0.81	0.85	0.82
1.43	0.29	71.7	1.52	0.60	0.056	0.033	0.81	0.78	0.79
1.03	0.36	65.1	1.93	0.56	0.032	0.025	0.76	0.79	0.78

L_r/h_0	D_r/h_0	angle(deg)	k_1	D_{cr}/h_0	V_{tip}/U_0	V_0/U_0	U_{base}/U_0	U_{tip}/U_0	U_{drop}/U_0
1.11	0.26	105.1	1.71	0.49	0.020	0.036	0.79	0.78	0.82
2.29	0.37	96.8	1.42	0.77	-0.024	-0.017	0.73	0.74	0.75
1.39	0.41	102.3	1.88	0.63	-0.026	-0.031	0.81	0.79	0.80
2.07	0.35	83.4	1.59	0.61	0.020	-0.010	0.73	0.74	0.73
2.94	0.28	78.9	1.45	0.68	-0.020	-0.019	0.83	0.84	0.79
2.66	0.41	74.3	1.48	0.65	0.012	-0.014	0.79	0.81	0.79
1.86	0.44	57.5	2.62	0.51	0.064	0.050	0.75	0.78	0.74
2.49	0.41	79.4	1.51	0.69	0.024	0.020	0.82	0.84	0.82
2.35	0.36	68.4	1.72	0.75	-0.012	0.015	0.81	0.85	0.80
1.47	0.33	78.7	2.47	0.46	0.068	0.049	0.75	0.76	0.75
2.93	0.41	58.4	2.09	0.58	0.084	0.080	0.74	0.69	0.69
1.31	0.32	57.1	1.40	0.58	0.040	0.033	0.85	0.85	0.86
1.47	0.39	69.7	1.59	0.77	0.000	-0.007	0.76	0.76	0.77
1.72	0.33	103.1	1.97	0.43	0.108	0.088	0.74	0.68	0.71
1.57	0.39	92.5	1.70	0.68	0.012	0.019	0.80	0.80	0.80
2.02	0.49	100.6	1.96	0.77	-0.004	-0.005	0.77	0.80	0.79
1.31	0.35	83.3	1.42	0.72	-0.008	-0.007	0.79	0.80	0.79
1.75	0.45	75.7	2.57	0.52	-0.016	-0.003	0.81	0.84	0.81
1.42	0.29	93.8	2.28	0.37	0.116	0.108	0.81	0.80	0.80
1.92	0.30	125.7	1.30	0.63	-0.012	0.029	0.84	0.78	0.87
1.05	0.45	96.5	1.97	0.71	-0.024	-0.021	0.80	0.82	0.80
1.72	0.43	124.2	1.74	0.75	-0.048	-0.064	0.86	0.84	0.83
2.17	0.36	71.1	1.99	0.56	0.060	0.034	0.78	0.79	0.76
2.59	0.33	31.2	2.19	0.52	0.112	0.076	0.80	0.88	0.74
1.68	0.39	95.1	1.77	0.63	-0.028	-0.013	0.89	0.87	0.86
1.23	0.31	86.1	1.75	0.56	-0.016	-0.004	0.77	0.80	0.79
2.83	0.40	47.7	1.64	0.71	-0.016	0.016	0.75	0.87	0.77
0.64	0.25	98.3	1.95	0.39	0.024	0.033	0.77	0.77	0.76
2.77	0.41	62.4	1.37	0.80	0.028	0.031	0.87	0.88	0.87
1.60	0.29	56.2	1.30	0.56	0.060	0.065	0.78	0.80	0.75
1.30	0.38	90.8	1.91	0.62	-0.012	-0.023	0.81	0.82	0.82
1.59	0.30	117.7	1.70	0.51	0.028	0.035	0.75	0.70	0.77
1.07	0.34	106.7	2.19	0.45	0.000	0.004	0.67	0.67	0.64
3.06	0.34	73.2	1.32	0.69	0.053	0.046	0.75	0.77	0.75

L_r/h_o	D_r/h_o	angle(deg)	k_1	D_{dr}/h_o	V_{tip}/U_o	V_o/U_o	U_{base}/U_o	U_{tip}/U_o	U_{drop}/U_o
2.11	0.49	90.9	1.74	0.78	0.000	0.010	0.80	0.82	0.82
1.50	0.34	84.4	1.98	0.48	0.093	0.090	0.70	0.68	0.68
1.85	0.54	76.3	1.80	0.86	0.000	-0.049	0.79	0.84	0.81
2.46	0.37	63.4	1.33	0.83	-0.028	-0.004	0.76	0.79	0.77
2.20	0.49	68.7	1.99	0.72	0.016	0.025	0.79	0.84	0.79
3.09	0.49	61.1	1.77	0.98	0.004	-0.016	0.73	0.76	0.72
1.04	0.42	61.3	1.80	0.68	0.004	-0.015	0.66	0.70	0.69
3.52	0.49	95.0	1.38	0.88	0.008	0.009	0.75	0.73	0.73
2.10	0.28	90.5	1.59	0.64	-0.020	0.016	0.67	0.68	0.70
1.18	0.32	62.1	1.30	0.59	0.044	0.012	0.79	0.78	0.77
1.95	0.44	89.8	2.00	0.57	-0.053	-0.030	0.74	0.70	0.76
1.69	0.50	125.5	2.82	0.46	0.065	0.036	0.75	0.56	0.71
1.51	0.56	108.8	2.83	0.46	0.024	-0.005	0.70	0.70	0.71
2.66	0.44	61.3	2.30	0.57	0.008	0.013	0.73	0.79	0.73
1.58	0.30	95.3	1.87	0.43	0.012	0.025	0.76	0.74	0.73
1.45	0.33	81.5	2.11	0.56	-0.040	-0.045	0.79	0.79	0.78
4.03	0.40	36.3	1.90	0.74	-0.020	0.013	0.73	0.81	0.68
1.32	0.37	95.2	1.95	0.67	-0.028	-0.040	0.76	0.77	0.76
1.57	0.33	43.7	1.49	0.68	0.028	0.034	0.72	0.80	0.70
2.32	0.39	94.0	1.65	0.61	0.032	0.035	0.75	0.77	0.77
1.75	0.37	88.6	2.05	0.57	0.000	0.025	0.76	0.76	0.76
2.37	0.44	84.0	1.50	0.85	-0.024	-0.024	0.68	0.72	0.68
3.18	0.36	73.5	1.47	0.74	0.065	0.045	0.74	0.77	0.75
1.75	0.41	85.2	1.98	0.59	-0.008	-0.004	0.77	0.81	0.78
1.42	0.51	89.7	2.68	0.57	-0.020	-0.027	0.72	0.74	0.72
3.39	0.62	30.8	2.38	0.70	-0.036	0.006	0.71	0.80	0.69
1.39	0.34	51.0	1.78	0.53	0.012	0.007	0.73	0.73	0.71
1.23	0.40	96.0	1.81	0.71	-0.057	-0.016	0.85	0.81	0.82
2.57	0.37	106.5	1.89	0.55	0.032	0.031	0.68	0.66	0.68

Wall type: Rough, Flat

$U_0 = 6.2 \text{ m/s}$

$h_0 = 5.8 \text{ mm}$

$k = 0.72 \text{ mm}$

L_r/h_0	D_r/h_0	angle(deg)	k_1	D_{dr}/h_0	V_{tip}/U_0	V_0/U_0	U_{base}/U_0	U_{tip}/U_0	U_{drop}/U_0
1.63	0.34	64.1	2.20	0.46	0.084	0.073	0.96	0.94	0.92
1.21	0.28	57.6	1.72	0.49	0.082	0.095	0.94	0.95	0.94
1.07	0.26	74.2	1.57	0.46	0.118	0.120	0.93	0.94	0.93
1.83	0.30	83.7	1.76	0.46	0.086	0.112	0.93	0.95	0.96
1.36	0.28	63.3	1.68	0.53	0.039	0.071	0.94	0.97	0.96
2.75	0.33	70.3	1.57	0.47	0.035	0.077	0.89	0.90	0.88
3.18	0.44	88.8	1.69	0.57	0.043	0.063	0.85	0.86	0.87
3.38	0.34	92.0	1.37	0.54	0.078	0.091	0.92	0.93	0.95
1.52	0.29	91.3	1.59	0.54	0.043	0.055	0.90	0.90	0.90
1.75	0.34	115.4	1.57	0.57	0.051	0.009	0.90	0.88	0.92
2.28	0.34	68.7	1.69	0.52	0.078	0.103	0.88	0.90	0.86
2.52	0.48	103.9	3.02	0.48	0.051	0.040	0.93	0.90	0.92
2.90	0.40	52.8	2.08	0.50	0.074	0.079	0.91	0.85	0.82
2.22	0.36	97.9	1.69	0.49	0.031	0.020	0.86	0.89	0.90
2.29	0.29	73.3	1.91	0.48	0.098	0.106	0.94	0.95	0.93
3.28	0.35	70.8	1.88	0.51	0.106	0.103	0.94	0.98	0.94
1.94	0.43	71.0	2.09	0.56	0.016	0.031	0.88	0.96	0.90
1.11	0.37	127.0	1.72	0.63	0.000	0.008	0.89	0.90	0.91
3.85	0.39	66.0	1.67	0.64	0.059	0.046	0.91	0.88	0.87
1.53	0.28	64.3	1.63	0.54	0.051	0.070	0.93	0.91	0.90
1.60	0.34	70.9	2.04	0.56	0.086	0.059	0.90	0.91	0.89
1.94	0.32	82.9	2.05	0.48	0.094	0.089	0.93	0.93	0.93
2.06	0.34	54.7	1.72	0.53	0.109	0.101	0.95	1.01	0.97
1.49	0.28	49.3	1.52	0.48	0.055	0.041	0.90	0.92	0.85
2.29	0.29	96.0	1.43	0.63	0.070	0.061	0.94	0.90	0.92
2.67	0.32	90.9	1.65	0.49	0.098	0.073	0.92	0.92	0.93
2.73	0.30	51.3	1.88	0.51	0.090	0.074	0.92	0.97	0.91
0.80	0.33	113.4	2.03	0.53	0.043	0.047	0.91	0.92	0.93
1.71	0.29	67.2	1.32	0.59	0.012	0.049	0.88	0.91	0.89

L_f/h_o	D_f/h_o	angle(deg)	k_L	D_{dr}/h_o	V_{tip}/U_o	Vo/U_o	U_{base}/U_o	U_{tip}/U_o	U_{drop}/U_o
1.76	0.35	78.3	1.54	0.64	-0.012	0.013	0.97	0.94	0.95
1.89	0.32	82.4	2.06	0.62	0.066	0.077	0.94	0.95	0.94
1.35	0.30	100.3	1.80	0.54	-0.008	0.001	0.94	0.93	0.94
1.48	0.29	86.5	1.98	0.60	0.059	0.058	0.91	0.88	0.87
2.48	0.29	82.3	1.58	0.60	0.047	0.072	0.86	0.88	0.91
3.24	0.43	47.5	2.19	0.52	0.047	0.063	0.93	0.96	0.89
3.21	0.42	70.7	2.01	0.46	0.129	0.100	0.87	0.90	0.88
4.20	0.40	109.2	1.66	0.63	0.008	-0.003	0.89	0.87	0.88
1.93	0.50	86.1	1.98	0.59	-0.008	-0.024	0.87	0.88	0.89
2.20	0.28	47.1	1.06	0.62	0.023	0.038	0.89	0.87	0.83
1.89	0.40	85.7	1.66	0.68	0.016	0.009	0.87	0.90	0.91
2.44	0.30	67.4	1.62	0.48	0.078	0.082	0.89	0.88	0.86
2.81	0.46	34.2	1.59	0.72	-0.008	0.021	0.87	0.86	0.81
3.93	0.45	59.0	1.59	0.71	0.047	0.049	0.85	0.85	0.81
1.28	0.33	88.5	2.14	0.49	0.051	0.049	0.86	0.89	0.89
2.13	0.43	71.7	1.51	0.69	-0.004	-0.019	0.91	0.94	0.90
2.35	0.50	87.6	1.57	0.69	0.000	0.007	0.86	0.87	0.84
1.22	0.35	112.7	1.88	0.55	-0.039	-0.048	0.89	0.88	0.88
1.56	0.35	69.8	1.53	0.61	-0.008	0.015	0.88	0.88	0.87
2.29	0.34	57.6	1.97	0.46	0.043	0.057	0.86	0.91	0.87
2.36	0.39	59.1	2.10	0.59	0.059	0.063	0.90	0.91	0.87
1.79	0.32	90.3	1.58	0.57	0.027	0.038	0.83	0.82	0.84
2.24	0.39	47.3	1.83	0.59	-0.043	0.041	0.88	0.91	0.88
2.14	0.37	79.5	1.90	0.47	0.082	0.094	0.86	0.87	0.87
3.54	0.43	57.1	1.62	0.75	0.000	-0.010	0.88	0.92	0.85
2.19	0.56	81.5	1.60	0.89	-0.039	-0.014	0.93	0.89	0.90
1.53	0.45	96.9	2.37	0.49	-0.027	-0.012	0.89	0.86	0.90
3.24	0.44	109.7	1.51	0.79	0.008	0.000	0.88	0.85	0.89
1.39	0.46	85.9	1.70	0.76	-0.031	0.007	0.92	0.92	0.91
3.26	0.35	57.9	1.43	0.65	0.031	0.031	0.91	0.99	0.89
2.88	0.46	93.1	1.74	0.84	0.031	0.042	0.86	0.81	0.81
2.10	0.28	72.5	1.95	0.43	0.078	0.076	0.85	0.87	0.86
4.50	0.43	74.7	1.96	0.66	0.078	0.068	0.89	0.90	0.91
2.98	0.44	49.0	1.50	0.67	-0.035	0.041	0.90	0.95	0.86

L_r/h_o	D_r/h_o	angle(deg)	k_1	D_{dr}/h_o	V_{tip}/U_o	V_o/U_o	U_{base}/U_o	U_{tip}/U_o	U_{drop}/U_o
2.02	0.26	50.8	1.34	0.37	0.086	0.069	0.83	0.89	0.79
3.23	0.43	48.4	1.74	0.70	0.023	0.026	0.83	0.83	0.83
2.36	0.35	74.6	1.92	0.62	0.023	0.014	0.85	0.94	0.87
3.68	0.40	41.0	1.68	0.59	0.082	0.088	0.86	0.86	0.78
2.11	0.34	83.1	2.16	0.48	0.047	0.040	0.78	0.77	0.77
3.50	0.46	46.1	2.12	0.71	0.078	0.043	0.80	0.80	0.77
4.16	0.53	68.7	1.57	0.82	-0.019	-0.025	0.78	0.77	0.77
1.89	0.43	59.3	1.75	0.65	0.000	0.000	0.78	0.77	0.76
1.63	0.31	119.0	1.98	0.46	0.039	0.043	0.82	0.83	0.85
2.93	0.34	66.6	1.42	0.59	0.023	0.030	0.81	0.84	0.81
2.62	0.35	61.3	1.56	0.69	0.051	0.033	0.81	0.84	0.81
1.85	0.35	86.9	1.55	0.64	-0.004	0.015	0.76	0.79	0.80
2.51	0.32	43.7	1.55	0.73	-0.008	0.019	0.83	0.88	0.80
2.56	0.28	51.7	1.59	0.53	0.043	0.026	0.79	0.84	0.77
2.76	0.56	100.3	1.76	1.02	-0.047	-0.039	0.87	0.86	0.88
2.03	0.36	101.5	1.75	0.61	0.004	-0.015	0.86	0.84	0.85
1.70	0.30	92.0	2.27	0.38	0.109	0.096	0.88	0.88	0.88
1.89	0.28	115.4	1.78	0.44	0.054	0.022	0.84	0.81	0.86
1.66	0.38	72.9	1.62	0.46	0.047	-0.022	0.76	0.81	0.78
2.94	0.50	33.0	2.23	0.60	0.023	0.047	0.79	0.81	0.74
2.94	0.32	42.2	1.57	0.70	0.023	0.016	0.84	0.77	0.78
1.52	0.33	63.9	1.73	0.54	-0.019	-0.010	0.82	0.86	0.84
2.02	0.36	74.3	1.91	0.69	0.051	0.024	0.85	0.87	0.86
4.97	0.64	126.0	2.09	0.96	-0.047	-0.014	0.84	0.82	0.88
2.60	0.43	55.6	2.39	0.45	0.140	0.132	0.82	0.83	0.79
2.11	0.40	49.1	1.96	0.67	0.019	0.006	0.86	0.88	0.84
2.51	0.28	73.2	1.82	0.53	0.070	0.055	0.78	0.84	0.80
1.28	0.45	90.4	1.66	0.76	-0.004	-0.008	0.91	0.92	0.91
2.04	0.38	35.1	1.64	0.83	-0.043	-0.017	0.79	0.88	0.77
1.12	0.34	91.3	1.88	0.56	-0.012	-0.018	0.81	0.81	0.83
1.13	0.41	83.7	1.74	0.68	-0.004	-0.008	0.84	0.87	0.85
2.79	0.37	53.7	1.73	0.57	0.062	0.046	0.88	0.92	0.86
1.62	0.26	37.3	1.40	0.49	0.051	0.033	0.75	0.86	0.75
3.02	0.43	74.7	1.50	0.85	-0.043	-0.027	0.83	0.87	0.83

L_r/h_o	D_r/h_o	angle(deg)	k_1	D_r/h_o	V_{tip}/U_o	V_o/U_o	U_{base}/U_o	U_{tip}/U_o	U_{drop}/U_o
1.61	0.32	92.4	1.73	0.54	0.008	0.031	0.79	0.79	0.80
2.65	0.37	91.8	1.52	0.66	0.066	0.048	0.79	0.79	0.81
1.86	0.35	59.6	1.79	0.53	0.051	0.045	0.71	0.73	0.69
1.67	0.31	75.7	2.04	0.41	0.062	0.056	0.75	0.75	0.74
1.73	0.38	72.2	1.92	0.58	0.051	0.030	0.79	0.83	0.81
1.66	0.38	86.6	1.71	0.59	0.012	0.038	0.80	0.85	0.83
1.87	0.32	73.9	1.70	0.56	0.047	0.016	0.84	0.84	0.82
1.16	0.31	81.8	2.07	0.46	0.008	0.014	0.76	0.80	0.77
1.54	0.31	82.9	1.61	0.62	0.043	0.015	0.76	0.77	0.78
2.29	0.44	46.9	1.51	0.75	-0.023	-0.056	0.75	0.87	0.80
1.98	0.37	47.2	1.67	0.65	0.031	0.014	0.72	0.74	0.70
1.98	0.33	78.2	1.70	0.66	-0.027	-0.003	0.84	0.87	0.86
2.01	0.41	104.3	1.58	0.85	-0.039	-0.037	0.81	0.81	0.83
2.03	0.35	101.9	1.86	0.61	0.019	0.016	0.83	0.85	0.85
2.31	0.30	78.1	1.88	0.57	0.035	-0.001	0.79	0.81	0.79
4.58	0.35	38.2	1.23	0.92	0.019	0.013	0.83	0.73	0.72
2.16	0.48	76.8	1.73	0.68	-0.004	-0.005	0.83	0.91	0.86
2.26	0.42	108.8	1.53	0.85	0.012	0.010	0.84	0.78	0.84
3.67	0.45	87.8	2.17	0.60	0.113	0.093	0.79	0.79	0.78
1.73	0.42	107.0	1.95	0.58	0.000	0.010	0.83	0.80	0.85
1.22	0.38	93.1	1.76	0.68	-0.023	-0.028	0.79	0.79	0.80
1.30	0.37	58.2	2.19	0.46	0.035	0.020	0.81	0.88	0.81
1.62	0.31	108.1	1.42	0.64	0.043	0.017	0.76	0.74	0.77
1.67	0.43	103.8	1.62	0.80	-0.039	-0.039	0.84	0.81	0.85
3.91	0.28	45.8	1.50	0.63	0.035	0.016	0.83	0.82	0.75
3.55	0.42	73.1	1.40	0.84	0.051	0.038	0.71	0.70	0.70
1.81	0.31	77.1	2.00	0.46	0.113	0.112	0.77	0.79	0.74
4.59	0.46	62.6	1.69	0.67	0.043	0.043	0.78	0.79	0.76
1.65	0.29	44.6	1.17	0.62	0.082	0.090	0.64	0.69	0.67
2.02	0.38	61.1	1.91	0.63	0.016	-0.018	0.75	0.80	0.79
1.13	0.40	73.4	2.41	0.54	-0.027	-0.034	0.81	0.82	0.82
1.61	0.42	79.1	1.89	0.62	0.043	0.000	0.75	0.74	0.73
2.48	0.53	36.9	1.68	0.99	-0.078	-0.080	0.71	0.80	0.75
1.86	0.41	65.5	1.91	0.55	0.062	0.062	0.70	0.72	0.69

L_r/h_o	D_r/h_o	angle(deg)	k_1	D_{dr}/h_o	V_{tip}/U_o	V_o/U_o	U_{base}/U_o	U_{tip}/U_o	U_{drop}/U_o
2.34	0.46	51.9	1.81	0.76	0.004	0.015	0.77	0.77	0.74
2.49	0.33	124.6	1.59	0.62	0.016	-0.013	0.74	0.73	0.77
5.46	0.42	50.6	1.38	0.75	0.043	0.036	0.78	0.80	0.73
1.74	0.29	110.9	1.51	0.49	0.008	0.020	0.69	0.69	0.71
3.82	0.43	76.8	1.47	0.86	0.020	-0.001	0.77	0.86	0.75
1.77	0.27	66.9	1.96	0.40	0.066	0.066	0.74	0.78	0.75
1.27	0.41	107.8	1.78	0.76	-0.051	-0.030	0.76	0.74	0.78
2.01	0.36	50.2	1.54	0.65	-0.043	-0.008	0.76	0.82	0.77
0.99	0.29	98.8	1.74	0.52	0.012	0.028	0.76	0.79	0.78
4.40	0.68	34.7	2.38	0.76	-0.016	0.008	0.71	0.78	0.70
6.36	0.82	39.7	2.43	0.91	0.039	-0.005	0.70	0.76	0.67
3.32	0.45	54.6	2.03	0.71	-0.016	0.009	0.76	0.82	0.77
1.94	0.47	89.0	1.52	1.01	-0.035	-0.013	0.80	0.80	0.82
2.09	0.58	62.3	1.57	0.98	-0.020	-0.025	0.71	0.73	0.72
1.54	0.46	100.3	1.37	0.80	0.008	-0.026	0.75	0.72	0.77
1.00	0.36	36.2	1.61	0.65	-0.004	0.008	0.70	0.70	0.71
1.77	0.51	112.8	1.75	0.83	-0.055	-0.060	0.80	0.77	0.78
2.68	0.42	30.8	1.57	0.80	0.016	0.014	0.72	0.76	0.69
2.26	0.44	96.6	3.20	0.42	0.031	0.036	0.71	0.70	0.70
3.21	0.52	84.8	1.95	0.74	-0.070	-0.047	0.77	0.76	0.79
2.90	0.38	67.3	1.61	0.63	0.039	0.035	0.73	0.80	0.76
1.47	0.37	114.7	1.86	0.51	-0.016	-0.014	0.65	0.62	0.66
1.56	0.36	105.7	1.64	0.71	-0.027	-0.007	0.76	0.78	0.77
2.83	0.46	81.1	2.01	0.66	-0.039	-0.023	0.79	0.80	0.77
3.07	0.34	67.6	0.89	0.58	0.102	0.044	0.68	0.72	0.66
3.12	0.49	46.6	2.20	0.57	0.047	0.048	0.76	0.74	0.70
1.48	0.60	67.2	1.88	1.00	-0.039	-0.044	0.69	0.69	0.69
4.33	0.46	85.1	1.74	0.71	0.055	0.035	0.67	0.70	0.69
2.70	0.26	42.4	1.05	0.60	0.074	0.081	0.76	0.80	0.67

Wall type: Rough, Flat

$U_o = 4.5 \text{ m/s}$

$h_o = 5.4 \text{ mm}$

$k = 0.72 \text{ mm}$

L_r/h_o	D_r/h_o	angle(deg)	k_1	D_{gr}/h_o	V_{tip}/U_o	Vo/U_o	U_{base}/U_o	U_{tip}/U_o	U_{drop}/U_o
2.21	0.39	62.4	1.59	0.66	-0.011	0.001	0.85	0.84	0.83
1.77	0.37	103.6	1.84	0.61	0.065	0.078	0.83	0.87	0.89
2.13	0.42	84.6	1.90	0.65	-0.005	0.005	0.88	0.89	0.88
1.62	0.36	102.6	1.58	0.68	0.011	0.021	0.84	0.85	0.87
1.90	0.35	91.4	1.78	0.45	0.102	0.092	0.88	0.87	0.87
1.90	0.30	59.4	1.86	0.48	0.097	0.149	0.85	0.89	0.85
1.52	0.44	104.9	2.02	0.65	-0.016	-0.006	0.81	0.78	0.81
2.26	0.53	67.5	2.09	0.73	-0.027	-0.047	0.84	0.87	0.83
1.65	0.52	81.0	1.48	0.83	0.005	-0.005	0.82	0.80	0.80
2.43	0.37	98.9	1.50	0.73	0.016	0.031	0.88	0.87	0.88
1.23	0.48	105.5	1.85	0.74	0.027	-0.023	0.89	0.88	0.90
1.33	0.49	83.8	1.89	0.67	0.000	-0.001	0.85	0.85	0.85
1.45	0.56	63.0	1.98	0.82	-0.053	-0.036	0.85	0.84	0.85
1.67	0.38	135.9	1.58	0.64	0.005	-0.009	0.79	0.85	0.84
4.24	0.51	75.5	1.45	0.79	0.074	0.033	0.80	0.83	0.82
1.25	0.31	68.6	2.24	0.38	0.196	0.183	0.88	0.89	0.85
2.75	0.40	64.8	1.74	0.57	0.058	0.069	0.79	0.86	0.77
2.75	0.35	75.3	1.06	0.81	0.027	-0.012	0.80	0.86	0.85
1.93	0.43	88.4	1.53	0.86	0.005	-0.003	0.78	0.81	0.83
1.78	0.48	63.8	1.77	0.81	-0.058	-0.070	0.85	0.90	0.86
2.95	0.38	68.1	1.33	0.80	0.048	0.008	0.78	0.86	0.80
1.69	0.45	86.4	2.04	0.56	-0.011	-0.020	0.82	0.84	0.83
2.05	0.40	99.0	1.84	0.57	-0.005	-0.012	0.83	0.80	0.82
1.35	0.42	106.9	1.73	0.66	-0.021	-0.003	0.81	0.88	0.86
1.55	0.32	89.0	2.45	0.35	0.112	0.127	0.78	0.78	0.78
1.43	0.35	103.3	1.44	0.65	-0.069	-0.034	0.86	0.87	0.86
2.74	0.33	68.8	1.64	0.49	0.037	0.040	0.78	0.84	0.80
1.43	0.29	91.1	1.31	0.57	0.069	0.037	0.66	0.69	0.69
1.57	0.41	87.5	2.13	0.67	-0.064	-0.027	0.84	0.88	0.85

L_r/h_o	D_r/h_o	angle(deg)	k_1	D_{dr}/h_o	V_{tip}/U_o	Vo/U_o	U_{base}/U_o	U_{tip}/U_o	U_{drop}/U_o
2.48	0.35	74.3	1.24	0.70	0.053	0.017	0.82	0.83	0.79
1.22	0.25	90.8	1.68	0.45	0.069	0.079	0.85	0.86	0.86
1.86	0.32	73.8	1.45	0.65	-0.037	-0.016	0.88	0.88	0.88
1.63	0.22	76.7	1.77	0.37	0.149	0.132	0.79	0.78	0.76
1.52	0.33	59.7	1.29	0.66	-0.005	-0.017	0.92	0.89	0.89
2.66	0.47	46.8	2.08	0.62	0.011	0.005	0.80	0.86	0.80
2.43	0.46	82.6	1.68	0.71	0.005	0.002	0.85	0.85	0.87
1.34	0.24	65.7	1.35	0.47	0.027	0.045	0.78	0.60	0.78
2.15	0.54	38.8	1.44	0.86	-0.032	-0.050	0.70	0.90	0.75
1.51	0.53	86.3	1.62	0.90	-0.053	-0.054	0.75	0.76	0.76
1.71	0.45	69.0	1.57	0.72	-0.042	-0.032	0.70	0.71	0.69
1.98	0.45	72.8	1.75	0.76	-0.047	-0.036	0.73	0.76	0.74
1.86	0.50	47.5	1.65	0.78	-0.079	-0.032	0.75	0.84	0.75
2.18	0.47	110.2	2.02	0.58	-0.053	-0.034	0.77	0.77	0.79
1.93	0.35	95.3	2.20	0.51	0.063	0.090	0.76	0.77	0.77
1.73	0.46	74.5	2.03	0.65	0.085	0.060	0.78	0.77	0.74
1.52	0.41	57.9	1.63	0.70	0.000	0.002	0.70	0.76	0.71
1.65	0.26	84.8	2.68	0.28	0.327	0.299	0.73	0.72	0.73
2.90	0.46	79.2	1.69	0.84	-0.005	0.004	0.78	0.80	0.77
1.12	0.28	77.2	1.61	0.50	0.069	0.056	0.78	0.79	0.78
1.85	0.40	68.9	1.52	0.72	-0.032	-0.015	0.82	0.83	0.79
1.25	0.29	51.3	1.50	0.54	-0.005	-0.008	0.75	0.76	0.73
1.33	0.33	108.7	2.54	0.37	0.079	0.070	0.71	0.72	0.75
1.29	0.42	91.6	1.66	0.73	-0.032	-0.011	0.82	0.84	0.82
1.57	0.33	41.6	1.50	0.69	0.016	0.028	0.73	0.83	0.73
1.49	0.33	77.6	1.84	0.51	0.042	0.049	0.74	0.75	0.72
1.48	0.22	128.2	1.99	0.34	0.127	0.110	0.78	0.80	0.90
0.99	0.28	85.7	2.61	0.33	0.066	0.048	0.73	0.72	0.73
1.81	0.79	67.1	3.17	0.60	-0.019	0.018	0.75	0.77	0.77
1.27	0.41	99.4	1.98	0.59	0.000	0.002	0.80	0.79	0.78
0.85	0.25	86.6	2.41	0.31	0.090	0.076	0.80	0.79	0.79
0.91	0.29	107.4	2.26	0.38	0.035	0.032	0.73	0.74	0.75
1.50	0.36	100.8	1.75	0.61	-0.019	-0.016	0.72	0.69	0.74
1.58	0.30	113.2	1.68	0.52	0.012	0.009	0.79	0.73	0.79

L_f/h_o	D_f/h_o	angle(deg)	k_1	D_{dr}/h_o	V_{tip}/U_o	Vo/U_o	U_{base}/U_o	U_{tip}/U_o	U_{drop}/U_o
1.19	0.38	110.8	2.20	0.54	-0.047	-0.036	0.76	0.81	0.78
2.07	0.52	59.7	2.11	0.82	0.004	-0.002	0.76	0.86	0.76
1.49	0.28	124.6	1.47	0.56	0.039	0.020	0.65	0.66	0.73
1.01	0.31	123.3	2.31	0.41	0.070	0.069	0.81	0.76	0.83
1.70	0.36	87.5	1.64	0.56	0.004	-0.002	0.78	0.80	0.80
1.48	0.51	83.4	2.16	0.67	-0.021	-0.017	0.72	0.73	0.72
2.80	0.34	86.7	1.58	0.67	0.080	0.046	0.70	0.71	0.71
1.35	0.28	111.8	2.04	0.41	0.122	0.130	0.68	0.67	0.73
1.06	0.44	90.5	2.20	0.71	-0.021	-0.041	0.67	0.70	0.71
1.66	0.43	106.9	1.70	0.61	0.016	-0.001	0.66	0.62	0.69
1.25	0.34	90.4	1.73	0.57	0.005	0.001	0.71	0.69	0.71
1.46	0.39	102.0	2.07	0.55	0.048	0.003	0.70	0.70	0.71
2.06	0.42	87.5	1.76	0.80	-0.032	0.005	0.73	0.73	0.76
2.21	0.53	43.4	1.71	0.87	-0.053	-0.025	0.56	0.62	0.59
1.14	0.36	88.7	1.88	0.51	0.021	0.024	0.74	0.75	0.73
1.51	0.59	70.0	1.93	0.75	-0.069	-0.028	0.73	0.71	0.68
1.59	0.51	95.5	1.72	0.86	-0.069	-0.074	0.75	0.71	0.70
1.76	0.57	80.9	2.02	0.74	-0.005	0.001	0.69	0.72	0.71
0.80	0.28	124.6	3.04	0.29	0.154	0.133	0.74	0.67	0.74
2.87	0.43	78.0	1.75	0.79	-0.016	-0.002	0.72	0.75	0.73
1.21	0.26	123.8	1.91	0.41	0.064	0.057	0.70	0.71	0.75
3.60	0.39	77.2	1.70	0.60	0.080	0.052	0.67	0.70	0.70
1.92	0.33	91.3	2.52	0.38	0.090	0.096	0.65	0.66	0.68
1.83	0.48	92.6	1.87	0.79	-0.027	-0.021	0.73	0.71	0.75
1.29	0.37	85.1	1.62	0.63	-0.027	-0.027	0.72	0.75	0.75
1.36	0.42	116.6	1.92	0.69	-0.004	-0.028	0.74	0.73	0.74
1.45	0.34	103.2	2.41	0.42	0.071	0.056	0.61	0.62	0.62
1.75	0.37	108.3	2.55	0.47	0.063	0.056	0.66	0.64	0.69
1.17	0.40	81.0	1.69	0.69	-0.031	-0.005	0.65	0.68	0.65
1.76	0.34	73.2	2.02	0.45	0.067	0.052	0.64	0.68	0.65
1.15	0.18	102.1	1.61	0.65	0.027	-0.005	0.65	0.66	0.68
1.21	0.41	122.6	2.47	0.44	0.012	0.001	0.65	0.66	0.71
1.78	0.55	64.2	2.92	0.53	0.020	0.007	0.77	0.80	0.74
1.06	0.36	72.6	2.03	0.58	-0.004	0.006	0.73	0.79	0.73

$L_r/h\sigma$	$D_r/h\sigma$	angle(deg)	k_t	$D_{cr}/h\sigma$	V_{tip}/U_0	V_0/U_0	U_{base}/U_0	U_{tip}/U_0	U_{dorp}/U_0
1.65	0.42	131.5	2.52	0.46	0.035	0.031	0.72	0.69	1.78
2.26	0.39	75.9	1.79	0.66	0.027	0.038	0.69	0.64	1.63
1.33	0.44	109.7	2.45	0.50	0.053	0.049	0.65	0.69	2.27
1.08	0.50	85.8	2.05	0.68	0.048	0.048	0.69	0.71	1.68
1.73	0.49	88.8	1.69	0.67	0.050	0.022	0.67	0.66	1.65
1.19	0.41	113.1	2.22	0.35	0.016	0.010	0.69	0.69	1.65
1.09	0.33	90.5	1.49	0.33	0.030	0.048	0.69	0.64	1.64
1.08	0.33	94.3	1.61	0.33	0.043	0.034	0.65	0.67	1.69
1.10	0.55	47.6	1.89	0.84	0.053	0.066	0.62	0.67	1.67
1.10	0.55	47.6	1.89	0.84	0.053	0.066	0.62	0.67	1.67
1.84	0.43	59.0	2.52	0.56	0.043	0.007	0.59	0.61	0.60
1.45	0.43	59.0	1.69	0.67	0.000	0.005	0.61	0.69	0.60
1.20	0.22	115.0	1.89	0.40	0.106	0.049	0.68	0.69	1.21
1.60	0.53	84.8	0.69	0.80	0.074	0.067	0.67	0.69	1.68
1.81	0.47	75.7	1.75	0.28	0.000	0.007	0.72	0.79	1.77
1.81	0.47	75.7	1.75	0.28	0.000	0.007	0.72	0.79	1.77
1.04	0.55	86.4	1.66	0.80	0.044	0.045	0.60	0.64	1.64
1.04	0.55	86.4	1.66	0.80	0.044	0.045	0.60	0.64	1.64
1.68	0.33	88.8	1.69	0.55	0.035	0.031	0.72	0.69	1.78

Wall type: Rough, 3 meter radius-of-curvature

$U_o = 6.2 \text{ m/s}$

$h_o = 6.0 \text{ mm}$

$k = 0.33 \text{ mm}$

L_r/h_o	D_r/h_o	angle(deg)	k_1	D_{gr}/h_o	V_{tip}/U_o	Vo/U_o	U_{base}/U_o	U_{tip}/U_o	U_{drop}/U_o
1.97	0.30	56.1	1.76	0.52	-0.023	-0.023	0.86	0.89	0.87
1.03	0.23	80.6	1.66	0.40	-0.043	-0.022	0.87	0.89	0.89
1.83	0.28	37.9	1.23	0.54	0.000	0.018	0.85	0.89	0.81
2.64	0.28	68.4	1.47	0.49	0.043	0.048	0.92	0.96	0.94
1.50	0.30	94.3	1.96	0.44	0.035	0.003	0.89	0.97	0.95
1.64	0.34	83.0	2.24	0.45	-0.023	-0.020	0.90	0.92	0.90
0.70	0.24	72.0	1.70	0.39	-0.008	-0.014	0.91	0.89	0.90
0.84	0.24	75.0	2.59	0.31	0.047	0.044	0.82	0.89	0.84
1.33	0.29	138.7	1.43	0.60	0.012	-0.011	0.92	0.85	0.95
0.85	0.28	123.8	1.80	0.43	-0.031	-0.033	0.96	0.97	0.97
1.51	0.27	73.6	0.94	0.45	0.000	-0.013	0.95	0.96	0.95
0.95	0.31	103.7	1.91	0.47	0.020	-0.006	0.89	0.91	0.91
1.73	0.32	55.8	1.92	0.49	0.023	-0.013	0.93	0.95	0.91
0.96	0.31	85.7	2.20	0.42	-0.031	-0.023	0.89	0.90	0.88
2.94	0.29	54.7	1.72	0.46	0.031	0.015	0.89	0.96	0.86
1.37	0.22	50.2	1.95	0.35	0.043	0.042	0.90	0.93	0.85
1.28	0.27	81.0	1.60	0.49	0.016	-0.001	0.93	0.94	0.94
1.92	0.30	69.4	1.70	0.48	0.031	0.037	0.94	0.96	0.94
1.15	0.28	81.2	2.08	0.39	0.043	0.064	0.95	0.95	0.95
0.80	0.33	91.2	2.11	0.50	-0.012	-0.010	0.88	0.94	0.93
1.36	0.29	76.4	1.64	0.49	0.023	0.004	0.81	0.84	0.83
1.70	0.24	73.5	1.72	0.40	0.067	0.073	0.85	0.84	0.82
2.01	0.27	86.3	1.52	0.45	0.031	0.052	0.88	0.92	0.89
0.87	0.23	114.4	1.65	0.38	0.000	-0.003	0.90	0.93	0.93
1.64	0.32	59.4	2.14	0.47	0.039	0.030	0.93	0.90	0.87
0.80	0.29	85.4	1.73	0.43	-0.039	-0.053	0.94	0.95	0.95
2.90	0.33	72.4	2.27	0.51	0.120	0.031	0.98	1.00	0.97
1.30	0.28	94.2	1.85	0.51	-0.023	0.000	0.85	0.89	0.86
2.39	0.36	69.0	2.16	0.47	0.020	0.032	0.90	0.95	0.92

L_f/h_0	D_f/h_0	angle(deg)	k_1	D_{cr}/h_0	V_{tip}/U_0	V_0/U_0	U_{base}/U_0	U_{tip}/U_0	U_{drop}/U_0
2.74	0.37	68.9	1.85	0.59	0.012	0.009	0.86	0.88	0.86
0.94	0.25	96.4	1.90	0.42	0.027	0.006	0.97	0.99	0.98
1.86	0.31	64.0	1.69	0.48	0.024	-0.016	0.84	0.88	0.85
2.67	0.28	85.8	1.78	0.40	0.063	0.064	0.88	0.88	0.87
1.30	0.27	60.1	1.61	0.51	-0.028	-0.010	0.83	0.85	0.85
1.54	0.43	92.7	2.07	0.59	-0.071	-0.077	0.88	0.88	0.90
1.60	0.32	65.7	1.81	0.54	-0.028	-0.064	0.85	0.88	0.85
2.86	0.25	69.7	1.63	0.36	-0.032	-0.009	0.85	0.91	0.89
1.31	0.22	79.3	1.30	0.38	0.036	0.038	0.94	0.93	0.93
2.51	0.36	96.7	1.83	0.57	-0.028	-0.013	0.83	0.84	0.84
1.10	0.22	71.4	1.55	0.44	0.004	-0.003	0.86	0.92	0.89
1.95	0.30	100.8	1.38	0.54	-0.036	-0.058	0.89	0.87	0.90
1.10	0.24	106.8	1.99	0.36	-0.040	-0.045	0.84	0.84	0.87
0.73	0.27	85.6	3.02	0.25	0.059	0.064	0.85	0.88	0.85
2.39	0.39	73.6	1.88	0.59	0.020	0.016	0.81	0.84	0.83
1.79	0.35	87.1	1.75	0.61	-0.079	-0.051	0.89	0.92	0.91
1.14	0.37	69.9	1.92	0.56	-0.048	-0.061	0.90	0.92	0.89
1.65	0.29	69.5	1.80	0.40	-0.008	0.012	0.91	0.93	0.90
1.56	0.27	87.6	1.10	0.55	-0.052	-0.048	0.89	0.90	0.90
0.88	0.24	94.8	2.10	0.33	0.040	0.038	0.86	0.89	0.89
3.24	0.31	56.7	1.27	0.62	-0.020	-0.021	0.89	0.94	0.91
3.02	0.57	50.0	2.03	0.72	-0.028	-0.033	0.87	0.91	0.87
0.74	0.18	96.3	1.89	0.28	-0.028	-0.025	0.92	0.91	0.92
0.99	0.37	106.8	1.72	0.60	-0.052	-0.079	0.92	0.90	0.90
0.85	0.26	85.1	2.01	0.43	-0.004	-0.003	0.94	0.94	0.94
1.85	0.26	74.2	1.52	0.51	-0.044	-0.035	0.84	0.89	0.86
1.08	0.28	60.2	1.86	0.40	-0.008	-0.014	0.94	1.00	0.91
2.21	0.32	79.4	1.43	0.72	-0.044	-0.055	0.81	0.84	0.83
2.87	0.41	57.8	1.46	0.76	-0.063	-0.053	0.77	0.82	0.80
1.56	0.43	74.2	1.58	0.74	-0.048	-0.069	0.84	0.87	0.85
1.91	0.39	100.1	1.52	0.66	-0.087	-0.085	0.91	0.86	0.90
3.36	0.34	58.6	1.80	0.54	0.040	0.044	0.88	0.92	0.85
1.69	0.32	105.4	1.58	0.50	0.008	0.008	0.83	0.82	0.86
1.83	0.31	91.5	1.59	0.50	-0.036	-0.029	0.82	0.83	0.83

L_f/ho	D_f/ho	angle(deg)	k_1	D_{gr}/ho	V_{tip}/U_o	Vo/U_o	U_{base}/U_o	U_{tip}/U_o	U_{drop}/U_o
1.79	0.34	82.7	1.79	0.54	0.012	0.026	0.77	0.76	0.77
1.08	0.40	71.4	1.76	0.64	-0.064	-0.027	0.78	0.81	0.81
1.66	0.42	64.4	1.52	0.80	-0.040	-0.052	0.76	0.83	0.79
0.77	0.41	58.5	2.12	0.60	-0.056	-0.038	0.88	0.86	0.85
1.35	0.38	143.3	1.64	0.63	-0.075	-0.047	0.85	0.88	0.86
2.41	0.35	98.8	2.46	0.36	0.087	0.087	0.81	0.81	0.83
1.17	0.24	113.4	1.87	0.28	0.079	0.059	0.82	0.83	0.85
0.93	0.28	100.1	1.79	0.48	0.000	-0.031	0.77	0.78	0.78
1.85	0.30	51.6	1.60	0.49	0.020	0.020	0.73	0.78	0.72
1.43	0.27	73.4	1.23	0.48	-0.008	-0.008	0.81	0.90	0.82
0.82	0.28	58.8	1.73	0.45	-0.012	0.003	0.81	0.84	0.83
2.06	0.26	89.6	1.41	0.46	0.028	0.011	0.71	0.76	0.76
0.87	0.30	87.8	1.68	0.52	-0.028	-0.043	0.84	0.87	0.86
2.20	0.36	88.7	2.32	0.46	0.004	0.001	0.83	0.83	0.81
1.27	0.32	74.4	1.65	0.60	-0.024	-0.021	0.79	0.87	0.82
1.67	0.35	66.4	1.68	0.62	-0.024	-0.033	0.81	0.86	0.83
1.12	0.23	107.0	1.99	0.26	0.079	0.099	0.79	0.79	0.81
1.35	0.31	82.4	1.76	0.53	-0.068	-0.052	0.83	0.86	0.84
1.28	0.35	96.2	2.07	0.54	-0.004	0.017	0.83	0.83	0.84
1.52	0.31	72.8	1.70	0.51	-0.016	-0.013	0.79	0.80	0.79
2.12	0.33	64.5	1.92	0.49	0.008	0.015	0.77	0.78	0.74
1.56	0.37	48.4	1.79	0.62	-0.032	-0.041	0.75	0.81	0.75
0.79	0.27	94.0	2.15	0.41	-0.020	-0.018	0.80	0.79	0.79
1.05	0.28	94.9	1.97	0.40	0.020	0.017	0.84	0.79	0.81
1.17	0.37	137.8	1.59	0.59	-0.072	-0.074	0.82	0.67	0.83
0.99	0.26	103.3	1.86	0.48	0.020	0.022	0.84	0.86	0.85
1.85	0.34	67.7	1.31	0.54	-0.020	-0.011	0.75	0.80	0.77
1.38	0.29	85.6	2.43	0.41	-0.004	-0.014	0.88	0.88	0.88
1.57	0.26	69.3	2.23	0.42	0.036	0.046	0.83	0.84	0.82
1.33	0.21	122.7	1.89	0.35	0.052	0.073	0.83	0.79	0.86
2.51	0.44	60.7	1.42	0.86	0.004	0.002	0.77	0.82	0.76
1.28	0.35	80.8	2.38	0.49	-0.008	-0.023	0.76	0.79	0.77
1.88	0.33	69.8	1.89	0.54	-0.008	-0.033	0.68	0.72	0.69
1.48	0.40	79.8	1.46	0.58	0.008	-0.009	0.73	0.77	0.73

L_t/h_0	D_t/h_0	angle(deg)	k_1	D_{gr}/h_0	V_{tip}/U_0	V_0/U_0	U_{base}/U_0	U_{tip}/U_0	U_{drop}/U_0
1.58	0.32	74.1	2.23	0.45	0.024	0.029	0.70	0.73	0.72
2.40	0.32	52.5	1.73	0.51	0.020	0.018	0.73	0.79	0.74
1.46	0.42	81.6	1.78	0.71	-0.064	-0.063	0.74	0.77	0.75
1.27	0.28	84.8	2.33	0.41	0.028	0.024	0.80	0.82	0.81
2.53	0.30	78.2	1.65	0.45	0.080	0.122	0.76	0.76	0.73
1.21	0.34	104.9	1.63	0.60	-0.044	-0.065	0.77	0.81	0.79
2.25	0.30	106.3	1.65	0.58	-0.008	0.024	0.76	0.75	0.78
1.12	0.32	71.3	2.13	0.37	-0.020	-0.033	0.78	0.78	0.76
1.54	0.27	56.5	1.77	0.39	0.016	0.004	0.72	0.79	0.71
1.09	0.29	102.2	2.87	0.28	0.084	0.065	0.72	0.72	0.74
1.05	0.18	78.8	2.30	0.28	0.060	0.065	0.78	0.76	0.74
1.06	0.39	90.4	1.62	0.59	-0.004	-0.011	0.72	0.75	0.75
1.13	0.31	87.1	2.39	0.43	0.008	0.024	0.73	0.76	0.74
1.12	0.42	63.4	1.88	0.69	-0.052	-0.063	0.79	0.80	0.78
2.29	0.43	58.3	2.20	0.53	0.020	0.016	0.70	0.73	0.72
1.04	0.32	110.3	1.90	0.53	-0.016	-0.026	0.76	0.81	0.79
1.25	0.22	123.8	1.68	0.33	0.084	0.072	0.74	0.73	0.76
1.43	0.34	112.6	2.09	0.41	0.016	0.027	0.70	0.68	0.70
1.39	0.37	72.5	1.99	0.60	-0.032	-0.024	0.73	0.79	0.76
2.01	0.34	67.5	2.75	0.36	0.036	0.022	0.79	0.79	0.74
1.20	0.31	72.2	1.93	0.49	0.004	-0.012	0.75	0.84	0.78
1.03	0.33	94.1	1.87	0.56	-0.044	-0.037	0.76	0.77	0.76
1.23	0.27	110.2	2.05	0.34	0.076	0.055	0.80	0.75	0.79
2.55	0.52	28.1	1.68	0.86	-0.084	-0.066	0.70	0.78	0.71
1.28	0.31	99.2	1.87	0.62	0.004	0.027	0.75	0.73	0.74
2.67	0.37	60.8	1.91	0.52	0.028	0.011	0.80	0.85	0.80
1.40	0.30	121.4	2.64	0.28	0.100	0.083	0.74	0.74	0.77
1.20	0.32	66.1	1.96	0.54	0.008	-0.010	0.70	0.72	0.69
1.18	0.32	77.1	2.37	0.35	0.012	0.005	0.63	0.65	0.64
1.41	0.39	78.6	1.75	0.54	0.004	-0.015	0.69	0.73	0.69
0.94	0.35	92.0	1.78	0.56	-0.064	-0.058	0.70	0.70	0.69
2.19	0.48	127.2	2.16	0.62	-0.044	-0.043	0.70	0.62	0.65
0.92	0.31	98.2	2.58	0.36	0.028	0.051	0.63	0.62	0.62
0.96	0.25	98.9	1.65	0.43	0.004	0.006	0.74	0.74	0.73

L_r/h_o	D_r/h_o	angle(deg)	k_1	D_{gr}/h_o	V_{tip}/U_o	Vo/U_o	U_{base}/U_o	U_{tip}/U_o	U_{drop}/U_o
2.13	0.51	61.9	2.42	0.66	0.000	-0.017	0.69	0.68	0.65
1.96	0.41	55.2	1.81	0.64	-0.024	-0.040	0.70	0.79	0.71
1.68	0.39	114.9	3.10	0.36	0.020	0.019	0.69	0.68	0.69
1.57	0.42	80.0	2.11	0.62	-0.044	-0.050	0.75	0.76	0.75
1.88	0.31	54.3	1.23	0.60	0.040	-0.007	0.70	0.70	0.70
1.24	0.36	107.7	2.28	0.48	0.000	-0.012	0.79	0.71	0.76
1.06	0.34	139.7	2.45	0.37	0.004	0.018	0.67	0.66	0.69
1.36	0.27	102.6	2.52	0.32	0.092	0.091	0.71	0.69	0.70
1.58	0.36	55.0	1.78	0.58	-0.028	-0.040	0.73	0.81	0.72
1.49	0.37	75.3	1.61	0.53	-0.028	-0.036	0.71	0.73	0.70
1.66	0.38	83.2	1.85	0.61	-0.004	0.011	0.66	0.68	0.67
0.82	0.34	91.2	1.85	0.53	-0.040	-0.040	0.71	0.75	0.72
1.48	0.33	109.5	2.71	0.37	0.160	0.094	0.70	0.72	0.74
1.40	0.46	104.0	1.87	0.93	-0.040	-0.068	0.70	0.72	0.71
1.26	0.35	108.7	1.72	0.57	-0.044	-0.065	0.71	0.69	0.67
1.38	0.30	102.7	1.56	0.51	-0.004	0.007	0.75	0.78	0.81
1.16	0.24	84.3	1.80	0.37	0.044	0.037	0.72	0.72	0.70
1.79	0.42	64.6	1.61	0.68	-0.020	-0.031	0.65	0.69	0.66
0.98	0.40	89.5	1.82	0.66	-0.008	-0.037	0.69	0.72	0.70
2.30	0.36	90.2	1.41	0.69	-0.044	-0.032	0.77	0.80	0.78
1.38	0.29	128.7	1.71	0.51	-0.028	0.010	0.72	0.73	0.73
0.91	0.28	132.8	1.74	0.54	0.028	0.017	0.70	0.68	0.68
1.05	0.48	87.8	2.96	0.51	0.004	-0.013	0.66	0.72	0.68
1.31	0.29	69.1	1.67	0.55	0.000	0.005	0.69	0.75	0.70

REFERENCES

- Andreopoulos, J. and Wood, D. H. 1982. "The response of a turbulent boundary layer to a short length of surface roughness," *Journal of Fluid Mechanics*, Vol. 118, pp. 143-164.
- Antonia, R. A. and Luxton, R. E. 1971. "The response of a turbulent boundary layer to a step change in surface roughness Part 1. Smooth to rough," *Journal of Fluid Mechanics*, Vol. 48, pp. 721-761.
- Benjamin, T. B. 1957. "Wave formation in laminar flow down an inclined plane," *Journal of Fluid Mechanics*, Vol. 2, pp. 554-574.
- Bergwerk, W. 1959. "Flow patterns in diesel nozzle spray holes," *Proceedings of the Institute of Mechanical Engineers*, Vol. 173, pp. 655-660.
- Binnie, A. M. 1957. "Experiments on the onset of wave formation flowing down a vertical plate," *Journal of Fluid Mechanics*, Vol. 2, pp. 551-553.
- Blake, W. K. 1970. "Turbulent boundary-layer wall-pressure fluctuations on smooth and rough walls," *Journal of Fluid Mechanics*, Vol. 44, pp. 637-660.
- Brattberg, T., Toombes, L. and Chanson, H. 1998. "Developing air-water shear layers of two-dimensional water jets discharging into air," ASME FED Summer Meeting June 21-25, 1998, Washington, D.C., Paper FEDSM98-4805, pp. 1-7.
- Briffa, F. E. and Dombrowski, N. 1966. "Entrainment of air into a liquid spray," *American Institute of Chemical Engineering Journal*, Vol. 12, pp. 708-717.
- Brown, D. R. 1961. "A Study of the behavior of a thin sheet of moving liquid," *Journal of Fluid Mechanics*, Vol. 10, pp. 297-305.
- Chubb, D. L., Calfo, F. D., McConley, M. W., McMaster, M. S., and Afjeh, A. A. 1993. "Geometry of Thin Liquid Sheet Flows," *American Institute of Aeronautics and Astronautics Journal*, Vol. 32, No. 6, pp. 1325-1328.
- Clift, R., Grace, J. R. and Weber, M. E. 1978. *Bubbles, Drops, and Particles*. Academic Press Inc., NY.
- Coleman, H. W. and Steele, Jr., W. G. 1989. *Experimentation and Uncertainty Analysis for Engineers*. John Wiley & Sons, NY.
- Craik, A. D. D. 1966. "Wind-generated waves in thin liquid films," *Journal of Fluid Mechanics*, Vol. 26, pp. 369-392.

- Crapper, G. D., Dombrowski, N., Jepson, W. P. and Pyott, G. A. 1973. "A note on the growth of Kelvin-Helmholtz waves on thin liquid sheets," *Journal of Fluid Mechanics*, Vol. 57, pp. 671-672.
- Crapper, G. D., Dombrowski, N. and Pyott, G. A. 1975. "Large amplitude Kelvin-Helmholtz waves on thin liquid sheets," *Proceedings of the Royal Society of London*, Vol. A342, No. 1629, pp. 209-224.
- Davies, J. T. 1972. *Turbulence Phenomena*. Academic Press Inc., NY.
- Dombrowski, N. and Fraser, R. P. 1954. "A photographic investigation into the disintegration of liquid sheets," *Philosophical Transactions of the Royal Society of London*, Vol. 247, No. A924, pp. 101-130.
- Dombrowski, N. and Hooper, P. C. 1962. "The effect of ambient density on drop formation in sprays," *Chemical Engineering Science*, Vol. 17, pp. 291-305.
- Finley, P. J., Khoo, C. P. and Chin, J. P. 1966. "Velocity measurements in a thin turbulent water layer," *La Houille Blanche*, Vol. 21, pp. 713-721.
- Ford, R. E. and Furnidge, C. G. L. 1967. "The formation of drops from viscous Newtonian liquids sprayed through fan-jet nozzles," *British Journal of Applied Physics*, Vol. 18, pp. 335-349.
- Gibbings, J. C. and Al-Shukr, S. M. 1997. "Effect of sandpaper roughness and stream turbulence on the laminar layer and its transition," *Aeronautical Journal*, Vol. 101, pp. 17-24.
- Goedde, E. F. and Yuen, M. C. 1970. "Experiments on liquid jet instability," *Journal of Fluid Mechanics*, Vol. 40, pp. 495-511.
- Grant, R. P. and Middleman, S. 1966. "Newtonian jet stability," *American Institute of Chemical Engineering Journal*, Vol. 12, pp. 669-678.
- Grass, A. J. 1971. "Structural features of turbulent flow over smooth and rough boundaries," *Journal of Fluid Mechanics*, Vol. 50, pp. 233-255.
- Hanratty, T. J. and Engen, J. M. 1957. "Interaction between a turbulent air stream and a moving water surface," *American Institute of Chemical Engineering Journal*, Vol. 3, pp. 209-304.
- Hoyt, J. W. and Taylor, J. J. 1977a. "Waves on water jets," *Journal of Fluid Mechanics*, Vol. 83, pp. 119-127.
- Hoyt, J. W. and Taylor, J. J. 1977b. "Turbulence structure in a water jet discharging in air," *Physics of Fluids*, Vol. 20, Pt. II, No. 10, pp. S253-S257.

- Hoyt, J. W. and Taylor, J. J. 1979. "Effect of nozzle shape and polymer additives on water jet appearance," *Journal of Fluids Engineering*, Vol. 101, pp. 304-308.
- Keane, R. D. and Adrian, R. J. 1992. "Theory of cross-correlation analysis of PIV images," *Measurement of Science and Technology* 2, pp. 191-215.
- Kim, H. T., Kline, S. J. and Reynolds, W. C. 1971. "The production of turbulence near a smooth wall in a turbulent boundary layer," *Journal of Fluid Mechanics*, Vol. 50, pp. 133-160.
- Kline, S. J. and McClintock, F. A. 1953. "Describing uncertainties in single-sample experiments," *Mechanical Engineering*, Vol. (Jan)75, pp. 3-8.
- Kline, S. J., Reynolds, W. C., Schraub, F. A. and Runstaller, P. W. 1967. "The structure of turbulent boundary layers," *Journal of Fluid Mechanics*, Vol. 95, pp. 741-773.
- Klebanoff, P. S. 1954. "Characteristics of turbulence in a boundary layer with zero pressure gradient," NACA Technical Note 3178.
- Knuth, E. L. 1954. "The mechanics of film cooling—part I," *Jet Propulsion*, Vol. 24, pp. 359-610.
- Kobayashi, R. and Fujisawa, N. 1983. "Turbulence measurements in wall jets along strongly concave surfaces," *Acta Mechanica*, Vol. 47, pp. 39-52.
- Komori, S., Hiraga, Y., Murakami, Y. and Ueda, H. 1987. "The generation of surface-renewal eddies in an open channel flow," *Proceedings of the Second International Symposium on Transport Phenomena in Turbulent Flows*, Tokyo, pp. 75-85.
- Kothe, D. B. and Mjolsness, R. C. 1992. "Ripple: a new model for incompressible flows with free surfaces," *American Institute of Aeronautics and Astronautics Journal*, Vol. 30, pp. 2694-2700.
- Krogstad, P.-Å. And Antonia, R. A. 1994. "Structure of turbulent boundary layers on smooth and rough walls," *Journal of Fluid Mechanics*, Vol. 277, pp. 1-21.
- Krogstad, P.-Å. And Antonia, R. A. and Browne, L. W. B. 1992. "Comparison between rough- and smooth-wall turbulent boundary layers," *Journal of Fluid Mechanics*, Vol. 245, pp. 599-617.
- Lee, H. C. 1974. "Drop formation in a liquid jet," *IBM Journal of Research and Development*, Vol. 18, pp. 364-369.
- Ligrani, P. M., Moffat, R. J. and Kays, W. M. 1979. "The thermal and hydrodynamic behavior of thick, rough-wall, turbulent boundary layers," Report HMT-29, Thermosciences Divison, Dept. of Mechanical Engineering, Stanford University.

Lin, S. P. and Reitz, R. D. 1998. "Drop and spray formation from a liquid jet," *Annual Review of Fluid Mechanics*, Vol. 30, pp. 85-105.

Lord Rayleigh 1945. *The Theory of Sound*. Dover Publications, New York.

Lourenco, L. and Krothapalli, A. 1995. "On the accuracy of velocity and vorticity measurements with PIV," *Experiments in Fluids*, Vol. 18, pp. 421-428.

Mansour, A. and Chigier, N. 1990. "Disintegration of liquid sheets," *Physics of Fluids*, Vol. A2, No. 7, pp. 706-719.

Mansour, A. and Chigier, N. 1991. "Dynamic behavior of liquid sheets," *Physics of Fluids*, Vol. A3, No. 12, pp. 2971-2980.

McCarthy, M. J. and Molloy, N. A. 1974. "Review of stability of liquid jets and the influence of nozzle design," *Chemical Engineering Journal*, Vol. 7, pp. 1-20.

Merrill, C. F. and Sarpkaya, T. 1998. "Spray formation at the free surface of a liquid wall jet," *AIAA Paper 98-0442*.

Miles, J. W. 1960. "The hydrodynamic stability of a thin film of liquid in uniform shearing motion," *Journal of Fluid Mechanics*, Vol. 8, pp. 593-610.

Moffat, R. J. 1982. "Contributions to the theory of single-sample uncertainty analysis," *Journal of Fluids Engineering*, Vol. 104, pp. 250-260.

Nayfeh, A. H. 1970. "Nonlinear stability of a liquid jet," *Physics of Fluids*, Vol. 13, pp. 841-847.

Nezu, I. and Nakagawa, H. 1993. *Turbulence In Open Channel Flows*. AA Balkema, Rotterdam, The Netherlands.

Nezu, I. and Rodi, W. 1986. "Open-channel flow measurement with a laser doppler anemometer," *Journal of Hydraulic Engineering*, Vol. 112, pp. 335-355.

Ohnesorge, W. 1936. "Formation of drops by nozzles and the breakup of liquid jets," *Zeitschrift für Angewandte Mathematik und Mechanik*, Vol. 16., pp. 355-358.

Pimenta, M. M., Moffat, R. J. and Kays, W. M. 1975. "Turbulent boundary layer: an experimental study of the transport of momentum and heat with the effect of roughness," Report HMT-21, Thermosciences Div., Dept. of Mechanical Engineering, Stanford University.

Ranz, W. E. 1958. "Some experiments on orifice sprays," *Canadian Journal of Chemical Engineering*, Vol. 36, p. 175-181.

- Raupach, M. R. 1981. "Conditional statistics of Reynolds stress in rough-wall and smooth-wall turbulent boundary layers," *Journal of Fluid Mechanics*, Vol. 108, pp. 363-382.
- Rein, M. 1996. "The transitional regime between coalescing and splashing drops," *Journal of Fluid Mechanics*, Vol. 306, pp. 145-165.
- Rein, M. 1998. "Turbulent open-channel flows: drop-generation and self-aeration," *Journal of Hydraulic Engineering*, Vol. 124, pp. 98-102.
- Reitz, R. D. 1978. "Atomization and other breakup regimes of a liquid jet," Ph.D. Thesis, Princeton University, p. 134.
- Robinson, S. K. 1991. "Coherent motions in the turbulent boundary layer," *Annual Review of Fluid Mechanics*, Vol. 23, pp. 601-639.
- Rouse, H. and Abol-Fetouh, A.-H. 1950. "Characteristics of irrotational flow through axially symmetric orifices," *Journal of Applied Mechanics*, Vol. 17, pp. 421-426.
- Rouse, H., Howe, J. W. and Metzler, D. E. 1951. "Experimental investigation of fire hose monitors and nozzles," *Proceedings of the American Society of Civil Engineers, Hydraulics Division*, Vol. 77, Sep No. 92.
- Roy, R. P. and Jain, S. 1989. "A study of thin water film flow down an inclined plate without and with countercurrent air flow," *Experiments in Fluids*, Vol. 7, pp. 318-329.
- Ruff, G. A., Sagar, A. D. and Faeth, G. M. 1989. "Structure and mixing properties of pressure-atomized sprays," *American Institute of Aeronautics and Astronautics Journal*, Vol. 27, pp. 901-908.
- Rupe, J. H. 1962. "On the dynamic characteristics of free liquid jets and a partial correlation with orifice geometry," *Jet Propulsion Laboratory Pasadena, CA Technical Report 32-207*, p. 207.
- Sarpkaya, T. 1977. "In-line and transverse forces on cylinders in oscillatory flow at high Reynolds numbers," *Journal of Ship Research*, Vol. 21, pp. 200-216.
- Sarpkaya, T. 1986. "Force on a circular cylinder in viscous oscillatory flow at low Keulegan-Carpenter numbers," *Journal of Fluid Mechanics*, Vol. 165, pp. 61-71.
- Sarpkaya, T. and Neubert, D. E. 1994. "Interaction of a streamwise vortex with a free surface," *American Institute of Aeronautics and Astronautics Journal*, Vol. 32, pp. 594-600.
- Schlichting, H. 1979. *Boundary-Layer Theory*. 7th Edition. McGraw-Hill Inc., NY.

- Smith, C. R. and Walker, J. D. A. 1995. "Turbulent wall-layer vortices," in *Fluid Vortices*, editor S. I. Green (Kluwer Academic Pub.: Boston, MA), pp. 235-290.
- Squire, H. B. 1953. "Investigation of the instability of a moving liquid film," *British Journal of Applied Physics*, Vol. 4, pp. 167-169.
- Sterling, A. M. and Sleicher, C. A. 1975. "The instability of capillary jets," *Journal of Fluid Mechanics*, Vol. 68, pp. 477-495.
- Tominaga, A. and Nezu, I. 1992. "Velocity profiles in steep open-channel flows," *Journal of Hydraulic Engineering*, Vol. 118, pp. 73-90.
- Tseng, L.-K., Ruff, G. A. and Faeth, G. M. 1992. "Effects of gas density on the structure of liquid jets in still gases," *American Institute of Aeronautics and Astronautics Journal*, Vol. 30, pp. 1537-1544.
- Van der Hegge-Zijnen, B. G. 1928. *Verhandel. Koninkl. Akad. Weten. Amsterdam*, Vol. 31, p. 499.
- Van Rossum, J. J. 1959. "Experimental investigation of horizontal liquid films: wave formation, atomization, film thickness," *Chemical Engineering Science*, Vol. 11, pp. 35-52.
- Volkart, P. 1980. "The mechanism of air bubble entrainment in self-aerated flow," *International Journal of Multiphase Flow*, Vol. 6, pp. 411-423.
- Weber, C. 1931. "Zum Zerfall eines Flüssigkeitsstrahles," *Zeitschrift für Angewandte Mathematik und Mechanik*, Vol. 11, pp. 136-154.
- Wu, P.-K. and Faeth, G. M. 1995. "Onset and end of drop formation along the surface of turbulent liquid jets in still gases," *Physics of Fluids*, Vol. 7, pp. 2915-2917.
- Wu, P.-K., Ruff, G. A. and Faeth, G. M. 1991. "Primary breakup in liquid-gas mixing layers," *Atomization and Sprays*, Vol. 1, pp. 421-440.
- Wu, P.-K., Tseng, L.-K. and Faeth, G. M. 1992. "Primary breakup in gas/liquid mixing layers for turbulent liquids," *Atomization and Sprays*, Vol. 2, pp. 295-317.
- Yuen, M. C. 1968. "Non-linear capillary instability of a liquid jet," *Journal of Fluid Mechanics*, Vol. 33, p. 151-163.

INITIAL DISTRIBUTION LIST

1. Defense Technical Information Center 2
8725 John J. Kingman Rd., STE 0944
Ft. Belvoir, VA 22060-6218
2. Dudley Knox Library 2
Naval Postgraduate School
411 Dyer Rd.
Monterey, CA 93943-5101
3. Department Chairman, Code ME..... 2
Department of Mechanical Engineering
Naval Postgraduate School
Monterey, CA 93943-5000
4. Professor T. Sarpkaya, Code ME-SL..... 5
Department of Mechanical Engineering
Naval Postgraduate School
Monterey, CA 93943-5000
5. Curricular Officer, Code 34 1
Naval Engineering Department
Naval Postgraduate School
Monterey, CA 93943-5000
6. Commander, Carderock Division 3
Naval Surface Warfare Center
9500 MacArthur Boulevard
West Bethesda, MD 20817-5700
ATTN: LCDR Craig F. Merrill

DUDLEY KNOX LIBRARY



3 2768 00366895 5